Molecular-scale analysis of cardiac calcium nanodomains and remodelling using expansion microscopy

Thomas Michael Dent Sheard, BSc, MPhil

Submitted in accordance with the requirements for the degree of

Doctor of Philosophy

The University of Leeds

School of Biomedical Sciences

June, 2021

Declaration of authorship

The candidate confirms that the work submitted is his own, except where work which has formed part of jointly-authored publications has been included. The contribution of the candidate and the other authors to this work has been explicitly indicated below. The candidate confirms that appropriate credit has been given within the thesis where reference has been made to the work of others.

Acknowledgements

I begin this thesis by thanking all the people who have supported me.

Izzy Jayasinghe, whose inspiring and personable mentorship has made the PhD a truly enjoyable experience.

Andrew Smith, whose guidance and contributions along the way have been invaluable.

John Colyer, for being a positive force as a supervisor and during my secondment to Badrilla, widening my perspectives on the best ways to approach science.

The DiMeN DTP for funding and training, and Emily Goodall for overseeing the DTP, my development has benefited from your hard work.

Sally Boxall, for providing endless support in the microscopy facility.

David Crossman, my host in Auckland. I will never forget catching snapper listening to Tool.

Miriam Hurley, who contributed so much to this research, both as a lab-mate and as a friend.

Ruth Norman, for help with monocrotaline and stimulation experiments, and being a beacon of positivity and reassurance.

Ed White and Eleftheria Pervolaraki, for their help during the monocrotaline project.

Derek Steele, for his wisdom regarding peptide experiments.

Sarah Calaghan, for fostering a togetherness in the cardiac group which made Garstang level 7 a joy to be a part of.

All cardiac group members, past and present.

Rob Walmsley, for offering support and friendship since we started our PhDs.

Harley and Maxx (of the Tenacious3), my music amigos.

Tim and Matt, supporting the reds and trips to Saltaire brewery.

Those at Leeds hockey club, up the magnificent 7s!

Jack and Jay, who have been with me through highs and lows.

Mum, Dad and Sarah, for their ever-present love and support.

Author publications

Work which has been presented in this thesis has featured in joint-author publications which are listed below. The contributions of co-authors to the work presented in this thesis have been listed in the various Methods sections.

Expansion microscopy of cardiomyocytes and α-actinin from Chapter 3, ryanodine receptor clusters and phosphorylation from Chapter 4, plus remodelling in monocrotaline-induced heart failure from Chapter 5, were included in Sheard *et. al.* (2019). The author performed all expansion microscopy experiments. The co-author contributions involved providing materials towards primary experiments, assistance with cardiomyocyte isolation, some data analyses, and writing of the manuscript.

The book chapter Sheard *et. al.* (2020) revisited figures from Sheard *et. al.* (2019) and provided more detail regarding the practical approach of applying expansion microscopy to cardiomyocytes.

Sheard, T. M., Hurley, M. E., Colyer, J., White, E., Norman, R., Pervolaraki, E., ... & Jayasinghe, I. (2019). Three-dimensional and chemical mapping of intracellular signaling nanodomains in health and disease with enhanced expansion microscopy. *ACS nano*, *13*(2), 2143-2157.

Sheard, T. M., & Jayasinghe, I. (2020). Enhanced expansion microscopy to measure nanoscale structural and biochemical remodeling in single cells. *Methods in Cell Biology*, *161*, 147-180.

Communications

Oral

"Visualising calcium-signalling nanodomain remodelling in right ventricular failure with X10 expansion microscopy". **3rd place prize**. *Post-graduate symposium*. 2019. Leeds, UK.

"Visualising cardiac signaling nanodomains with expansion microscopy". *Invited seminar at University of Auckland*. 2018. Auckland, New Zealand.

"Molecular-scale analysis of pathological remodelling in cardiomyocytes". *North East Post Graduate conference*. 2017. Newcastle, UK.

Poster

"Enhanced expansion microscopy allows three-dimensional and biochemical mapping of intracellular signalling nanodomains at single channel resolution". *Single Molecule Localisation Microscopy Symposium*. 2019. Delft, Netherlands.

"Expansion microscopy reveals dyadic ryanodine receptor nanodomain phosphorylation changes in monocrotaline-induced right ventricular heart failure." *Northern Cardiovascular Research Group meeting*. 2019. Leeds, UK.

"Visualising pathological remodelling in monocrotaline-induced heart failure with expansion microscopy". **1st place prize**. *Post-graduate symposium*. 2018. Leeds, UK.

"Visualising pathological remodelling in monocrotaline-induced heart failure with expansion microscopy". *MRC conference*. 2018. Manchester, UK.

Abstract

Ryanodine receptors (RyRs) are Ca^{2+} channels inside cardiomyocytes. Interior clusters of RyRs associated with t-tubules (called dyads) are poorly characterised due to the lack of a suitable imaging technique. The spatial arrangements of the anchoring protein junctophilin (JPH) and RyR phosphorylation, which both affect RyR function, are poorly understood. Dysfunctional Ca^{2+} signalling in heart failure (HF) can arise due to structural remodelling or RyR hyper-phosphorylation. In right ventricular (RV) HF, a leading cause of death with no targeted treatment, cluster remodelling and phosphorylation has yet to be explored. Stem cell-derived cardiomyocytes (SC-CMs) are used as comparable models to adult, but the maturity of the Ca^{2+} signalling structures is unknown.

A 3-dimensional (3D) imaging technique termed enhanced expansion microscopy (EExM) was optimised to image RyR clusters with 15 nm lateral resolution, and was implemented at sufficient depths to visualise dyadic clusters for the first time.

EExM imaging of surface clusters was similar to DNA-PAINT, and allowed a detailed description of the organisation of RyR and JPH in interior clusters. Phosphorylated serine-2808 (pSer2808) was quantified *in situ*, while experimentally-induced changes to pSer2808 were detected after β-adrenergic stimulation.

Cluster remodelling was observed in monocrotaline-induced RV HF, entailing fragmented RyR interior clusters and fewer JPH. pSer2808 was increased in interior clusters and was concentrated towards the centre of surface clusters.

Induced pluripotent SC-CMs lacked t-tubule precursors but had primitive Ca^{2+}-signalling clusters. Co-clustering of RyR and JPH was prominent at Day2, while a sarcomeric RyR arrangement was more visible between Day4 and Day7.

The enhanced resolution and 3D capabilities of EExM have revealed structural and functional insights in healthy cells, pathological cluster remodelling in MCT-RV HF, and has characterised the structural maturity of SC-CMs, at an unprecedented level of spatial detail.

Contents

List of tables

List of figures

Chapter 1. Introduction

1.1 Preface

Each heart cell (or cardiomyocyte) is a highly specialised unit, functioning in a contracting syncytium which controls the flow of blood around the body. Cellular contraction is the culmination of a vast array of dynamic, chemical signalling processes and complex protein organisation.

Scientific understanding of how cardiomyocytes function has progressed significantly over the last decade on a multitude of fronts (structural, functional, pathological), owing to evolving experimental technologies. Research has uncovered fundamental mechanisms relating to excitation-contraction (EC) coupling and the underlying cycles of calcium (Ca^{2+}) release. Insights into the dysfunction that arises during heart failure (HF), where cardiac output does not meet the body's demands for oxygen, have enabled significant upgrades in diagnoses and clinical treatments. In addition, stem cell-derived cardiomyocytes (SC-CMs) have been created and used to learn about and treat cardiac diseases.

Despite all of the discoveries made over the 50 years since the earliest observations of Ca^{2+} release in cardiac muscle (Allen and Blinks, 1978), much is still to be determined. While there is a detailed picture of the clustering organisation of Ca^{2+} channel proteins (called ryanodine receptors (RyRs)) at the surface of a cardiomyocyte (Jayasinghe *et al.*, 2018), the same description does not exist for interior clusters (known as dyads) deeper in the cell, which account for the majority (75%) of a cardiomyocyte's Ca^{2+} release channels (Shen *et al.*, 2018). Further, imaging is yet to provide *in situ* information on the incidence of post-translational modifications (such as phosphorylation) which are critical in regulating channel function.

Improved understanding of subcellular structures has been enabled by advances in imaging techniques. Novel optics and approaches have lead to improved microscopy techniques which are able to circumvent traditional biophysical limits on the achievable resolution, allowing structures to be visualised with more detail. Super-resolution microscopy techniques are fluorescent imaging techniques which now allow scientists to visualise the nanoscale arrangements of proteins within biological samples. It is with such techniques that it could be possible to obtain a better understanding of the structural organisation of the dyadic organisation of RyRs.

Cardiovascular disease (CVD) is the umbrella term covering all instances of HF, which can occur due to many different reasons, including cardiomyopathy, pulmonary hypertension, inherited conditions, arrhythmias, valve damage and viral infection. CVD is the leading cause of death globally by non-communicable disease (Wang *et al.*, 2016). In the UK, CVD accounts for 27% of all deaths, equating to around 460 deaths every day (~167,000 per year) (*Heart Statistics, British Heart Foundation*, 2021). An estimated 7.4 million individuals live with CVD in Britain, leading to an average annual healthcare cost of around £9 billion.

In right ventricular (RV) HF, which is the leading cause of death in patients with pulmonary arterial hypertension (PAH), the RV fails to generate enough stroke volume to meet bodily demands. RV HF is a serious disease accounting for 3% of HF admissions (Greyson, 2008). There is a poor prognosis for those afflicted, with the median survival time just 5-6 years (Benoist *et al.*, 2014). While some traditional hallmarks of HF have been observed in failing RV cardiomyocytes, including structural remodelling and compromised Ca^{2+} signalling, little is known about remodelling within RyR clusters at the individual protein level. It is important that more is understood about the pathological mechanisms in RV HF, as there are no specialised effective treatments for this disease.

The work contained within this thesis is motivated by a desire to better understand RyR clusters in healthy cardiomyocytes, and also in failing cardiomyocytes from an animal model of RV HF. The focus is on the molecular-scale organisation of RyRs, the arrangement of neighbouring proteins, such as the anchoring protein junctophilin, and also RyR phosphorylation. In addition, the work aimed to characterise the structural maturity of SC-CMs, whose morphology differs significantly from adult cardiomyocytes. In order to obtain these insights, the novel super-resolution technique called expansion microscopy (ExM) has been adapted to visualise nanometre-sized structures.

1.2 Sarcolemma, sarcoplasmic reticulum and t-tubules

The cycling of ions between the extracellular space and various intracellular compartments is critical to cardiac contraction.

The sarcolemma is the water-impermeable lipid bilayer which forms the external membrane of the cardiomyocyte, enveloping the bundles of actin and myosin myofilaments (Figure 1-1). The sarcolemma (and the ion channels situated there) is responsible for maintaining a gradient of ions between the cytosol and the extracellular matrix. These gradients account for the fact

that cardiomyocytes are polarised, meaning there is an electrical voltage across the membrane. L-type Ca^{2+} channels (LTCCs) (also known as dihydropiridine receptors) situated at the sarcolemma are the main Ca^{2+} influx mechanism into the cell. Another sarcolemmal ion channel involved in Ca^{2+} homeostasis is the sodium (Na^+)-Ca^{2+} exchanger (NCX), which pumps one Ca^{2+} out for every three Na^+ ions into the cell, but can also operate in reverse mode to enable Ca^{2+} influx. A number of other channels and receptors which are crucial to cellular function are also situated at the sarcolemma, including Na^+ channels, potassium (K^+) channels, a Na^+-K^+ pump, and chloride channels.

The sarcoplasmic reticulum (SR) is a tubular, membranous network which acts as the internal store for Ca^{2+} (Figure 1-1). Release of Ca^{2+} from the SR occurs through the ryanodine receptor-2 (RyR) channels, which are clustered at specialised junctional regions also known as Ca^{2+} release units (s). The junctional SR is often situated adjacent to the sarcolemma, bringing the RyRs close to the LTCCs, usually spaced 15 nm apart (Junker *et al.*, 1994). These CRUs at the cell surface are also known as peripheral couplings. The junctional SR is tethered to the sarcolemma by an anchoring protein called junctophilin-2 (JPH), which sits within the RyR cluster. The narrow junctional cleft created between the SR and the sarcolemma is a diffusion-restricted space, allowing an increase in $[Ca^{2+}]_i$ following LTCC activity which is needed to trigger release from RyRs. Another channel, the ATPase known as SERCA, allows Ca^{2+} ions back into the SR, in a manner regulated by levels of a protein called phospholamban (PLB), which when unphosphorylated inhibits the ATPase.

T-tubules are deep invaginations of the sarcolemmal membrane (Figure 1-1) (Sommer and Johnson, 1969), facilitating synchronous cell-wide activation by ensuring the electrical excitation reaches the cell interior with minimal delay. The network of t-tubules (also known as the t-system) effectively reduces the distance which Ca^{2+} must diffuse in order to reach the deepest regions of the cell. The particular CRUs formed by t-tubular LTCCs clustering with RyR are known as dyads. T-tubules are critical to contraction in various mammalian species, allowing greater numbers of cross-bridges and thus increasing unitary contractile force. Without their existence, mammalian cells would not be able to sustain the wide geometry. In mammalian ventricular cardiomyocytes, t-tubules form 27-36% of the whole surface area (Satoh *et al.*, 1996). Typically t-tubules cross transversely, in other words perpendicular to the orientation of the cell, but they are also capable of forming longitudinal branches, known as axial tubules (Brandenburg *et al.*, 2016). In ventricular cardiomyocytes of larger mammalian species, t-tubules appear in a well-ordered, regular pattern. T-tubule morphology, including the

diameter and number of branch points, is species-dependent. For instance, the rat t-system is made up of an extensive network of relatively small, 250 nm diameter t-tubules (Soeller and Cannell, 1999), whereas in rabbit and human tissue the 300-500 nm t-tubules have a simpler layout (Jayasinghe, Crossman, *et al.*, 2012).

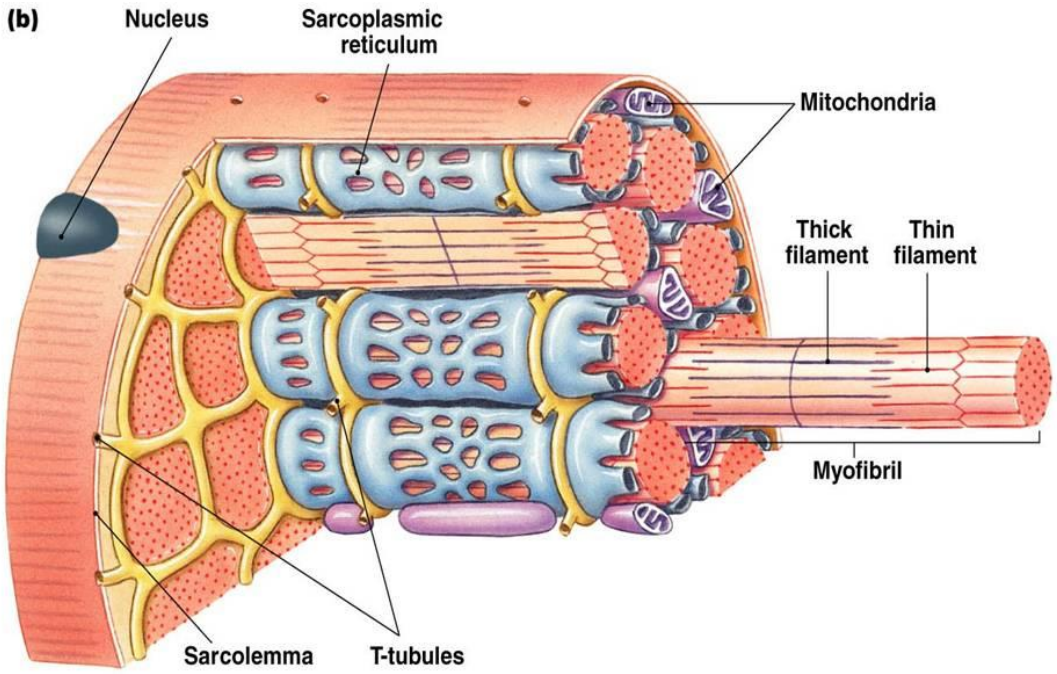

Figure 1-1. Cardiomyocyte structure

Schematic of a cardiomyocyte. The bundled contractile myofilaments are enveloped by a network of SR and neighboured by chains of mitochondria. The t-tubules, which are invaginations of the surface sarcolemma, run deep into the centre of the cardiomyocyte. Image from https://www.austincc.edu/apreview/PhysText/Muscle.html, accessed on 25/6/20.

1.3 Excitation-contraction coupling

Ca^{2+} is the critical messenger relating electrical excitation to myofilament contraction, in the process of EC coupling (Figure 1-2) (Stern, 1992; Bers, 2002).

At rest, non-pacemaking cardiomyocytes have a membrane potential of around -90 mV, but when the action potential occurs there is a brief reversal in membrane potential, which is caused by voltage-gated ion channels. The membrane depolarisation (to more positive voltage) leads to the activation of LTCCs, and causes the movement of a small amount of extracellular Ca^{2+} into the cell. These Ca^{2+} ions activate clusters of RyRs if $[Ca^{2+}]_i$ within the junctional space reaches a threshold concentration, and subsequently causes a greater release of Ca^{2+}, in a process termed Ca^{2+}-induced Ca^{2+} release (CICR) (Fabiato and Fabiato, 1975).

The free Ca^{2+} which is released then enables myocyte contraction by binding to troponin C, causing tropomyosin to reveal the myosin binding sites on actin filaments. Subsequently, through myofilament heads hydrolysing ATP, the myosin heads bind to actin and move it toward the centre of the sarcomere, causing the physical shortening of the cell. This process occurs until $[Ca^{2+}]_i$ returns to resting conditions following its removal from the cytosol, allowing muscle relaxation. Ca^{2+} re-uptake into the SR by SERCA accounts for 70% of removal, whilst transport back across the sarcolemma by NCX accounts for ~28% (Bers 2002). The remainder is removed by sarcolemmal Ca^{2+} ATPases and mitochondrial uniporter.

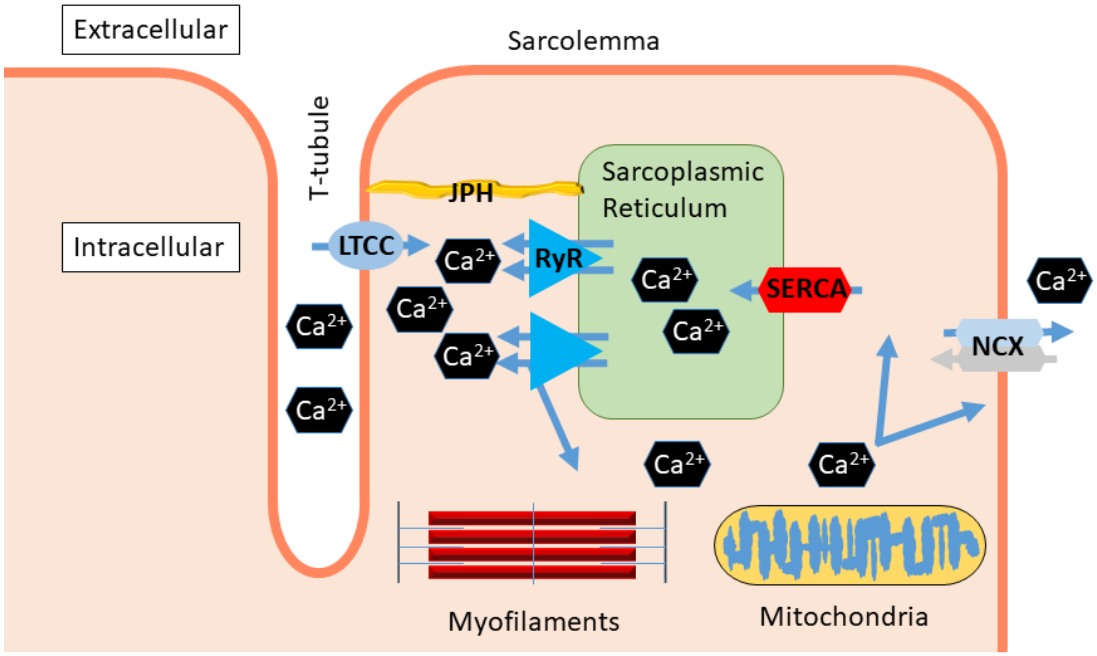

Figure 1-2. EC coupling

Schematic of EC coupling. Initiated by depolarisation of the sarcolemmal membrane, extracellular Ca^{2+} is transported into the cytosol by LTCCs. Ca^{2+} activates RyRs, causing a greater release of Ca^{2+} from the SR, in a process termed Ca^{2+}-induced Ca^{2+} release. This leads to a global increase in $[Ca^{2+}]_i$, enabling myofilament contraction and mitochondrial function. To restore equilibrium, Ca^{2+} is taken back into the SR (by SERCA) and is transported out of the cell (by NCX). The anchoring protein JPH tethers the sarcolemma and SR and helps to maintain the spacing of the junctional cleft.

1.4 Ca^{2+} release and local control

Each elementary release of Ca^{2+} from the RyR, lasting roughly 40 ms and restricted to ~2 μm in diameter, is called a Ca^{2+} spark (Cheng *et al.*, 1993). Sparks can be evoked in the CICR process following electrical stimulation or can arise spontaneously. The cell-wide Ca^{2+} transient is formed by the summation of 10^4 elementary spark releases (Cannell *et al.*, 1994; Shang *et al.*, 2014).

The local control theory describes how Ca^{2+} from the LTCC, as opposed to global cytosolic $[Ca^{2+}]$, enables graded RyR activation (Cannell and Kong, 2012). Local control ensures that there is high gain in CICR and that the SR Ca^{2+} response is synchronised with the amplitude and time course of the trigger Ca^{2+} influx. Without local control, a positive feedback loop would lead to regenerative SR Ca^{2+} release.

The likelihood of spark generation depends on several factors, including the open probability (P_o) of each individual RyR channel, which is controlled by several ligands and regulatory interactions which are detailed in the next section. One of the key determinants of spark generation and kinetics is the size and arrangement of RyR clusters. Larger and denser clusters have higher spark fidelity, which is the probability that a single RyR opening triggers a spark, due to inter-RyR coupling (Walker *et al.*, 2014), and the effect of size and geometry on spark amplitude is less critical when more than nine RyRs are present (Cannell *et al.*, 2013). In addition, the geometry of the junctional cleft (the space between the SR and sarcolemma) makes a diffusion-limited subspace, which dictates $[Ca^{2+}]$ on the cytosolic side of the RyR and therefore the excitability of a cluster (Stern, 1992; Soeller and Cannell, 1997).

As well as Ca^{2+} sparks, there can be short, asynchronous Ca^{2+} release through RyRs which have not closed, known as SR leak. SR leak is a normal part of diastole, maintaining a homeostasis by balancing SERCA Ca^{2+} uptake into the SR. The amount of leak is also linked to cluster size and arrangement (Fill and Gillespie, 2021).

Spark termination is necessary to prevent uncontrolled positive feedback or self-perpetuating release. Mechanisms for spark termination include emptying of the SR, as well as the inactivation of RyR release brought about at high $[Ca^{2+}]_I$, involving Ca^{2+} binding to the high-affinity, slow-association site on the RyR, in a negative feedback loop termed autoregulation (Eisner *et al.*, 1998). Several other interactions and mechanisms for terminating release of Ca^{2+} are detailed in the next section.

1.5 The ryanodine receptor

1.5.1 Isoforms and structure

The RyR is composed of four identical monomers (each with a molecular weight of 565 kDa) forming a mushroom-shaped, homotetrameric protein exceeding 2 MDa (Figure 1-3), making it the largest known ion channel. The cytoplasmic region enables interactions with a plethora of ligands, while the transmembrane region contains the ion-conducting pore (Takeshima *et al.*, 1989).

There are three isoforms of RyR which have similar functional responses; RyR1, most abundant in skeletal muscle; RyR2, most abundant in cardiac muscle; and RyR3, found to a lesser extent in striated muscle. There are differences in the way the isoforms engage in EC coupling, for instance RyR2 has no physical interaction with the LTCC (hence the requirement for CICR), while RyR1 does (Dhindwal *et al.*, 2017). The isoforms share ~70% sequence similarity, and cryo-electron microscopy crystal structures (at a resolution of 4.4 Å) of RyR1 and RyR2 appear structurally similar (Yan *et al.*, 2015; Peng *et al.*, 2016). Key differences in the sequences of the isoforms fall within three divergent regions (DR), possibly bestowing functional differences. For instance, differences in DR1 are thought to modulate the sensitivity of Ca^{2+} inactivation (Du *et al.*, 2000), and DR3 is believed to interact with the LTCC in RyR1 (Proenza *et al.*, 2002), while in RyR2 it is required for FKBP 12.6 interaction (Zhang *et al.*, 2003).

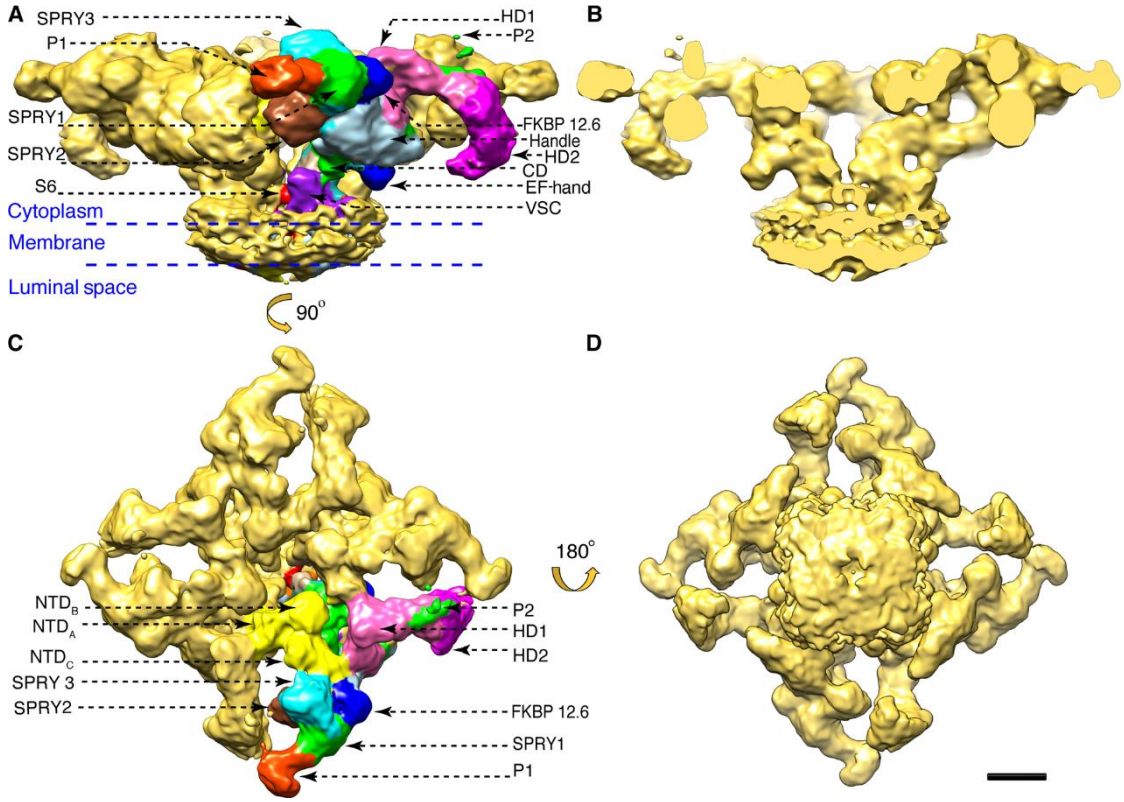

Figure 1-3. Atomic models of RyR2

Atomic models of the rabbit RyR2 tetramer. The base is embedded in the SR membrane, while the head extends out into the cytoplasm. The RyR is regulated by way of various sites of phosphorylation (P1, P2) and interactions with the regulatory subunit FKBP 12.6. Image from (Dhindwal et al., 2017). **Scale bar:** 50 Å.

1.5.2 Ryanodine receptor clustering

RyRs are arranged into clusters, allowing them to work in unison, through coupled gating, as a functional CRU to increase cytosolic [Ca^{2+}] (Sobie *et al.*, 2006). RyRs open in a concerted manner, with one channel opening invoking nearby channels to open (Marx *et al.*, 2001), assuming the local [Ca^{2+}] reaches a threshold level.

The advancement of imaging technologies over the last 40 years has allowed a vast improvement in the understanding of the organisation of RyR clusters. The earliest observations using electron microscopy (EM) showed the cytoplasmic regions of individual RyRs, present as electron-dense projections from the SR (Saito *et al.*, 1984; Sun *et al.*, 1995). Later, 3D tomography showed that RyRs were not uniformly arranged within a cluster (Figure 1-4A) (Hayashi *et al.*, 2009; Asghari *et al.*, 2014).

With diffraction-limited light microscopy, the rough outlines of clusters were visible (Soeller *et al.*, 2007), but the positions of individual RyRs within them were not, due to insufficient resolution. Cluster size (the number of RyRs per cluster) as estimated in confocal by considering the area was initially deemed to be > 100 RyRs.

Super-resolution techniques, which are light microscopy techniques with improved resolution, have been instrumental in better visualising protein clusters. More detailed information about these techniques and the concept of resolution will be covered in Section 1.9. Direct stochastic optical reconstruction microscopy (dSTORM), a super-resolution technique enabling 20 nm resolution (Heilemann *et al.*, 2008), revealed heterogeneous arrangements of RyRs in surface clusters (Baddeley *et al.*, 2009). The estimate of surface cluster size with dSTORM was around 14 RyRs, which was significantly smaller than previous estimations with diffraction-limited microscopy, owing to the improved resolution. The molecular-level description of surface clusters was obtained using the technique DNA-based point accumulation for imaging in nanoscale topography (DNA-PAINT), which enables sub-10 nm resolution (Jungmann *et al.*, 2014). DNA-PAINT was able to localise individual RyRs (Figure 1-4B), allowing accurate quantification of cluster size, revealing surface clusters had an average of 8.8 RyRs (Jayasinghe *et al.*, 2018), suggesting that the dSTORM value was a slight over-estimation. Further, it was possible to use the precise positional information to perform distance analyses, showing that RyRs in these peripheral couplings had a mean distance to the nearest neighbour (NND) of 40 nm.

Analysis of internal RyR clusters, likely corresponding to dyadic CRUs associated with t-tubules, comes predominantly from dSTORM (due to limitations in applying DNA-PAINT deeper in a sample), meaning that the organisation of RyRs in internal clusters is less well described than for surface clusters. dSTORM imaging of tissue sections estimated an interior cluster size around 4 times larger than at the periphery (Hou *et al.*, 2015), although more recent 3D dSTORM analysis suggests an average cluster size of 23 RyRs, owing to the improved axial resolution of this technique (Shen *et al.*, 2018).

Also present within the RyR cluster is the anchoring protein JPH, which physically couples the SR and sarcolemma. The relationship of JPH with RyR has been investigated in surface clusters with both DNA-PAINT and dSTORM (Jayasinghe, Baddeley, *et al.*, 2012; Jayasinghe *et al.*, 2018). The two proteins are preferentially co-clustered, with a high density of JPH within 50 nm of RyRs. The average ratios of JPH to RyR varies between 0.5 to 3.5, with a mean of 1.38 JPH:RyR (Jayasinghe *et al.*, 2018). RyR cluster structure heavily depends on JPH, as in a study that overexpressed JPH, increased RyR cluster size was observed (Munro et al., 2016). JPH also has a direct stabilising effect on RyR, whereby loss of JPH can increase Ca^{2+} leak and arrhythmic behaviour (Beavers *et al.*, 2013), and poor co-localization of RyR with LTCC, due to a decoupling of the sarcolemma and SR, leads to reduced CICR (van Oort et al., 2011).

While understanding of RyR and JPH clustering has progressed a great amount, the detailed organisation of interior dyadic clusters has yet to be obtained, due to the lack of a suitable 3D imaging technique with sufficient resolution. Without a better understanding of the organisation of dyads, the peculiarities of Ca^{2+} spark production remain unknown.

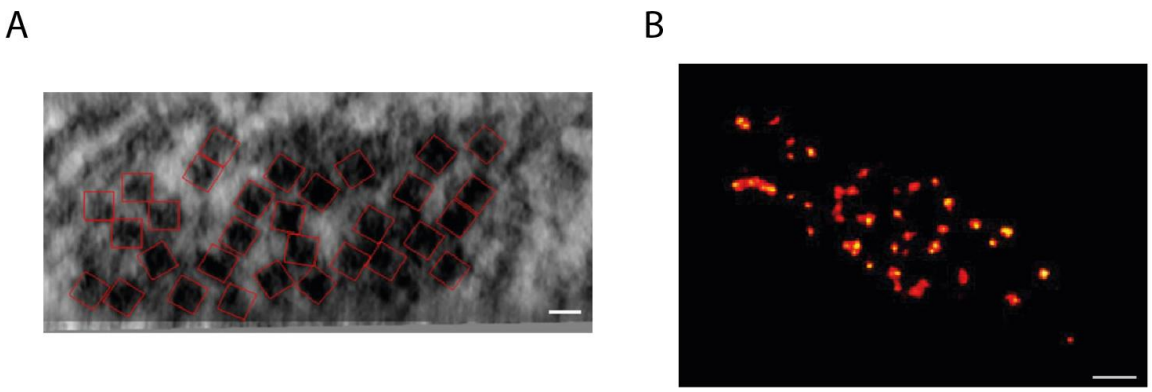

Figure 1-4. RyR clusters

Images of an RyR cluster from rat ventricle, as imaged with **(A)** electron tomography (red boxes identifying locations of individual RyRs) and **(B)** the super-resolution method DNA-PAINT, whereby individual RyRs are clearly resolved in a punctate pattern. Images from (Asghari et al., 2014) and (Jayasinghe et al., 2018). **Scale bars:** A 30 nm, B 100 nm.

1.5.3 Interactions

RyR is a ligand-gated channel, meaning it has regulating factors and ions which determine the P_o and quantity of Ca^{2+} release.

RyR P_o is most dependent on Ca^{2+} (Meissner and Henderson, 1987). Ca^{2+} can promote activation or in-activation, by binding to sites on the cytosolic and luminal sides of the channel (Bassani *et al.*, 1995). The concentration of Ca^{2+} within the SR ($[Ca^{2+}]_{SR}$) (also known as the SR load) has a significant impact on channel activity, for instance a four-fold increase in RyR P_o is seen when SR load increases (Cheng *et al.*, 1993). The SR load depends on the balance of release by RyR, re-uptake by SERCA and NCX activity, and is also regulated by a trio of SR lumen proteins; the Ca^{2+}-binding calsequestrin (CSQ), and the junctional proteins triadin and junctin, which together form a quaternary complex which buffers luminal Ca^{2+} and mediates the effects on RyR.

The concentration of Mg^{2+} ions also affects RyR activity, due to competitive displacement of Ca^{2+} from binding sites. For instance, 3 mM Mg^{2+} greatly reduces the release rate of the RyR (Meissner and Henderson, 1987). In addition, several other ions can affect RyR activity, including H^+, Fe^{2+}, Ba^{2+}, Cd^{2+}, La^{2+}.

ATP is another ligand which leads to RyR activation, for instance 5 mM ATP increases Ca^{2+} release 2-fold in cardiac vesicles (Meissner and Henderson, 1987). ATP also affects RyR through a change in $[Mg^{2+}]$, whereby a decrease in [ATP] increases $[Mg^{2+}]$, inhibiting RyR activation.

FK-506 binding proteins (FKBP 12 and FKBP 12.6) are regulatory subunits which reportedly stabilise the channel in its closed state and prevent long-lasting sub-conductance states. While FKBP 12 does not alter Ca^{2+} spark production, 12.6 does infer a slight inhibitory effect (Guo Tao *et al.*, 2010).

CaM is a Ca^{2+}-binding protein which affects RyR, as well as other Ca^{2+}-handling proteins such as LTCCs and SERCA. The influence of CaM on RyR comes via inhibition by direct binding, but also by the action of CaMKII, which is detailed more in the next section. CaM has been shown to reduce CICR 3-6-fold (Meissner and Henderson, 1987).

1.5.4 Phosphorylation

Phosphorylation of RyR serine residues has a significant effect on P_o and Ca^{2+} release, and exists as a sensitive control mechanism that is regulated by kinases and phosphatases, as well as cAMP and phosphodiesterases (PDEs) (which hydrolyse cAMP).

The main phosphorylation sites that have been studied include pSer2808 and pSer2814 (both found in the RyR phosphorylation hotspot), and to a lesser extent pSer2030. While additional phosphorylation sites have been identified at Ser2810, Ser2811, Ser2797 and Thr2876 using mass spectrometry (Yuchi *et al.*, 2012), these have not been functionally characterised in detail.

pSer2808 was originally proposed to be a CaMKII phosphorylation site (Witcher *et al.*, 1991), but has since been shown to also be phosphorylated by PKA (Rodriguez *et al.*, 2003) and cGMP-dependent kinase (Xiao *et al.*, 2006). In contrast, pSer2814 is only phosphorylated by CaMKII (Wehrens *et al.*, 2004), and pSer2030 is exclusively phosphorylated by PKA (Xiao *et al.*, 2005).

The amount of basal phosphorylation varies at the three sites. In isolated adult rat cardiomyocytes there is a substantial amount of pSer2808 phosphorylation at rest (54%), a smaller amount at pSer2814 (16%) and none at pSer2030 (Huke and Bers, 2008). The fraction of phosphorylation can be increased in *in vitro* experiments using β-adrenergic agonists, for instance treatment of rat cardiomyocytes with 1 μM isoproterenol for 1 minute leads to an pSer2808 increase from 69% to 83%, and pSer2814 increase from 15% to 60% (J. Li *et al.*, 2013). pSer2030 sees a larger increase in phosphorylation after isoproterenol than pSer2808, given pSer2808 is already substantially phosphorylated at rest (Xiao *et al.*, 2006).

The effect of phosphorylation on RyR activity is a complicated research area, with often-conflicting accounts of the importance of residues on diastolic Ca^{2+} release. While P_o is typically low at intermediate pSer2808 phosphorylation (75% at baseline in sheep SR vesicles), unique channel behaviours including increased activity have been seen at maximal and minimal phosphorylation (Carter *et al.*, 2006). PKA phosphorylation has been implicated in reducing channel sensitivity to Mg^{2+} and ATP in some studies (Uehara *et al.*, 2002; J. Li *et al.*, 2013), although other studies suggest PKA phosphorylation does not affect diastolic release (comprising sparks, waves or leak) (Li *et al.*, 2002; Stange *et al.*, 2003; Xiao *et al.*, 2005; Xun *et al.*, 2005; Curran *et al.*, 2007; Bers, 2012). Another paper attributes the PKA-mediated increase in spark activity to PLB, not RyR (Li *et al.*, 2002). pSer2808 and pSer2814

phosphorylation both influence CaM regulation of RyR (Fukuda *et al.*, 2014; Uchinoumi *et al.*, 2016; Walweel *et al.*, 2019).

There is evidence to suggest that pSer2814 has a larger functional impact on RyR activity. CaMKII phosphorylation at pSer2814 has been shown to increase RyR activity (Wehrens *et al.*, 2004), with increased frequency of spark production and Ca^{2+} leak (Guo Tao *et al.*, 2006). In line with this, Ca^{2+} leak following isoproterenol addition has been shown to be based on CaMKII, not PKA (Curran *et al.*, 2007). Interestingly, EM revealed that pSer2814 phosphorylation induces rearrangements in cluster organisation (Asghari *et al.*, 2014).

Regarding the third site, pSer2030 is thought to be necessary for a complete β-adrenergic response, while ablation of this site leads to diminished EC coupling gain and spark frequency at rest (Potenza *et al.*, 2018).

The inter-connected (and possibly compensatory) nature of the phosphorylation sites, as well as the multi-site aspects of the kinases PKA and CaMKII, adds to the difficulty in elucidating the role and importance of each site. That PKA and CaMKII have other targets other than RyR adds further complexity to considering the functional effects of adrenergic stimulation, for instance through altered Ca^{2+} flux through LTCCs, or altered SR load through PLB-regulated SERCA activity. In addition to the effects of phosphorylation at sites on a single RyR monomer, there is the added complexity of the combinations across all four monomers in the tetramer, which may entail different functional phenotypes. The complexities regarding the interplay of the various sites are yet to be fully explored.

1.6 Heart failure

1.6.1 Introduction

HF is a condition where the heart is unable to supply enough blood to meet the demands of the body. The exact progression of HF and the mechanisms involved depend on the disease variant, including whether the left ventricle (LV) or right ventricle (RV), or both, are affected.

HF typically starts with an initial event such as myocardial infarction (MI), overload or valve malfunction. To maintain cardiac output, compensatory mechanisms are engaged, such as improving contractility by cardiomyocyte hypertrophy, normalising wall stress, or increased sympathetic drive by circulating catecholamines. Eventually, the compensatory mechanisms

become maladaptive. For instance, there is a diminished inotropic reserve, with desensitisation of the adrenergic receptors which relay the sympathetic response. Other components which contribute towards the HF end-point include metabolic derangement, myocardial fibrosis (causing muscle stiffness), the renin-angiotensin-aldosterone axis, electrical conduction defects and dysfunctional Ca^{2+} homeostasis.

The main causes of death in HF relate to reduced pump function and arrhythmias (which are changes in heart rate). Arrhythmias are responsible for sudden cardiac death in 30-50% of mortality cases in HF, predominantly due to ventricular tachycardia (Røe *et al.*, 2015).

HF treatments often only address the symptoms of the condition and not the cause. At present, lipid-lowering and anti-hypertensive drugs are the leading prescriptions for HF patients, greater than Ca^{2+} blockers, nitrates, anti-anginal and anti-platelet drugs, and diuretics. There is a need for tailored treatments which consider the multi-factorial nature of HF disease progression.

1.6.2 Ca^{2+} homeostasis dysfunction

Contractile dysfunction in failing cardiomyocytes arises largely through dysfunctional Ca^{2+} dynamics, such as changes to the Ca^{2+} transient, SR load, diastolic SR leak and slowed SR Ca^{2+} uptake. These changes partly result from functional alterations to the channels, but also due to structural remodelling of Ca^{2+}-handling structures, which is discussed further in the next section.

Failing cardiomyocytes typically have dyssynchronous Ca^{2+} release (Figure 1-5), with late or missed release contributing to spatiotemporal variation in the Ca^{2+} wavefront (Song *et al.*, 2006). Generally, the amplitude of transients is smaller due to reduced EC coupling gain (Gómez *et al.*, 1997). Decoupling of the CICR mechanism has been demonstrated by increased latency in LTCC-RyR coupling in pressure overload (Xu *et al.*, 2007). Decoupling compromises Ca^{2+} spark generation and leads to slower spark kinetics, which contribute to a less uniform release across the cell (Louch *et al.*, 2013).

Given that SR load is a key determinant of RyR activity, it is unsurprising that it is altered in HF. Both increased and reduced SR load have been reported in different pathologies. High SR load leads to more spontaneous Ca^{2+} release, while decreased SR load (linked to downregulated SERCA function) can contribute to reduced transient amplitude (Mercadier *et al.*, 1990).

While SR leak plays a part in normal Ca^{2+} homeostasis, leak reduces $[Ca^{2+}]_{SR}$ and can promote arrhythmogenic activity. While some groups have reported that a leak-induced reduction in $[Ca^{2+}]_{SR}$ decreases the amplitude of the Ca^{2+} transient, this results from the effects of compromised SERCA and NCX activity. SR leak by itself has no effect on transient amplitude, due to the phenomenon of autoregulation, whereby a reduction in SR load leads to a larger fractional release by increased RyR sensitivity (Eisner *et al.*, 1998).

Propagative Ca^{2+} waves can arise where SR load is higher, or with increased RyR sensitivity, even without an initiating current (Cheng *et al.*, 1996). Ca^{2+} waves can compromise contractility and cause arrhythmic activity through depolarising membrane currents (triggering spontaneous action potentials). One arrhythmogenic mechanism is the delayed afterdepolarisation (DAD), which arises when spontaneous Ca^{2+} release is extruded by NCX, causing a net inward current capable of triggering an action potential (Røe *et al.*, 2015). DADs occur after the action potential is complete, unlike another arrhythmogenic mechanism known as early afterdepolarisations (EAD), which result during the action potential downstroke, prior to repolarisation (Edwards and Louch, 2017). EADs represent a reduced repolarisation reserve and occur through an increased I_{CaL} window current, due to overlap in both steady state activation and inactivation.

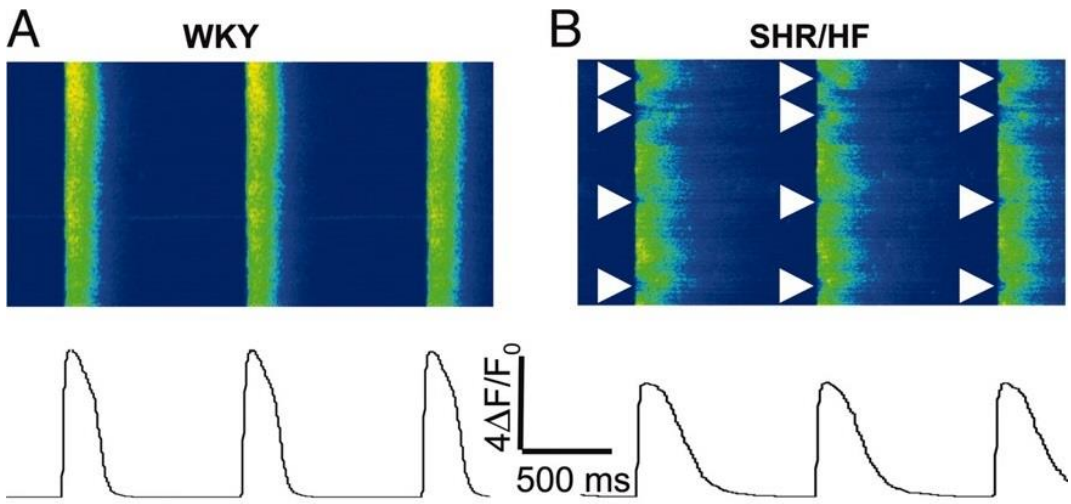

Figure 1-5. Heart failure - dysfunctional Ca^{2+} signalling

Line scan images (upper) show field-stimulated Ca^{2+} transients in isolated cardiomyocytes, obtained using the fluo-4 reporter, and the corresponding fluorescent records (lower). The myocytes from **(A)** control Wistar-Kyoto rats demonstrate uniform waveforms, while **(B)** those from a spontaneous hypertensive model of heart failure show dyssynchronous release. Arrowheads mark positions in which Ca^{2+} releases were missing in consecutive beats in the same cell. Image from (Song et. al., 2006).

1.6.3 T-tubule and calcium release unit remodelling

One of the main structural hallmarks of HF is t-tubule remodelling (Figure 1-6) (Song et al., 2006), entailing disorganisation, an increased proportion of longitudinally-oriented tubules and occasionally dilation (Crossman *et al.*, 2017). In this way, failing cardiomyocytes can resemble immature, developing myocytes, which typically lack t-tubules (Lipsett *et al.*, 2019). While the mechanisms driving t-tubule remodelling are poorly understood, contributing factors include mechanical load (Ibrahim and Terracciano, 2013), elevated wall stress (Frisk *et al.*, 2016) and fibrosis (Crossman *et al.*, 2017), as well as JPH remodelling, which is detailed below.

T-tubule remodelling is prevalent in a number of human HF conditions (Kaprielian *et al.*, 2000; Vatta *et al.*, 2002; Louch *et al.*, 2004; Lyon *et al.*, 2009; Crossman *et al.*, 2011, 2017; H. B. Zhang *et al.*, 2013; Seidel *et al.*, 2017) and in a number of animal models of HF (He *et al.*, 2001; Wei *et al.*, 2010; Kemi *et al.*, 2011; Ibrahim *et al.*, 2012; Sacconi *et al.*, 2012; Wagner *et al.*, 2012; Pinali *et al.*, 2017; Lawless *et al.*, 2019; Seidel *et al.*, 2019).

T-tubule remodelling has negative effects on Ca^{2+} homeostasis and arrhythmogenesis. There is compromised Ca^{2+} extrusion due to the altered distribution of NCX, and the altered distribution of LTCCs disrupts the local arrangement of dyads, impairing EC coupling and CICR. Orphaning of RyRs increases the distances over which Ca^{2+} must diffuse between neighbouring clusters to propagate release or to activate the myofilaments (Song *et al.*, 2006). Correspondingly, t-tubule disruption accounts for reduced synchrony of Ca^{2+} release (Louch *et al.*, 2004).

The anchor protein JPH is crucial to the structural integrity of t-tubules (Chen *et al.*, 2013; Reynolds *et al.*, 2013), and consequently loss of JPH is one proposed mechanism for t-tubule remodelling in HF. Alterations to JPH have been observed in human hypertrophic and dilated cardiomyopathies (Landstrom *et al.*, 2007; H. B. Zhang *et al.*, 2013). Down-regulation of JPH has also been seen in animal models such as mouse hypertrophic and dilated cardiomyopathies (Minamisawa *et al.*, 2004), mouse aortic pressure overload (Brandenburg *et al.*, 2019), thoracic aortic band rat (Wei et al., 2010), MI rat (Frisk *et al.*, 2016) and aortic constriction mouse (Reynolds *et al.*, 2016; Ujihara *et al.*, 2016).

JPH is critical in maintaining the diffusion-restricted space between the SR and the sarcolemma at the dyad, therefore loss of JPH in HF compromises this dyadic space, impairing CICR. Further, loss of the stabilising effect of JPH on RyR results in Ca^{2+} leak and arrhythmic behaviour (van Oort *et al.*, 2011; Beavers *et al.*, 2013). Loss of JPH could arise via numerous

mechanisms, including calpain mediated cleavage (Guo *et al.*, 2015; Lahiri *et al.*, 2020), defects in microtubule-mediated trafficking (Zhang *et al.*, 2014) or by microRNA 24 regulation (Xu *et al.*, 2012; R. C. Li *et al.*, 2013).

Nanoscale RyR cluster remodelling has been revealed in HF, leading to slower spark kinetics (Louch *et al.*, 2013). RyR dispersion (entailing more smaller clusters which were closer together) was observed in infarcted rat hearts, leading to augmented SR leak (Kolstad *et al.*, 2018). When grouping clusters closer than 150 nm into functional CRUs, there were more clusters per CRU, albeit fewer RyRs per CRU (given smaller cluster size). Cluster fragmentation has also been seen in AF using STED microscopy (Macquaide *et al.*, 2015), whereby clusters were closer together, and they saw more clusters per CRU, but less filled CRUs (although there was no change to cluster size). In addition, there were more clusters between Z-lines, indicative of disorganisation. Disorganisation of LTCC and RyR has also been shown by dSTORM in transverse aortic constriction mice (Hadipour-Lakmehsari *et al.*, 2019).

To summarise, the structural defects in HF, comprising remodelling of t-tubule networks and RyR and JPH in CRUs, partly underlies the dysfunctional Ca^{2+} dynamics.

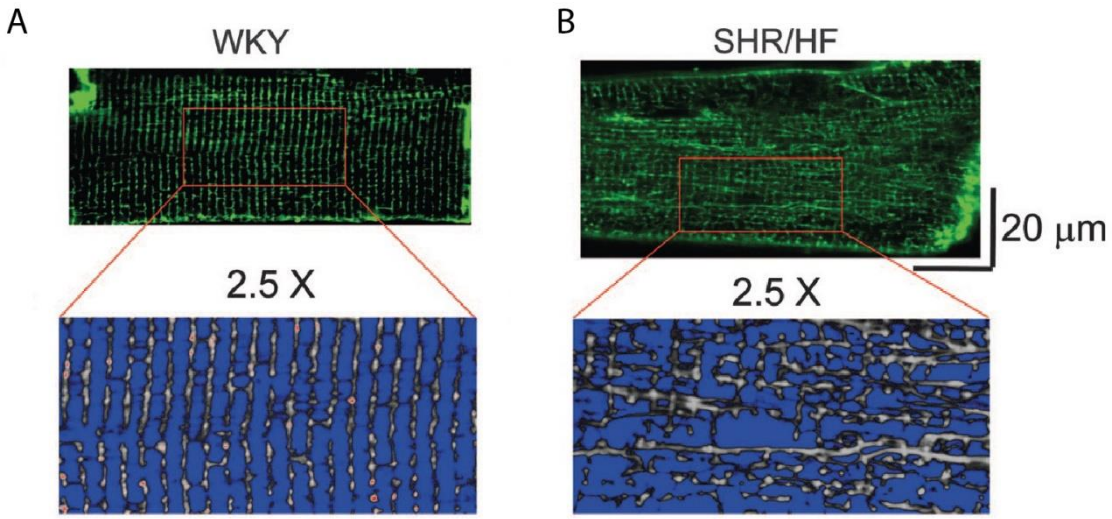

Figure 1-6. Heart failure - t-tubule remodelling

Confocal images of cardiomyocyte membranes labelled with Di-8-ANEPPS. (**A)** Control Wistar-Kyoto rats have a uniform network of t-tubules, which are primarily transverse in orientation, whereas **(B)** in myocytes from a spontaneous hypertensive model of heart failure this network is highly disordered, with a larger proportion of longitudinally oriented tubules. Image from (Song et. al., 2006).

1.6.4 Ryanodine receptor phosphorylation in heart failure

During HF, RyR activity is impacted by changes in catecholamines, kinases, phosphatases and PDEs. As mentioned previously, hyper- or hypo- phosphorylation can increase Ca^{2+} leak (Carter *et al.*, 2006; Bovo *et al.*, 2017).

pSer2808 hyper-phosphorylation was first implicated in HF in 2000, and was suggested to cause FKBP12.6 dissociation, leading to SR Ca^{2+} leak and systolic dysfunction (Marx *et al.*, 2000). Since the initial observation by Marx *et. al.*, hyper-phosphorylation of pSer2808 has been reported in various HF cases, including MI and hypertrophic cardiomyopathy rat (Reiken *et al.*, 2003), in LV of MI rats with CHF (Obayashi *et al.*, 2006) and in spontaneously hypertensive rats (Chen-Izu *et al.*, 2007). The increased expression of pSer2808 in aortic constriction rabbit was normalised with the β-blocker metoprolol (S. Zhang *et al.*, 2012). While pSer2808 was shown to be increased in canine HF, Ca^{2+} leak was not stopped by PKA inhibitor (Xun *et al.*, 2005). Interestingly in a study where JPH was knocked down or over-expressed, there was a respective reduction and increase in pSer2808, implicating pSer2808 phosphorylation with cluster remodelling (Brandenburg *et al.*, 2019).

Despite the number of papers reporting pSer2808 hyper-phosphorylation, other papers have observed no increase in pSer2808, for instance in canine HF (Jiang *et al.*, 2002; Xiao *et al.*, 2005) and rat aortic banding (H. Zhang *et al.*, 2015). Research using mutations to constitutively hyper-phosphorylate or prevent pSer2808 phosphorylation altogether has drawn a particularly conflicting story about the involvement of this site in HF (Wehrens *et al.*, 2006; Benkusky *et al.*, 2007; MacDonnell *et al.*, 2008; H. Zhang *et al.*, 2012; Ullrich *et al.*, 2012; Liu *et al.*, 2014; Alvarado *et al.*, 2017).

There is a substantial body of research implicating pSer2814 as a more significant contributor to dysfunction in HF. In human HF, CaMKII expression and pSer2814 phosphorylation is increased and caused SR leak, whilst CaMKII inhibition reduced leak by 80% (Neef Stefan *et al.*, 2010; Fischer *et al.*, 2013, 2014). In dilated CM and ischemic CM, CaMKII was found to be increased in both RV and LV (Sossalla *et al.*, 2010). Another study reported increased phosphorylation by CaMKII in non-ischemic dilated CM, but not in ischemic CM (Respress *et al.*, 2012). Increased CaMKII activity has also been demonstrated in a number of animal models, including transgenic cardiac hypertrophy mice (Wu *et al.*, 2002). In aortic constriction rabbits, there was increased pSer2814 expression, which was normalised with metoprolol (S. Zhang *et al.*, 2012), and the increased arrhythmias were suppressed by CaMKII inhibitor (Xun

et al., 2005). Rate-dependent CaMKII phosphorylation of RyR was defective in coronary artery ligation in rats (Wehrens *et al.*, 2004). Rapid atrial pacing in mice caused increased CaMKII, while inhibition of CaMKII prevented AF inducibility (Chelu *et al.*, 2009). While there are studies reporting no change in pSer2814, for instance in rat aortic band (H. Zhang *et al.*, 2015), the general consensus is that increased CaMKII phosphorylation involving pSer2814 is implicated in HF.

There is far less research regarding the involvement of the third site at pSer2030 in HF, but it has been shown that there is no significant pSer2030 phosphorylation in failing rat hearts (Xiao *et al.*, 2006), or aortic constriction rabbit (S. Zhang *et al.*, 2012).

While research continues to unveil the changes at each phosphorylation site in various HF conditions, and consider their relative contribution to dysfunction, there are many unknowns in the complex interplay of the sites controlling RyR activity. Importantly, almost all the research detailed above comes from biochemical analyses, without a count of the amount of phosphorylation at the level of the individual RyR, or estimations of the fraction of phosphorylation per cluster.

1.7 Right ventricular heart failure

1.7.1 Introduction

RV failure entails an inadequate blood supply to the pulmonary circulation and systemic venous congestion (Mehmood and Frank, 2016). Failure of the RV is in fact common to many human cardiac diseases due to the inter-dependence of the ventricles (Haddad, Hunt, *et al.*, 2008).

While the pathobiology of RV failure bears similarities to LV failure, including compensatory hypertrophy to preserve cardiac output, with eventual RV dilatation (Dignam *et al.*, 2021), there are different mechanisms involved in disease progression, given the structural and biochemical differences between the two ventricles (Friedberg and Redington, 2014). For instance, the RV is more sensitive to stresses (such as increased afterload) than the LV (Xie *et al.*, 2012). The RV and its failure is comparatively understudied compared to the LV, and this is indicated in the array of treatment options relating to LV failure, while none specifically address RV failure (Haddad, Doyle Ramona, *et al.*, 2008).

RV failure is the leading cause of death in PAH (Prisco *et al.*, 2020), whereby an increased pulmonary resistance increases the afterload on the RV. At present, there is no cure for PAH, while treatment options include optimising preload with diuretics, reducing afterload with pulmonary vasodilators (such as PDE inhibitors) and inotropic agents to improve contractility (Mehmood and Frank, 2016).

It is possible to learn more about the progression of RV HF by observing the changes that occur in animal models of disease. One such rat model involves a single intraperitoneal injection of the 11-membered, macrocyclic pyrrolizidine alkaloid monocrotaline (MCT). MCT is activated to the reactive pyrrole metabolite form (dehydromonocrotaline) in the liver (Gomez-Arroyo *et al.*, 2012). This short-lived form is then pumped into the pulmonary vasculature and damages the endothelium. Several weeks post-injection, rats develop PAH and consequently pressure overload with compensatory RV hypertrophy (Kay et al., 1967). It should be mentioned however that MCT animals do not display severe plexiform lesions typically associated with PAH (Gomez-Arroyo *et al.*, 2012), and several aspects found in the MCT model (pulmonary interstitial edema, myocarditis, and hepatic veno-occlusive disease) are not found in severe human PAH.

In MCT hearts there is tachycardia (rapid heart rate) and ventricular fibrillation (Benoist *et al.*, 2011, 2012), with a negative force-frequency relationship and blunted post-rest potentiation, suggesting an impaired ability of the SR to store Ca^{2+} during extended periods of rest (Kögler *et al.*, 2003). There is increased electrical heterogeneity and steeper electrical restitution, along with a prolonged monophasic action potential duration (Benoist *et al.*, 2011; Hardy *et al.*, 2018). The changes to the ventricular gradient and QT interval found in MCT recapitulate that found in human HF (Benoist *et al.*, 2012).

As is the case in most branches of HF, in MCT hearts there is a chronic, systemic increase of catecholamines, leading to a downregulation of β-adrenergic receptors (Ishikawa *et al.*, 1991; Leineweber *et al.*, 2003) and a reduced inotropic response (Brown *et al.*, 1998). The desensitisation to adrenergic stimulation culminates in a reduced production of cAMP by adenylate cyclase (Yoshie *et al.*, 1994; Leineweber *et al.*, 2003) and alters the activity of PKA and CaMKII.

1.7.2 Ca^{2+} dysfunction in the monocrotaline model

SR content is increased in MCT cardiomyocytes at the point of failure (Benoist *et al.*, 2012; Sabourin *et al.*, 2018), which seems at odds with reports that SERCA is downregulated (Kögler *et al.*, 2003; Benoist *et al.*, 2012, 2014; Xie *et al.*, 2012; Fowler, Drinkhill, Norman, *et al.*, 2018). However, this could be explained by increased phosphorylation of PLB, which would induce more Ca^{2+} uptake (through SERCA inhibition) (Sabourin *et al.*, 2018). That SERCA2 is downregulated recapitulates the observation in human HF (Hasenfuss *et al.*, 1994).

Ca^{2+} homeostasis dysfunction is well documented in MCT RV HF. Ca^{2+} transients are increased in early hypertrophy, but upon progression to severe failure the transient amplitude decreases (Kuramochi *et al.*, 1994). There is an increased fractional release from the SR (Benoist *et al.*, 2012) and increased spark frequency at the point of failure (Fowler, Drinkhill, Norman, *et al.*, 2018; Sabourin *et al.*, 2018). Spark mass is reported to be increased in one study, even at the hypertrophic stage (Benoist *et al.*, 2012), and unchanged in another (Fowler, Drinkhill, Norman, *et al.*, 2018). Increased Ca^{2+} leak, which appears to increase through hypertrophy and into failure, places the RyR in a refractory state, causing fluctuations in Ca^{2+} release. These fluctuations lead to discordant (out of phase) alternans in Ca^{2+} transient at the point of failure (Benoist *et al.*, 2012). *In vivo* electrocardiogram recordings have shown T-wave alternans (relating to ventricular repolarisation), which are indicative of Ca^{2+}-cycling abnormalities (Benoist et al., 2014). Impaired Ca^{2+} release has been seen in trabeculae of MCT animals taken at the 4-week time-point, with a 45% delay in time to peak (Power *et al.*, 2018). Furthermore, the stress in trabeculae could not be increased when increasing the stimulation frequency (Power *et al.*, 2018).

One study found a decreased expression of LTCC subunit Cav1.2 at the point of failure, linking it to a decrease in transient amplitude and a less synchronous release of Ca^{2+} from the SR (Xie et al., 2012). There is reportedly no difference in I_{CaL} density or inactivation as stimulation frequency was increased (Benoist *et al.*, 2012). Another study reported larger I_{Ca} density by day 14 before a decrease (Lee *et al.*, 1997), which would account for the action potential duration prolongation.

NCX has been reported to be reduced in expression (Xie *et al.*, 2012) and activity (Benoist *et al.*, 2012) at failure, although another study found no changes to NCX (Kögler *et al.*, 2003).

There is conflicting information regarding changes to RyR in MCT. While one study found decreased mRNA expression (Kögler *et al.*, 2003), another reported no change to expression

(Sabourin *et al.*, 2018). In this latter study, they also reported no change to pSer2814 phosphorylation. While they saw no pSer2808 phosphorylation at all in MCT RV, they also suggested there was none in control either, which casts doubt on their ability to detect phosphorylation (Sabourin *et al.*, 2018).

The variability in the reported findings relating to protein expression and activity could arise from differing origins/ages or weights of animals. Alternatively, the conflicting results could arise through different severities of HF used, whether the animals are observed at early hypertrophy or are observed once they have progressed to the point of congestive HF at the failure point.

1.7.3 Structural remodelling in the monocrotaline model

As in other HF cases including that of human and animal models, there is drastic t-tubule remodelling in MCT RV HF, with a reduction in JPH protein expression (Xie *et al.*, 2012; Prins *et al.*, 2017), although a different study reported no change in JPH expression (Fowler, Drinkhill, Norman, *et al.*, 2018).

There is evidence of an increased density of microtubule network in the MCT RV (Stones et al., 2013). The effect of this on Ca^{2+}-handling is thought to be minimal, given that colchicine (a microtubule depolymerising agent) failed to increase contraction or alter the response to increased stimulation frequency. Another study correlated microtubule densification with a decrease in JPH and disruption to the t-tubule network (Prins et al., 2017). These changes were partially reversed by colchicine, diminishing hypertrophy and improving function.

Scanning EM has revealed a decreased SR network density (Kuramochi *et al.*, 1994), while another EM study reported enlarged SR, dissolution of myofilaments and broken Z-lines (Zuo *et al.*, 2012).

The sarcomeric length (SL) is the distance between two adjacent z-discs, denoting the ends of the sarcomere contractile units. In healthy cardiomyocytes the SL ranges from 1.7 μm (fully contracted) to around 2.3 μm at rest (de Tombe and ter Keurs, 2016). The average SL is shorter in MCT hearts (mean SL 1.79 μm, versus 1.91 μm in control), and was unaffected by colchicine (Stones *et al.*, 2013). Shortening was increased at a stimulation of 1 Hz, but not at 5 Hz. The shorter diastolic SL was shown to be Ca^{2+}-independent, and sensitive to cross bridge cycling inhibition (Fowler *et al.*, 2015).

1.7.4 Outlook

While previous studies in MCT RV cardiomyocytes have characterized gross structural changes and suggested altered expression of Ca^{2+}-handling proteins, there is no imaging data clarifying whether there is remodelling of RyR clusters, or whether JPH is differentially arranged at the dyad. Further, there is limited research into the extent of phosphorylation in MCT.

A more complete description of the molecular level organisation of RyR and JPH clusters, as well as the incidence of phosphorylation, is needed to better understand how Ca^{2+} dysfunction arises and to begin to formulate approaches to tackle the pathological remodelling mechanisms.

1.8 Stem-cell derived cardiomyocytes

1.8.1 Introduction

Stem cells are undifferentiated (or partially differentiated) precursors, which can give rise to different cell types, including cardiomyocytes. Stem cell-derived cardiomyocytes (SC-CMs) represent a powerful *ex vivo* tool, without requiring the use of animals.

SC-CMs have been useful in understanding and tackling cardiac disease. Patient-specific SC-CMs (which can recapitulate genetic diseases in the donor) have been generated to investigate pathological characteristics (Moretti *et al.*, 2010; Davis *et al.*, 2021). Engineered human cardiac tissues derived from SC-CMs , could potentially be transplanted as a means to replace lost tissue after HF (Archer *et al.*, 2018; Liu *et al.*, 2018; Ronaldson-Bouchard *et al.*, 2018; Murphy *et al.*, 2019). SC-CMs have also been especially useful in screening for drug compound toxicity *in vitro* (Cohen *et al.*, 2011).

During the maturation of a cardiomyocyte, there is a shift in structural organisation, proteome composition and functional signalling. One of the biggest differences in neonatal mammalian cardiomyocytes compared to adult is the absence of t-tubules, as these structures often appear post-natally (Louch *et al.*, 2015). While RyR clusters are arranged in a striated manner in the cell interior before t-tubule formation in post-natal cardiomyocytes, JPH is localised predominantly at the periphery (Ziman *et al.*, 2010). As t-tubules develop, JPH becomes more colocalised with RyR in the interior. Corresponding to the immature organisation of the Ca^{2+}-handling network, Ca^{2+} signalling in developing cardiomyocytes is distinctly different to that

in adults, entailing slower transients and regional differences in Ca^{2+} concentration (Haddock *et al.*, 1999).

SC-CMs, like developing cardiomyocytes, typically lack t-tubule membranes (Lieu *et al.*, 2009), and RyR clusters in these cells do not colocalise with LTCCs. Ca^{2+} signalling in SC-CMs is vastly different to that in adult cardiomyocytes, initiating at the cell periphery and diffusing towards the centre after a short delay (Satin *et al.*, 2008). The immaturity of SC-CMs and developing cardiomyocytes (in both structure and function) shares similarities with the pathological phenotype of HF, suggesting comparable genetic switches between developing and failing cardiomyocytes (Lipsett *et al.*, 2019).

In order to use SC-CMs as biologically-comparable models of adult cardiomyocytes, and thus to trust observations and outcomes (such as drug efficacy), it is important to fully characterise the structural and functional baseline, including the extent and maturity of Ca^{2+}-handling structures. In addition, by better understanding the similarities and differences between developing and failing cardiomyocytes, it may be possible to develop approaches which tackle the detrimental cellular remodelling in HF.

1.8.2 Cardiomyocytes from embryonic and induced pluripotent stem cells

The research of this thesis focuses on two types of SC-CMs, those generated from endogenous cardiac stem cells (eCSCs), which exist within the adult myocardium of many species (Bearzi et al., 2007), and those generated from induced pluripotent stem cells (iPSCs), which are reprogrammed human adult cells (Takahashi and Yamanaka, 2006).

eCSC-derived cardiomyocytes (eCSC-CMs), are produced via the formation of CardioStem spheres and exposure to various growth factors (Smith et al., 2014). eCSC-CMs express cardiomyocyte lineage markers such as cardiac troponin I, well-ordered sarcomeric bands of s-actinin, and gap junctions containing connexin-43 (Smith et al., 2014). eCSC-CMs have synchronised rhythmic beating, with robust transients enabled by functional SR, SERCA and NCX (Vicinanza *et al.*, 2017). The structural maturity of Ca^{2+}-handling features, such as the relationship of RyR and JPH, has not yet been fully established in eCSC-CMs.

Cardiomyocytes generated from iPSCs (iPSC-CMs) have been more extensively researched. iPSC-CMs replicate many aspects of adult cardiomyocytes, forming beating syncytia with similar electrical and chemical signalling (Zhang et al., 2009). iPSC-CMs have Ca^{2+} transients which are modulated by contributions from LTCCs, IP3Rs, RyRs and SERCA (Itzhaki et al.,

2011). Stochastic sparks produced in iPSC-CMs are comparable to those in adult cardiomyocytes (G. Q. Zhang *et al.*, 2013). Furthermore, aspects of structural maturity have been observed, such as peripheral couplings of junctional SR adjoined to the sarcolemma (Gherghiceanu *et al.*, 2011), and punctate clustering of RyR (X.-H. Zhang *et al.*, 2013).

Despite the similarities to adult cardiomyocytes, iPSC-CMs more closely resemble prenatal cardiomyocytes, as they are smaller and rounder in shape, and with a poor alignment of sarcomeres (Lundy *et al.*, 2013; Rao *et al.*, 2013). There is a poorly-developed SR network (Gherghiceanu *et al.*, 2011), which is mostly distributed in the perinuclear region (Koivumaki *et al.*, 2018). As with other SC-CMs, there is a lack of t-tubules (Lundy *et al.*, 2013), which accounts for profound differences in the Ca^{2+}-handling compared to adult cells. In iPSC-CMs there is a slower rate of Ca^{2+} transient rise and decline (Lee *et al.*, 2011) and non-uniform spread across the cell, with a rise of Ca^{2+} at the periphery and a delay before diffusion to the interior.

Given the uncertainties regarding the maturity of SC-CMs, caution should be taken when using these as a parallel for adult cardiomyocytes. There is a need for a full characterisation of the structural maturity in both eCSC-CMs and iPSC-CMs. In particular, it is important to understand the extent of CRU development and their distribution in relation to membranes.

1.9 Super-resolution microscopy

1.9.1 Concept of resolution

The principle behind light microscopy techniques involves the detection of photons, often emitted by fluorophores. The resulting diffraction pattern from a single point source appears as a point spread function (PSF), where there is a peak intensity at the centre of the object, with a blurred outline radiating outward with a lower intensity (Figure 1-7A), which is a product of the diffraction limit (or Abbe limit). When two point sources are positioned close together, the PSFs overlap and the objects appear to be continuous. In other words, they cannot be resolved as distinct separate points (Figure 1-7B).

According to the Rayleigh criterion, two illuminated objects can be resolved only if they are separated by a minimum distance, *d*, roughly half of the wavelength of light used (Abbe, 1873; Rayleigh, 1903).

$$d = 0.61 \text{ x } \lambda \text{ / } (NA)$$

Where λ is the wavelength of light, and NA relates to the numerical aperture of the objective.

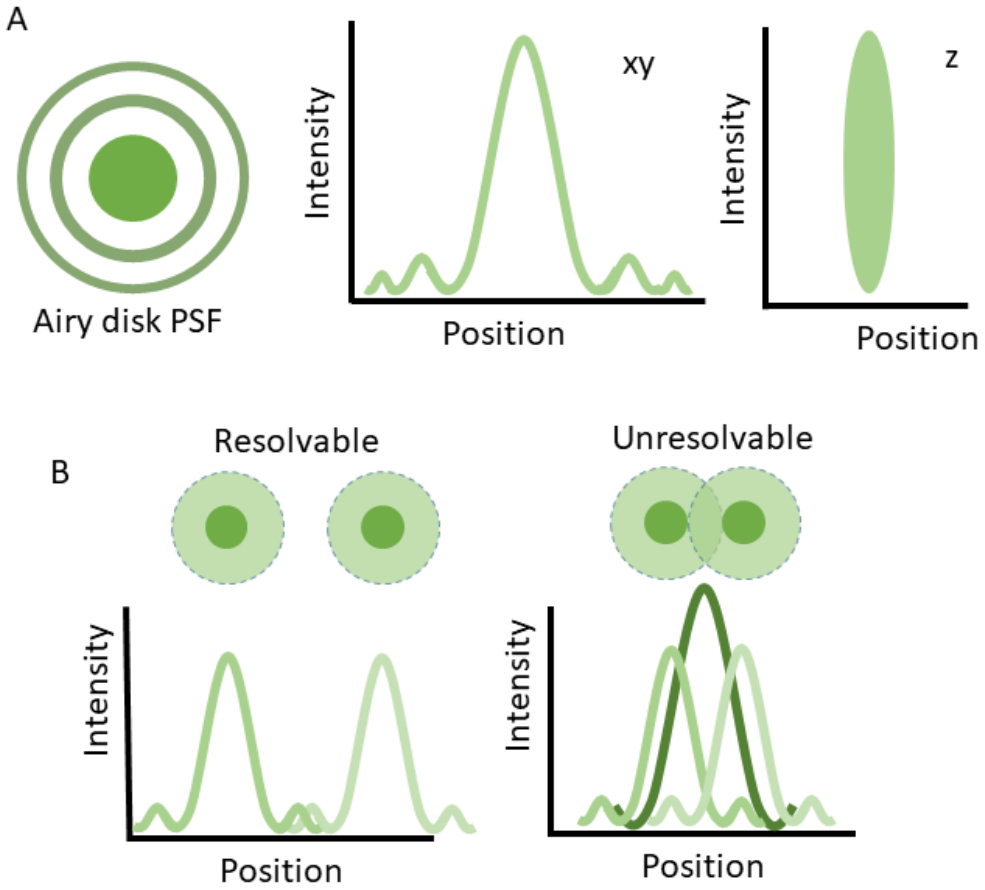

Figure 1-7. Point spread functions (PSFs) and concept of resolution

(A) The PSF is the image of a point source, also known as an Airy disk diffraction pattern. This entails a peak at the centroid of the source and multiple surrounding concentric rings. A point source appears elongated in z due to poorer resolution in that plane.

(B) Two light sources can be resolved as separate entities if there is enough distance between them. If they are closer than a minimum distance, and the first minimum of one Airy disk overlaps with the primary peak of the second, the emissions interfere and the light sources appear as a single point, so that the individual points cannot be identified. This minimum distance is the resolution limit.

1.9.2 Advances in light microscopy

For diffraction-limited microscopy, the resolution is typically ~250 nm in the x and y planes and >450 in z (Galbraith and Galbraith, 2011). While this allows visualisation of larger structures in biological samples (such as organelles), it is not sufficient to see smaller structures or the organisation of individual proteins. In order to visualise features smaller than the resolution limit, alterations to optics and photo-physics have been invented.

Confocal microscopy was introduced to reject out-of-focus light using a pinhole (Minsky, 1988). Through optical sectioning, the resolution is improved compared to standard widefield imaging, optimistically reaching 200 nm and 400 nm, in-plane and axially. Airyscan microscopy is a more recent innovation which replaces the traditional confocal pinhole and photomultiplier tubes with a 32-element detector array and algorithmic pixel reassignment. Airyscan enables 1.7x better resolution than the diffraction-limited confocal system (Huff *et al.*, 2017), yielding approximately 120 nm laterally and 350 nm axially.

The first super-resolution techniques, such as STED (Hell and Wichmann, 1994) and SIM (Gustafsson, 2000), improved the resolution well below the diffraction limit, allowing visualisation at the nanometre scale. A group of super-resolution techniques broadly referred to as single molecule localisation microscopy (SMLM) hinge upon the concept of stochastically activating subsets of fluorophores. By capitalizing on spatial and temporal separation it is possible to pinpoint their exact locations. Perhaps the most widely used SMLM technique is dSTORM, which achieves 20 nm resolution by photo-switching small subsets of fluorophores between an off-state and a short-lived on-state (Heilemann *et al.*, 2008). Another technique called DNA-PAINT enables sub-10 nm resolution through the use of transiently binding oligonucleotides (Jungmann *et al.*, 2014).

An example of the improvement in resolution is evident when applied to biological structures. When microtubules in cultured cells are viewed with confocal microscopy, the structures appear blurred (Figure 1-8A), whereas the improved resolution of dSTORM allows individual tubules to be seen (Figure 1-8B). The nanoscale resolution afforded by these super-resolution techniques now allows researchers to visualize structures within cells at the scale of individual proteins.

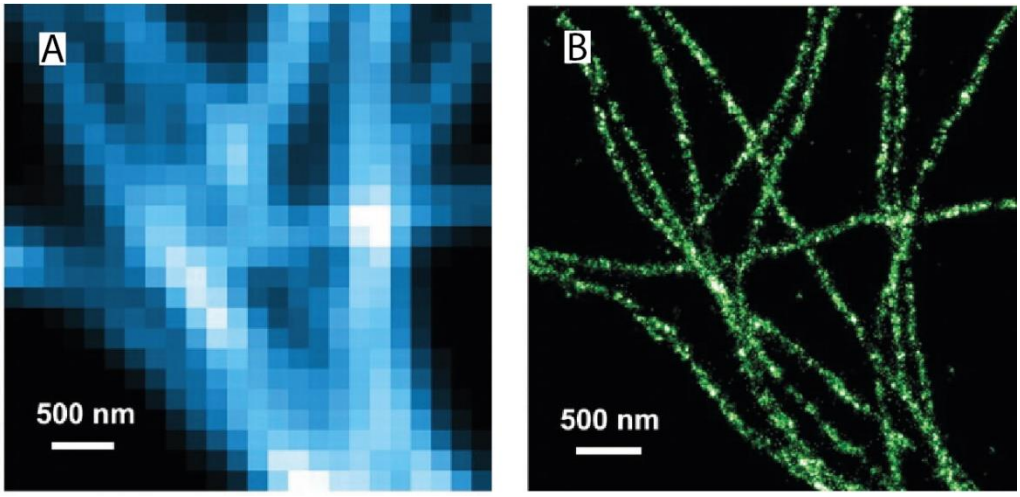

Figure 1-8. Super-resolution microscopy resolves finer structural details

(**A**) When microtubules are imaged with confocal microscopy the structure of individual tubules are not clearly defined, appearing instead as a blurred, larger object. (**B**) When the same sample is imaged with STORM, which has improved resolution, the microtubules are more clearly visualised. Image from (Bates et. al., 2007).

1.9.3 Super-resolution microscopy for 3D imaging

As emphasised earlier, the focus of this thesis regards imaging RyR clusters located deep in the cell, which have complex 3D geometries. This calls for a technique with powerful resolution capabilities (< 20 nm), at significant depths into a sample and in three dimensions.

Of the techniques introduced, only a handful can facilitate 3D imaging at depths beyond a few microns, and they are often subject to pitfalls which hamper the practicality of their use. That SMLM is typically performed in 2D relates to the increased difficulty in separating axially-overlapping fluorophores (Lu *et al.*, 2019), but options like PSF engineering with induced astigmatism exist to enable 3D imaging (Huang *et al.*, 2008). While one-colour 3D dSTORM has been used to visualise RyR clusters inside cardiomyocytes at a depth of 6 µm, through the use of PSF modification (Shen *et al.*, 2018), greater working distances are required to explore deeper regions of the cell. 3D DNA-PAINT has been successfully validated for synthetic calibration structures under advantageous conditions of low background (Lin *et al.*, 2019), but it's use for imaging biological structures deep inside cells, in far less favourable conditions, is not guaranteed.

Whilst high NA objectives allow working distances of 100+ microns into a sample, numerous SMLM approaches implement light sheets which are practically much shallower in order to remove out of focus light (due to the highly-scattering properties of the cell interior). In doing so, the signal to noise ratio of events is increased, allowing better determination of single molecules from the background (Tokunaga *et al.*, 2008; Jungmann *et al.*, 2014). For instance, illumination methods such as HILO (highly inclined and laminated optical sheet) which is commonly used for STORM and TIRF (total internal reflection fluorescence) which enables DNA-PAINT, ultimately limit these techniques to the first few microns of a biological sample. Features such as biplane imaging (whereby imaging occurs simultaneously at two different focal planes at a fixed distance apart) can improve depth discrimination (Winterflood *et al.*, 2015; Song *et al.*, 2019), pending successful alignment and calibration of PSF patterns (Kirshner *et al.*, 2012). A combination of photoactivated localisation microscopy and two-photon temporal focusing has provided up to 10 µm imaging depth in biological samples (Vaziri *et al.*, 2008).

In summary, there is not currently an imaging technique practical for biological imaging which is both high resolution (<20 nm), functional for imaging at depths of 10s of microns and

compatible with 3D imaging. Therefore, new imaging methods are required to observe RyR cluster morphology deep inside a cardiomyocyte.

1.10 Aims

This study aimed to gain insight into cardiac Ca^{2+}-handling machinery by the application of expansion microscopy (ExM), a novel technique capable of visualising 3D structures deep in cells with individual protein resolution. The background of ExM is detailed in Section 2.3.

Due to the limitations of imaging deep into a sample with previous techniques, dyadic CRUs situated at t-tubules have remained relatively un-characterised at individual protein resolution. This work aimed to describe the organisation of RyRs and JPH within dyads at individual protein level, as has been done for surface clusters. As cluster organisation directly controls function, this description of dyad morphology will improve understanding of CICR and spark production. The work also aimed to characterise the amount of RyR phosphorylation *in situ* for the first time, to learn of the incidence of these post-translational modifications at the cluster level.

Having characterised clusters in healthy cells, it was then of interest to observe the differences which could account for Ca^{2+} dysfunction in the pathological state of HF, using the MCT model of RV HF following PAH. This comprised remodelling of clusters of RyR and JPH, as well as investigating RyR hyper-phosphorylation. With this improved understanding of the changes in RV HF, it is hoped that a better understanding of the mechanistic steps is achieved and could reveal avenues for treatment.

In addition, it was of interest to explore the maturity of SC-CMs, with regards the contractile machinery, t-tubules and precursor CRUs.

The specific aims were:

i. To optimise ExM for use in cardiac samples and validate the isotropy.
ii. To describe the organisation of RyR, JPH and *in situ* phosphorylation (with an emphasis on 3D dyadic clusters).
iii. To observe pathological changes to cluster organisation and phosphorylation in the MCT model of RV HF.
iv. To characterise the structural maturity of SC-CMs and investigate the development of CRU progenitors.

Chapter 2. Methods

2.1 Cardiomyocyte isolation

Experiments were performed in line with the UK Animals (Scientific Procedures) Act of 1986, the EU Directive 2010/63/EU and with UK Home Office (and local ethical) approval. Adult male Wistar rats (200 ± 20 g) were obtained from central Biomedical Services (University of Leeds) and housed at 20-22°C, 50% humidity and with a 12-hour light/dark cycle, plus *ad libitum* access to food and water. Animals were euthanised according to the approved UK Home Office Schedule 1 method for rodents, by concussion followed by cervical dislocation. The heart was promptly excised and washed in isolation solution.

In order to isolate individual cardiomyocytes, hearts were attached to a Langendorff perfusion system (Figure 2-1). The heart was cannulated using the aorta, which was secured with a clip and suture thread. The heart was perfused with three oxygenated solutions (the compositions of which are provided in Table 2-1), which were circulated at 7 ml/min and maintained at 37^{o}C. First, 750 µM Ca^{2+}-containing isolation solution was perfused for 5 mins to clear the coronary system of blood. Second, 0.1 mM EGTA-containing solution was perfused for 4 minutes to terminate contraction. Finally, enzyme solution, comprising 40 mg/ml collagenase (type 2, Worthington Biochemicals, USA) and 3.2 mg/ml protease (Sigma-Aldrich (Sigma), UK), was perfused for 6-8 mins to digest the tissue.

Some cardiomyocytes imaged in this thesis were obtained from isolations performed by Hannah Kirton and Zhaokang Yang. The isolation of MCT cardiomyocytes, as specified in Section 5.2.1, was performed alongside Miriam Hurley.

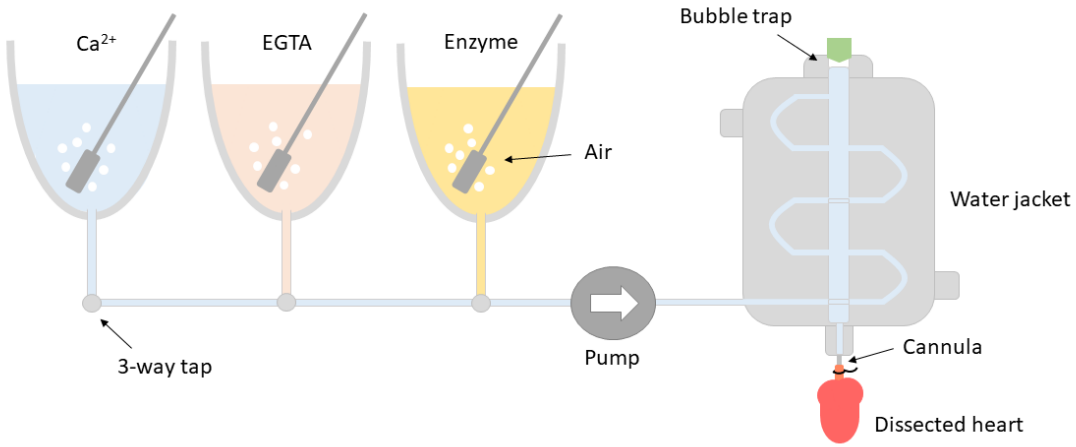

Figure 2-1. Langendorff heart perfusion for cardiomyocyte isolation

The dissected heart was cannulated by the aorta, secured with suture thread and perfused with three solutions to release individual cardiomyocytes. Perfusion with Ca^{2+}-containing solution was performed to clear the coronary circulation, with EGTA-containing solution to cease contraction and finally with enzymes (collagenase and protease) to break down the tissue. The solutions were oxygenated and maintained at 37°C with a water jacket. A peristaltic pump ensured constant speed of perfusion, and solutions were passed from the reservoirs through silicon tubing, with a bubble trap to prevent air bubbles entering the heart and disrupting perfusion.

Chemical	*Isolation solution*	*Ca^{2+} isolation solution*	*EGTA isolation solution*	*Enzyme isolation solution*	*Tyrode's solution*
NaCl	130	130	130	130	136.9
KCl	5.4	5.4	5.4	5.4	5.4
$MgCl_2$	1.4	1.4	1.4	1.4	0.5
NaH_2PO_4	0.4	0.4	0.4	0.4	0.33
HEPES	5	5	5	5	5
Glucose	10	10	10	10	5.6
Taurine	20	20	20	20	-
Creatine	10	10	10	10	-
EGTA	-	-	0.1	-	-
$CaCl_2$	-	0.75	-	-	1
Collagenase	-	-	-	1 mg/ml	-
Protease	-	-	-	0.08 mg/ml	-
pH	7.5	7.5	7.5	7.5	7.4

Table 2-1 Cardiomyocyte isolation solutions

All concentrations are in mM unless stated otherwise.

Following perfusion with enzymes, the digested heart was removed from the rig and the ventricles were dissected, weighed and diced to liberate ventricular myocytes. The diced tissue was shaken several times with enzyme solution, in conical flasks suspended in a water bath. After each shake, the solution was strained through 200 μm^2 nylon mesh gauze and centrifuged (50 x g for 40 seconds) to obtain pellets of isolated cardiomyocytes, and the tissue retrieved from the gauze was shaken further with fresh enzyme solution until none remained, or sufficient cell harvests were obtained. The pellets of cells were resuspended in fresh Ca^{2+}-containing solution, washed several times with more solution to remove dead cells, yielding a suspension containing >60% rod-shaped cardiomyocytes. Cells were adhered to imaging chambers (acrylic rectangle to fit microscope stage with a circle cut out (custom-made, Ponoko, https://www.ponoko.com/), attached to #1.5 coverslips, which were coated with 11.7 µg/ml laminin overnight at room temperature (RT)), for 2 hours at 37ºC.

Once adhered to chambers, cells either proceeded to the beta-adrenergic stimulation protocol (Chapter 4), or were fixed immediately *in situ* with 2% paraformaldehyde (PFA; Sigma) (w/v) in phosphate-buffered saline (PBS, Sigma) at RT for ten minutes. Cells were stored in fixed cell storage solution until immunostaining.

2.2 Immunofluorescence labelling

The compositions of solutions used in the immunolabelling steps are detailed in Table 2-2, and the details of antibodies (including manufacturers and catalogue numbers) are located in Tables 2.3 and 2.4. For all antibody incubation steps, antibodies were diluted in incubation buffer containing (w/v or v/v) 0.05% NaN_3; 2% bovine serum albumin; 2% normal goat serum (NGS, Thermo Fisher Scientific (Thermo), UK); 0.05% Triton X-100 dissolved in PBS. Janelia Fluor 549 secondary conjugates were prepared using unlabelled, affinity-purified anti-mouse and anti-rabbit IgG (Jackson ImmunoResearch, US), and Janelia Fluor 549 SE labelling kits (Janelia, US).

Cells were permeabilised with 0.1% Triton X-100 (Sigma) in PBS for 10 mins at RT, then blocked with 10% NGS in PBS for one hour at RT. After blocking, cells were incubated in primary antibodies overnight at 4°C. Samples were washed three times in fresh PBS at RT for 10 mins, before being incubated in secondary antibodies for 2 hrs at RT. Samples were washed three times in fresh PBS at RT for 10 mins.

Cells were imaged to confirm suitable quality of labelling ahead of performing expansion microscopy steps. These pre-expansion images were also used to determine EF.

Chemical	*Permeabilisation solution*	*Blocking solution*	*Antibody incubation solution*	*Fixed cell storage solution*
PBS	1x	1x	1x	1x
Bovine serum albumin	-	-	2%	0.5%
Triton X-100	0.1%	0.05%	0.05%	-
Normal goat serum	-	10%	2%	-
NaN_3	-	-	0.05%	0.01%

Table 2-2 Immunolabelling solutions

Details of the composition of solutions used in the immunolabelling step.

Primary antibody	Manufacturer	Dilution	Catalogue number
Mouse monoclonal anti-RyR2 IgG1	Thermo, UK	1:200	MA3-916
Rabbit polyclonal anti-RyR2	Sigma, UK	1:200	HPA020028
Rabbit polyclonal anti-JPH2	Thermo, UK	1:250	40-5300
Mouse monoclonal anti-Cav3	BD Biosciences, US	1:200	610420
Mouse monoclonal anti-NCX	Swant, Switzerland	1:200	R3F1
Mouse monoclonal anti-α-actinin	GeneTex, USA	1:200	GTX29465
Rabbit monoclonal anti-α-tubulin (Alexa Fluor 647)	Abcam, UK	1:200	ab190573
Rabbit polyclonal anti-RyR2 phospho. Serine-2808	Badrilla, UK	1:200	A010-30AP
Rabbit polyclonal anti-RyR2 phospho. Serine-2814	Badrilla, UK	1:200	A010-31AP
Rabbit polyclonal anti-RyR2 phospho. Serine-2030	Badrilla, UK	1:200	A010-32
Rabbit polyclonal anti-Dystrophin	Abcam, UK	1:200	ab15277
Mouse monoclonal anti-calnexin	Thermo, UK	1:200	MA3-027
Rabbit polyclonal anti-KDEL	Thermo, UK	1:200	PA1-013
Mouse monoclonal anti-SERCA2 ATPase	Abcam, UK	1:200	ab2861
Rabbit polyclonal anti-RyR3	Sigma, UK	1:200	ab9082
Rabbit polyclonal anti-IP3R-1	Thermo, UK	1:200	PA1-901

Table 2-3 List of primary antibodies

Details of primary antibodies and dilutions used in the immunolabelling step.

Secondary antibody	Manufacturer	Dilution	Catalogue number
Alexa Fluor 488, goat anti-mouse IgG	Thermo, UK	1:200	A11001
Alexa Fluor 488, goat anti-rabbit IgG	Thermo, UK	1:200	A11008
Alexa Fluor 594, goat anti-mouse IgG	Thermo, UK	1:200	A11005
Alexa Fluor 594, goat anti-rabbit IgG	Thermo, UK	1:200	A11012
Atto647N, goat anti-rabbit IgG	Sigma, UK	1:200	40839-1ML-F
Janelia Fluor 549[1], conjugated to Affinipure goat anti-mouse IgG[2]	[1]Tocris, Biotechne, UK [2]Jackson ImmunoResearch, US	1:200	6147, 115-005-146
Alexa Fluor 680, goat anti-mouse	Thermo, UK	1:200	A21076

Table 2-4 List of secondary antibodies

Details of secondary antibodies and dilutions used in the immunolabelling step.

2.3 Expansion microscopy

2.3.1 Principle

ExM is a novel super-resolution microscopy method which involves spatially separating point sources of light using expandable acrylamide hydrogels (Figure 2-2A) (Chen et al., 2015). By de-crowding a fluorescently labelled sample, ExM reduces the overlapping of PSFs, enabling the visualization of structures beneath the resolution limit that would otherwise be indistinguishable.

The generic protocol of ExM is shown in Figure 1-9B. Fluorescent molecules (corresponding to labelled targets in a sample), are crosslinked into a hydrogel matrix by methacryloyl group additions to the labels. Next, degradation of the original biological material leaves behind the fluorescent labels suspended in the gel. Expansion of the gel is achieved by a series of washes in high purity H_2O, which washes away the positively-charged Na^+ ions from the sodium acrylate in the gel, leaving negatively charged $COOH^-$ groups which repel each other. The expansion factor (EF) of ExM hydrogels differs depending on the specific gel chemistry, including the amount of crosslinks and the concentration of sodium acrylate, as well as the salinity of the solution used to expand the sample.

ExM enhances the effective resolving power of any conventional microscope, yielding image voxels equivalent to that of a super-resolution microscope, but that are obtained with the faster throughput of a diffraction-limited microscope. While the diffraction limit is an upper limit for resolution, the resolution of ExM in practice is still dependent on aspects such as spherical aberrations occurring through refractive index mismatch and chromatic aberrations. A key advantage to ExM over other super-resolution techniques is that thereis an improved imaging depth, aided by the removal of background light in the clearing process. Crucially, it is straightforward to acquire 3D data by imaging ExM gels using confocal microscopes with z-stack functionality.

A crucial aspect involved with ExM is in the validation of the isotropy, or even-ness of expansion. Artefacts and distortions arising from gel expansion are possible in scenarios where the sample is improperly digested, or if the nanoscale structure of the gel matrix was heterogeneous. The topic of isotropy is visited in more detail in Chapter 3.

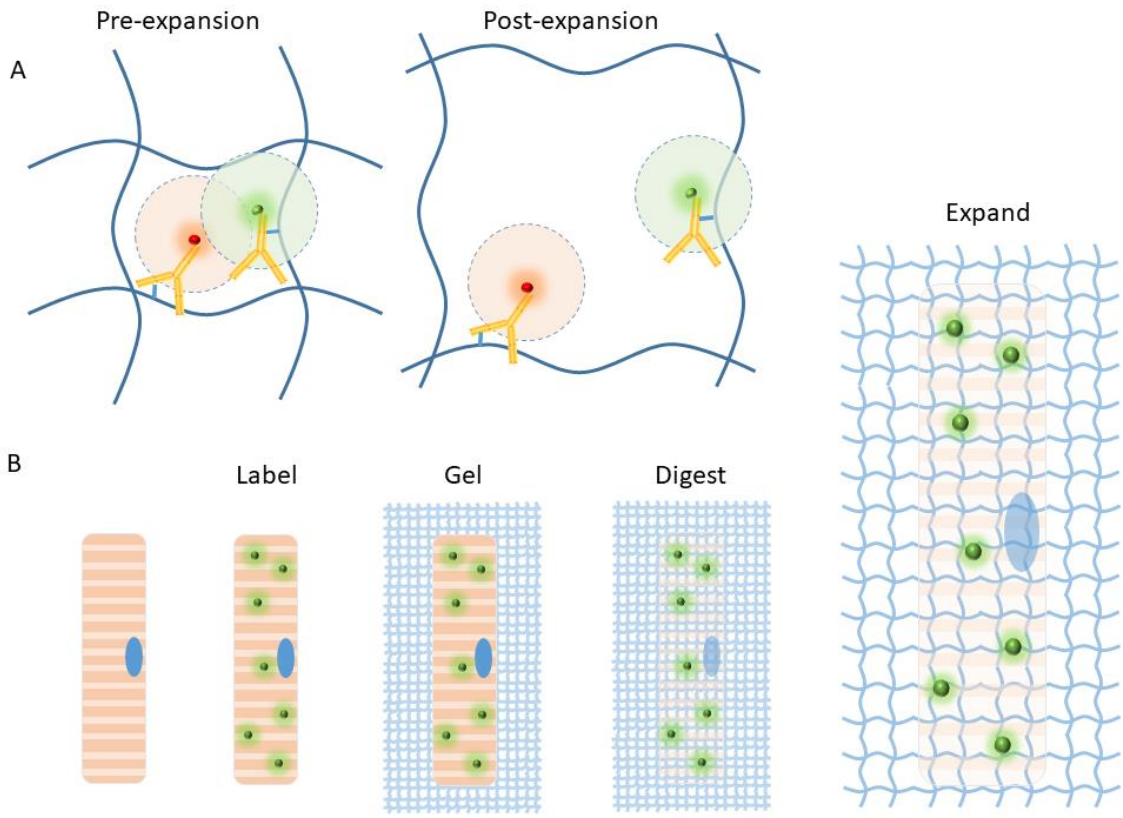

Figure 2-2. ExM - principle and protocol

(A) Spatial separation of fluorophores by gel expansion ensures that there is less overlapping of PSFs, so the effective resolution of the imaging system is improved.

(B) Schematic showing the protocol of ExM. The cell is labelled with fluorescent probes which are modified with acryloyl-X, preparing them for incorporation into a gel matrix. The gel is polymerised on the sample, integrating the fluorescent probes. The gel is placed in digestion solution to fully remove the solid biological material. After digestion, the gel (bearing just the fluorophores) is expanded in several washes in pure water.

2.3.2 Advances in expansion microscopy

The original ExM approach involved labelling targets of interest with an antibody-oligonucleotide construct, which was capable of hybridizing with a custom-made label (comprising a complementary oligonucleotide, a fluorophore and a methacryloyl functional group). The gel itself was formed of acrylamide and the crosslinker N,N'-methylenebisacrylamide (Figure 2-3A). A more user-friendly variant of the technique was published, known as protein retention ExM (proExM) (Tillberg et al., 2016), allowing the use of conventional antibodies instead of the tri-functional oligonucleotides. Following immunostaining, incubation with acryloyl X (AcX), a succinimidyl ester, marks amine groups on proteins with an acrylamide functional group, allowing their direct incorporation into the gel matrix.

In 2018, Truckenbrodt *et. al.* published a technique termed X10 expansion microscopy (X10), in which gels expanded 10-fold in each dimension (or 1000-fold in volume). X10 capitalises on a different acrylamide variant, the self-crosslinking N,N-dimethylacrylamide monomer (DMAA) (Figure 2-3B). This gel recipe has a reduced number of crosslinks compared to the original recipe, enabling the increased EF. The 10-fold improvement in resolution means that basic confocal microscopes possessing ~ 200 nm resolution can produce super-resolution quality imaging datasets with 20 nm resolution, using commercially available reagents.

Aside from innovations in gel chemistry, improved resolution has been achieved by imaging ExM gels with other super-resolution techniques, for instance ExSTED (Gao *et al.*, 2018; Kim *et al.*, 2019), ExSIM (Gustafsson, 2000; Cahoon *et al.*, 2017; Halpern *et al.*, 2017; Wang *et al.*, 2018), ExSTORM (Shi *et al.*, 2019; Xu *et al.*, 2019), ExSOFI (Li *et al.*, 2018) and ExLSM (light sheet microscopy) (Düring *et al.*, 2019; Gao *et al.*, 2019; Hörl *et al.*, 2019).

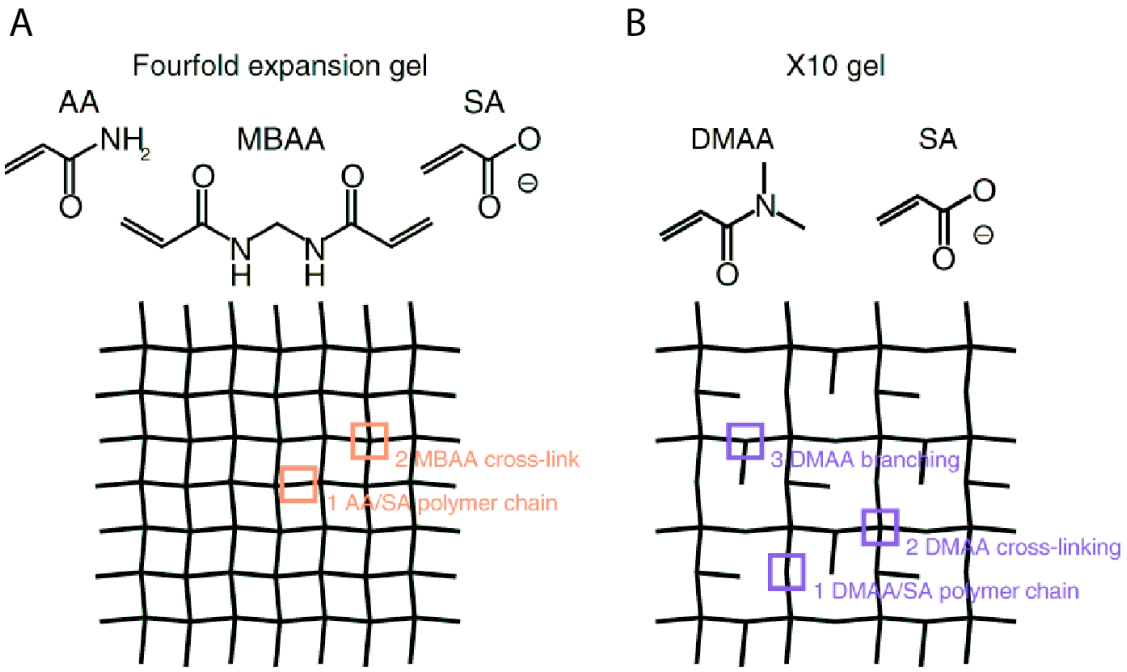

Figure 2-3. ExM - gel chemistry

ExM gels are acrylamide matrixes which contain the ionic sodium acrylate (SA), allowing the gel to expand upon addition of water. **(A)** The original gel recipe expands by 4.5-fold, and uses the standard acrylamide monomer (AA) as the backbone, with the crosslinker N,N'-Methylenebisacrylamide (MBAA) (Chen et al., 2015). **(B)** X10 expansion microscopy introduced the self-crosslinking dimethylacrylamide (DMAA). The X10 gel possesses altogether fewer crosslinks than the original four-fold expanding gel, therefore enabling the enhanced expansion factor to 10-fold. Image from (Truckenbrodt et. al., 2019).

2.3.3 Expansion protocol

The pipeline for each ExM protocol, whether proExM or X10, is demonstrated in the schematic in Figure 2-4. The practical optimisation of the ExM technique for cardiac biological samples is detailed in Chapter 3.

After immunofluorescent labelling, cells were incubated with the anchoring reagent 0.1 mg/ml Acryloyl-X (AcX, Thermo), in PBS overnight at 4°C, then washed in PBS immediately prior to addition of gel solution from either the proExM or X10 protocols, the composition of which are detailed in Table 2-5.

The polymerisation reaction, where the gel solution reacts with the labelled sample, was performed in a sealed acrylic chamber comprising two coverslips (one bearing the sample) and coverslip spacers (created by cutting coverslips into rectangular strips with a diamond-tipped glass cutter).

ProExM (also known as 4x ExM) was performed as previously described (Tillberg *et al.*, 2016). Gel monomer solution was made in advance of the experiment at a higher strength (1.06x) to account for the dilution caused by the addition of PBS, the initiator ammonium persulfate and accelerator N,N,N',N'-Tetramethylethylenediamine (TEMED). Cells were incubated with gel solution (((w/v) 8.6% sodium acrylate, 2.5% acrylamide; 0.15% N,N'-Methylenebisacrylamide, 11.7% NaCl, PBS) with 0.1% ammonium persulfate and TEMED) for 30 mins at 4°C and then over 2 hrs at 37°C, until fully polymerised.

10x ExM preparation was performed as previously described (Truckenbrodt *et al.*, 2018). Gel monomer solution (4:1 molar ratio of dimethylacrylamide and molecular-grade SA, dissolved in deionized H_2O (dH_2O)) was made fresh for each experiment, and was bubbled with N_2 gas for over 1 hour on ice. Potassium persulfate (Sigma) was added at 0.4% molar relative to monomer concentration from a 0.036 g/ml stock, made fresh for each experiment, and the solution was bubbled for another 15 mins on ice. 500 µl of the gel monomer solution was mixed rapidly with 2 µl of TEMED and quickly added to the cells. Gels were polymerised after 2 hours, but were typically left overnight to ensure complete polymerisation.

Following polymerisation, gels were ejected from chambers by gently sliding a razor blade between the coverslips and spacers, and were cut into an asymmetric shape to ensure the correct orientation was kept through the followings steps. The major axes of the gel were measured to calculate the pre-expansion size used in the macroscale EF calculation. The gel was then

digested in 0.2 mg/ml proteinase K (ProK, New England Biolabs) dissolved in digestion buffer (50 mM Tris pH 8.0, Thermo; 1mM ethylenediaminetetraacetic acid (EDTA, Sigma); 0.5% Triton X-100; 0.8M guanidine HCl, Sigma; dH_2O) overnight at RT.

Gels were expanded by gentle washing in fresh dH_2O, until there was no further change in the gel size. Washes were performed in a dark room to limit light exposure to the sample. The final gel size was measured to calculate the macroscale EF. Nuances of the ExM method relating to gel polymerisation, handling and imaging are the focus of Chapter 3.

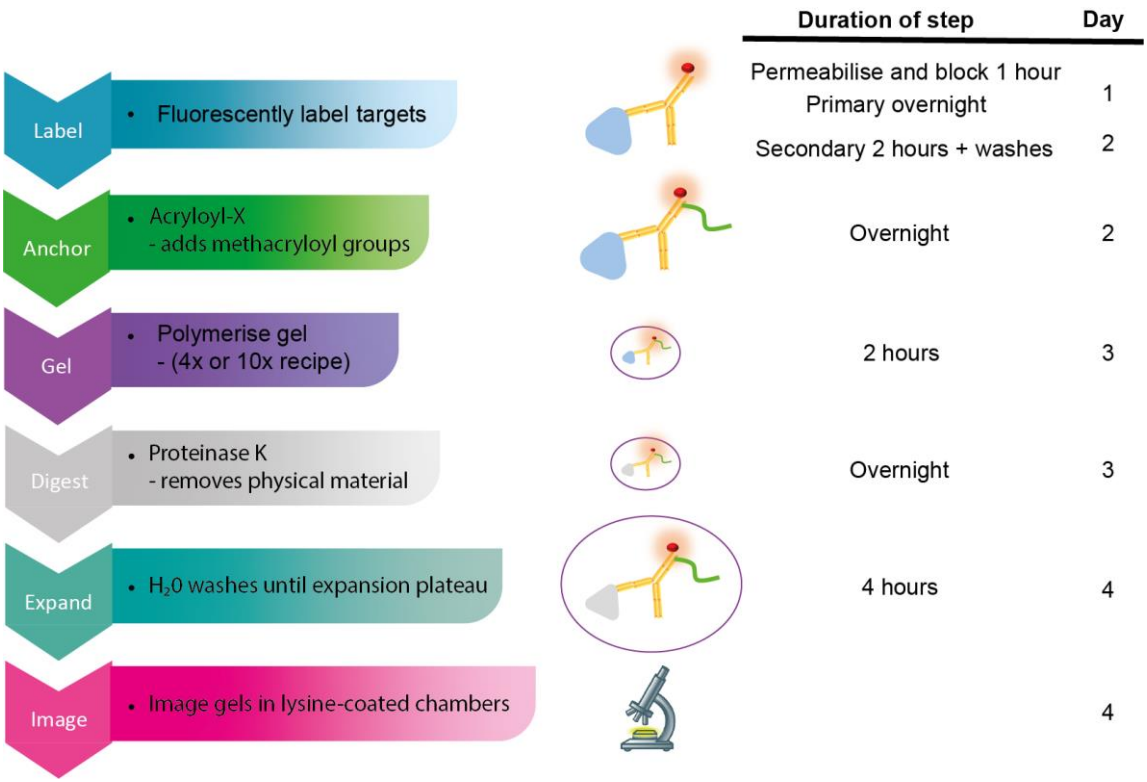

Figure 2-4. ExM protocol pipeline

The schematic depicts the major steps in the ExM protocol, the length of each step and the day on which each step is performed.

Chemical	*proExM gel solution*	*X10 gel solution*
Acrylamide	2.5%	-
N,N'methylenebisacrylamide	0.15%	-
N,N-dimethylacrylamide	-	26.64%
Sodium acrylate	8.6%	6.26%
Sodium chloride	11.7%	-
PBS	1x	-
TEMED	0.1%	0.4%
Ammonium persulfate	0.1%	-
Potassium persulfate	-	0.36%

Table 2-5 Expansion microscopy gel solutions

Details of the composition of gel solutions used in gel polymerisation.

Chemical	*Digestion solution*
Guanidine hydrochloride	0.8
Tris pH 8	0.05
EDTA	0.001
Triton X-100	0.5%
Proteinase K	8 units/ml

Table 2-6 Expansion microscopy digestion solution

Composition of digestion solution used in both ExM protocols. Concentrations are in M unless stated otherwise.

2.4 Imaging

2.4.1 Sample imaging

Where ExM samples were imaged with Airyscan, this was termed enhanced expansion microscopy (EExM).

For imaging ExM samples, squares of gel were cut out using spatulas and excess liquid was removed using paper towels. These gels were placed into imaging chambers (acrylic rectangle to fit microscope stage with a square cut out (custom-made, Ponoko, https://www.ponoko.com/), attached to #1.5 coverslip, coated with 0.1% (v/v) poly-L-lysine for 1 hour at RT). The technicalities of imaging ExM samples are discussed in Chapter 3.

2.4.2 Confocal microscope (with Airyscan)

For confocal and Airyscan imaging, an inverted LSM880 (Carl Zeiss, Jena) was used with a Plan-Aprochromat 63x 1.4 NA objective with a working distance of 0.19 mm. The use of an oil-based objective to image ExM samples (which are 99% water) is likely to have introduced spherical aberrations when imaging deeper into samples, due to refractive index mismatch. This objective was chosen because the high NA would enable more light collection, which was critical given the low fluorescence nature of expanded samples, and would thus aid resolution.

Alexa Fluor 488 and Janelia Fluor 549 were excited with 488 nm and 561 nm DPSS lasers. Emission bands were sub-selected using the in-built spectral detector. In confocal mode, the emission was recorded using an in-built photomultiplier tube placed behind a pinhole, set to 0.7 Airy Units. For Airyscan, the emission was recorded with the in-built 32-element GaAsP detector. Pixel sampling of primary data was < 90 and < 40 nm/px for confocal and Airyscan respectively. For acquisition of 3D datasets, samples were imaged up to a sample depth of 50 µm where possible, at step sizes of 150 and 75 nm for confocal and Airyscan imaging.

2.4.3 Nikon microscope

Some samples were screened using a Nikon eclipse TE2000-U inverted microscope with 60x oil objective (pixel size = 0.1 µm), and images were taken with an Andor Zyla sCMOS camera. Illumination was achieved using a Nikon intensilight C-HGFI arclamp or Viasho red laser (671

nm) with filter sets corresponding to excitation wavelengths required. This setup was used for dSTORM imaging of SC-CMs, as described further in Chapter 6.

System	Objective	Imaging technique	Post-processing
Nikon	60x, 1.49 NA, oil immersion	Widefield	N/A
Nikon	60x, 1.49 NA, oil immersion	dSTORM (HILO)	Drift correction using piecewise linear method (built-in algorithm within PYME). Jittered triangulation image produced.
Nikon	60x, 1.49 NA, oil immersion	DNA-PAINT (TIRF)	Drift correction using piecewise linear method (built-in algorithm within PYME). Jittered triangulation image produced, pixel size 5 nm.
LSM880	63x, 1.4 NA, oil immersion, 0.19 mm WD	Confocal	Pinhole set to 0.7 Airy units. Pixel size 90 nm. Richardson-Lucy maximum-likelihood deconvolution within IDL.
LSM880	63x, 1.4 NA, oil immersion, 0.19 mm WD	Airyscan / EExM	In-built 32-element GaAsP detector. Pixel size 40 nm. Pixel re-assignment and linear Wiener deconvolution within Zen.

Table 2-7 Image acquisition table

The different data acquisition setups used in this thesis are listed here.

2.5 Image analysis

2.5.1 Pre-processing and general steps

For confocal pre-processing, to enhance the signal-to-noise ratio, 3D z-stacks were subjected to a Richardson-Lucy maximum-likelihood deconvolution (Fish *et al.*, 1995), implemented in interactive data language (IDL) computing environment (ITT, Boulder, CO) (https://www.l3harrisgeospatial.com/Software-Technology/IDL).

Airyscan datasets were subjected to pixel-reassignment and linear Wiener deconvolution using the internal process within the software of Zen (Zeiss) (https://www.zeiss.com/microscopy/int/products/microscope-software/zen.html).

Single molecule data, encompassing dSTORM and DNA-PAINT datasets, were pre-processed within the Python Microscopy Environment (PYME) (http://python-microscopy.org/), which was created by David Baddeley, including dh5view and visGUI. Drift correction was performed using an in-built piecewise linear algorithm, and a jittered triangulation image was produced (Baddeley *et al.*, 2010).

Generic image processing steps (such as cropping, splitting channels and adding scale bars) were performed within the FijiJ software (https://imagej.net/Fiji). In all image analyses of distances, and for image scalebars, distances in expanded simples were normalised using the EF, either calculated at the microscale from the SL, or at the macroscale using the physical gel size. 3D reconstructions of datasets (including surface and volume renderings) were created in Amira (Thermo Fisher Scientific).

2.5.2 Cluster analyses

Cluster analyses yielding counts of number of proteins and spatial NND information form the greater part of the work presented in this thesis. There were two major analysis approaches used which span Chapters 4 and 5. The steps involved in these two approaches have been shown in analysis pipelines (Figure 2-5). Other analyses which are Chapter-specific are detailed in the each Chapter Methods.

The first major cluster analysis approach, entailing centroid detection for count and distance analyses of RyR and RyR-pSer2808 labelled datasets, was performed by Izzy Jayasinghe.

First, cluster outlines were obtained from RyR densities using an extension of a cluster segmentation protocol which was developed for DNA-PAINT images (Jayasinghe *et al.*, 2018), by applying a global threshold (set at 80% of the integrated intensity of a given image) to yield a binary mask. Within RyR cluster regions, holes smaller than 3000 nm^2 in 2D data, or smaller than 160,000 nm^3 in 3D data, were filled to obtain a robust segmentation.

A detection algorithm similar to that used previously (Jayasinghe *et al.*, 2018) was performed in PYME to record the coordinates of the centroid of each punctum within the cluster outline. Surface clusters underwent a 2D detection, whereas interior clusters underwent 3D detection. First, images were smoothed with a Gaussian kernel (in-plane sigma of 14 nm; axial sigma of 35 nm) and a threshold was applied according to a multi-threshold series to segment regions detected as unitary puncta (puncta translates as small, distinct points, relating to individual proteins (Jayasinghe *et al.*, 2018)). The parameters which yielded the most consistent detection results were a threshold of 1.5-3.5 and a blur size of 3.0-4.0. Next, an adaptive Gaussian shape was fitted to each region to localise its sub-pixel coordinates. Variation in the fitted widths of the puncta were observed (most likely due to local heterogeneity in fluorophore density), therefore puncta up to the size (FWHM of the fit) of ~ 20 nm, in-plane, were accepted as individual proteins. For volumes acquired deeper within the sample, where the in-plane FWHM of the PSF was larger, this criterion was relaxed up to 25 nm. The detected centroids were used for count and NND analyses performed in a custom-written IDL script. For two-protein analysis of RyR and pSer2808, the coordinates of labelling puncta were detected independently (in separate channels of the two-colour dataset), and each detected pSer2808 punctum was paired with an RyR punctum within 30 nm. Only a single RyR was marked as phosphorylated for a given pSer2808 punctum, and pSer2808 puncta which were not neighbouring to RyR puncta were excluded from analysis. For analysis of spatial phosphorylation density within a cluster, a Euclidean distance transform was created from the cluster outline binary mask in a fashion similar to that used previously (Jayasinghe *et al.*, 2009).

The second major analysis approach entails 3D count and distance analysis of RyR-JPH datasets using the Fiji plugin 3D ImageJ suite (ImageJ3D) (Ollion *et al.*, 2013). Individual clusters were manually cropped. Background subtraction was performed by using the image calculator in Fiji and subtracting a Gaussian blurred image (Gaussian filter parameter: 10).

These images were subjected to a 3D iterative thresholding algorithm (within ImageJ3D), which allowed separate objects (relating to individual JPH and RyR puncta) to be determined. The results from ‘Measure’ and ‘Distances3d’ functions were sorted using a custom-written Python code (using pandas and openpyxl libraries, composed in the Sublime text editor) to count the number of RyR and JPH objects per cluster, and to calculate the NND (using centre-centre distances) for each object.

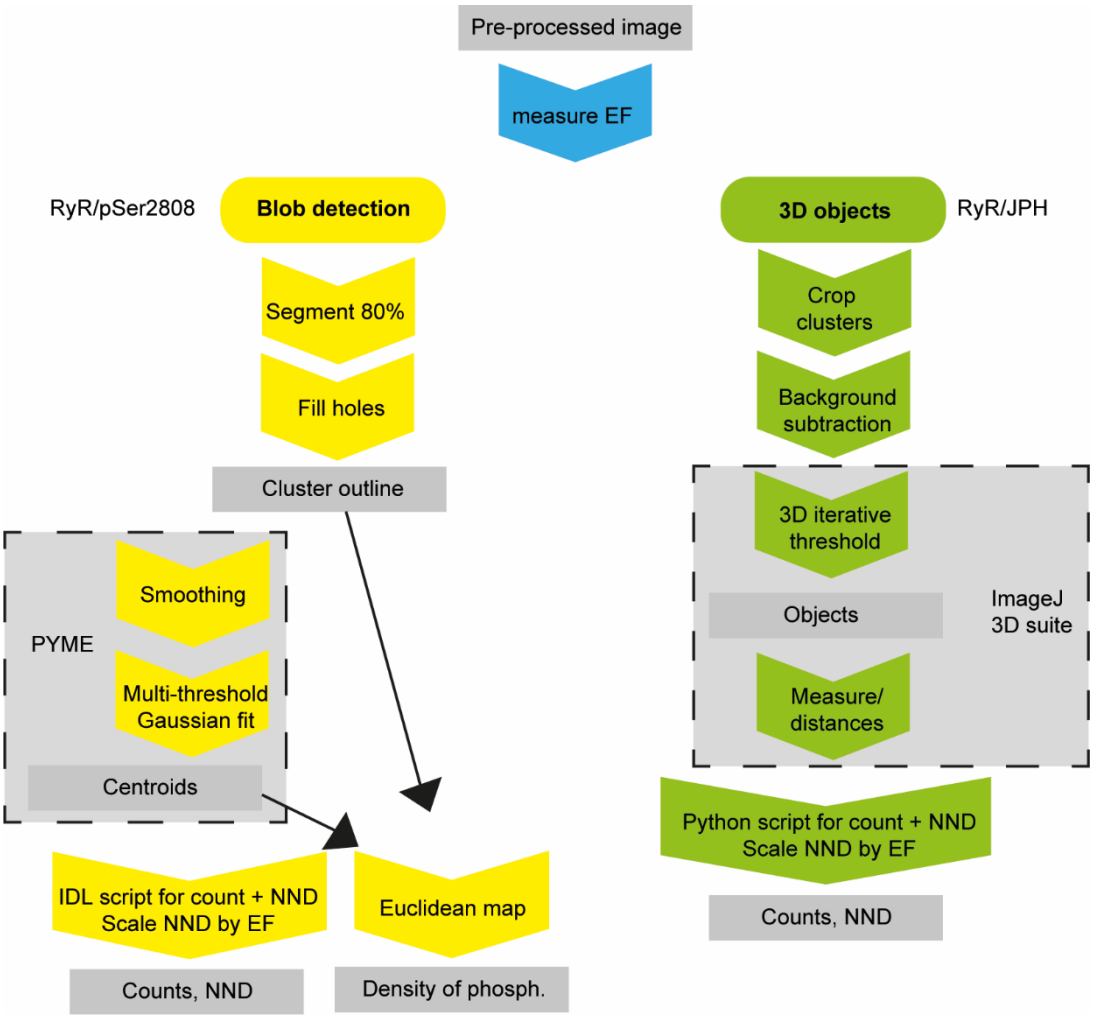

Figure 2-5. Cluster analysis pipelines

Shown are the two major cluster analysis pipelines used in this thesis.

2.6 Statistical analysis

Data analysis was performed in Graphpad Prism 8.4.3 (Graphpad, La Jolla, CA). Normality tests judged on skewness were used to determine whether to use parametric tests. For comparisons of 2 groups, an unpaired Student's T-test was used when the data were normally distributed with an equal SD. When not normally distributed, a Mann-Whitney test (with a Bonferroni correction) was used. For comparisons of groups of 3+, a one-way ANOVA (with a Tukey correction for multiple comparisons) was used when the data was normally distributed with equal SD. When not normally distributed, a Kruskall-Wallis test was used.

Data and graphs are presented as mean ± SEM, unless stated otherwise. The number of replicates, n, within each experimental analysis is stated in the figure legend. The degrees of significance are *$p<0.05$, **$p<0.01$, ***$p<0.001$, ****$p<0.0001$.

Chapter 3. Adapting expansion microscopy to resolve cardiac ultrastructure

3.1 Introduction

A technique capable of visualising proteins in complex 3D nanodomains located deep inside the cell is needed to better understand structures such as the cardiac dyad. This technique must be able to resolve individual proteins (~20 nm resolution), whilst at significant depths from the surface of the sample (20+ μm) and in a 3D capacity.

The novel super-resolution technique ExM, involving swellable acrylamide hydrogels which spatially separates a fluorescently labelled sample (Chen *et al.*, 2015), offers a possible approach. In order to apply ExM to cardiac biological material, parts of the technique must be optimised, for instance the process of polymerising a gel to incorporate isolated cardiomyocytes, as well as tailoring the digestion steps for the unique physical and mechanical properties.

To trust the measurements obtained through ExM, it is important to validate the isotropy (how uniform the expansion process is) to confirm that any distortions introduced are minimal. Anisotropy can arise from improper gel composition, or insufficient digestion leading to physical disruption of the gel upon expansion. While the benchmark for isotropy validation is image the same area before and after expansion (Chen *et al.*, 2015), it is practically challenging to locate the same area in the expanded rotated gel. Further, this pre-expansion imaging ought to be performed with another super-resolution technique to enable genuine error calculation at the nanoscale. Alternative approaches to isotropy validation include measuring internal structures with uniform or predictable geometries as rulers (Pesce *et al.*, 2019).

This chapter sought to optimise the practical approach of applying ExM (combined with Airyscan) to cardiac samples (isolated cardiomyocytes). The two ExM protocols used were proExM (Tillberg *et al.*, 2016) and X10 (Truckenbrodt *et al.*, 2018). First, the resolution of the techniques was demonstrated, both theoretically (relating to the PSF), as well as in practice when applied to biological structures. Subsequently, the isotropy of the expansion process was verified to ensure that measurements taken with the technique were reliable.

3.2 Methods

Cardiomyocytes were obtained by the Langendorff perfusion method detailed in Section 2.1.

The samples were fluorescently immunolabelled with antibodies as detailed in Section 2.2. proExM or X10 expansion microscopy were performed as outlined in Section 2.3. The samples were then imaged as in Section 2.4. The nuances of the steps are discussed within this Results chapter.

To estimate the chromatic alignment at varying imaging depths, an acrylamide gel from the proExM recipe was polymerised containing 100 nm Tetraspeck multi-emission beads. Imaging was performed at depths of 0 µm and 28.5 µm. In 2-colour images, the offset of centroids was calculated.

To obtain PSF estimates, 3D stacks were taken of 100 nm and 20 nm yellow-green or red-orange Fluosphere Polystyrene Microsphere beads (ThermoFisher) suspended within an acrylamide gel. PSFs for confocal and Airyscan data were measured, , while PSFs for EExM were scaled from the measured Airyscan PSF. The estimated PSF for dSTORM was simulated.

DNA-PAINT imaging of α-actinin was performed by Miriam Hurley, while dSTORM datasets were provided by Izzy Jayasinghe. The analysis measuring the longitudinal separation between the double-band of α-actinin in 10x EExM and DNA-PAINT data was performed by Izzy Jayasinghe, whereby the sub-pixel centroids of each intensity peak were calculated using a Gaussian line profile fitting procedure.

The FWHM of microtubules was obtained by drawing a line profile across individual microtubules.

In order to assess EF, the physical gel size was measured before and after expansion using a ruler. The SL was measured in datasets where striations were visible for instance with labelling of α-actinin, RyR, JPH or t-tubules. The average SL measured was taken across 5 sarcomeres.

To verify microscale isotropy, the SL was measured for cardiomyocytes which were oriented in different angles in the same gel. To verify nanoscale isotropy, the distance between the double-band of α-actinin was measured in relation to the EF of the gel.

3.3 Results

3.3.1 Protocol optimisation

This section focuses on the optimisation of methodological steps to perform ExM on isolated cardiomyocytes.

Cardiomyocytes were typically adhered to a no. 1.5 coverslip, which was attached to an acrylic chamber to facilitate changing solutions during labelling and anchoring incubation steps, and to allow pre-expansion imaging on a microscope stage. When using cells attached to coverslips, it was critical to use a high density per μm^2 because a fraction of cells are lost with fixation, and each wash or incubation step. If the cell density on the coverslip gets too low, it becomes challenging to find the sample in the expanded gel, particularly because of the fluorescence reduction which occurs during the ExM process. Sample gelation was carried out in a sealed chamber, with one layer of coverslip spacers (coverslip cut into 4 rectangular strips with a diamond-tipped glass cutter) used in order to form a gel of a practical height (Figure 3-1A).

The alternative approach for a suspension of fixed, labelled and anchored cardiomyocytes requires mixing with gel solution and pipetted into the gelation chamber. The advantage to using a cell suspension was being able to ensure a dense concentration of cells in the gel, avoiding the scenario which sometimes occurred with cells attached to a coverslip. One caveat to this approach was the requirement for the sample to be as close to the bottom of the gel as possible, due to the limited working distance of microscope objectives. To ensure more cardiomyocytes sank further to the coverslip, a lower concentration of the gel polymerisation initiator and accelerator was used (0.1% compared to 0.2%) to slow the polymerisation. The other caveat to this approach is there was not a practical step for pre-expansion imaging, necessitating loading a microscope slide with a small amount of labelled cell suspension.

Several pieces of equipment were used to make the ExM protocol more efficient and minimise damage to gels, reducing the chance of distortions (Figure 3-1B). Two long-handled metal spatulas were used for transporting gels between chambers, as well as a long coverslip. Expansion of the gel following digestion was performed in a Petri dish of sufficient size to accommodate the fully-expanded gel, which could be up to 15 mm depending on the starting size. The dishes were wrapped in foil to minimise exposure to light. A Pipette pump was used during the expansion step to carry out larger water changes, necessary due to the high-volume (400+ ml) required to submerge the expanded gels within the large Petri dishes. Due to the

optical transparency of the expanded gel when submerged in water, water changes were done behind a ruler to minimise the chance of the gel being damaged. The gels were measured with a ruler after polymerisation to obtain the macroscale pre-expansion size, and also after expansion (just prior to imaging) for the post-expansion size.

For imaging expanded ExM samples, gels were loaded into imaging chambers, comprising a no. 1.5 coverslip attached to a large square acrylic chamber (Figure 3-1C). The coverslip was coated with 0.1% poly-L-lysine just prior to loading, to reduce drift during image acquisition.

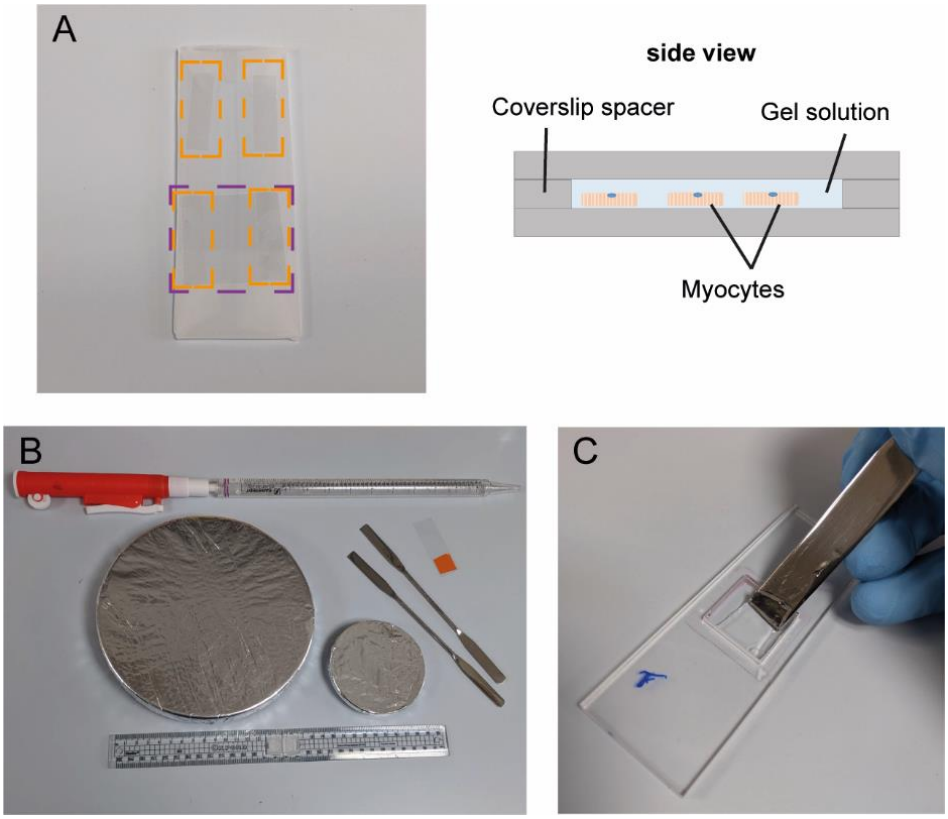

Figure 3-1. Method optimisation

(A) Gelation was performed in a chamber, with coverslip spacers defining the height of the polymerised gel. The myocytes were either adhered to the bottom coverslip (through laminin substrate attachment), or were in suspension and pre-mixed with monomer solution before pipetting into the chamber.. **(B)** To minimise physical damage, the gels were handled with a pair of spatulas (or a long coverslip) and were stored in foil-wrapped Petri dishes. Efficient gel washes during expansion were performed with a 25ml pipette pump, allowing large water changes with low damage risk to the gel. **(C)** After expansion, a square of gel was loaded into a custom-made imaging chamber, comprising a coverslip attached to an acrylic chamber.

3.3.2 Imaging expansion microscopy samples

ExM samples were imaged on a confocal system with Airyscan super-resolution, which will be described more in the next section. One of the key advantages to the use of a conventional confocal microscope is the plethora of emission and excitation bands which enable multi-colour imaging with relative ease.

There are several nuances and technicalities involved with imaging expanded samples which can compromise data collection. Firstly, the relatively limited working distance associated with high NA objectives can make regions higher up within the sample inaccessible. As shown in the schematic (Figure 3-2), the expanded samples are often positioned higher in the gel than they would typically be if situated flat against the coverslip, depending on where they were positioned once polymerisation was complete, plusthe degree of expansion. Given the height of the sample pre-expansion, this being expanded 10x in each direction, it is often not possible to resolve through the full height of a sample.

In some cases, it was challenging to find the sample given the lower brightness which results from fluorescence reduction during free radical polymerisation and digestion, as well as the effective dilution of sample fluorophore density in space. Particular dyes are significantly degraded, for instance the carbo-cyanine family dyes including Alexa Fluor 647, cy3 and cy5. The secondary antibodies which performed best (with the least reduction in fluorescence), were Alexa Fluor 488, Alexa Fluor 594, Janelia 549 and ATTO 647N. The combination of Alexa Fluor 488 and Alexa Fluor 594 was the most consistently used for 2-colour experiments. The lower brightness was countered by using longer exposure times and increasing digital gain or laser power, although this can increase photo-bleaching in expanded samples. Other approaches to reduce the issue of sample dimness include labelling with a higher concentration of secondary antibody, or delivering secondary antibodies post-expansion so they are not exposed to the harsh fluorescence reduction of the ExM protocol (Tillberg *et al.*, 2016). Sample brightness can also be improved by performing anchoring at 4°C, minimising the length of digestion time and minimising exposure to light throughout the preparation process.

During image acquisition, gel drift was a particularly prominent issue, given the physical properties of the gel, which can render entire imaging datasets unusable. Use of a poly-L-lysine coverslip coating helped to minimise gel drift. In addition, excess water was removed from the gel chamber, and the gel was cut to a size similar to the chamber dimensions.

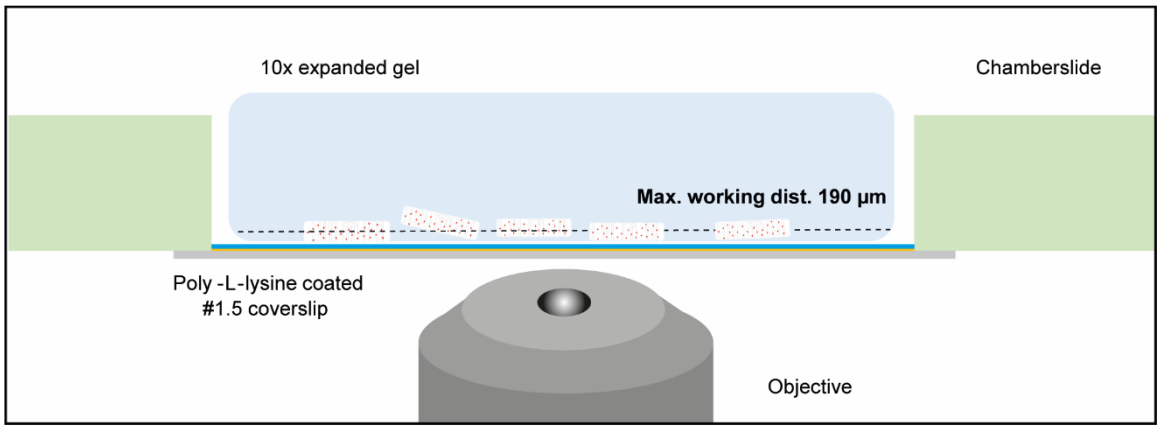

Figure 3-2. Imaging technicalities

Schematic of imaging, depicting the implications of the limited working distance of the objective (190 µm). Depending on the expansion factor, there could be regions of the cell that are out of reach (for instance a cell with pre-expansion width (along shortest axis) of 30 µm becomes 300 µm after 10x expansion). To ensure as much of the sample can be imaged as possible, it is important to ensure the gel is the correct way up (sample side down), is laid flat and thatresidual liquid is removed from the chamber to ensure the gel is not raised higher. Drift during image acquisition is a prominent issue, which is addressed by minimising the amount of liquid in the chamber and by coating the coverslip with poly-L-lysine.

A common cause of poorer resolution is depth-dependent spherical aberration and scattering. To determine whether there was chromatic alignment of green and red emission channels when imaging ExM samples at varying imaging depths, 3D datasets were acquired of TetraSpeck multi-emission beads. The average (± SD) in-plane offset of the centroids of the beads were 1.42 ± 0.04 nm at a depth of 0 µm and 1.57 ± 0.07 nm at depth of 20-30 µm (Figure 3-3A). The spatial error between the channels (as judged by dividing the offset by the in-plane 15 nm resolution) was ~ 10%, which suggested that ExM would be reliable for 2-colour imaging comparisons at depths of at least 30 µm. Axially, the offsets were 4.7 ± 0.1 nm at 0 µm and 5.9 ± 0.1 nm at 20-30 µm, equating to an error of roughly 13% and 17% respectively (when dividing by the axial resolution of 35 nm) (Figure 3-3B).

Traditionally, fluorescently labelled samples are imaged in a mounting medium to match the refractive index of the sample to the objective immersion oil and reduce photobleaching. Two mounting media were trialled for ExM gels; a recipe involving PBS and 90% glycerol, and another based on 80% sucrose in H_2O (5 g sucrose, water added to 8 g, dissolved, then heated to 6.3 g). The PBS-based medium lead to gel shrinkage, thus rendering it inappropriate given the desire for the highest EF to achieve the greatest resolution increase. The sucrose mounting medium (in H_2O, thus free of salt) had the tendency to dry out and crystallise around the gel, compromising the image quality and rendering the re-use of gels particularly problematic. Therefore, no mounting medium was used for the expanded gels.

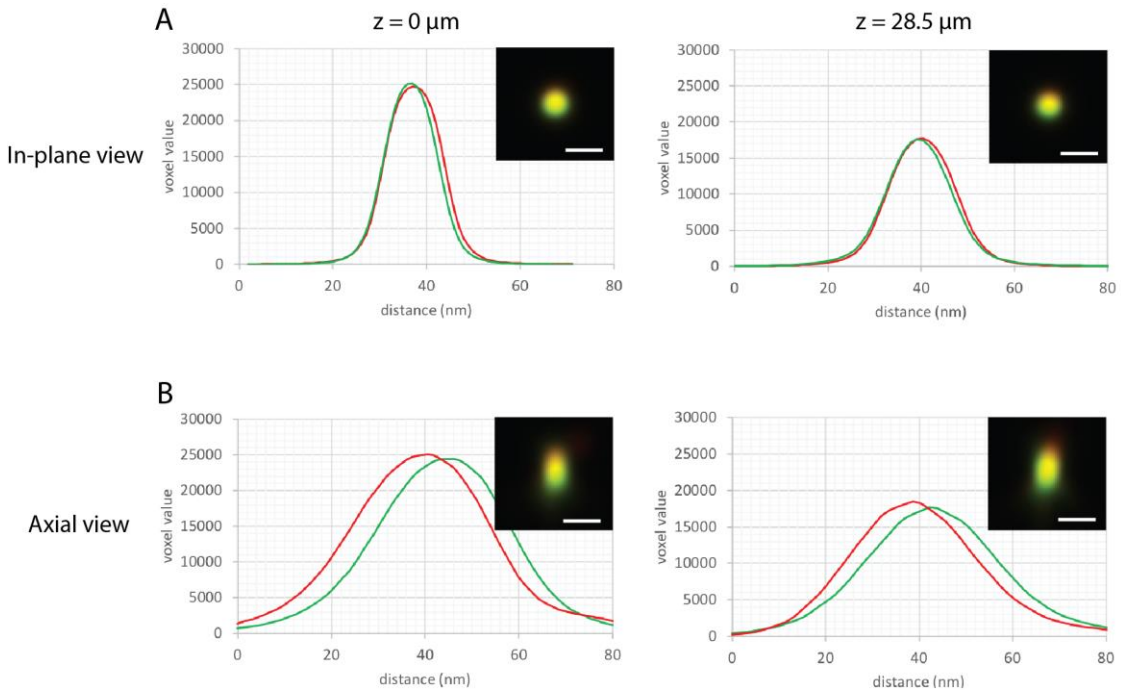

Figure 3-3. Chromatic alignment estimation

The chromatic alignment of the point spread function was estimated using individual 100-nm TetraSpeck multi-emission beads, with imaging performed through the green and red emission bands. Shown are line-intensity profiles across each bead, with an image projection of the bead shown in the inset. The in-plane and axial line-intensity profiles were compared at sample depths of 0 µm and 28.5 µm. **(A)** The average in-plane offset of the centroids of the beads were 1.42 ± 0.04 (SD) nm at depth of 0 µm and 1.57 ± 0.07 nm at depth of 20-30 µm, culminating to an in-plane alignment error of ~ 10% compared to the estimated resolution. **(B)** The equivalent comparison for axial alignments yielded an offset of 4.7 ± 0.1 nm at 0 µm and 5.9 ± 0.1 nm at 20-30 µm. (n = 4 beads at 0 µm, 3 beads at 28.5 µm). **Scale bars:** 30 nm.

3.3.3 Technique resolution in theory

Before observing the resolution by imaging biological structures, insight into the theoretical resolution can be gained by studying the effective PSF (Figure 3-4A).

Confocal microscopy makes an improvement in resolution compared to widefield imaging by introducing optical sectioning, but still entails simultaneous excitement of multiple labels throughout a volume. The resolution can theoretically be enhanced by closing the pinhole, albeit at the expense of signal, but regardless 200 nm in-plane and 500 nm axial resolution are optimistic, as demonstrated in the broad PSF (both in-plane and axially) (Figure 3-4A). By capitalising on a 1.7-fold resolution improvement with Airyscan (Huff *et al.*, 2017), which yields approximately 120 nm laterally and 350 nm axially, the effective PSF in an Airyscan image is therefore roughly half the size of the confocal PSF.

As a benchmark for super-resolution imaging, a simulated PSF relating to a single molecule imaged with dSTORM (capable of 20 nm lateral resolution) is shown. This simulated PSF is based on the known axial localisation precision and HILO illumination with widefield detection. While dSTORM has a smaller in-plane estimated PSF than confocal and Airyscan, attributable to the precision of localisation of isolated emitters, the axial PSF is comparable to confocal, due to lower localisation precision in this plane.

With physical expansion of the sample in ExM, the original PSF of the imaging system is effectively scaled down relative to the sample geometry, both in-plane and axially. By imaging ExM samples with Airyscan (EExM), the resolution improvement was enhanced further compared to confocal. The degree of PSF scaling directly corresponds to the EF. Therefore, 10x EExM (X10 expansion samples imaged with Airyscan) has the smallest PSF, smaller than dSTORM in-plane, and most importantly smaller in the axial plane.

Aside from the theoretical effective PSFs, the resolution at various imaging depths was estimated by measuring the FWHM of line profiles across 100 nm yellow-green or red-orange Fluosphere beads suspended within an acrylamide gel (Figure 3-4B). At depths of 5, 30 and 47 μm in a gel, the in-plane FWHM were 13.3, 14.8 and 17.3 nm (and axial 33.4, 39 and 46 nm). This resolution change at varying depths is indicative of spherical aberrations, likely due to the refractive index mismatch.

.

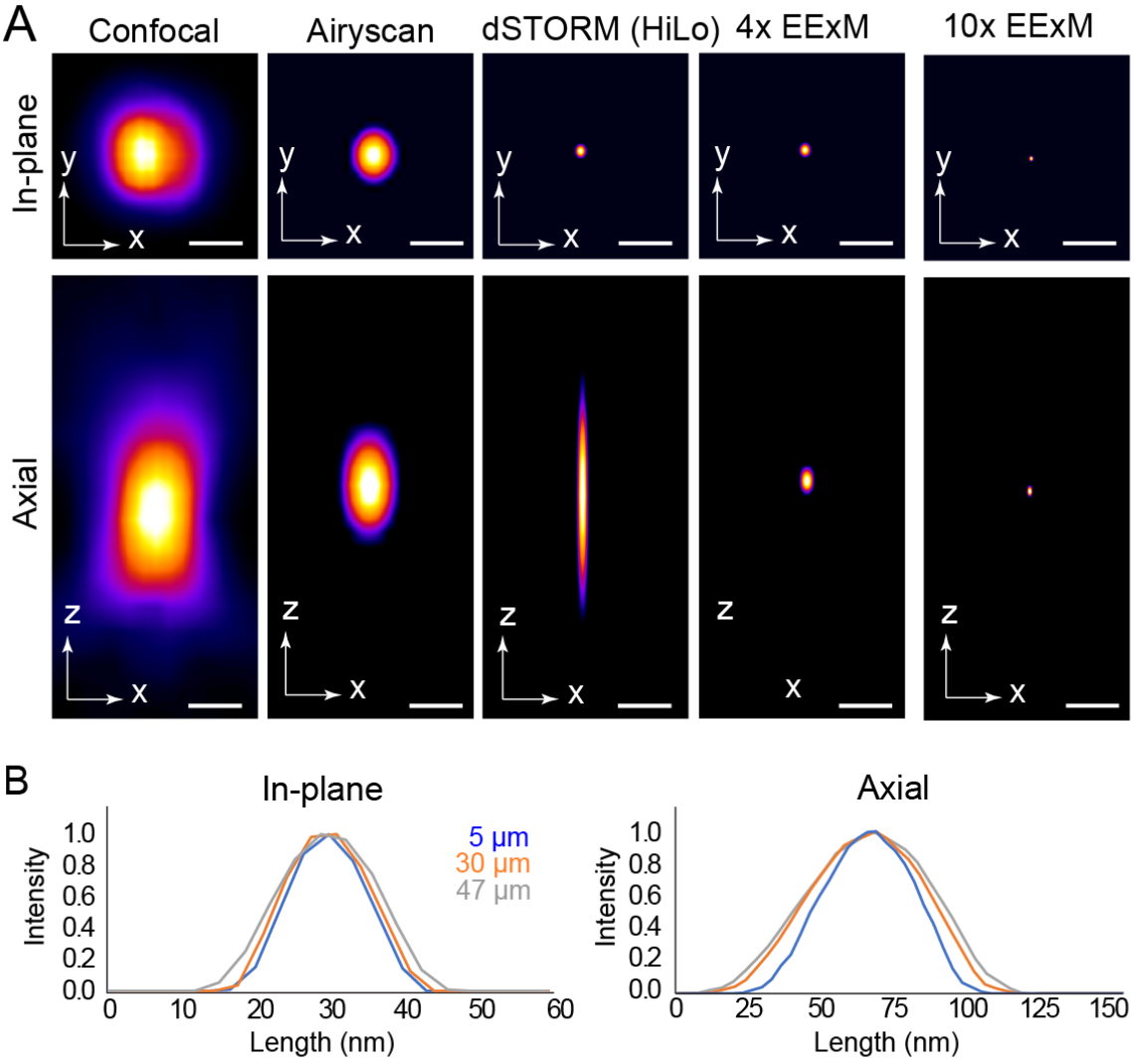

Figure 3-4. Resolution - PSF and bead line profiles

(A) Estimated PSFs are shown for various imaging modalities. The confocal and Airyscan PSFs were measured, while the 4x EExM and 10x EExM PSFs were scaled from the Airyscan PSF. The dSTORM (widefield detection under HILO illumination) PSF was simulated. **(B)** Intensity line profiles taken in-plane (upper) and axially (lower) through 3D images of fluorescent beads embedded within a gel at depths of 5 µm (blue), 30 µm (orange) and 47 µm (grey). The resolution at the different imaging depths varied, which can be attributed to index mismatch-related aberrations. The length scale shown is adjusted to demonstrate PSF dimensions of an X10 experiment. **Scale bars:** 250 nm.

3.3.4 Technique resolution in practice

Having studied the theoretical resolution of the ExM techniques, it was next appropriate to study the resolution in practice when applied to biological structures. We compared different imaging modalities in their ability to observe structures and measure the separation of features.

The z-disc is one of the most prominent structures in the adult cardiomyocyte, with a highly ordered pattern corresponding to the sarcomeres. This regular structure could serve as an intrinsic standard with which to compare the resolution of various microscopy techniques. The z-discs were labelled using antibodies for α-actinin, which is a z-disc protein which binds to and arranges actin filaments (Figure 3-5A). With confocal, the z-disc appeared as a single linear structure with no apparent underlying intricacies. Using dSTORM, the structure appeared to be narrower than shown in confocal. With 4x EExM, the z-disc was not a uniform structure, featuring a slight dip in intensity at the centre, as visible in a line-profile taken perpendicular to the orientation of the z-disc. This new observation in z-disc α-actinin arrangement was enabled by the improved axial resolution with EExM compared to dSTORM.

Using the sub-15 nm resolution techniques of 10x EExM and DNA-PAINT, the multiple band nature of the z-disc was clearly visible, with a distinct drop in intensity in the line profile perpendicular to z-disc orientation (Figure 3-5B). The distance between the two peaks of the α-actinin double-band was measured in 10x EExM and DNA-PAINT. The measurements were consistent between the two techniques, with a mean distance of 74 nm and 71 nm respectively ($p = 0.31$), confirming the comparable resolution (Figure 3-5C). The observation of z-disc sub-structure, in this case a double-band of α-actinin, has not been demonstrated previously with light microscopy. In addition, when comparing the FWHM of a line-profile drawn across each band, the 4x EExM reported a FWHM of 72 ± 4 nm, while 10x EExM reported a smaller FWHM of 41 ± 3 nm.

Another commonly-used cellular structure benchmark to demonstrate and quantify resolution is the microtubule, given its consistent diameter close to the resolution limit. Antibody-stained microtubules are typically 60 nm wide, given the physical displacement of the fluorophore at the end of the primary and secondary antibody complex. By taking the FWHM of a line-profile across a microtubule, it was possible to evaluate each technique's resolution (Figure 3-6). Confocal microscopy, limited to 200 nm resolution, was incapable of reporting the true diameter of a microtubule. 4x EExM reported a smaller FWHM of 79 ± 5 nm, closer to the absolute structure diameter. 10x EExM reported a FWHM of 50 ± 1 nm, which is comparable

to the 56 nm estimation of antibody-labelled microtubule width using dSTORM (Bates *et al.*, 2007).

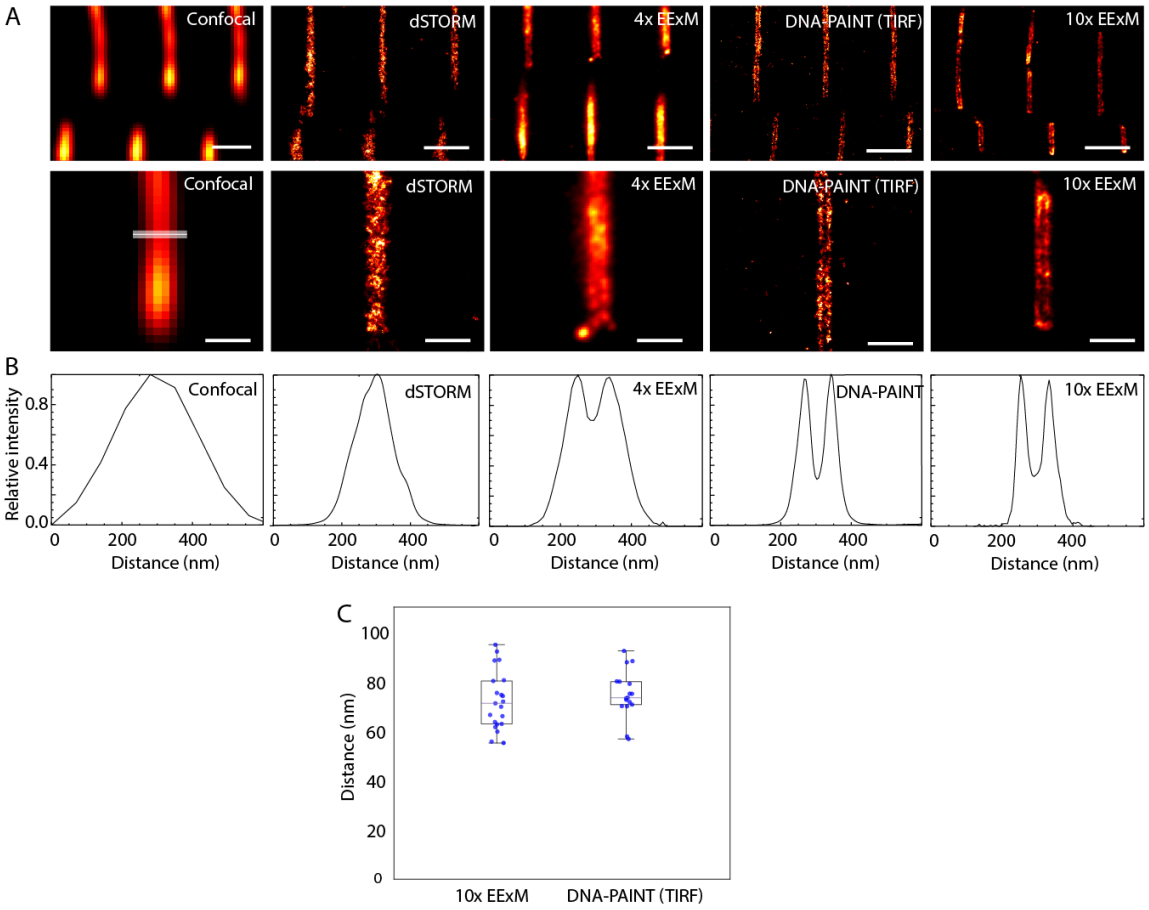

Figure 3-5. Resolution - z-disc technique comparison

(A) Z-discs were labelled using α-actinin antibodies and served as a standard to gauge the resolution of various imaging techniques in practice. **(B)** Intensity line profiles perpendicular to the orientation of the z-disc convey the double-banded nature of this structure when imaged with the higher-resolution techniques 10x EExM and DNA-PAINT. **(C)** The distance between the two α-actinin bands was 70.10 ± 2.22 nm using 10x EExM and similarly 74.05 ± 3.12 nm using DNA-PAINT ($p = 0.31$, two-tailed t-test). ($n = 21$ ExM, 17 DNA-PAINT). EF = 10. **Scale bars:** top 1 μm, bottom 500 nm.

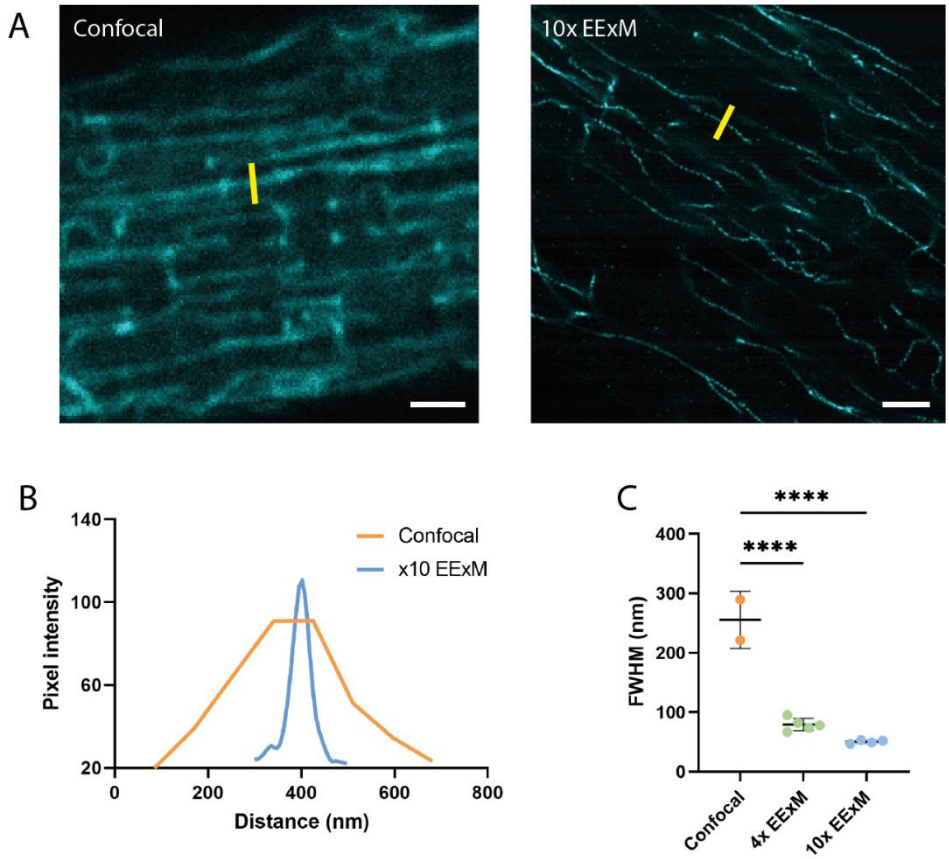

Figure 3-6. Resolution – microtubule FWHM comparison

(A) Confocal and 10x EExM images of α-tubulin-labelled microtubules were used to infer the resolution of each technique. A line-profile (yellow) was drawn across individual microtubules. **(B)** Confocal vastly over-estimates the width of a microtubule, while 10x EExM reports a much narrower structure. **(C)** The measured line-profile FWHM was significantly smaller in ExM versus confocal ($p < 0.0001$, one-way ANOVA). (n = 2 confocal, 5 4x EExM, 4 10x EExM). EF = 10. **Scale bars:** A 2 µm; B 1 µm.

3.3.5 Isotropy validation

The EF is the parameter used to scale measurements in expanded images. In the ExM literature, it is common to measure the EF using the physical gel size and by measuring intrinsic biological structures with robust dimensions as internal rulers. In cardiac tissue, the sarcomere length (SL) (the distance between bands of α-actinin at each z-disc), provided one such ruler at the micron-scale (Figure 3-7A). The average SL in unexpanded cells pre-expansion as 1.84 μm ± 0.08 SD (n = 7 animals, 52 cells). The EF reported by the physical gel size (Figure 3-7B) was compared with that determined by the SL. The relationship was not linearly proportional, for instance a gel that physically expanded 8 times might have an SL EF of 6.5 (Figure 3-7C). This could have arisen due to inaccurate measurements of gel size which over-estimate EF, or that the expansion within the sample region was smaller than the gel EF, possibly due to local physical resistance. Where possible, the microscale EF determined by the SL was used to scale images and measurements presented in this thesis.

The gold standard approach to verify isotropy is to image the same area pre- and post-expansion. This is technically challenging, necessitating finding the region imaged in a sample after it has been digested, embedded in a gel and rotated. This is particularly challenging in cardiac tissue which lacks easily recognisable geographical landmarks aiding location determination. In addition, pre-expansion imaging must be performed with a super-resolution technique, which further shrinks the area to find in the expanded sample, and also requires a different fluorophore to that suited to ExM.

The isotropy at the microscale was investigated by measuring the SL with relation to the angle of the cardiomyocyte within the gel (Figure 3-8A). The measured SL was found to be independent of cardiomyocyte orientation (Figure 3-8B). The SL was approximately Normally distributed, with a standard deviation of 0.16 μm, which is within the 10% range of biological variation seen previously (Jayasinghe *et al.*, 2010).

The isotropy at the nanoscale was also investigated, using an intrinsic biological structure an order of magnitude smaller than the SL, as evidence that the spatial measurements were unaffected by gel-to-gel variations in the EF. The double-banded morphology in α-actinin labelling was measured (Figure 3-9A). Practically, the distance between peaks when plotting a line profile across a single z-disc labelled for α-actinin was measured, as a function of microscale EF calculated using the local SL. The distance between the peaks varied related to the EF in a proportional manner (Figure 3-9B).

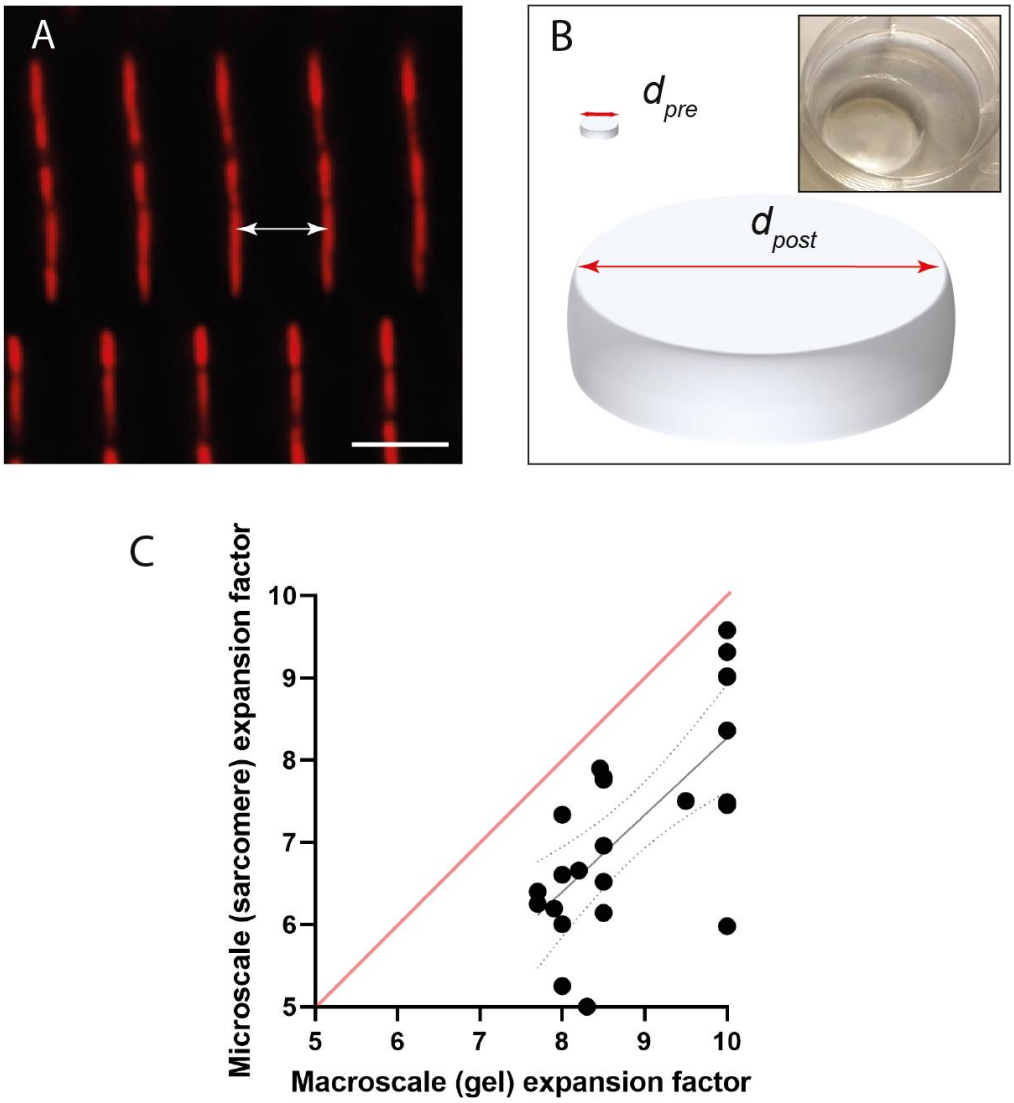

Figure 3-7. Determining expansion factor - microscale (sarcomere length) v macroscale (gel)

The expansion factor (EF) is calculated to obtain the true measurements adjusted for the physical swelling incurred in ExM. **(A)** To calculate the EF at the microscale (in the region of the sample) the sarcomere length (the gap between 2 z-disc bands of α-actinin staining) was measured. To get a more accurate value of the average sarcomere length, measurements were taken across 5 spacings. **(B)** To estimate the macroscale EF, the physical gel size was measured pre- and post- expansion (in mm). **(C)** There was a non-proportional linear relationship between the EF calculated at micro- and macroscale. The EF reported by the gel size was larger than that calculated using the sarcomere length. (n = 24 gels). **Scale bar:** 2 µm.

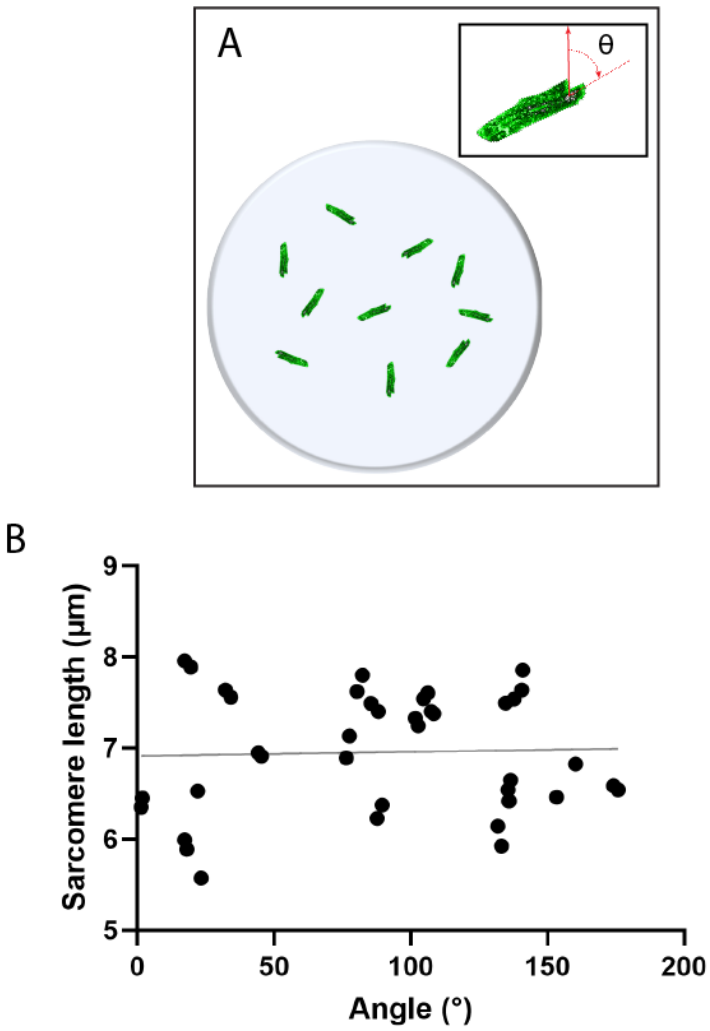

Figure 3-8. Microscale isotropy validation – sarcomere length

To assess isotropy at the microscale, the sarcomere length (SL) was observed in relation to the orientation within the gel. **(A)** The SL was measured using myocytes positioned in different locations of a single gel. **(B)** The scatterplot of average SL against the relative angle (°) within the gel demonstrates that the measured SL was independent of the angle. (n = 40 cells).

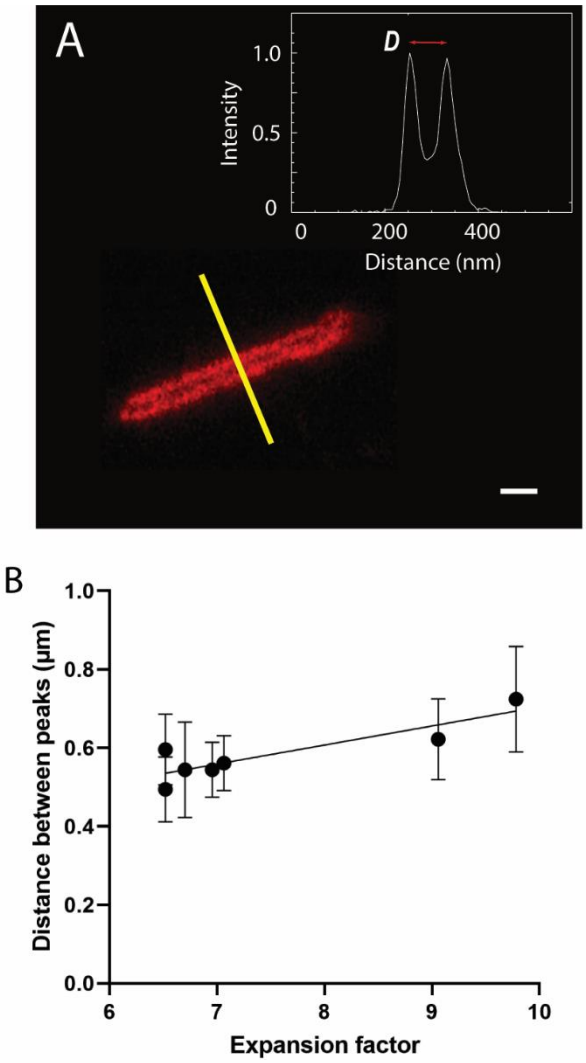

Figure 3-9. Nanoscale isotropy validation – z-disc bands

To assess isotropy at the nanoscale, the relationship between the distance between peaks of the double-banded z-disc and the local expansion factor (EF) reported by the sarcomere length was investigated. **(A)** From images of the z-disc, the separation between double-bands from intensity line-profiles taken orthogonally to the z-discs (D in inset) was measured. **(B)** Plot of the average (± SD) distance between the α-actinin double-bands (unscaled) as a function of the EF varying between ~ 6.5x and 10.5x revealed that the distances varied in a manner proportional to the EF. (n = 5 cells per gel). EF = 10. **Scale bar:** 100 nm.

3.4 Discussion

3.4.1 Expansion microscopy as an imaging tool

When ExM first emerged it stood out as somewhat of a novelty technique, due to it employing an entirely different approach to conventional super-resolution techniques, but it has since established itself as a reliable and powerful tool in a number of research fields. Practically, the technique requires no additional hardware or training beyond what any confocal microscopy facility can provide, making ExM a wholly accessible approach for researchers.

The workflow of ExM was optimised to apply it to cardiomyocytes attached to coverslips (the conventional approach for imaging, or for cells undergoing stimulation), as well as on cell suspensions. The approach is straightforward, adding two extra days onto the sample preparation timeline before imaging is possible.

ExM is particularly advantageous in that while other techniques are harder to implement in 3D, ExM samples can be imaged on any microscope possessing z-stack capabilities. Further, while other modalities operate with limited fields of illumination (for instance DNA-PAINT with TIRF), the working distance of ExM is not subject to such parameters.

While ExM easily enables 2-colour imaging, multiplexing to 3+ targets becomes challenging due to requiring spectrally distinct fluorophores, as well as the limited number of IgG antibodies from different animal species, although fluorescent proteins may be a practical workaround to this limitation. For the typical 2-colour imaging combination of Alexa Fluor 488 and Alexa 594, there was minimal offset (~ 1.5 nm) in green and red emission channels when imaging beads up to depths of 30 µm. At best, 3-colour imaging could be performed simultaneously with Alexa Fluor 488, Alexa Fluor 594 and ATTO 647N (not shown).

One downside of ExM, like confocal, is that it is not inherently quantitative, because it is not possible to mathematically determine the number of targets emitting fluorophores (as can be done for other super-resolution techniques, such as qPAINT (Jungmann *et al.*, 2016)).

There are several practical limitations and drawbacks involved with implementing ExM. First and foremost, ExM can only be performed on fixed specimens, and is not capable of live cell imaging given the highly toxic nature of free radical polymerisation, digestion and expansion. The process works best on smaller cells with less physical resistance, but with careful optimisation can be applied to robust cells, as showcased with plant and bacteria, making use

of particular enzymes to efficiently digest the cellular wall (Kao and Nodine, 2019; Lim *et al.*, 2019). ExM is applicable to tissue sections, yielding vast improvement in resolution through the clearing of out of plane background fluorescence, although the resolution increase is slightly poorer than for cultured cells. ExM has been demonstrated for thick tissue sections of 100s of microns and even entire organs (Düring *et al.*, 2019; Gao *et al.*, 2019; Hörl *et al.*, 2019).

One of the biggest challenges within ExM is the low sample brightness occurring due to the physical expansion in space, effectively diluting the sample labelling density. For a 10x expanded gel, the volume labelling density is reduced by a factor of 1000 (Truckenbrodt *et al.*, 2019). Low sample brightness makes finding the sample challenging and compromises image quality in some cases. It also means that ExM samples have a limited lifetime, exacerbated by fluorescence loss caused by antibody dissociation when stored in pure water, as is required to allow maximal expansion (Yu *et al.*, 2020). These factors put a significant pressure to commence imaging soon after expanding, and re-imaging samples over multiple days is not recommended. Use of a mounting medium with salt would better preserve sample fluorescence, but this would shrink the gel, inhibiting the full resolution increase and necessitating another time-consuming expansion step to re-achieve maximal expansion. While the sucrose in H_20 mounting medium offered the most viable option, it did not drastically improve imaging quality. A mounting medium would also be beneficial with regards to matching the refractive index of the water-based sample to that of the oil on the objective, in order to minimise the amount of spherical aberrations when imaging at depth. The rationale for using the oil objective was that it would provide increased resolution and light collection due to sample dimness.

Another difficulty regarding imaging ExM samples is that the gels are prone to drift in the imaging chamber, occasionally severe enough to affect even 2D image acquisition. Poly-L-lysine countered most of the drift, so long as excess liquid had been removed from the chamber when the gel was added. There was a limited longevity to an imaging session, as drift worsens over time due to electrostatic bonds disappearing and the changing shape of the gel (and water level) in the chamber. While other groups have prevented drift by polymerising another acrylamide gel or agarose around the ExM sample gel to hold it in place, this prevents the easy transport of the gel and can aggravate issues of working distance if the gel is raised higher from the objective.

3.4.2 Imaging resolution of enhanced expansion microscopy

ExM was combined with Airyscan to yield a doubly-increased resolution compared to confocal microscopy. The theoretical resolution possible based on a 4-fold increase with proExM reaches 35 x 70 nm, and by using the 10-fold expanding X10 gel recipe reaches 15 nm in-plane and 35 nm axially.

The theoretical resolution provided by 10x EExM parallels that of DNA-PAINT (<10 nm). While DNA-PAINT achieves a profound resolution for 2D imaging near the coverslip, ExM is a more all-round technique allowing enhanced resolution at various imaging depths for visualisation of all manner of 3D structures. In practice, the ExM resolution was larger than the hypothetical based on the EF, attributable to the loss of sample labelling density. Another common limiter of resolution is depth-dependent spherical aberration, but the bead FWHM showed minimal variation between 5 and 50 µm.

The resolution in practice was observed by applying EExM to study biological structures, in this chapter focusing on the z-disc and microtubules. The ability to resolve the narrow width of the microtubule was achieved by 10x EExM and was equivalent to dSTORM, whereas 4x EExM still provided an over-estimation. 10x EExM still falls short of being able to resolve the hollow core of the microtubule, and the beads-on-a-string appearance demonstrates that sample labelling of α-tubulin was not complete. The cardiac z-disc proved to be a useful standard for comparing techniques. With confocal microscopy and labelling of α-actinin, the z-disc appeared as a uniform band, with no underlying sub-structure. Only 10x EExM and DNA-PAINT were capable of clearly visualising the double-band of α-actinin. 4x EExM was closer in practice to dSTORM, revealing that the width of the z-disc was narrower than insinuated by confocal, but both techniques lacked the resolution needed to distinguish the z-disc sub-structure. Another direct comparison between the techniques in terms of resolution will be provided in Chapter 4, regarding RyR clusters.

The observation of a double-band of α-actinin at the z-disc was an interesting discovery. Different species are believed to possess varying numbers of α-actinin layers per z-disc, but the mammalian cardiac z-disc is proposed to have six longitudinally-arranged bands of α-actinin (Burgoyne *et al.*, 2015). These bands were spaced longitudinally at 19 nm and transversely at 10 nm, suggesting that this structure is particularly dense, which could potentially account for the gradient of antibody labelling. One possible explanation is that while

the outer rows of actinin are efficiently labelled (90%), the efficiency drops towards the centre of the z-disc, giving the impression of two bands.

3.4.3 Expansion of cardiomyocytes is isotropic

Validating the isotropy of ExM was important in order to trust that measurements obtained from the images accurately correspond to the native sample (and are not affected by distortions). Isotropy of ExM has been previously evaluated in several different cell types using the root mean square (RMS) error of measurements made pre- and post-expansion. The original ExM approach calculated an RMS of <1% of distance, which is within the PSF of SIM (Chen *et al.*, 2015), and X10 reports a similar RMS error of 100-200 nm over a distance of 5 μm (Truckenbrodt *et al.*, 2019). Whilst RMS estimation is the best evaluation of isotropy, it is difficult to do in practice. Owing to the trust in the ExM approach (with the increasing accumulation of isotropy validations), many publications feature ExM without the RMS error validation, making use of other estimations of isotropy.

Arguably the most frequently-used approach to validate isotropy involves measuring intrinsic standards of known and constant dimensions, such as the nuclear pore complex (Pesce *et al.*, 2019). Aside from biological structures, other groups have trialled synthetic rulers, based on DNA scaffolds which have dyes molecules separated a known distance (Scheible and Tinnefeld, 2018).

The EF was calculated here using the SL, which is a robust, repeating distance found in all parts of the sample, as well as the physical gel size. While SL naturally varies around 20% depending on the relaxation state (de Tombe and ter Keurs, 2016), it was possible to calculate an average for each batch of cells pre-expansion with relative ease. The SL was used to measure EF at the microscale, and there was a discrepancy between this and that calculated using the macroscale physical gel size. This could be due to a poorer accuracy of measurement at the millimetre scale using a ruler, but may also result from a smaller expansion within the region of the sample, perhaps due to more physical resistance by the remnants of the cell. The SL measure of EF (which better represents the local expansion of the imaged and measured area) was used wherever possible in all subsequent ExM experiments and analyses. The isotropy at the microscale and nanoscale was assessed using intrinsic biological structures. The SL measurement was found to be independent of the orientation of the cardiomyocyte within the gel, and was within the normal biological variation. As another standard, the measured distance

between the double-band feature of the z-disc was proportional to the EF. These validations using the SL and α-actinin double-band give confidence that 10x expansion of cardiomyocytes was isotropic, and that measurements obtained in EExM images were reliable reproductions of the native sample. While we have verified isotropy in several capacities here, we have not yet characterised how the expansion and isotropy varies as a function of depth into the gel.

Regarding the future prospects of isotropy validation, the homogeneity of the gel mesh is likely to be a significant influence on the even-ness of expansion. The standard ExM gel matrix has a spacing on the order of 1-2 nm (Cohen *et al.*, 1992), and is influenced by the gel recipe and the careful mixing during the process of polymerisation and delivery into the sample. However, the nanoscale homogeneity is dependent on the formation of acrylamide lattices, and as such is out of the user's control. Free-radical based gel polymerization has been shown to create relatively heterogeneous matrices, but recently a novel approach to improve isotropy utilises gels polymerised with synthetic monomers which form more ordered lattices, which could revolutionise the ExM field if made more accessible (Gao *et al.*, 2021).

3.5 Concluding remarks

This chapter has detailed the adaptation of ExM for imaging the cardiac ultrastructure. The ExM methodology was optimised for isolated cardiomyocytes plated on coverslips. By imaging ExM samples with Airyscan microscopy, in an approach called EExM, the resolution was further increased over confocal, enabling up to 15 nm in the lateral plane and 35 nm in the axial plane.

The resolution of EExM was demonstrated both in principle, by considering the PSF, and in practice, by imaging z-disc and microtubule structures. 4x EExM was comparable in resolution to dSTORM, and 10x EExM was comparable in resolution to DNA-PAINT (with regards 2D imaging).

The isotropy of ExM was verified at the macroscale (using the physical gel size), the microscale (using the SL) and at the nanoscale (with the z-disc double-band). This verification of isotropy means that measurements obtained using this imaging technique were indicative of the genuine arrangement in the native structure.

Chapter 4. Characterisation of ryanodine receptor clusters with expansion microscopy

4.1 Introduction

The excitability of RyRs is controlled partly by their organisation within a cluster, and is also regulated by numerous interacting proteins and post-translational modifications. The organisation of surface RyR clusters in isolated cardiomyocytes has been well-described with DNA-PAINT (Jayasinghe *et al.*, 2018), However, the organisation of dyadic clusters (associated with t-tubules) remains relatively unknown, due in part to the inability to perform DNA-PAINT deeper in the cell, due to a shallow imaging depth imposed by the thin, selective planar TIRF illumination. DNA-PAINT is also not straightforward to perform in a 3D capacity, which is an important aspect of dyadic cluster morphology. While 3D dSTORM has been used to study the rough geometry of dyads (Shen *et al.*, 2018), this lacks the resolution needed to resolve individual RyRs, which has been suggested by simulations to be around 15 nm (Jayasinghe *et al.*, 2018).

Similarly the organisation of the anchoring protein JPH, which is critical to the integrity of the RyR cluster arrangement and the dyadic space, has been well-described for surface clusters (Jayasinghe *et al.*, 2018), but less so in interior clusters. Basic JPH-RyR co-clustering was observed in interior clusters using dSTORM in tissue sections (Hou *et al.*, 2015), without insight into the spatial distribution of the individual proteins.

Phosphorylation directly regulates RyR physiology, dictating P_o in tandem with the adrenergic state of the heart. Estimates of phosphorylation typically come from biochemical experiments including Western blots and *in vitro* kinase assays (Carter *et al.*, 2006; Huke and Bers, 2008; J. Li *et al.*, 2013). These studies show that basal phosphorylation varies depending on the particular serine residue, and can be modified according to the activity of phosphatases and kinases. Observing the extent of RyR phosphorylation *in situ* within a cluster, as well as the changes following β-adrenergic stimulation, would be desirable to understand the involvement of this post-translational regulation.

The aim of this chapter was to describe the organisation of RyR clusters with the newly validated ExM protocol from Chapter 3. In particular, it was desired to obtain a better understanding of the organisation of 3D dyadic clusters deep in the cardiomyocyte interior, to

describe the co-clustered relationship of RyR with JPH in dyads, and to quantify phosphorylation at the level of the individual RyR.

4.2 Methods

4.2.1 Cardiomyocytes

Isolated rat ventricular cardiomyocytes were obtained by the Langendorff perfusion method detailed in Section 2.1. RyR and JPH datasets were collected from cardiomyocytes taken exclusively from the LV, while RyR and pSer2808 datasets were from cardiomyocytes of both ventricles.

In experiments observing differences following β-adrenergic stimulation, isolated ventricular cells were adhered to coverslips for 2 hours, then stimulated with electrical field stimuli at 1 Hz for 10 mins, while undergoing perfusion with Tyrode's containing 100 nM isoproterenol (Sigma). Cells were then fixed *in situ* with 2% PFA in PBS at RT.

4.2.2 Imaging and analysis

Samples were fluorescently immunolabelled with antibodies for RyR2, JPH2, pSer2808, pSer2814 and pSer2030, as detailed in Section 2.2. proExM or X10 expansion microscopy were performed as outlined in Section 2.3 and samples were imaged as in Section 2.4.

dSTORM and DNA-PAINT images of RyR clusters were acquired by Izzy Jayasinghe and Miriam Hurley.

The specific pipeline of image analyses is detailed in Sections 2.5. The simulations of RyR detection, the centroid detection analysis of RyR, and pSer2808 fractional phosphorylation were performed by Izzy Jayasinghe. The interior analyses were performed using 3D detection, while surface analyses used 2D detection.

4.3 Results

4.3.1 Expansion microscopy of ryanodine receptor clusters

Adult ventricular cardiomyocytes were immunolabelled with antibodies for RyR and imaged with confocal (pre-expansion), 4x and 10x EExM imaging techniques. The striated labelling pattern of RyR clusters in the interior of the cardiomyocyte corresponds to their sarcomeric arrangement (Figure 4-1). With confocal microscopy (possessing 200 nm lateral resolution), RyR clusters appeared as blurred structures, often 500 nm in length, with no cluster sub-structure visible. 4x EExM (possessing 35 nm lateral, 70 nm axial resolution) allowed a drastic improvement in dyadic RyR cluster definition, revealing smaller sub-clusters of RyRs which were not visible in confocal images. These sub-clusters often aligned in two rows, which could likely be due to the presence of a t-tubule in-between. Despite the improvement seen with 4x EExM, the resolution was not sufficient to resolve individual RyR channels. In 10x EExM images (possessing 15 nm lateral, 35 nm axial resolution), individual RyRs in dyadic clusters were visible for the first time, enabling a significant improvement in detail compared to confocal and 4x EExM.

A series of simulations were performed to assess how the imaging resolution impacts the ability to detect individual RyRs (Figure 4-2). Two example model clusters (250 nm diameter and a narrower 100 nm diameter) were simulated with RyR positions (white) based on experimental data. Each cluster was convolved with a PSF estimation to simulate an image, then underwent a 3D detection protocol to determine the 3D centroids of each RyR, as has been previously established (Jayasinghe *et al.*, 2018). For the 250 nm diameter cluster, 10x EExM detected almost all (~95%) RyRs within 15 nm of their positions, regardless of the imaging orientation relative to the cluster. 4x EExM had a lower detection success rate (70-80%), whereby certain RyRs could not be resolved due to poorer axial separation (regions annotated with dashed lines). The detection of individual RyRs with 4x EExM was slightly improved when the cluster was imaged end-on, compared to side-on. For the narrower 100 nm diameter cluster, 10x EExM was still capable of detecting >95% of RyRs, while the poorer resolution of 4x EExM meant that only 70-80% of RyRs could be detected.

These simulations suggest that the ability to successfully detect individual RyRs was dependent on achieving the maximal 10x expansion, with an approximate halving of the effective resolution in 4x expansion leading to a ~20-30% drop in the accuracy of detection.

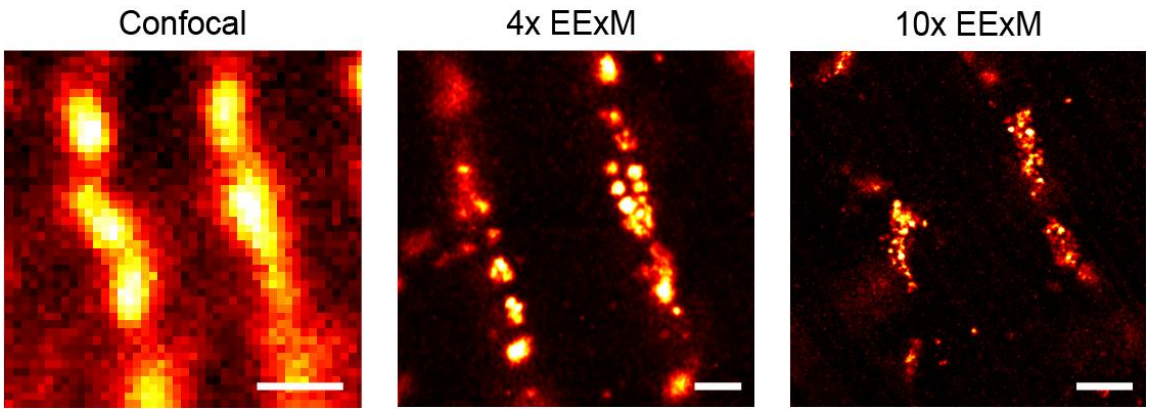

Figure 4-1. ExM imaging of RyR clusters

Rat cardiomyocyte interior RyR clusters as imaged by confocal microscopy (not deconvolved), 4x EExM and 10x EExM. Confocal microscopy offers no information about the organisation of RyRs within a cluster. The improved resolution of 4x EExM allows greater understanding of sub-cluster morphology to be obtained, but was not able to resolve individual RyRs. 10x EExM enables individual RyRs in dyadic clusters to be resolved for the first time. EFs = 4 and 10. **Scale bars:** (left to right) 1 μm, 500 nm, 500 nm.

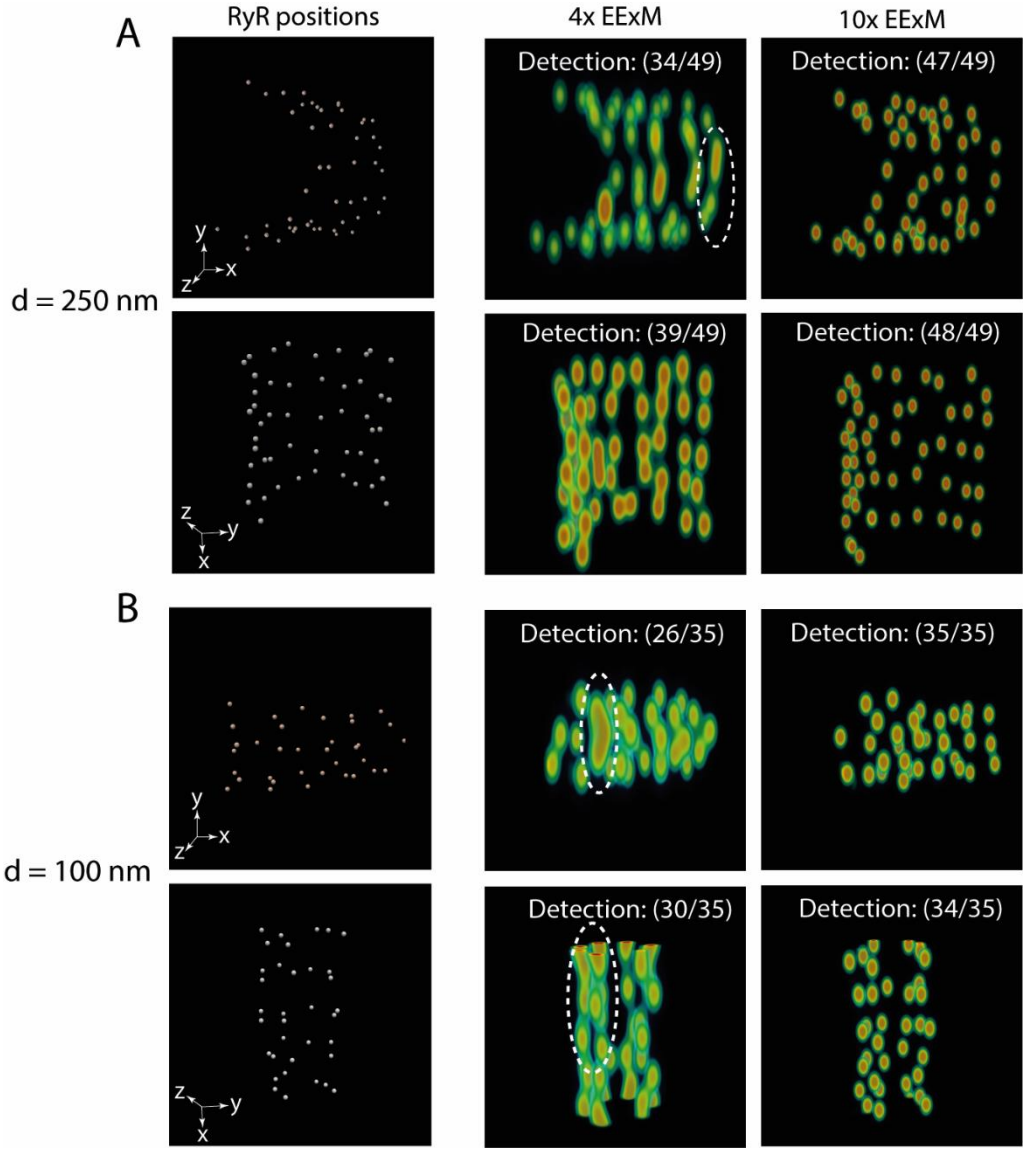

Figure 4-2. Simulations of ability to detect individual RyRs

Model clusters were simulated to understand how the resolution of the 4x and 10x EExM techniques governs their ability to detect RyRs. Two model clusters of RyRs (white) with diameters of **(A)** 250 nm and **(B)** 100 nm were simulated, with two orientations relative to the imaging plane (conveyed using xyz annotation). 4x EExM failed to detect some RyR positions due to overlapping (regions with dashed lines), whereas 10x EExM localized nearly all RyRs within 15 nm of the original positions.

4.3.2 Comparison to other imaging techniques

10x EExM images of RyR clusters were compared to those taken with the next-best super-resolution imaging techniques.

For surface clusters, the benchmark technique DNA-PAINT (operating in TIRF) clearly resolved individual RyRs, given the <10 nm in-plane resolution (Figure 4-3A). 10x EExM images were qualitatively similar to DNA-PAINT, in that 10x EExM could also resolve individual RyRs. The clusters were punctate in appearance, separated evenly and with minimal overlap of puncta. One apparent difference between the 10x ExM and DNA-PAINT images was the number of clusters visible in the same plane, which was due to differences in cell attachment. DNA-PAINT cardiomyocytes had a thorough poly-L-lysine attachment to ensure the cell was flatter to the coverslip, increasing the number of clusters in a single plane, because of the 2D limitations of this technique.

For interior clusters, dSTORM is the most robust method for imaging, because the TIRF light sheet used in DNA-PAINT limits its ability to image further from the coverslip. dSTORM imaging at a depth of ~10 μm from the cell surface provided a rough outline of interior clusters, but lacked the in-plane and axial resolution needed to resolve individual RyRs (Figure 4-3B). 10x EExM imaging of internal clusters enabled individual RyRs to be resolved, and was qualitatively comparable to the surface clusters imaged with 10x EExM, without a noticeable drop in resolution. The ability to resolve individual RyRs here was enabled by the enhanced in-plane and axial resolution of 10x EExM, as demonstrated in the RyR detection simulation in Figure 4-2.

While surface clusters were often circular and clearly visible in a 2D image, due to a flatter alignment of the SR terminus with the surface sarcolemma (which itself is aligned in a single plane), the interior clusters were more extended in shape, and were not fully visible in one plane of a 2D image, given their curved 3D morphology inherent in their apposition to t-tubule membranes.

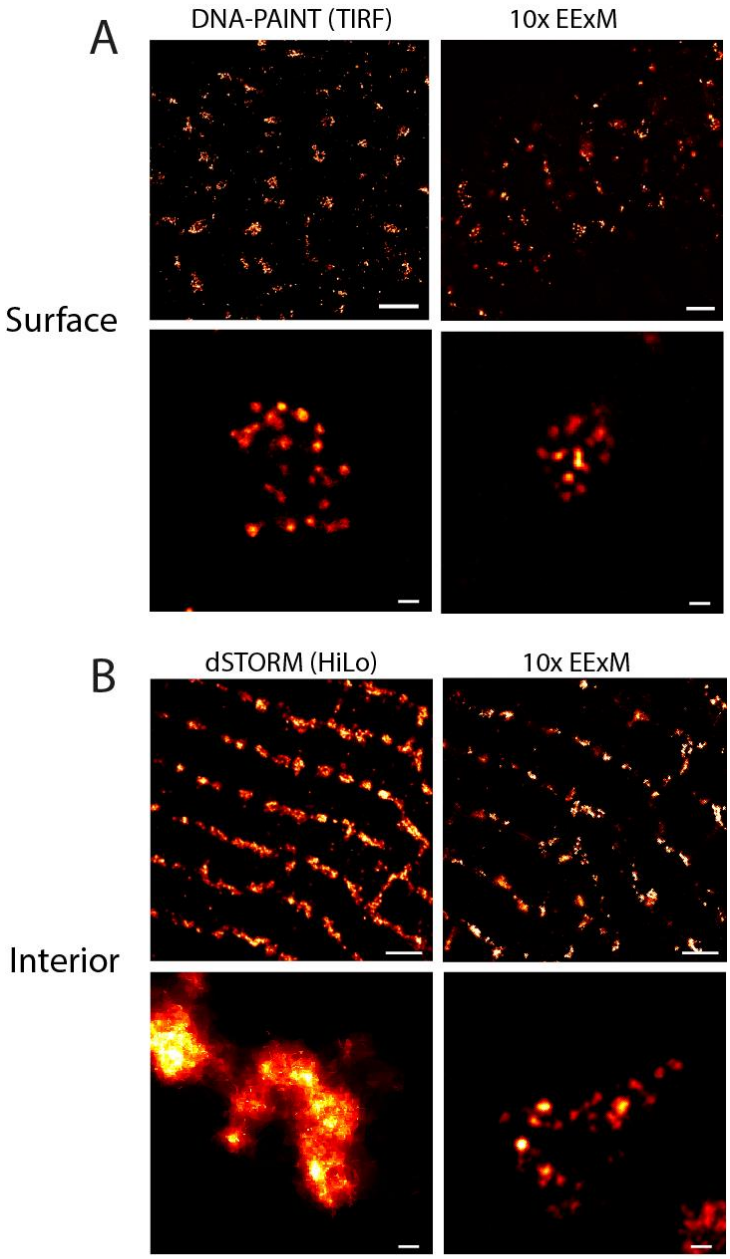

Figure 4-3. 10x EExM imaging of RyR clusters compared to benchmark techniques

10x EExM was compared to existing benchmarks for RyR cluster images. Displayed are low-magnification images (top row) showing RyR clusters across multiple sarcomeres, and representative images of single clusters (from different images) (bottom row). **(A)** At the cell surface, DNA-PAINT (operating in TIRF) clearly resolved individual RyRs. This was recapitulated when imaging with 10x EExM. **(B)** In the cell interior (where DNA-PAINT is less suitable), dSTORM provided a rough outline of a cluster, but does not give the positions of individual channels. 10x EExM resolved individual RyRs in interior clusters without a noticeable drop in resolution as compared to surface imaging. EF = 10. **Scale bars:** Upper 1 µm, lower (single cluster) 50 nm.

Following the qualitative comparison to other imaging techniques, it was next appropriate to validate the quantitative capabilities of 10x EExM alongside DNA-PAINT, and to describe interior clusters at the individual channel level for the first time.

For the following analyses, a cluster was determined by applying a signal fraction (calculates a threshold needed to capture a percentage of signal, in an image often 0.8), which yields an outline of the clusters. These clusters were then subjected to a detection algorithm within PYME which records the co-ordinates of the centroids of individual RyRs.

The first quantitative metric used was the number of RyRs per cluster, also known as cluster size (Figure 4-4). The distributions of cluster size as obtained with DNA-PAINT (surface) and 10x EExM (surface and interior) are shown. The mean surface cluster size in DNA-PAINT of 7.87 ± 0.39 RyRs per cluster was slightly lower than the estimate of 8.98 ± 0.44 RyRs in 10x EExM, but the overall distributions were similar. The percentage histogram shows an exponential distribution of interior cluster size, akin to that observed in surface clusters, wherein there were many clusters containing five or fewer RyRs, including many lone RyRs that were not clustered with neighbours. (Jayasinghe *et al.*, 2018). The average interior cluster size was 8.23 ± 0.51 RyRs.

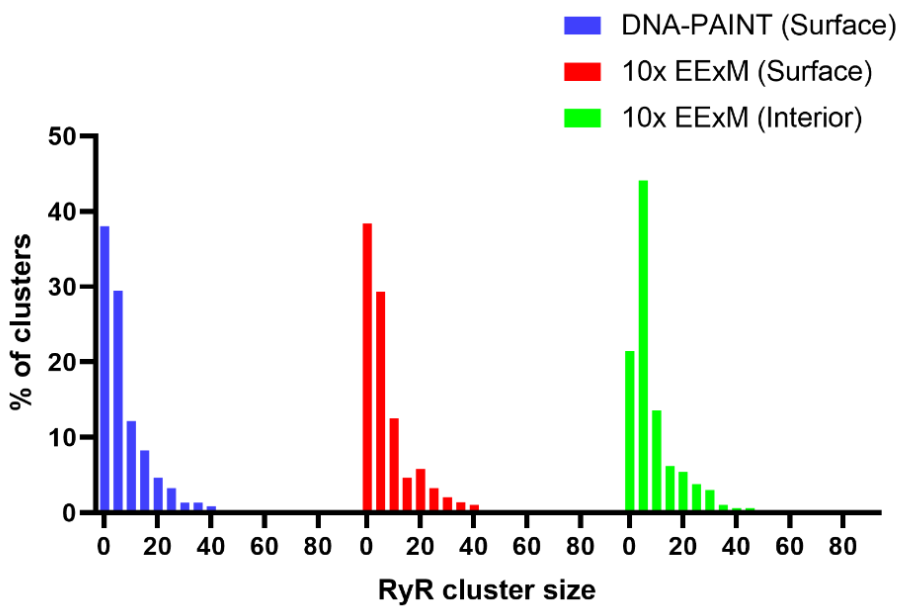

Figure 4-4. RyR cluster size

Percentage histograms of cluster size (no. of RyRs per cluster), as determined for surface clusters by DNA-PAINT and 10x EExM, and for interior clusters by 10x EExM. Distributions for surface clusters were very similar. The average surface cluster size as calculated with DNA-PAINT of 7.87 ± 0.39 RyRs/cluster was similar to the 8.98 ± 0.44 RyRs/cluster measured with 10x EExM. The average interior cluster size as measured with 10x EExM was 8.23 ± 0.51 RyRs/cluster. (n (cell, clusters) = 11, 1912 ExM interior; 12, 3209 DNA-PAINT (surface); 11, 1491 ExM surface).

The arrangement of RyRs is critical to cluster excitability and the process of Ca^{2+} release (Walker *et al.*, 2014). To understand the organisation of RyRs within a cluster, it is prudent to study the NND, which is the closest distance each RyR had to the neighbouring RyR. This measure of clustering has been implemented previously in both DNA-PAINT (Jayasinghe *et al.*, 2018) and electron tomography datasets (Asghari *et al.*, 2009, 2014). The three-neighbour distance (3ND), which is the mean distance from each RyR to its three closest neighbours, is another useful measure of cluster spacing.

Using the coordinates of RyR positions following centroid detection, the NND and 3ND were calculated for 2D surface clusters with 10x EExM, and was compared to estimates from DNA-PAINT. The surface cluster NND of 42.04 ± 4.8 nm with 10x EExM was similar to the DNA-PAINT estimate of 40.0 ± 4.7 nm ($p = 0.34$) (Figure 4-5A), as well as to the 37 nm NND observed by electron tomography (Asghari *et al.*, 2014). The 3NDs were also similar, 60.1 ± 8.5 vs 64.5 ± 9.6 nm in DNA-PAINT and 10x EExM respectively ($p = 0.24$) (Figure 4-5B). Both NND and 3ND shared common modes. The longer rightward tail in 10x EExM histograms could indicate differences in the ability to detect smaller RyR populations, but the overall shapes of NND and 3ND distributions were independent of the imaging method.

The similarity of 10x EExM to DNA-PAINT, in terms of surface cluster size and distance analyses, provides confidence that the expansion process was isotropic and that distortions introduced were minimal, given the ability to replicate nanoscale measurements.

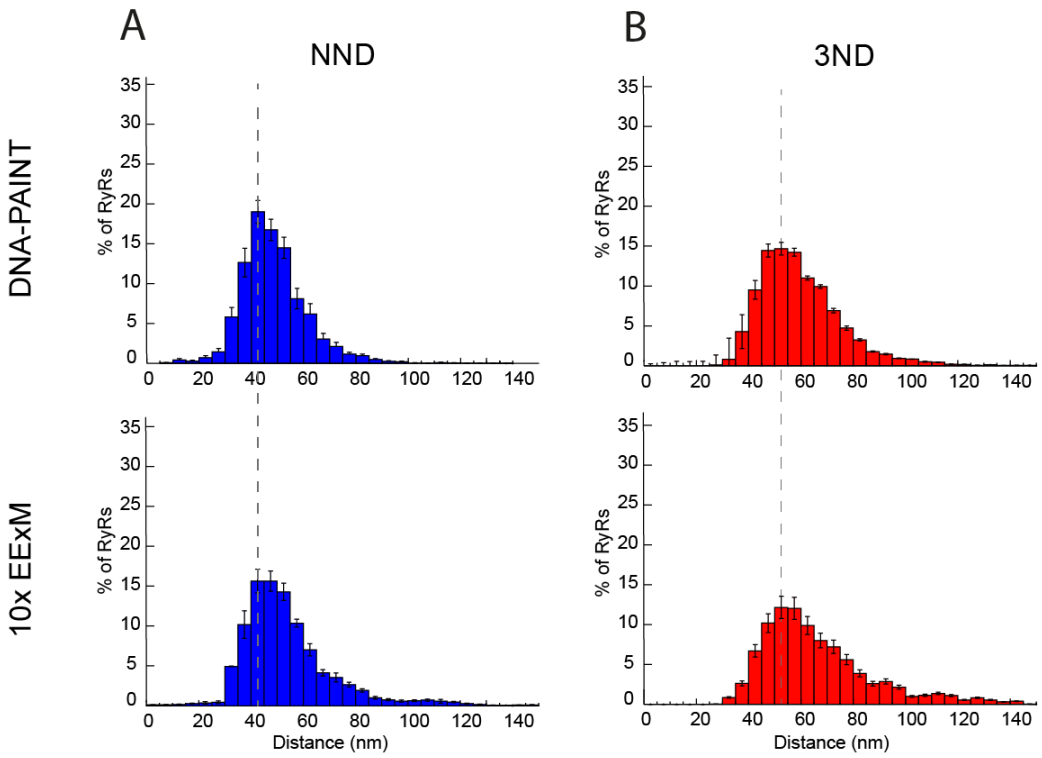

Figure 4-5. RyR 2D surface cluster distance analysis

Histograms showing the distribution of **(A)** nearest neighbour distance (NND) and **(B)** 3-neighbour distance (3ND) in surface clusters (containing >3 RyRs). Dashed lines show that the mean NNDs were similar between DNA-PAINT and 10x EExM, 40.0 ± 4.7 nm compared to 42.04 ± 4.8 nm respectively ($p = 0.34$, student's t-test). The 3NDs were also not statistically different, 60.1 ± 8.5 nm compared to 64.5 ± 9.6 nm ($p = 0.24$, Mann-Whitney test). ($n = 19$ cells).

4.3.3 Understanding dyad organisation

RyR interior clusters, due to their curvature around t-tubules, are 3D and morphologically complex. Therefore, 3D imaging is required to appropriately interpret these structures. 3D ExM is straightforward by capitalising on the z-stack functionality of the Zeiss Airyscan microscope.

A 10x EExM volume over a depth of 10 µm of expanded gel corresponds to 1 µm of cellular contents, containing numerous clusters at various heights within the cell interior. Using a maximum intensity projection (colour coded for depth) it was possible to see the layout of RyRs within internal clusters (Figure 4-6A). Clusters varied dramatically in size, including large clusters of 10+ RyRs, as well as solitary RyRs. It was common to observe 2 parallel rows of RyRs, which were likely to be either side of a t-tubule.

For an example cluster with a curved topography, shown in-plane (Figure 4-6B, left), a surface rendered model (middle) was created to demonstrate the ability of 10x EExM to visualise the curved 3D geometry. The schematic (right) demonstrates the way such a cluster might be wrapped around a t-tubule. Clearly, the full extent of this cluster would not be visible when imaged in a single dimension.

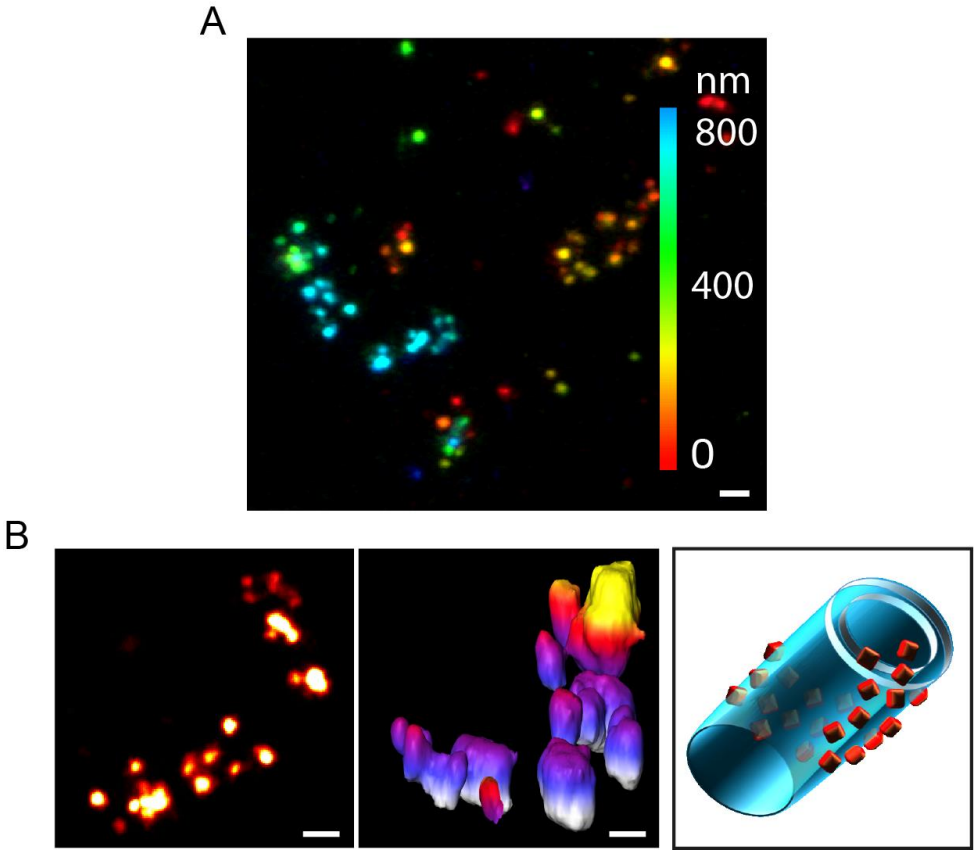

Figure 4-6. 3D imaging of interior RyR cluster

(A) A maximum-intensity projection of a 1 μm-deep cell volume with RyR labelling, colour coded for depth. **(B)** An example RyR cluster is shown in-plane (left), whose 3D topography is visible in a surface-rendered image, colour-coded for depth (middle). The schematic illustration (right) depicts the arrangement of RyRs (orange) relative to the t-tubule (cyan). EF = 10. **Scale bars:** 50 nm.

To better understand dyad organisation, 2-colour imaging of RyR alongside the anchoring protein JPH was performed. JPH extends from the SR (where the C-terminus transmembrane domain is docked) to contact the sarcolemma, physically anchoring the two membranes together and maintaining the dyadic space.

At the cell surface, the punctate appearance of JPH resembled that of RyR, whereby each punctum was of a similar size (Figure 4-7). The individual JPH puncta were spaced at a similar arrangement to the RyR, suggesting that these were individual proteins. Typically, clusters contained both JPH and RyR, with few clusters composed of exclusively one or the other. JPH typically fitted into the gaps within the RyR array, which is because the JPH antibody recognises the C-terminal region, located at the SR side.

The interior clusters largely resembled surface clusters, as they contain both RyR and JPH, but they do extend beyond a single imaging plane as they are less flat. Consequent with the linear t-tubule structures that the dyad is formed in relation to, most interior clusters were elongated in one direction. Like the surface clusters, JPH often appeared to be more central to the backbone of the cluster shape, with RyRs positioned slightly further out.

3D datasets were obtained and surface-rendered models were created to better visualise the 3D morphology of curved dyadic clusters which span multiple axial planes. Most dyads possessed closely positioned JPH and RyR (Figure 4-8A). Clusters were mostly aligned in a sarcomeric pattern, in a transverse orientation relative to the direction of myofilaments, coincident with the layout of the t-system. As well as these transversely arranged clusters, there were also clusters oriented perpendicular to the sarcomeres.

Within a single cluster, JPH was typically located more centrally, closer to the axis of the cluster, while RyR puncta were often spread slightly further outside of the area that JPH occupies (Figure 4-8B). The schematic demonstrates the curved nature of interior RyR clusters, in comparison to the relatively flat surface clusters (Figure 4-8C).

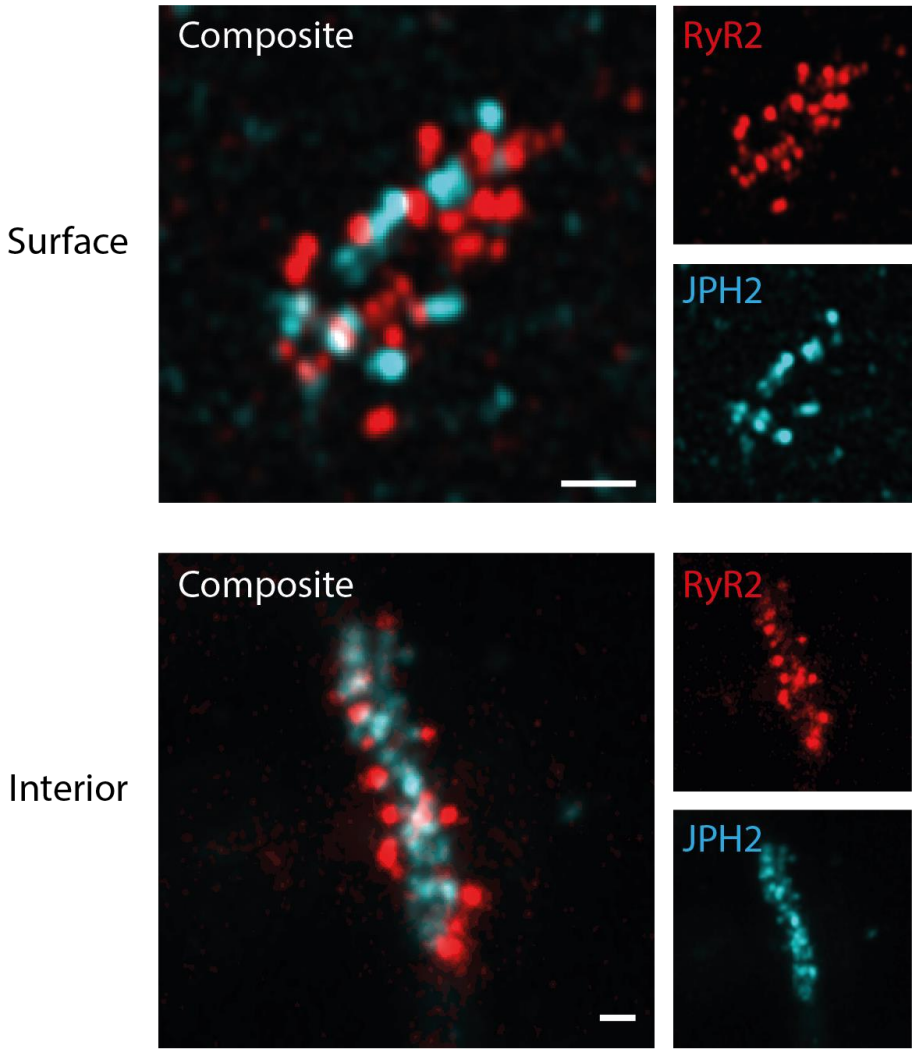

Figure 4-7. 10x EExM imaging of dual-labelled, RyR and JPH clusters

Two-colour 10x EExM of RyR (red) and JPH (cyan) in clusters at the surface and interior. In surface clusters, the gaps within the RyR arrays are often occupied by JPH. In interior clusters, the relationship and ratio of the proteins was similar to at the surface. EF = 10. **Scale bars:** 100 nm.

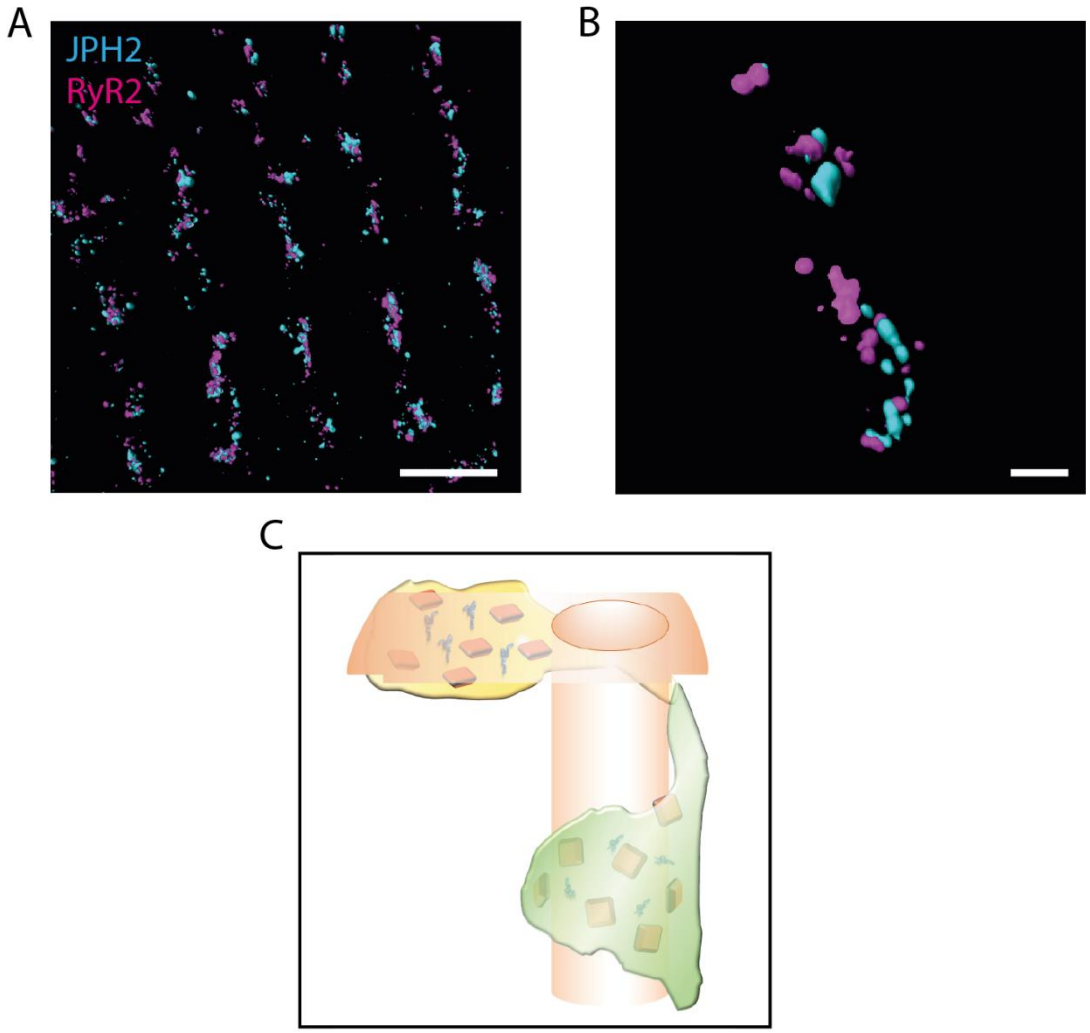

Figure 4-8. 3D arrangement of RyR and JPH in the dyad

(A) 3D surface rendering of JPH and RyR in dyadic clusters in the cardiomyocyte interior. **(B)** JPH was often located more centrally within a cluster, forming the backbone, while RyR extends slightly further beyond the cluster outline. **(C)** Schematic showing the difference between the arrangement of RyR and JPH in surface clusters and in interior clusters associated with the curved t-tubule. EF = 10. **Scale bars:** left 2 µm, right 100 nm.

The counts and arrangements of RyR and JPH in dyadic clusters were quantified using 3D 10x EExM datasets. In contrast to the centroid detection-based analyses performed earlier, a different 3D approach was used wherein clusters were cropped manually and subjected to a 3D iterative thresholding algorithm which separated objects (Figure 4-9A). This alternative approach was performed due to difficulties in applying centroid detection for the 3D JPH datasets.

The average RyR interior cluster size using this approach was 18 ± 2.9 RyRs (Figure 4-9B), which was twice as large as that estimated with the centroid detection approach (~9 RyRs). The cluster selection in this analysis favoured larger clusters, critically selecting fewer small (<10 RyR) clusters, which was likely a consequence of subjective bias during the cropping process. While the larger RyR clusters with 60+ receptors could be functionally relevant as Ca^{2+}-release units providing Ca^{2+} to metabolically-hungry intracellular regions, they could also relate to imaging artefacts.

The average JPH cluster size as calculated with the 3D iterative thresholding approach was 16 ± 2.4 JPHs (Figure 4-9C). This quantification assumed that individual puncta were single JPH molecules, the implications of which are discussed in Section 4.4.2. Given the suggested bias toward larger clusters in the RyR analysis, it is assumed that this estimation of JPH cluster size is similarly over-estimated.

For the purpose of evaluating the relative proportion of JPH to RyR, the potential over-estimations of the 3D iterative thresholding approach are less important. Considering whether clusters comprised of similar numbers of JPH compared to RyR, the average cluster had a ratio of 0.94 ± 0.08 JPHs to RyR (Figure 4-9D). The maximum range of this JPH:RyR ratio was 0.4 to 2, indicating that the ratio of the two proteins is somewhat variable, and supports the idea that RyRs are differentially regulated by JPH (Jayasinghe *et al.*, 2018). A previous 2D analysis of JPH:RyR ratio in surface clusters with DNA-PAINT reported a ratio of 1.38 JPH per RyR and a range of 0.5-3.5 (Jayasinghe *et al.*, 2018). This could indicate a lower incidence of JPH in dyads as compared to surface clusters, potentially due to a reduced need for structural attachment, or less of a requirement for a stabilising effect of JPH on RyR. These points are considered in Section 4.4.2.

3D distance analyses were performed to understand the co-clustering relationship between RyR and JPH. The majority of JPH proteins were between 50-100 nm from an RyR (Figure 4-10). This is larger than previous 2D estimations in surface clusters using DNA-PAINT, which found that most JPH were within 50 nm of RyR (Jayasinghe *et al.*, 2018). The larger NND here could be due to the introduction of a third dimension, which would factor in larger distances in z, or

due to the bias for larger clusters. It is worth noting that RyR-RyR NND distances in this 3D analysis were larger than that from the 2D analysis, suggesting distances analysed here might also be slightly overestimated.

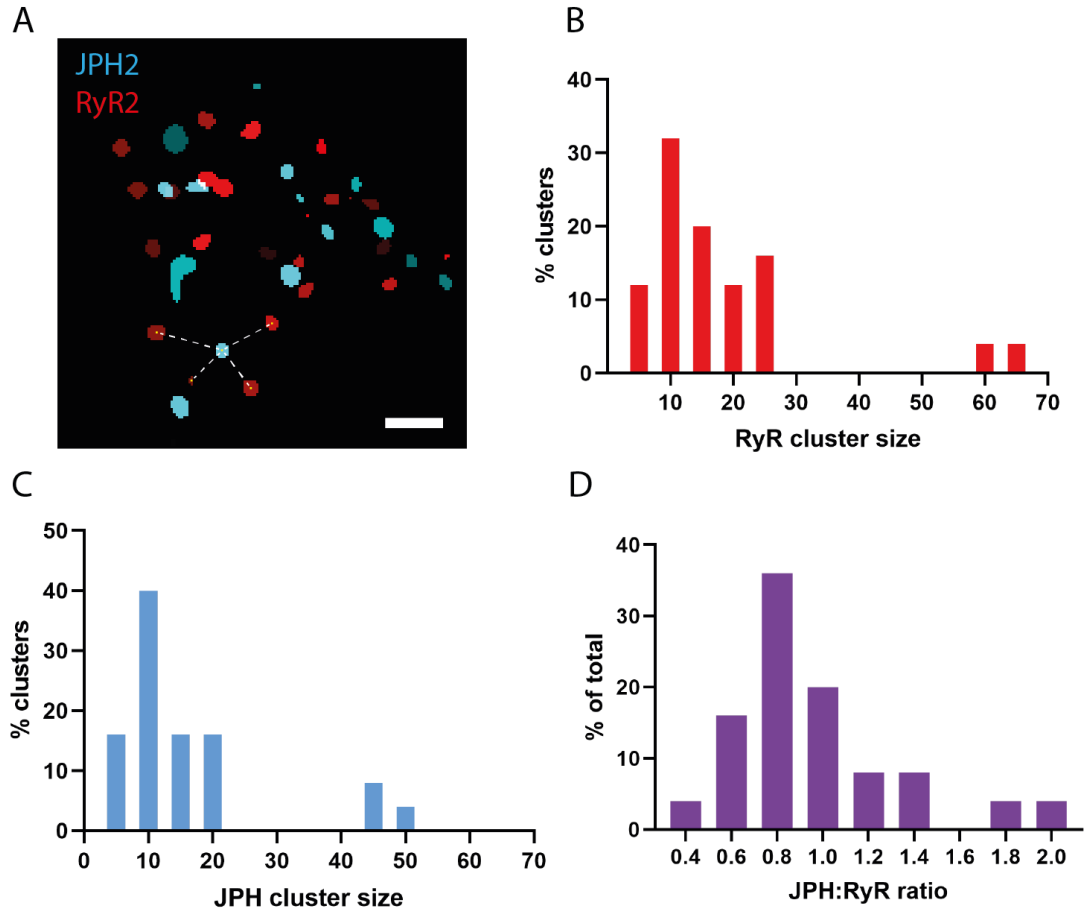

Figure 4-9. JPH cluster size and ratio to RyR in interior clusters

3D JPH RyR datasets were analysed using a different approach to centroid detection, involving iterative thresholding which separated the puncta into separate objects, allowing count and distance analyses. **(A)** A 2D slice from a 3D stack, showing the clearly separated objects of RyR and JPH obtained following the iterative threshold. The centroids (yellow) were used to calculate NND distances (white) in Figure 4-10. **(B)** The average RyR cluster size of 18 ± 2.9 was higher than that estimated using the centroid detection method, suggesting a bias towards larger clusters. **(C)** The average JPH cluster size was 16 ± 2.4 JPHs **(D)** and the average ratio of JPH:RyR was 0.94 ± 0.08 per cluster. (n = 3 cells, 25 clusters). **Scale bar**: 100 nm.

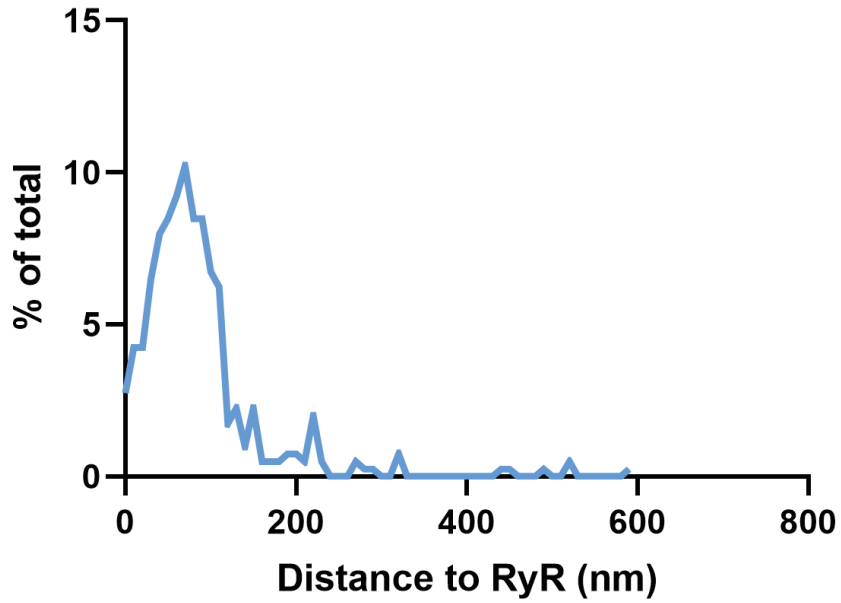

Figure 4-10. JPH-RyR 3D distance analysis in interior clusters

Interior clusters underwent a 3D distance analysis following iterative thresholding, which measured the centre-to-centre NND between object centroids. The frequency histogram of the mean NND shows that most JPH are within 50-100 nm from an RyR. (n = 3 cells, 25 clusters, 401 JPHs).

4.3.4 Visualising ryanodine receptor phosphorylation *in situ*

Phosphorylation of individual RyRs *in situ* would allow a direct quantification of the fraction of phosphorylation in a cluster for the first time. To visualise RyR phosphorylation, antibodies which recognise site-specific phosphorylated RyR2 were used, which bind to the RyR if a particular serine residue is phosphorylated. The specificity of the site-specific phospho-RyR antibodies were validated in 2-colour imaging alongside the standard RyR antibody (Thermo Fischer, MA3-916). Given that the antigen which the standard antibody recognises is not specified, it is not possible to speculate whether binding would preclude binding of the phospho-RyR antibody.

The first phosphorylation site investigated was serine-2808 (pSer2808), which is phosphorylated *in vitro* by both PKA and CaMKII. Using confocal microscopy pre-expansion, the pSer2808 labelling pattern resembled standard RyR labelling, with a striated appearance and minimal puncta in between striations (Figure 4-11A). In the composite image, the overlap of the two antibodies (white in composite) suggested that labelling was specific.

The specificity of the pSer2808 antibody for RyR was evaluated at a higher resolution with 10x EExM (Figure 4-11B). At the cell surface, pSer2808 labelling was often directly within RyR clusters. While this does not confirm binding specificity of the antibody for the exact phosphorylated residue, it at least confirmed specificity of the antibody to regions containing the target protein. Deeper in the cardiomyocyte, interior RyR clusters were arranged in striations, with few RyRs present in-between sarcomeres. The minimal pSer2808 labelling in these regions suggests the high specificity of this antibody. There were a few instances of pSer2808 labelling outside of RyR clusters, or positioned in clusters but without a nearby RyR label. This could be attributed to non-target binding by pSer2808, or dissociation of the standard RyR antibody.

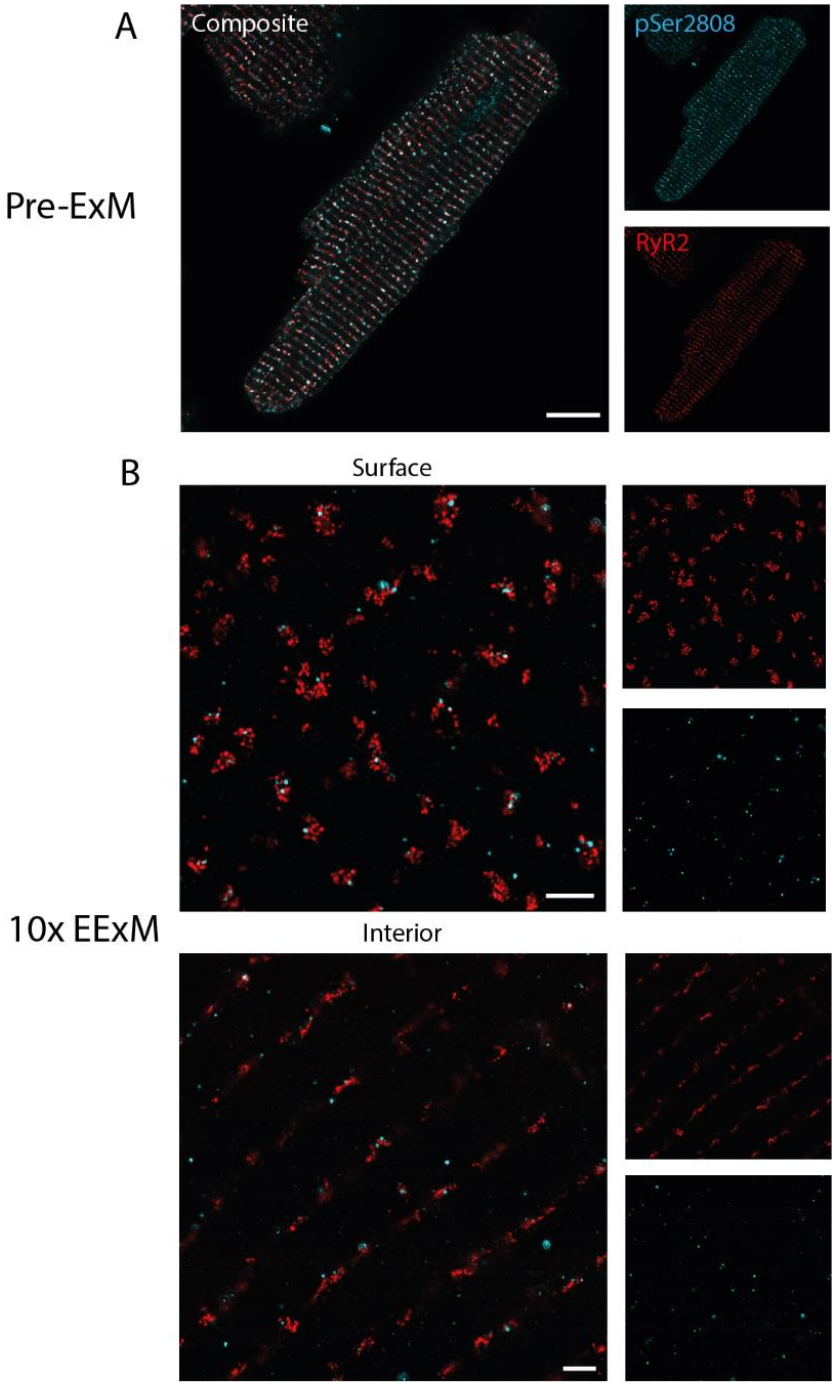

Figure 4-11. In situ visualisation of pSer2808

The specificity of the anti-pSer2808 antibody was validated alongside a standard RyR antibody. **(A)** Using confocal imaging pre-expansion, the pSer2808 labelling pattern coincided with RyR labelling, sharing a similarly punctate appearance. **(B)** Using 10x EExM, most individual pSer2808 labels existed closed to RyR labels, roughly within the area of the clusters. EF = 10. **Scale bars:** A 10 µm, B 500 nm.

Next, it was of interest to determine if it was possible to detect experimentally-induced changes in the amount of phosphorylation. In order to artificially evoke β-adrenergic stimulation, cardiomyocytes were stimulated with the β-agonist isoproterenol (100 nM) and electrical pacing at 1 Hz for 10 minutes (McMartin and Summers, 1999; Collins and Rodrigo, 2010; Wypijewski *et al.*, 2015). In Control cardiomyocytes which possess a basal level of phosphorylation, the density of pSer2808 within surface clusters appeared to be relatively low, with just a few phosphorylated RyRs per cluster (Figure 4-12A, left). In cardiomyocytes after β-adrenergic stimulation, the density of pSer2808 was visibly increased (Figure 4-12A, right).

To directly quantify the change in the fraction of phosphorylation, the centroid detection protocol was used to count the number of pSer2808 puncta in relation to the number of RyR puncta. In Control cardiomyocytes the average fraction of phosphorylation was 0.31 ± 0.10 SD for surface clusters and 0.28 ± 0.11 for interior clusters (Figure 4-12B). Very few clusters were maximally or minimally phosphorylated. After β-adrenergic stimulation, the fractional phosphorylation was increased to 0.48 ± 0.06 at the surface and 0.60 ± 0.12 in the interior ($p < 0.0001$).

Given that SL was used to calculate the EF to normalise the expanded images and verify isotropy, it was important to determine whether the SL of stimulated cells was altered. The SL of the stimulated cells was 1.82 ± 0.03 μm, which was not significantly different to that of the Control, unstimulated cells 1.84 ± 0.01 μm ($p = 0.45$) (Figure 4-13).

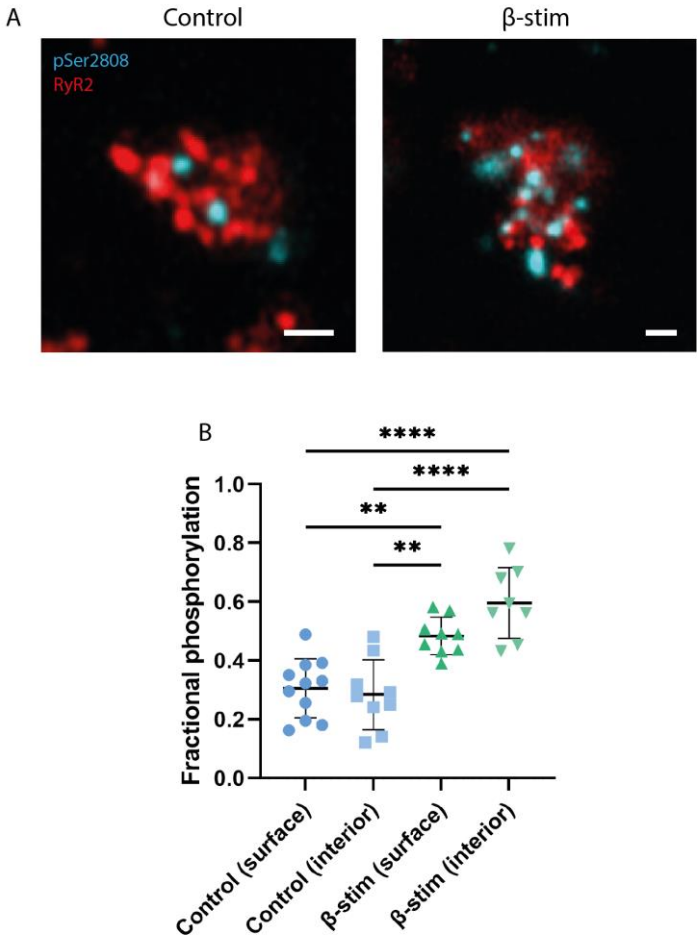

Figure 4-12. Increased pSer2808 phosphorylation after β-adrenergic stimulation

(A) Images of pSer2808 and RyR labelling in control cardiomyocytes (representing basal phosphorylation) and in stimulated cardiomyocytes which were incubated with the β-adrenergic agonist isoproterenol (β-stim). β-stim had a visibly increased number of pSer2808 labels per cluster. **(B)** Comparison of the fractional pSer2808 phosphorylation between control cardiomyocytes and those in the β-stimulation experiment, in clusters containing >3 RyRs. Mean (± SD) fractional phosphorylation in Control surface was 0.31 ± 0.10, and in Control interior was 0.28 ± 0.11. After β-stim, surface phosphorylation was increased to 0.48 ± 0.06, and interior phosphorylation was increased to 0.60 ± 0.12. (**p < 0.01, ****p < 0.0001, One-way ANOVA). (n (cells) = 11 Control surface, 9 Control interior, 9 β-stim surface, 8 β-stim interior). EF= 10. **Scale bars** = 100 nm.

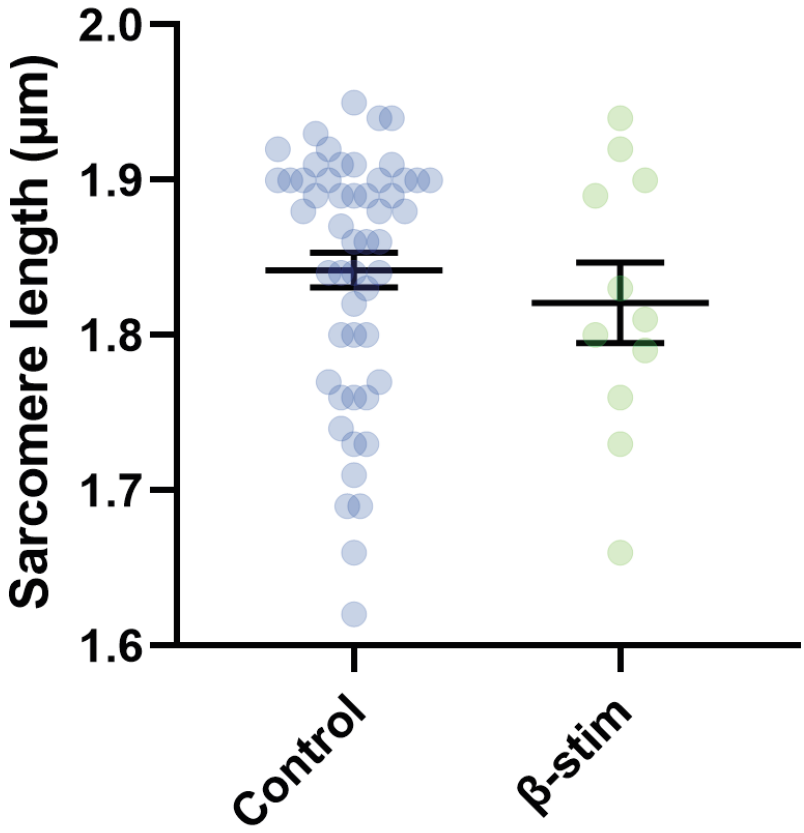

Figure 4-13. β-adrenergic stimulation effect on sarcomere length

The sarcomere length (the distance between sarcomeric striations) was observed in the β-stimulation experiment, due to the implications on calculating EF and verifying isotropy. The sarcomere length of 1.82 ± 0.03 µm in stimulated cells was not different to 1.84 ± 0.01 µm in control (p= 0.45, Mann-Whitney test). (n (animals, cells) = 7,52 control; 3,11 stimulated).

The second phosphorylation site was serine2814 (pSer2814), which is the main CaMKII target and is physiologically important and thought to contribute more significantly to dysfunction in HF, arising through hyper-active CaMKII (Wu *et al.*, 2002; Sossalla *et al.*, 2010). In pre-expansion imaging there appeared to be regions of colocalisation between pSer2814 and RyR labelling, but also a large amount of labelling that did not overlap (Figure 4-14A). There was also nuclear labelling (arrows), which can be indicative of non-target antibody binding. In 10x EExM images, non-specific labelling was observed, evidenced by pSer2814 labels outside of RyR clusters (arrow) (Figure 4-14B). pSer2814 labelling was distributed evenly, irrespective of the position of RyR clusters, although there were some instances of seemingly specific pSer2814 labelling at RyR clusters (dashed regions).

By enhancing phosphorylation, we speculated that more target binding could outweigh non-target labelling, and allow pSer2814 fractional phosphorylation to be quantified. Using electrical stimulation with 100 nM isoproterenol, while the pSer2814 fluorescence intensity increased overall when imaged pre-expansion, there was still a significant amount of non-target labelling outside of RyR clusters in the 10x EExM images (not shown).

Due to the extent of non-target labelling and the inability to decipher genuine pSer2814 RyR labelling from non-target labelling, it was unfeasible to attempt to quantify pSer2814 fractional phosphorylation as performed for pSer2808.

The third and final phosphorylation site was serine2030 (pSer2030), which is exclusively phosphorylated by PKA, and is necessary for a functional β-adrenergic response (Potenza *et al.*, 2018). Pre-expansion pSer2030 labelling was striated, but not particularly punctate (Figure 4-15A). The intensity of pSer2030 labelling was increased by β-adrenergic stimulation. Using 10x EExM, pSer2030 labelling was distributed uniformly across an image, regardless of the positions of RyR clusters (Figure 4-15B). This labelling non-specificity was apparent both at the surface and the interior.

A second pSer2030 antibody, gifted by Professor Hector Valdivia, was also tested. This antibody labelling possessed a similar amount of non-specific labelling (not shown).

Quantification of pSer2030 phosphorylation was not possible due to the amount of non-specific labelling.

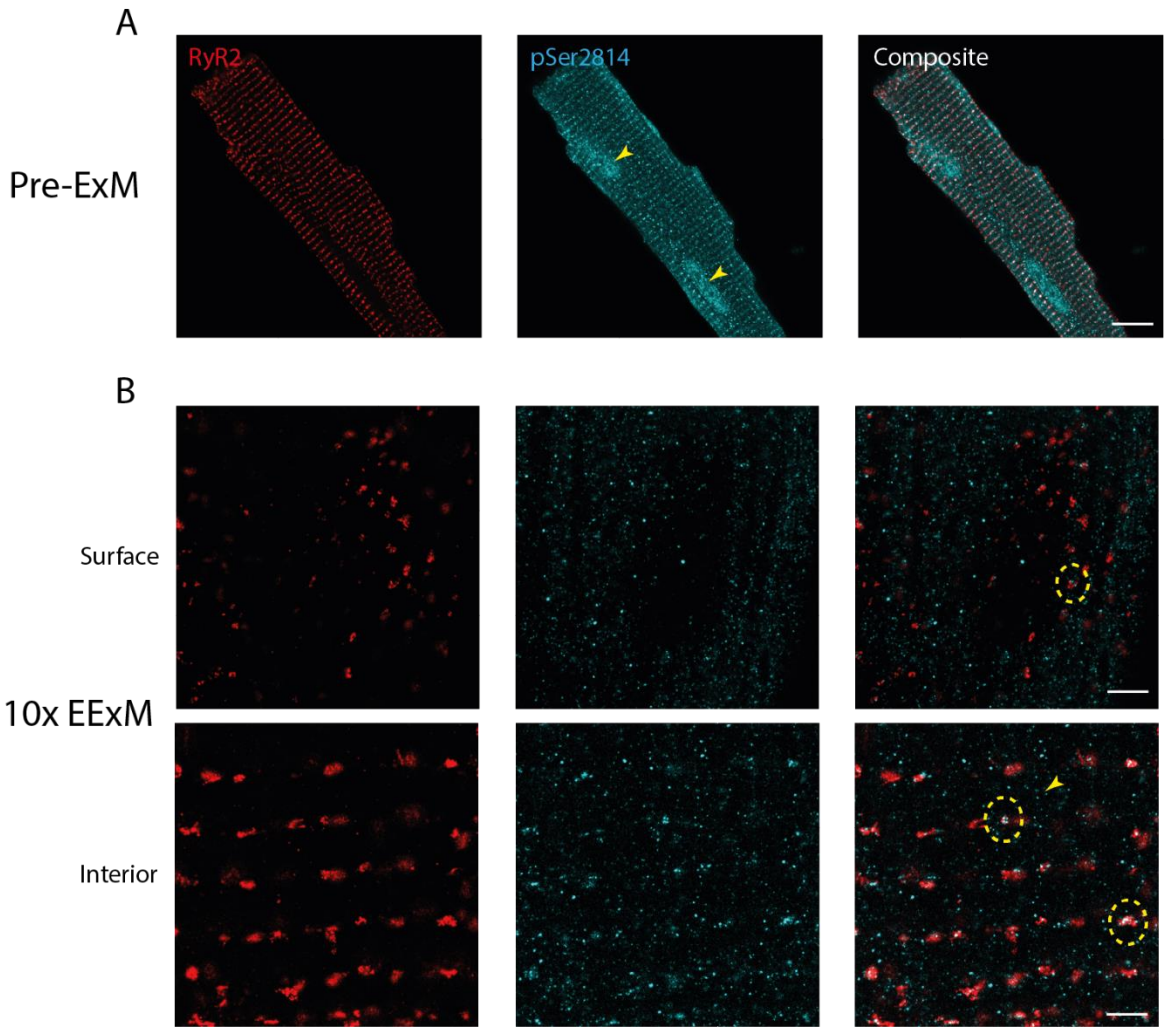

Figure 4-14. In situ visualisation of pSer2814

The specificity of the anti-pSer2814 antibody was validated alongside a standard RyR antibody. **(A)** Pre-expansion, there was minimal colocalisation of pSer2814 with RyR. There was also nuclear labelling (arrows). **(B)** Using 10x EExM, there were few instances of pSer2814 labelling RyR clusters (regions marked by dashed lines), but generally pSer2814 labelling was generally distributed outside of RyR clusters, suggesting non-specific labelling. This was especially apparent in the interior view, with pSer2814 puncta (arrow) in between the RyR striations. EF = 10. **Scale bars:** A 10 µm, B 1 µm.

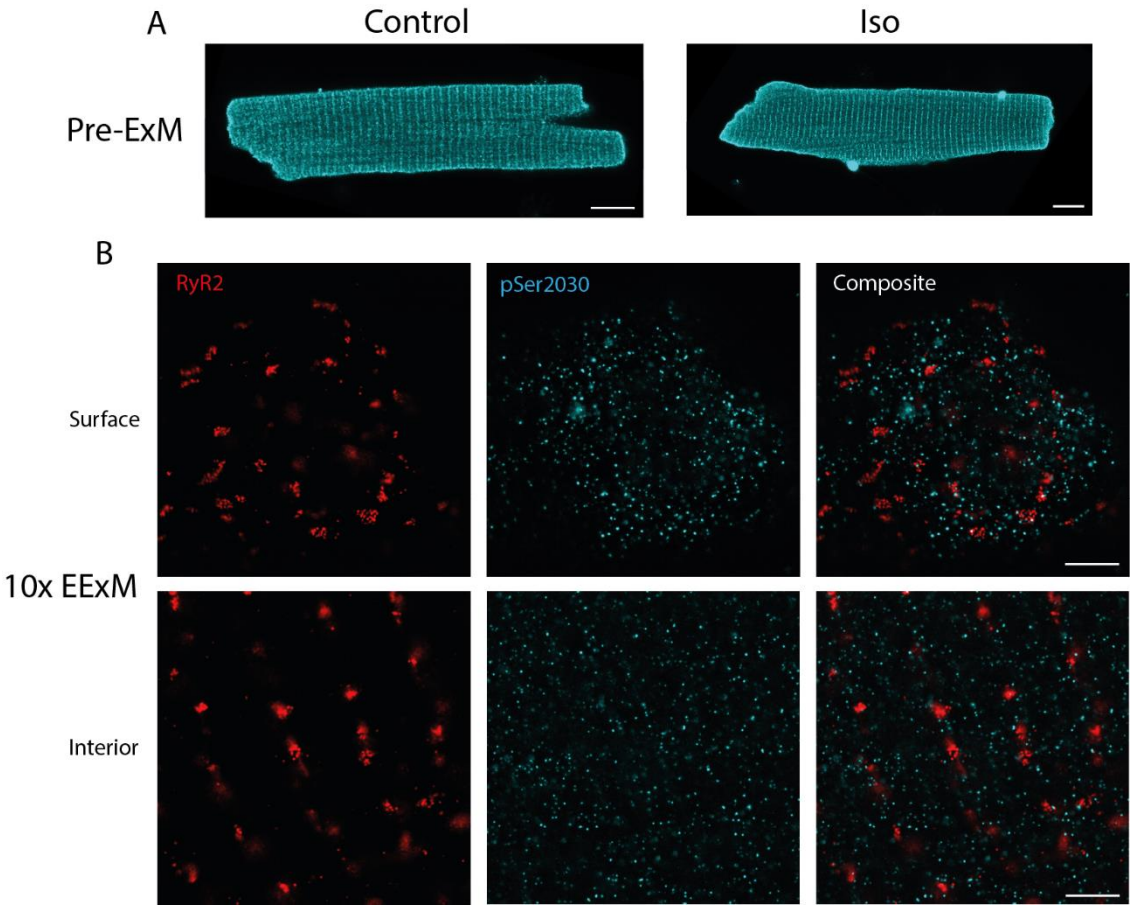

Figure 4-15. In situ visualisation of pSer2030

The specificity of the anti-pSer2030 antibody was validated alongside a standard RyR antibody. **(A)** Pre-expansion, pSer2030 labelling had a striated appearance which appeared to increase in intensity following β-adrenergic stimulation. **(B)** Poor specificity for RyR was seen in 10x EExM imaging, with a relatively uniform distribution of pSer2030 labels irrespective of cluster locations. EF = 10. **Scale bars:** A 10 µm, B 1 µm.

4.4 Discussion

4.4.1 10x enhanced expansion microscopy of ryanodine receptor clusters

10x EExM was suitable in its application to visualise RyR cluster organisation, given the established in-plane and axial resolution which was sufficient to resolve individual proteins. While the localisation accuracy of dSTORM and DNA-PAINT suffers due to high autofluorescence from the sample, optical clearing with ExM enhances the detection of low marker densities. Further, the ability of ExM to operate beyond a 10 µm depth enabled it to visualise dyadic clusters located deeper within the cardiomyocyte.

10x EExM imaging was able to replicate the qualitative and quantitative description of 2D surface clusters that was previously established with DNA-PAINT. This cross-validation with a reliable imaging technique suggests that the ExM process was isotropic and that most fluorophores were retained in the gel. One assumption made was that each puncta related to a single RyR, based on antibody binding models and quantitative PAINT experiments suggesting that only one primary-secondary antibody complex can bind to each RyR (Jayasinghe *et al.*, 2018).

Interior clusters as quantified using the centroid detection method were similar in size to surface clusters and had a similar spacing arrangement. The cluster size estimates were smaller than those from transverse tissue sections with dSTORM (Hou *et al.*, 2015), attributable to the improved axial resolution of 10x EExM.

4.4.2 Understanding 3D dyad organisation with junctophilin

Given the availability of antibody species, fluorophores and the multiplexing capabilities of a confocal microscope, it is trivial to upgrade ExM from a single-protein imaging technique to one that can observe multiple proteins at the same time. By performing multi-colour imaging, the relationship of RyR with JPH could be investigated, which had only previously been determined in surface clusters with DNA-PAINT.

JPH was observed to often occupy a central location within the cluster. This could be due to this central region of the dyad being a specialised structural domain, ensuring a consistent uniform attachment between the sarcolemmal and SR membranes, and crucially maintaining the dyadic space.

Using a 3D analysis (in part due to the less uniform nature of the JPH puncta), the average dyad contains 16 JPH and 18 RyRs, with an average JPH:RyR ratio of 0.94:1. 2D DNA-PAINT estimates of surface clusters reported a ratio of 1.38 JPH per RyR (Jayasinghe *et al.*, 2018), possibly relating to a different importance of JPH between the different cluster types. The structural implications of a reduced JPH:RyR ratio could result from the curved morphology of dyads, with potentially fewer JPH proteins required to maintain the dyadic space, or simply that the area of attachment is smaller and thus less space for JPH. Alternatively, it is possible that surface clusters may require added anchoring strength of SR-sarcolemma attachment, perhaps due to larger strain on these clusters incurred by the effects of stretch on the cell surface. Furthermore, given the stabilising effect of JPH on RyR activity, the functional implications related to a reduced JPH:RyR ratio in dyads could be that their Ca^{2+} release does not need to be as critically stabilised.

The quantitative analysis used here took a different approach to the centroid detection analysis and appeared to bias toward larger clusters, as demonstrated by an increased RyR cluster size. This bias during the manual cropping of clusters likely arises due to a reduced ability for the human eye to recognise smaller clusters.

Another consideration to make when interpreting the data is that while each JPH puncta was taken to be a single protein, it is possible that the number of puncta does not directly equal the number of proteins, partly because the JPH antibody is polyclonal. A previous study observing JPH at a similar resolution (using quantitative DNA-PAINT) saw that puncta were individual labelling units, but this is not proof that a single punctum equals a single JPH molecule (Jayasinghe *et al.*, 2018).

Future efforts to infer the orientation of RyR clusters relative to the membrane will require labelling of other protein targets. Previous efforts to visualise the t-system involve immunolabelling t-tubule proteins such as Cav3 and NCX and diffraction-limited imaging at 200 nm resolution, but at 10 nm resolution the distribution of these individual proteins (which are not found in the dyadic space) is less useful. The most appropriate protein to observe would be the LTCC, given the direct relation to RyRs, but commercially available antibodies for this target have poor specificity, rendering them of limited use at this resolution.

4.4.3 Quantification of ryanodine receptor phosphorylation *in situ*

In visualising individual Ser2808-phosphorylated RyRs with 10x EExM, it was possible to quantify the amount of phosphorylation at the cluster level for the first time.

The basal pSer2808 phosphorylation was relatively low at around 30% and increased almost 2-fold in the interior following β-adrenergic stimulation. These relatively intermediate levels of pSer2808 phosphorylation are thought to bestow modest changes in RyR activation when compared to maximal and minimal phosphorylation (Carter *et al.*, 2006; Bovo *et al.*, 2017). The exact functional phenotype will depend on a number of factors including the cluster arrangement and contributions from other regulatory interactions. It would be interesting to correlate these *in situ* counts of phosphorylation with functional cluster properties using correlative imaging experiments.

The estimates of fractional phosphorylation are lower than that in the literature, which come almost exclusively from biochemical experiments. This discrepancy could be due to methodological differences, such as incomplete immunolabelling in imaging, or unaccounted selectivity in membrane fractionation methods (Carter *et al.*, 2006). There is the added possibility that the phosphorylation state observed here is altered during the Langendorff cardiomyocyte isolation process (Stensløkken *et al.*, 2009). While there was an increase in phosphorylation fraction to ~60% with the β-stimulation protocol, it is possible that phosphorylation could be further increased with a more extreme concentration of β-adrenergic agonist.

pSer2808 labels were assigned to nearby RyR puncta, allowing for a distance offset relating to the linkage error associated with antibodies. Future studies would benefit from more compact probes which minimise this linkage error, such as nanobodies. There were a few instances where pSer2808 puncta existed without an associated RyR puncta, which could result from non-specific binding by the pSer2808 antibody, or an unlabelled (or dissociated) RyR label. Given that the antigen which the standard antibody recognises is not specified, it is not possible to confirm whether one antibody binding precludes the binding of the other. Labelling patterns in a previous study using DNA-PAINT lead to the assumption that the standard antibody binding site was near the centre of the RyR molecule (Jayasinghe *et al.*, 2018). Given that the pSer2808 residue is located on the outer edge of the RyR lends to the prospect that pSer2808 antibody binding does not prevent binding of the standard antibody, and is suggested by the

fact that the RyR labelling density was not visibly lower in the presence of the pSer2808 antibody.

While these analyses simply determined whether an RyR bore a phosphorylation label in proximity or not, there can be multiple pSer2808 modifications per RyR tetramer (one per monomer). The distance between the different pSer2808 sites on a single RyR (of less than 30 nm) theoretically allows them to be observed as distinct points, but typically only single pSer2808 puncta were observed next to each RyR. Occasionally individual puncta were larger than the RyR puncta, which could relate to multiple antibodies too close to resolve as separate.

Future studies should quantify the contributions of pSer2814 and pSer2030 phosphorylation alongside pSer2808 to gain insight into the compensatory nature. Given the poor specificity of pSer2814 and pSer2030 antibodies, it was not possible to quantify basal levels of phosphorylation at these sites. Alternative antibodies or more effective blocking steps might be necessary to obtain effective results.

4.5 Concluding remarks

This chapter has used 10x EExM to characterise CRUs in greater detail. With individual protein resolution, the findings of RyR cluster size and arrangement in surface clusters were cross-validated with the description provided by DNA-PAINT, offering another validation of 10x EExM alongside those provided in Chapter 3. The relationship of JPH was also investigated in dyadic clusters in 3D, revealing close positioning to RyR and even counts of the two proteins.

RyR phosphorylation was also explored at the level of the individual protein within a cluster, for three different phospho-serine sites. It was possible to robustly quantify pSer2808 phosphorylation and detect experimentally-induced changes following β-adrenergic stimulation. The incidence of Ser2814 and Ser2030 phosphorylation remains undefined due to non-specific labelling.

Chapter 5. Visualising remodelling in the monocrotaline model of right ventricular heart failure

5.1 Introduction

Despite RV failure being a common feature in many cardiac diseases, there is currently no targeted clinical treatment for this condition. Mechanistic insights into pathological remodelling are required to develop treatment strategies and prevent disease progression.

The MCT animal model of PAH-induced RV HF provides an opportunity to study the remodelling mechanisms involved in pathogenesis. Ca^{2+} homeostasis dysfunction in MCT-RV, entailing a decrease in transient amplitude, increased frequency of spark production and SR leak, arises following t-tubule remodelling (Kuramochi *et al.*, 1994; Benoist *et al.*, 2012; Fowler, Drinkhill, Norman, *et al.*, 2018; Sabourin *et al.*, 2018). There are reports that RyR expression is reduced (Kögler *et al.*, 2003), but there is no account of changes to the organisation of RyR clusters. There are conflicting reports regarding changes to the expression of JPH. One study suggests there is a reduction in JPH expression(Xie *et al.*, 2012), accounting for t-tubule remodelling (Prins *et al.*, 2017), while another study found no change in expression (Fowler, Drinkhill, Norman, *et al.*, 2018). Changes to the quantity or arrangement of JPH have yet to be verified at the cluster level. While hyper-phosphorylation of RyR has been implicated in a number of HF variants, there is very little information about the role of phosphorylation in MCT-RV.

While the MCT model is useful for replicating features of RV HF, there are several considerations and limitations. The toxological mechanisms by which MCT initiates lung damage are unclear, and it is possible that effects on the heart are not solely due to pressure overload, but from more direct effects of the drug. Further, the initial insult and the onset to failure in the MCT model are incredibly fast. The validity of the model has been questioned given it does not replicate severe plexiform lesions typically associated with PAH (Gomez-Arroyo *et al.*, 2012). Several aspects of the MCT syndrome (such as pulmonary interstitial edema, myocarditis, and hepatic veno-occlusive disease) are not found in severe human PAH. The electrophysiology of rodents is also distinct from humans (Benoist *et al.*, 2012). Despite the limitations, the benefits of this animal model aside from replicating features of RV HF are the technical simplicity, reproducibility and low cost.

The aim of this chapter was to characterise the MCT model of RV HF in terms of RyR cluster organisation, JPH organisation and pSer2808 phosphorylation.

5.2 Methods

5.2.1 Monocrotaline model

Work relating to the MCT model, including injection, weighing and cardiomyocyte isolation, was performed along with Miriam Hurley. Adult male Wistar rats, aged ~ 5 weeks (200 ± 20 g) were given an intraperitoneal injection of 60 mg/kg (of body weight (BW)) MCT solution, prepared as follows. 68 mg of crotaline (Sigma) was dissolved in 0.5 ml of 1 M HCl and pH-ed to 7.4 dropwise with NaOH, then 140 mM NaCl was added up to 3.4 ml. Control animals were injected with a comparable volume of saline (140 mM NaCl).

Following injection, MCT is converted to the short-lived reactive pyrrole metabolite form, which damages the pulmonary vasculature, and after several weeks the rats develop PAH and RV hypertrophy (Gomez-Arroyo *et al.*, 2012). MCT animals were weighed every 2-3 days for the first 3 weeks, then daily near the failure point (between days 21 and 28). When there were signs of HF (cold extremities, piloerection, lethargy and dyspnoea), or a weight loss of 10% on a single day, or losses on consecutive days, animals euthanised, entailing a concussive blow to the head then cervical dislocation. There was one unexpected death on day 20, just before the failure period. No controls died of natural causes, and were taken for cardiomyocyte isolation on the median survival day.

Isolated ventricular cardiomyocytes were obtained by the Langendorff perfusion method detailed in Section 2.1. The RV and LV were separated prior to shaking to yield separate cell suspensions.

The number of organ and ventricle weights stated in the subsequent statistical analyses differ. This is because for some hearts the ventricles were separated immediately from fresh tissue, in order to be fixed tissue samples, while most underwent collagenase digestion prior to ventricle separation, and therefore the ventricle weights between the two groups were not comparable. Therefore the ventricular weights specified below were from the digested hearts, given that they were the most prevalent sample type.

5.2.2 Imaging and analysis

The samples were fluorescently immunolabelled with antibodies for RyR2, JPH and pSer2808, as detailed in Section 2.2.

proExM or X10 expansion microscopy were performed as outlined in Section 2.3. The samples were then imaged as in Section 2.4.

The pipeline of image analyses used for JPH-RyR is detailed in Section 2.5.2. Analysis used on RyR-pSer2808 is detailed in Section 2.5.1 and was performed by Izzy Jayasinghe. For the phosphorylation density analysis, a Euclidean distance map was constructed within the cluster area using the binary masks constructed during segmentation.

5.3 Results

5.3.1 Monocrotaline model

The growth of Control and MCT animals was monitored by weighing over the course of the experiment. The growth curves reveal that MCT animals had slower growth (Figure 5-1), with a plateau in weight gain as animals approached the failure period (between 21 and 28 days) and a weight drop-off coinciding with HF. The mean day of failure was day 24. The average (± SD) final MCT animal BW of 277 ± 17 g was significantly less than Control, which was 324 ± 25 g ($p < 0.0001$).

On the failure day, the major organs were weighed. The lungs of the MCT animals were significantly heavier than in the Control animals ($p < 0.0001$) (Figure 5-2A), which confirms the development of pulmonary remodelling. There were no significant differences in the liver weights between MCT and Control (Figure 5-2B).

Heart hypertrophy was assessed using a few parameters, including heart weight (HW):BW, RV:LV and RV:BW. There was a significant increase in the HW:BW ratio in MCT compared to Control ($p = 0.0242$) (Figure 5-3A). This increase can be attributed to RV hypertrophy, as gauged by a significant increase in the RV: BW ratio ($p = 0.0024$) (Figure 5-3B) and an increase in the ratio of RV:LV, albeit this was not significant ($p = 0.1433$) (Figure 5-3B). There was no difference in the ratio of LV:BW between Control and MCT animals (Figure 5-3D).

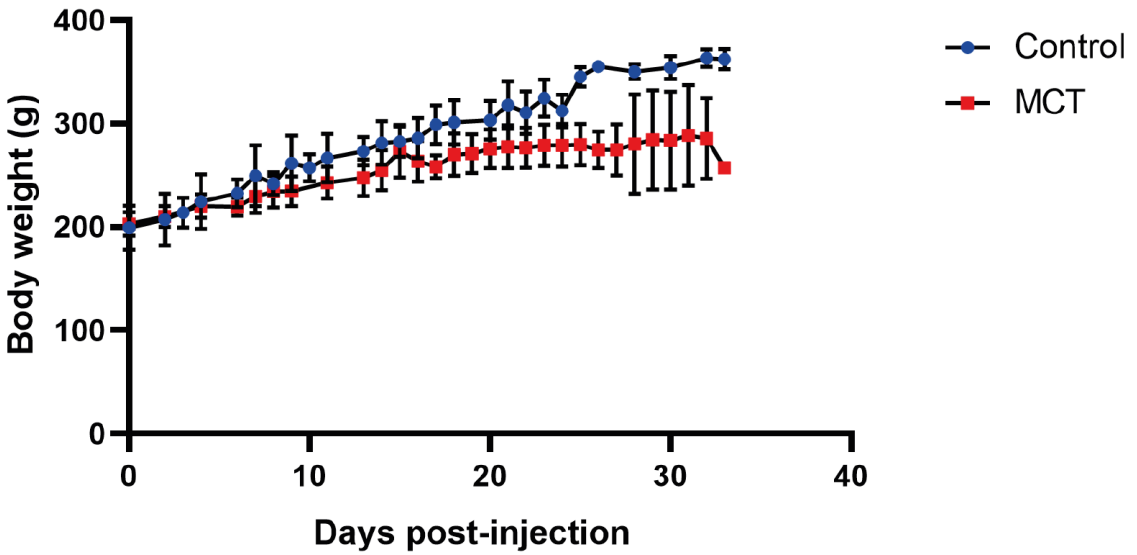

Figure 5-1. Growth curves

Growth curve showing the mean (± SD) body weights of Control and MCT animals over the course of the experiment. Following day 14, MCT animals were weighed daily, while the Control animals were weighed every few days. MCT weight gain plateaued around day 21, near the failure period, commencing around day 21, before there was a drop-off, indicated by the larger error bars. (n = 15 Control, 21 MCT).

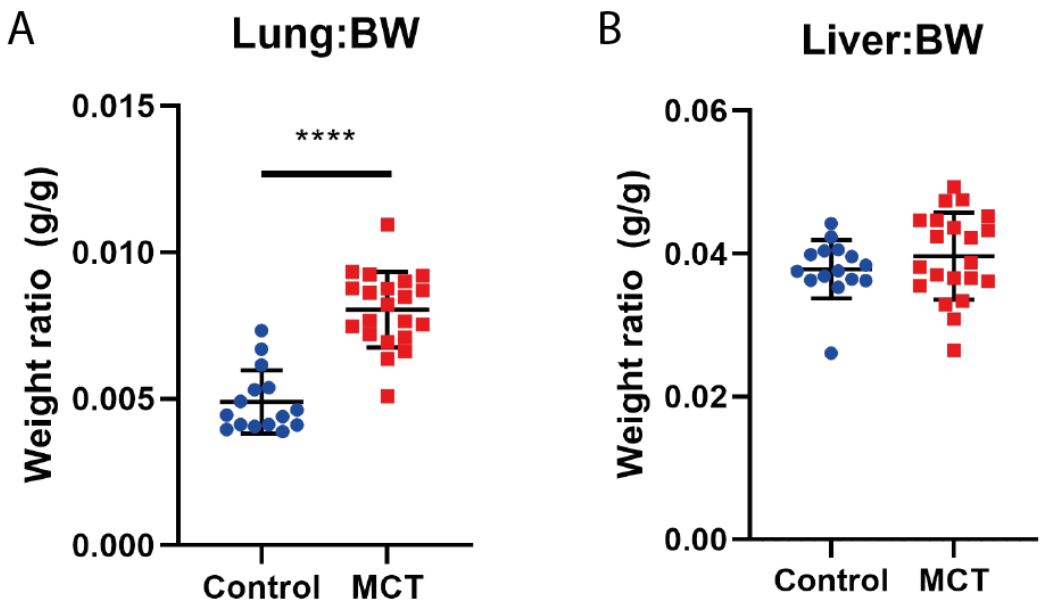

Figure 5-2. Organ weights

At the end-point, the vital organs were dissected and weighed. The mean organ weight (± SD) is presented. (A) MCT lungs were significantly heavier than control ($p < 0.0001$, Mann-Whitney test). (B) The liver weight ratios were not different between the two groups ($p > 0.05$, unpaired t-test). (n = 15 control, 21 MCT).

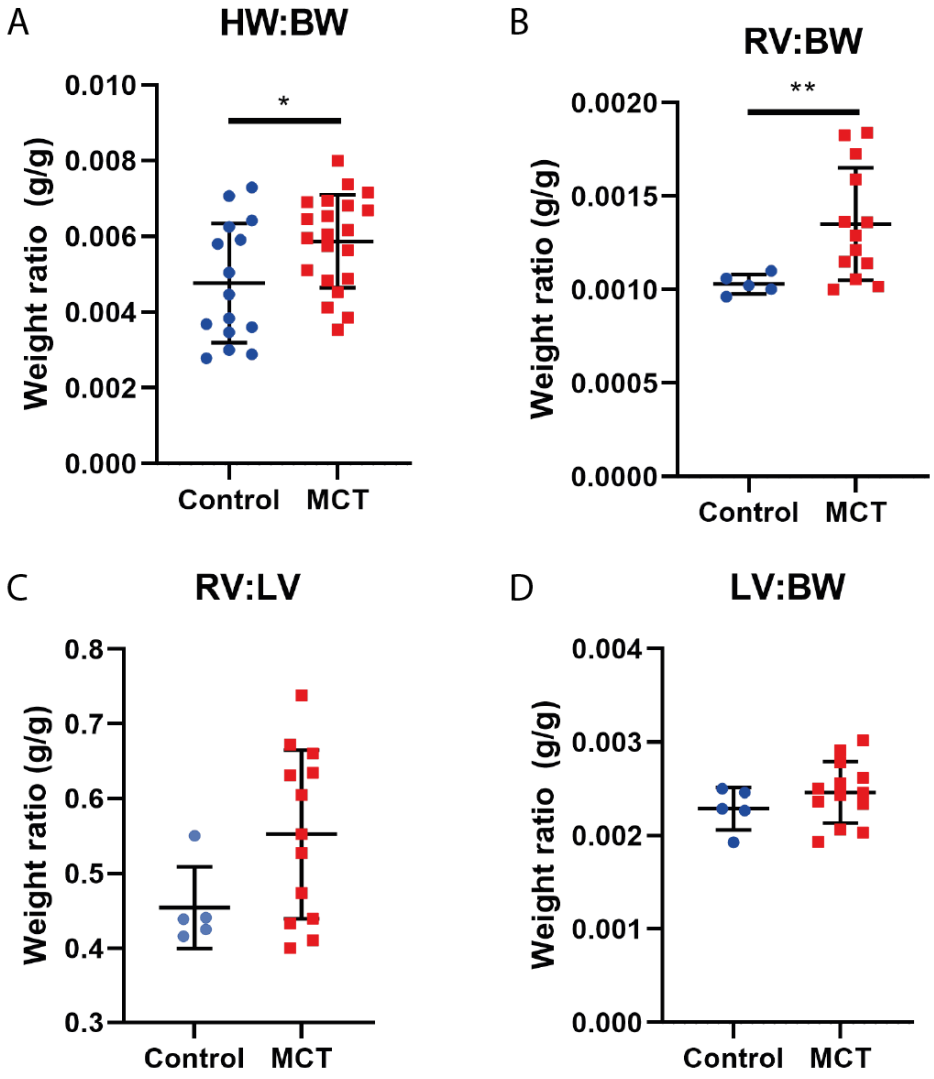

Figure 5-3. Heart and ventricle weights

Weight ratio data are presented as mean ± SD. (A) There was a significant increase in heart weight relative to body weight in MCT ($p = 0.0242$, Unpaired t-test), (B) as well as a significant increase in RV weight relative to body ($p = 0.0024$, Welch's t-test). (C) The RV:LV weight ratio was not significantly different ($p = 0.1433$, Mann-Whitney test). (D) There was no significant difference in the weight of LV relative to body weight ($p = 0.2268$, Welch's t-test). (n = (A,B): 15 control, 21 MCT; (C,D): 5 control, 13 MCT).

5.3.2 Sarcomere length

The SL was determined in MCT-RV cardiomyocytes, given that it was used to calculate the EF and correctly normalise expanded measurements, as well as the implications on cardiomyocyte contractility through the effect of inter-RyR cluster distances on Ca^{2+} propagation (Izu *et al.*, 2006).

The SL was measured (by averaging across 5 sarcomeres) in LV and RV cardiomyocytes of Control and MCT, using images labelled for α-actinin, RyR or t-tubule proteins (Figure 5-4). The SL in Control LV and RV was similar, 1.84 ± 0.08 μm and 1.82 ± 0.09 μm respectively. While the SL was not significantly different in MCT-LV (1.81 ± 0.08 μm), the MCT-RV SL was significantly shorter at 1.73 ± 0.10 μm. This shorter SL was factored in for analyses to ensure the correct EF was calculated and used to normalise distances.

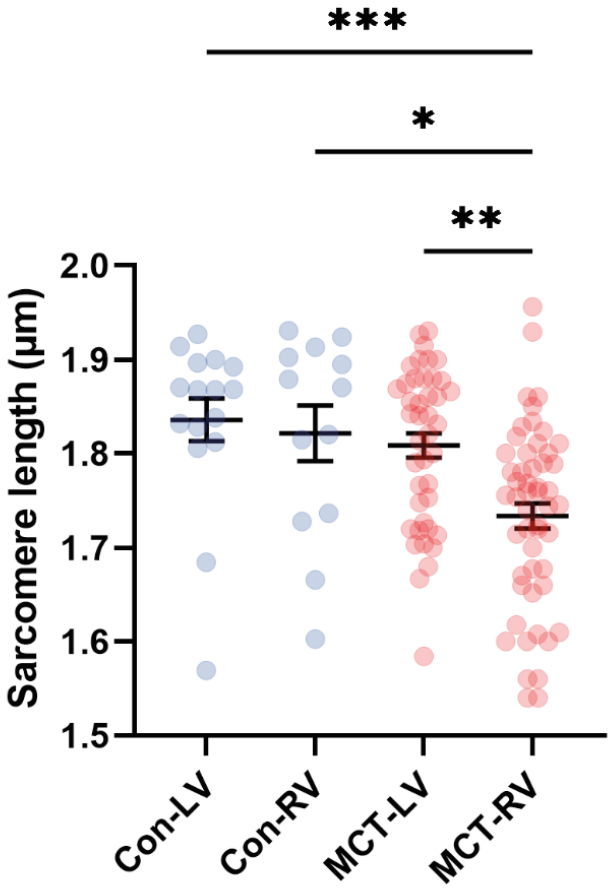

Figure 5-4. Sarcomere length

The sarcomere length was compared between the LV and RV of control and MCT. Con-LV, Con-RV and MCT-LV were not significantly different, while MCT-RV was significantly shorter than all 3 other groups (*$p < 0.05$, **$p < 0.01$, ***$p < 0.001$, Kruskall-Wallis test). (n (cells) = 16 Con-LV, 13 Con-RV, 42 MCT-LV, 52 MCT-RV).

5.3.3 Monocrotaline ryanodine receptor cluster remodelling

Nanoscale RyR cluster remodelling has been documented in a number of different HF conditions (Macquaide *et al.*, 2015; Kolstad *et al.*, 2018), but it is has not yet been investigated in MCT RV HF.

Dual label 10x EExM imaging for RyR and JPH was performed to visualise clusters in isolated cardiomyocytes. RyR clusters in the interior of Con-RV were evenly balanced in terms of numbers of RyR and JPH (Figure 5-5A). Con-RV clusters were elongated and evenly ordered, in relation to the intact t-system. In contrast, MCT-RV clusters appeared to be fragmented into smaller clusters, with more curved shapes. MCT-RV clusters were visually smaller, containing less JPH (Figure 5-5B). Similar remodelling was observed in surface RyR clusters (not shown).

RyR interior cluster size was quantified by implementing the 3D iterative thresholding approach used in Chapter 4. The cluster size in MCT-RV was 8.75 ± 0.73 RyRs, which was around 50% smaller than Con-LV (18.24 ± 2.94 RyRs) ($p = 0.0051$) and was smaller (but not statistically different) than Con-RV (11.68 ± 0.95 RyRs) (Figure 5-6A).

The estimates of RyR density (the number of RyRs/μm^3) followed a similar relationship, whereby MCT-RV (54.93 ± 4.02 RyRs/μm^3) was significantly smaller than Con-LV (80.83 ± 6.57 RyRs/μm^3) ($p = 0.0188$), but was not significantly different to Con-RV (76.31 ± 5.97 RyRs/μm^3) (Figure 5-6B). One observation of note is that the MCT-RV point distribution appeared to be narrower, which could represent a self-selection effect where cell survival after isolation occurs for those with a preserved RyR density.

These density estimates are smaller than previously made with dSTORM (suggesting 134 RyRs/μm^3) (Hou *et al.*, 2015), which is attributable to the increased resolution enabling counts of individual proteins, rather than area-based over-estimations of cluster number. The smaller cluster size and density analyses indicate a fragmenting of interior clusters in MCT-RV, as has been seen in other HF variants (Macquaide *et al.*, 2015).

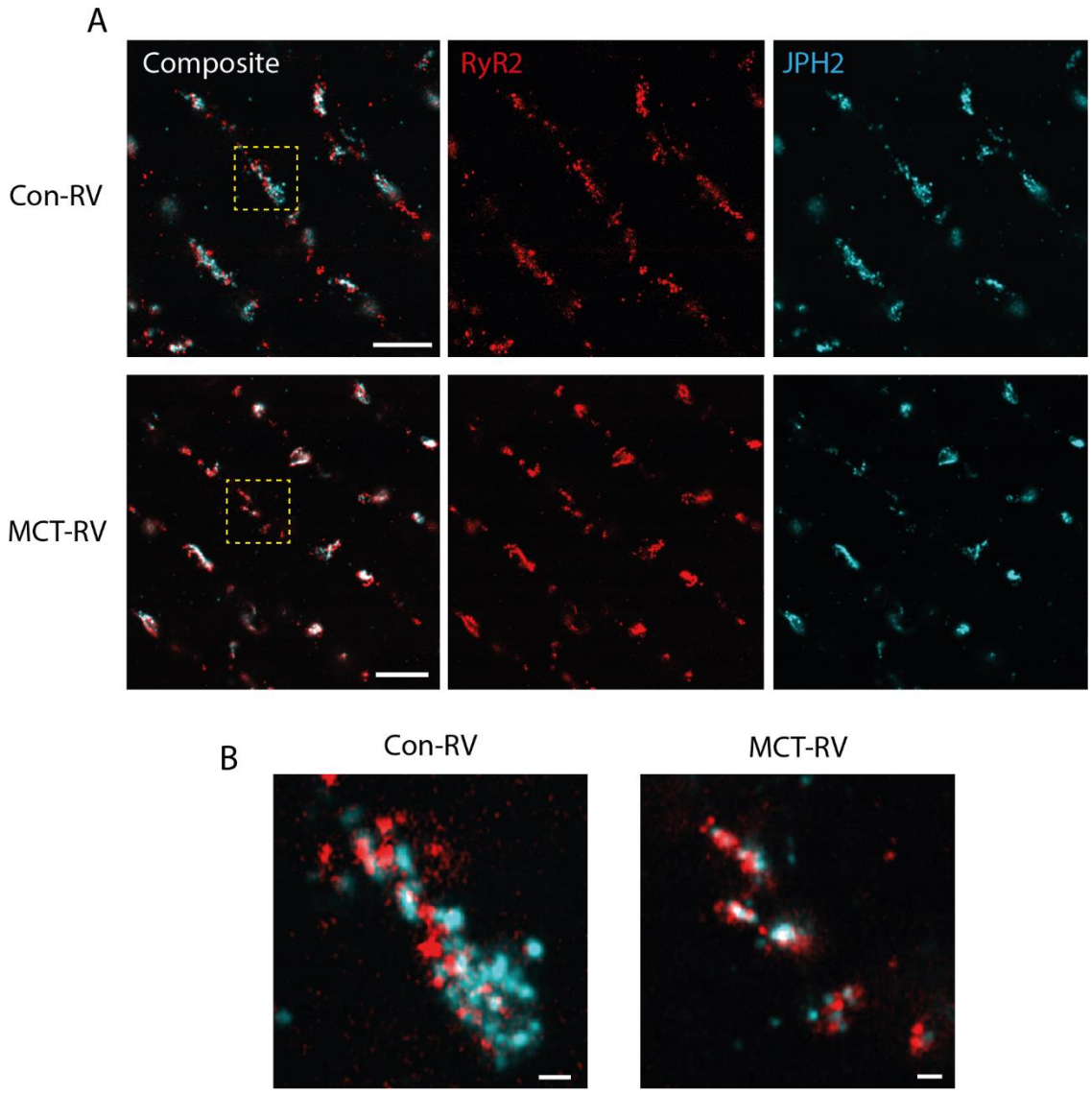

Figure 5-5. MCT cluster remodelling

Pathological remodelling was investigated in images of interior clusters from control (Con-RV) and MCT-RV isolated cardiomyocytes. **(A)** MCT-RV clusters appeared smaller and more fragmented. The MCT-RV clusters were less elongated than Con-RV clusters and were often unusually curved. **(B)** Example individual clusters, indicating the fragmented nature of MCT-RV clusters, containing less JPH. EF = 10. **Scale bars:** A 1 µm, B 100 nm.

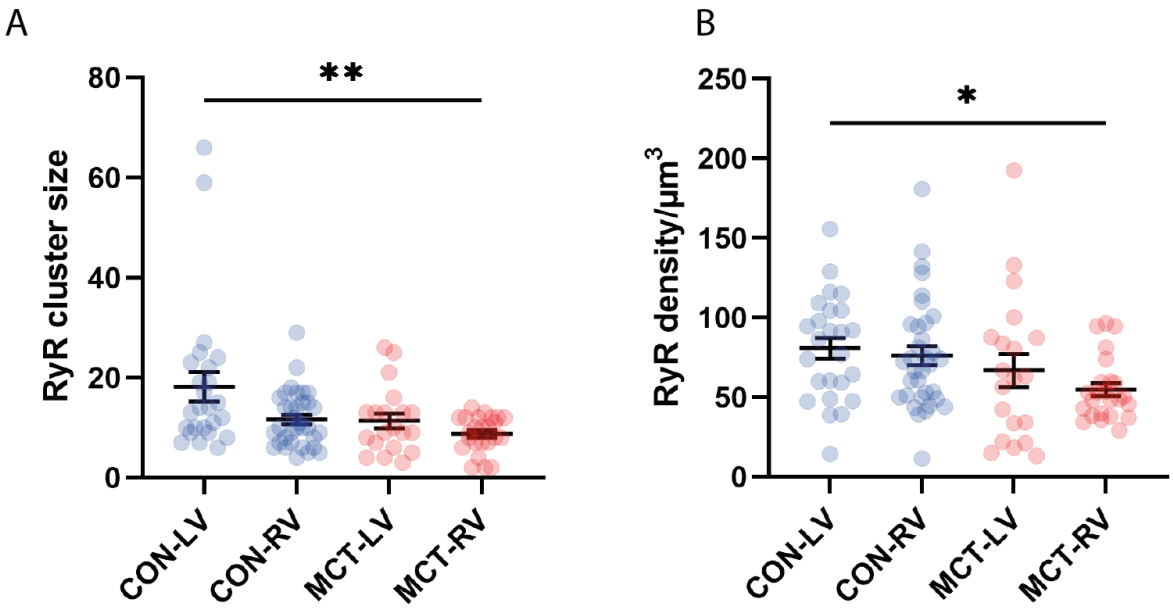

Figure 5-6. RyR remodelling – interior cluster size and density

(A) Dot-plots comparing cluster size distributions reveal that interior MCT-RV clusters were significantly smaller than those in Con-LV ($p = 0.0051$, Kruskall-Wallis). **(B)** The distributions of density per volume (number of RyRs/µm^3) followed a similar relationship. ($p = 0.0188$, Kruskall-Wallis). (n (cells, clusters) = 3,25 Con-LV, 5,34 Con-RV, 7,20 MCT-LV, 3,24 MCT-RV).

To understand the organisation of RyRs with a cluster, the 3D distance analysis as in Chapter 4 was performed. There was a trend for an increased NND in MCT-RV of 128 nm when compared to Con-LV (119 nm), Con-RV (118 nm) and MCT-LV (107 nm), but this was not statistically significant (Figure 5-7A). The frequency distribution shows that MCT-RV NND were shifted to the right compared to Con-LV, indicating a loosening of cluster organisation (Figure 5-7B).

Control NNDs were <100 nm, which was over twice as large as NND reported in 2D surface clusters (with DNA-PAINT and 10x EExM) using the centroid detection analysis approach. This could indicate a different spatial organisation in dyadic clusters, as RyRs are spread over a larger area due to surrounding a t-tubule. Other possibilities are the inclusion of 3D distances in z, or due to biasing for larger clusters.

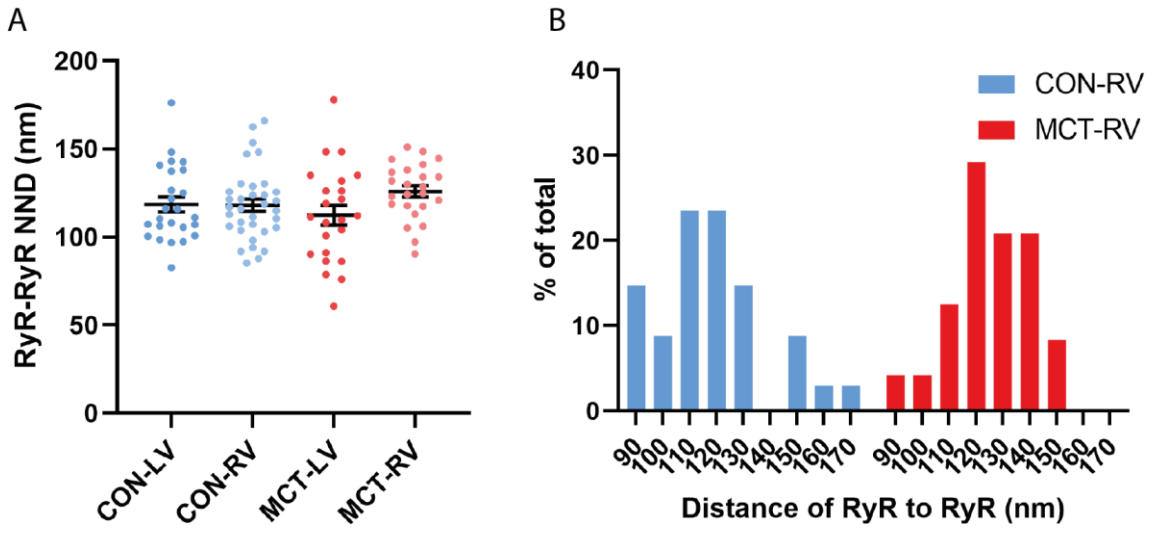

Figure 5-7. RyR remodelling – distance analysis

(A) MCT-RV NND measurements in interior clusters were increased, but there were no significant differences ($p > 0.05$, Kruskall-Wallis). **(B)** Frequency distributions shows the rightward shift in NND in MCT-RV compared to Con-LV. (n (cells, clusters) = 4,25 Con-LV, 5,34 Con-RV, 5,24 MCT-LV, 3,24 MCT-RV).

5.3.4 Junctophilin remodelling

The quantity and organisation of JPH was observed in MCT-RV clusters, to investigate previous findings of reduced JPH expression in MCT RV HF (Xie *et al.*, 2012; Prins *et al.*, 2017). For the following quantification it was assumed that each JPH puncta related to a single JPH molecule, as done in Chapter 4.

The JPH cluster size of 5.88 ± 0.61 in MCT-RV was significantly smaller than in Con-RV (10.65 ± 0.88) ($p = 0.0016$) and Con-LV (16.04 ± 2.44) ($p < 0.0001$) (Figure 5-8A). The density of JPH had a similar relationship, whereby it was reduced in MCT-RV at 35.18 ± 3.83 JPH/μm^3 compared to Con-LV and Con-RV, which were both around 69 JPH/μm^3 ($p < 0.0005$) (Figure 5-8B). There was a trend for a reduction in the ratio of JPH to RyR, whereby it was 0.69 ± 0.05 in MCT-RV compared to 1.01 ± 0.09 in Control, although this was not significantly different ($p = 0.0586$) (Figure 5-9). These results suggest that in the fragmented RyR clusters of MCT-RV, there was an even greater reduction in JPH.

Next, the organisation of JPH in relation to RyR was investigated in MCT-RV. There was no difference in the average distance of JPH to RyR ($p = 0.1236$), suggesting the arrangement of JPH within these clusters was not altered, despite their reduced size (Figure 5-10).

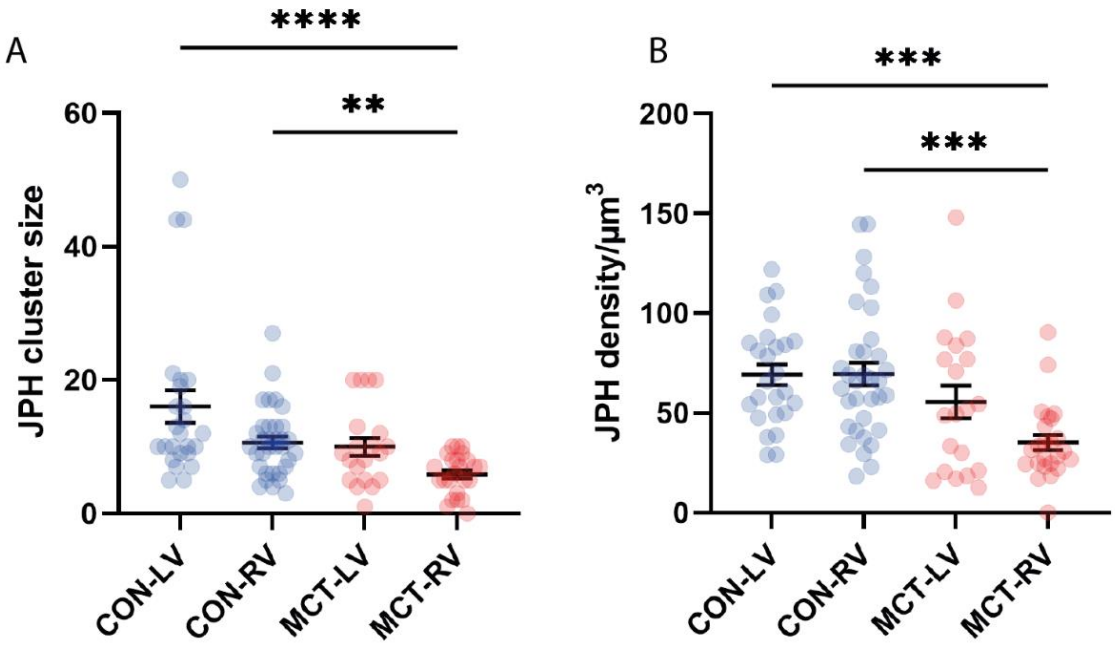

Figure 5-8. JPH remodelling – cluster size and density

(A) JPH cluster size was significantly smaller in MCT-RV than Con-LV and Con-RV. (** $p = 0.0016$, ****$p < 0.0001$, Kruskall-Wallis). **(B)** JPH density was smaller in MCT-RV compared to Con-LV and Con-RV ($p < 0.0005$, Kruskall-Wallis). (n (cells, clusters) = 3,25 Con-LV, 5,34 Con-RV, 7,20 MCT-LV, 3,24 MCT-RV).

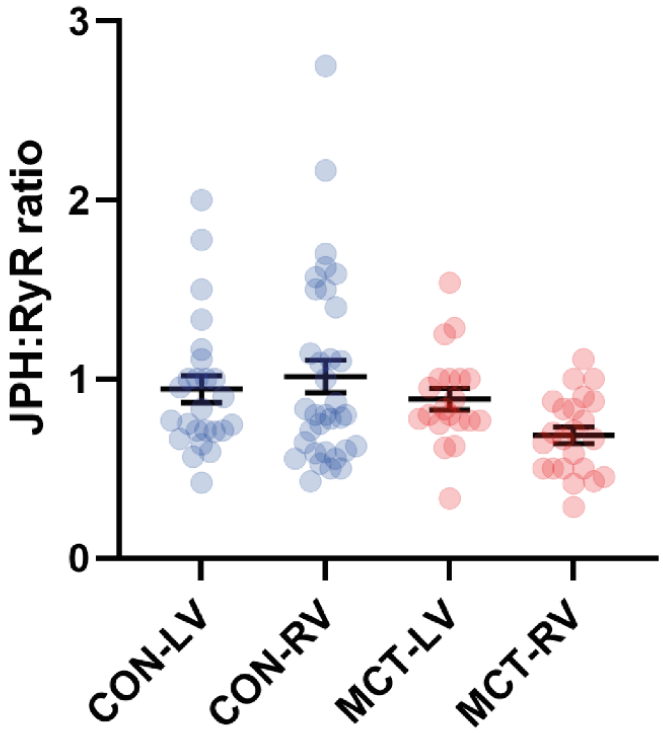

Figure 5-9. JPH remodelling - ratio to RyR

The ratio of JPH to RyR was smaller in MCT-RV, but not significantly different (p = 0.0586, Kruskall-Wallis). (n (cells, clusters) = 3,25 Con-LV, 5,34 Con-RV, 7,20 MCT-LV, 3,24 MCT-RV).

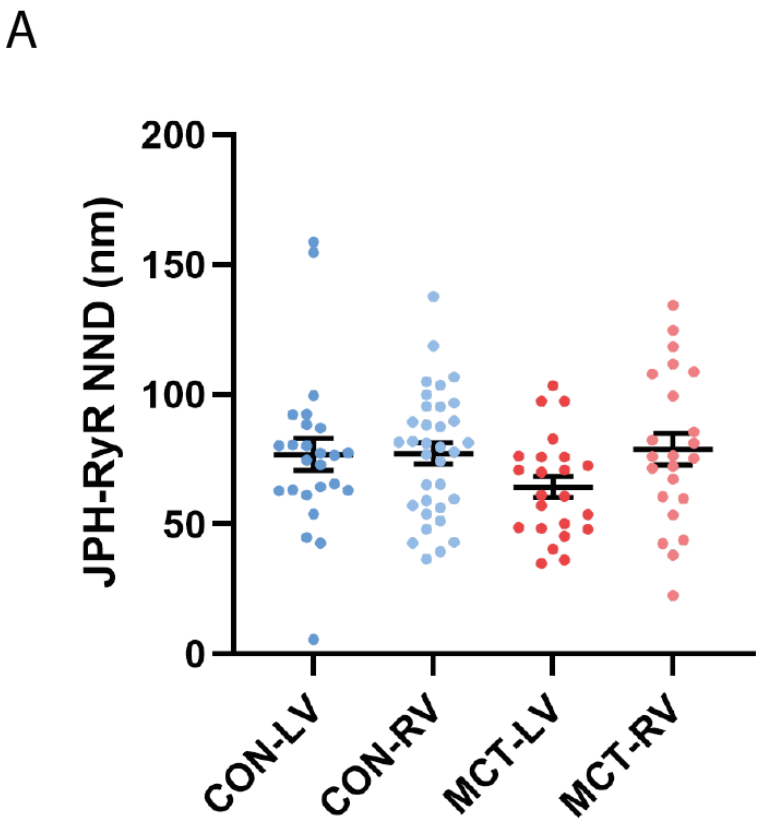

Figure 5-10. JPH remodelling – distance analysis

(A) The NND from JPH to RyR was not different between chambers (p = 0.1236, Kruskall-Wallis). (n (cells, clusters) = 4,25 Con-LV, 5,34 Con-RV, 5,24 MCT-LV, 3,24 MCT-RV).

5.3.5 pSer2808 phosphorylation

Due to the propensity for chronic β-adrenergic stimulation in MCT RV HF, and the corresponding potential impacts to PKA and CaMKII activity, the levels of pSer2808 phosphorylation were investigated in clusters of MCT-RV. The analyses compared MCT-RV cardiomyocytes to Control cardiomyocytes (that were obtained from both the LV and RV).

The density of pSer2808 was visually comparable between Control and MCT-RV, but given the smaller cluster sizes in MCT-RV these appeared to have an increased proportion of pSer2808 to RyR labelling. As in Chapter 4, the fraction of RyRs which were phosphorylated was quantified. In surface clusters, the fractional phosphorylation in MCT-RV was 0.30 ± 0.12 SD, which was no different to 0.31 ± 0.10 in Control (Figure 5-11). In interior clusters, the mean fractional phosphorylation of 0.45 ± 0.07 in MCT-RV was greater than the 0.27 ± 0.09 in Control ($p = 0.022$). This increased fractional phosphorylation in MCT-RV, evident by the right-ward shift in the histogram distribution, was similar to that observed following the β-adrenergic stimulation of Control cardiomyocytes in Chapter 4 (Figure 4-12).

The spatial distribution of phosphorylation was investigated in surface clusters, capitalising on the more straightforward 2D geometry. The analysis determined the density of phosphorylation relating to the distance from the edge of the cluster. In Control, the phosphorylation was uniformly distributed (Figure 5-12), in a manner that was consistent with a random probability simulation (not shown). In cells which had undergone β-adrenergic stimulation the density of phosphorylation was higher than in Control, and the distribution was also uniform. In MCT-RV cells, the pSer2808 phosphorylation density was graded across the cluster, with a higher density in the centre.

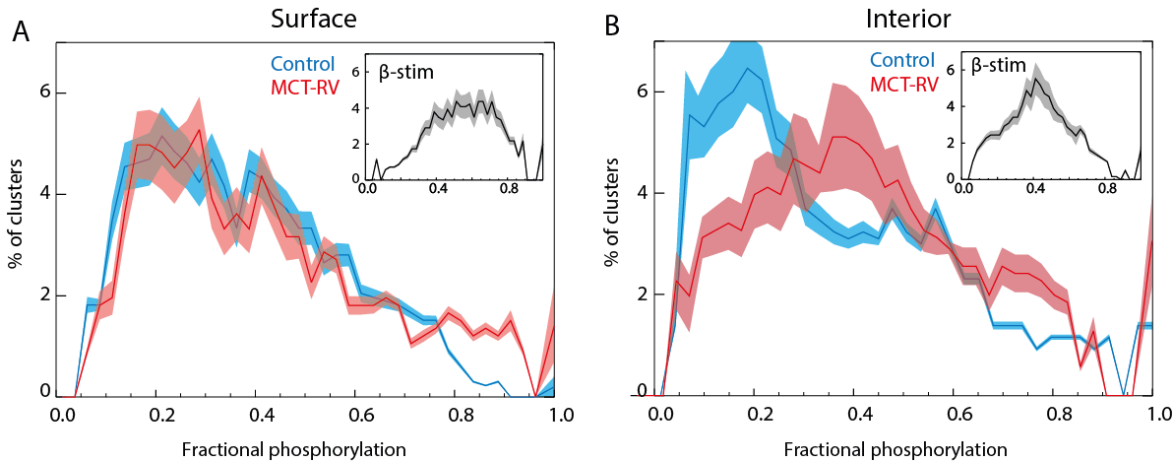

Figure 5-11. pSer2808 fractional phosphorylation

The percentage histograms show the quantified fractional phosphorylation as a percentage of the clusters, with SD plotted as the shaded area. **(A)** In surface clusters, the fraction of phosphorylation was similar between Control (0.31 ± 0.10 SD) and MCT-RV (0.30 ± 0.12) ($p > 0.05$, Mann−Whitney test, Bonferroni-corrected, df = 20). **(B)** In interior clusters, MCT-RV had a slightly increased fractional phosphorylation (0.45 ± 0.07) which was shifted to the right compared to Control (0.27 ± 0.09) ($p = 0.022$, Mann−Whitney test, Bonferroni-corrected, df = 19). This right-shift was like that of Control cells stimulated with isoproterenol and simultaneous electrical pacing at 1 Hz (inset). (n (cells) = 11 Control surface, 11 MCT-RV surface, 9 β-stim surface, 9 Control interior, 12 MCT-RV interior, 8 β-stim interior).

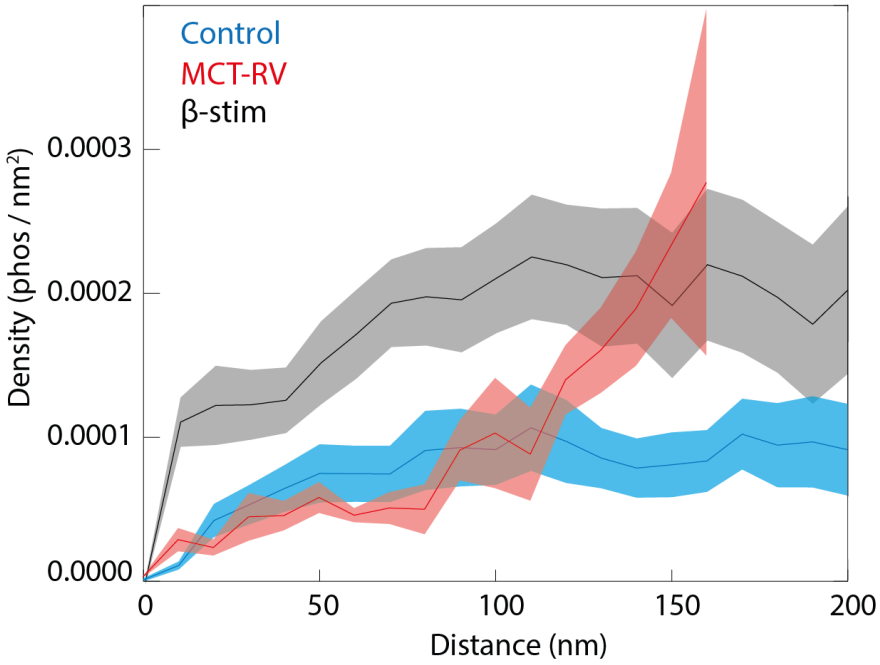

Figure 5-12. Density of pSer2808 phosphorylation in surface cluster

Histogram of pSer2808 density as a function of 2D distance from the cluster boundary, with the SD plotted as the shaded area. The density of phosphorylation in Control (blue) was uniform across the cluster, while MCT-RV (red) phosphorylation was higher towards the centre of the cluster. Stimulated (black) cells had a uniform density of phosphorylation across the cluster, but this level was higher than that in Control. (n (cells) = 11 Control, 11 MCT-RV, 9 β-stim).

5.4 Discussion

5.4.1 Monocrotaline animal model parameters

MCT-induced RV HF is a robust, well-validated animal model, and the traditional hallmarks of the MCT model were observed, including slower weight gain and a plateau prior to the drop-off associated with the onset of RV HF. Pulmonary remodelling, indicated by significantly heavier lungs of MCT animals compared to Control, and RV hypertrophy, suggested by increased RV:BW and RV:LV parameters, both resembled that seen previously (Stones *et al.*, 2013; Benoist *et al.*, 2014; Fowler, Drinkhill, Stones, *et al.*, 2018). The absence of LV hypertrophy (based on ventricle weights) was expected, and coincided with no observed remodelling to RyR or JPH clusters in MCT LV cardiomyocytes.

5.4.2 Remodelling of ryanodine receptor and junctophilin clusters

There are reports of reduced RyR expression in MCT RV HF (Kögler *et al.*, 2003) and reduced JPH expression (Xie *et al.*, 2012), but there are no observations of remodelling to clusters from microscopy studies.

Nanoscale RyR cluster fragmentation was observed in interior clusters of MCT-RV HF, comprising smaller clusters and a reduced density of RyR/μm^3. The fragmentation is consistent with that seen in other branches of HF (Macquaide *et al.*, 2015). Slightly increased inter-RyR distances within a cluster was observed, meaning a less closely packed organisation.

In MCT-RV, there has previously been reported to be an increased frequency of spark production (Fowler, Drinkhill, Norman, *et al.*, 2018), or an increased spark mass (Benoist *et al.*, 2012), associated with increased SR load and ultimately a decrease in Ca^{2+} transient amplitude at the severe stage of HF (Kuramochi *et al.*, 1994). RyR cluster fragmentation could theoretically lead to diminished functional coupling, less positive feedback for CICR, unsynchronised openings, failed spark production and reduced spark amplitude. Computational modelling has shown that reduced RyR density, or the existence of sub-clusters, can lead to slower sparks and increase the variability of their production (Louch *et al.*, 2013). In addition, the remodelling of t-tubules compromises the coupling between LTCCs and RyRs, further affecting the synchronicity of cell-wide Ca^{2+} signalling. Ultimately, the slowed Ca^{2+} release kinetics in MCT-RV result in weakened contraction in late-stage HF.

Typically it is larger, denser clusters which have increased spark fidelity (due to inter-RyR coupling) (Walker *et al.*, 2014), while more dispersed clusters have lower fidelity (Kolstad *et al.*, 2018; Marchena and Echebarria, 2018). The increased frequency of spark production in the fragmented clusters in MCT-RV could be explained by changes to inter-cluster distances, and the concept that groups of closely-positioned clusters can function as one super-cluster (Baddeley *et al.*, 2009; Louch *et al.*, 2013). Indeed, cluster fragmentation has been linked to increased spark frequency (and increased time to peak and duration) by taking into account smaller 'satellite' clusters which neighbour a larger cluster (Macquaide *et al.*, 2015). These smaller clusters may underlie repetitive spark sites, and enable inter-cluster activation which encourages the generation of waves. Smaller clusters have also been shown to enhance SR leak, another pro-arrhythmic mechanism (Kolstad *et al.*, 2018).

The increased spark frequency in MCT-RV could also arise due to changes in regulation of individual RyR channels, or the high SR load. Interestingly, SR load alone does not completely account for the increase in fractional SR release or leak, evidenced by the fact that hypertrophied myocytes (an intermediate between control and failing) possessed these changes without an increase in SR load (Benoist *et al.*, 2012). The reduction in JPH could contribute to lost regulation of RyR (through a lost stabilising effect) and exacerbate leak (Beavers *et al.*, 2013; Wang *et al.*, 2014). Given that JPH is critical for maintaining the connection between the SR and sarcolemma, loss of JPH could loosen the dyadic space, meaning that Ca^{2+} cannot build up as it would normally, consequently affecting spark rate and leak (Walker *et al.*, 2014).

JPH remodelling is thought to be a causal component enhancing disease progression (van Oort *et al.*, 2011). A ~50% reduction in JPH cluster size and density was observed, with a reduction in the ratio of JPH to RyR which suggested a greater loss of JPH compared to RyR in dyads. This could be due to reduced expression, or detaching from the SR and remaining attached to the remodelled t-tubule membrane. JPH remodelling correlates with t-tubule remodelling (Wei *et al.*, 2010), a hallmark which has been shown in MCT-RV previously (Prins *et al.*, 2017) and was observed in cardiomyocytes used in this study (confocal data not shown). JPH remodelling could account for the remodelling of RyR clusters (Munro *et al.*, 2016), but it is difficult to infer whether cluster remodelling occurs as a direct consequence of t-tubule remodelling, or occurs independently.

The known mechanisms for loss of JPH include calpain-mediated cleavage (Guo *et al.*, 2015; Lahiri *et al.*, 2020), defects in microtubule-mediated trafficking (Zhang *et al.*, 2014) and

microRNA-24 regulation (Xu *et al.*, 2012; R. C. Li *et al.*, 2013). Microtubule densification has been observed in MCT-RV and directly correlated with JPH remodelling (Prins *et al.*, 2017). JPH expression in that study was restored by the microtubule depolymeriser colchicine, with a consequent improvement to t-tubule architecture, indicating a direct mechanistic link.

5.4.3 Increased pSer2808 phosphorylation

Increased pSer2808 fractional phosphorylation was observed in interior clusters of MCT-RV, akin to hyper-phosphorylation observed in other branches of HF (Marx *et al.*, 2000). Few clusters possessed maximal or minimal phosphorylation, which are the scenarios expected to lead to unique channel behaviours with the highest RyR activities. Any phosphorylation-induced change in RyR excitability will exacerbate the spark fidelity of a cluster, adding to the effects of the modified geometry and altered inter-cluster distances as mentioned before, as well as the increased SR load incurred by the effects of sympathetic activity on PLB and LTCC (Houser, 2014). The observation of increased phosphorylation may relate to changes in the activity of PDEs and phosphatases, which have yet to be explored in MCT-RV HF. The altered RyR phosphorylation could be a compensatory mechanism to normalise spark fidelity following changes to cluster morphology and lost regulation by reduced JPH. The implications of an increased pSer2808 phosphorylation on RyR activity will also depend on the interplay of other phosphorylation sites which could counteract this change.

It is difficult to determine whether the phosphorylation change occurs as a direct consequence of spatial cluster remodelling and reduction in JPH. Another component linked to regulating RyR phosphorylation is the membrane scaffolding protein called bridging integrator 1 (BIN1), which helps to form membrane folds (Hong *et al.*, 2014),. The interaction of BIN1 with RyR is increased after pSer2808 phosphorylation (Fu *et al.*, 2016). In addition, when BIN1 is reduced in human HF it correlated with a lost organisation of pSer2808, implicating BIN1-based alterations of phosphorylation in disease progression (Fu *et al.*, 2016).

A shorter SL was observed in MCT-RV compared to Con-RV, Con-LV and MCT-LV, which lines up with that published previously (Stones *et al.*, 2013; Fowler *et al.*, 2015). The shorter SL in MCT-RV has implications on Ca^{2+} signalling, potentially leading to move waves due to easier Ca^{2+} propagation between sarcomeres (Izu *et al.*, 2006). Interestingly, shortened SL and increased pSer2808 phosphorylation has been observed in spontaneously hypertensive rats previously (Chen-Izu *et al.*, 2007).

In control cardiomyocytes which underwent β-adrenergic stimulation, the increased phosphorylation was observed in both surface and interior clusters. The observation of an interior-only phosphorylation increase in MCT-RV may indicate a broader change in β-adrenergic signalling in RV HF. Although the MCT-RV surface clusters did not appear different in terms of the absolute fraction of phosphorylation, there was a redistribution of the density of phosphorylation towards the cluster centre. This could result from structural remodelling, such as an unravelling of the cluster from the membrane allowing spatial redistribution of PKA or phosphatase activity.

Despite noting increased phosphorylation in MCT-RV, it is not possible to determine if this is saturated. It would be interesting to perform future experiments to explore whether MCT-RV cluster phosphorylation can be increased using the β-adrenergic stimulation protocol.

Descriptions of the changes to other phosphorylation sites, including pSer2814 and pSer2030 (particularly given the potentially greater importance of these sites), as well as other components regulating RyR activity, are needed to better understand the pathological landscape in MCT-RV. In addition, nuanced correlative experiments which directly link spark activity to the underlying cluster geometry and phosphorylation level would be desirable to better understand both the structure-function relationships of RyR clusters as well as the importance of post-translational modifications to channel activity.

A significant limitation relating to this analysis is that pSer2808 phosphorylation in MCT RV cardiomyocytes was compared to that of a mixed population of LV and RV from Control cardiomyocytes. Evidently, making such a comparison is not ideal, given the potential for inter-ventricle differences in phosphorylation, and the relative size of the ventricles which would favour LV rather than RV. Given this consideration, it is possible that differences in phosphorylation between Control and MCT-RV observed here could result from ventricle differences, as opposed to that incurred by the MCT pathology.

5.5 Concluding remarks

This chapter has characterised several aspects of pathological remodelling in the MCT model of RV HF. The absolute patterns of individual RyRs within MCT-RV interior clusters has been observed, revealing pathological fragmentation, with fewer RyR and JPH per cluster, which recapitulated observations of reduced expression of these targets. These observations are the first of compromised arrangement of individual proteins in HF, as other studies observing

changes with STORM and STED only observed changes to the outlines of clusters (Macquaide *et al.*, 2015; Kolstad *et al.*, 2018).

Increased pSer2808 phosphorylation was seen in MCT-RV interior clusters, which was like that observed under experimentally-induced β-adrenergic stimulation. While there was no increase in fractional phosphorylation in surface clusters, the distribution of phosphorylation was different, with higher density located at the centre of the cluster.

These new observations help to detail some of the pathological traits involved in MCT-induced RV HF which could account for the Ca^{2+} homeostasis dysfunction at the cellular level. The findings from this research will need to be placed into the wider pathogenesis of MCT-RV, including changes to electrical activity, adrenergic receptor expression, metabolism and fibrosis.

Chapter 6. Characterising structural maturity of stem cell-derived cardiomyocytes

6.1 Introduction

SC-CMs offer a powerful *ex vivo* tool to study cardiac physiology and pathology (Moretti *et al.*, 2010; Davis *et al.*, 2021), and have been used in therapeutic areas of research including drug discovery (Cohen *et al.*, 2011; Archer *et al.*, 2018) and transplantation to impart paracrine effects for regeneration (Baraniak and McDevitt, 2010) or replace lost tissue (Liu *et al.*, 2018; Ronaldson-Bouchard *et al.*, 2018; Murphy *et al.*, 2019). SC-CMs are structurally and functionally immature in comparison to adult cardiomyocytes (Satin *et al.*, 2008; Lieu *et al.*, 2009). It is important to characterise SC-CM maturity to better infer how observations in SC-CMs will translate to adult cardiomyocytes.

SC-CMs also offer a window to study the development of CRUs prior to the appearance of t-tubules. In both eCSC-CMs and iPSC-CMs, there is a relatively poor understanding of the organisation of CRUs, with no information of the nanoscale arrangement of RyR and JPH. Further, given the similarities in morphology to failing cells, by studying the SC-CM Ca^{2+}-handling structures it is possible to gain insight into mechanisms of dysfunction.

The aim of this chapter was to characterise the structural maturity of two types of SC-CMs, eCSC-CMs and iPSC-CMs. It was of interest to describe the arrangement of contractile machinery, Ca^{2+} stores and membranes, and to understand the timeline of CRU development and the involvement of JPH.

6.2 Methods

6.2.1 eCSC-CMs

Rat eCSCs were used which had already been isolated, characterised and maintained in culture, obtained according to the previously published technique (Smith *et al.*, 2014). In brief, c-kit-positive, CD45-negative eCSCs were isolated from whole rat hearts following enzymatic digestion and magnetic activated cell sorting. The purity of eCSCs was confirmed by flow cytometry.

eCSCs were maintained on 1.5% gelatin coated plates, in growth medium (45% Neurobasal medium, 45% DMEM-F12 Ham's, 10% embryonic stem cell–qualified FBS, 2% B27 supplement, 1% N2 supplement, 1% insulin-transferrin-selenium, 1% penicillin/streptomycin (P/S), 0.1% gentamicin, 0.1% fungizone, 10 ng/ml leukaemia inhibitory factor (LIF), 20 ng/ml epidermal growth factor, 10 ng/ml basal fibroblast growth factor), at 37°C in 5% CO_2. eCSCs were passaged using trypsin upon reaching ~80% confluency to prevent contact-induced differentiation.

To elicit differentiation to cardiomyocytes, eCSCs were primed by adding 100 nM oxytocin to growth medium for 72 hours. Next, 5000 eCSCs were transferred to a Lumox dish and cultured in LIF-deprived growth medium for 4 days, allowing the formation of cardiospheres (primitive clusters of eCSCs). Cardiospheres were deposited onto laminin-coated coverslips in differentiation medium (α-modified Eagle's minimum essential medium, 2% foetal calf serum, 1 μM dexamethasone, 50 μg/ml ascorbic acid, 100nM oxytocin acetate, 10 mM β-glycerophosphate, 1% P/S, 0.1% gentamicin, 0.1% fungizone. On days 1-4, differentiation medium also contained 10 ng/ml BMP-2, 10 ng/ml BMP-4 and 5 ng/ml TGF-β1. From day 5 onwards, BMPs and TGF-β1 were removed and replaced with 150 ng/ml Dkk-1 (Wnt inhibitor), fresh medium being added every 3 days. At the desired timepoint, cells were fixed in 2% PFA in PBS at RT for 10 minutes.

6.2.2 iPSC-CMs

Cryofrozen iCell Cardiomyocytes (Cellular Dynamics International), were thawed and plated onto coverslips coated with 0.1% gelatin, at a plating density of $6.3x10^4$ cells/cm^2. iPSC-CMs were cultured in iCell Cardiomyocyte Maintenance Medium at 37°C, in 5% CO_2. At various timepoints (Day2, Day4, Day7, Day14), iPSC-CMs were fixed in 2% PFA in PBS at RT for 10 minutes.

6.2.3 Imaging

At Day 7, a live cell experiment was performed in iPSC-CMs with ER-Tracker Green. The cells were pre-incubated with 1 μM ER-Tracker Green in Hank's balanced salt solution (with Ca^{2+} and Mg^{2+}) for 20 minutes at 37°C. The dye was then washed off with fresh Hank's salt solution prior to imaging.

Fixed SC-CM samples were immunolabelled with antibodies as detailed in Section 2.2. proExM or X10 expansion microscopy were performed as outlined in Section 2.3. The samples were then imaged as in Section 2.4.

dSTORM experiments were performed using anti-mouse IgG conjugates of Alexa Fluor 680, mounted in a switching buffer containing 90% glycerol and 20 mM cysteamine (Sigma) in PBS. Widefield fluorescence imaging was done on a Nikon eclipse TE2000-U inverted microscope with a 60x oil objective (pixel size = 0.1 µm), with an Andor Zyla sCMOS camera. Illumination was achieved with a Viasho red laser (671 nm), in an oblique light sheet setup with HILO (Tokunaga *et al.*, 2008) . The intensity was adjusted to optimize event activity versus decay. The area of interest was pre-bleached prior to image series acquisition at 50 ms per frame, and a threshold was set up for event detection. Images were acquired until the event activity dropped. Following drift correction using piecewise linear methods (a built-in algorithm within PYME), a jittered triangulation image was produced (pixel size 5 nm). Cluster analysis was achieved by applying a 0.8 threshold within PYME visualise, generating a mask and analysing particles (low threshold 1 RyR = 0.0009 μm^2) using Fiji.

6.3 Results

6.3.1 Structural maturity of eCSC-CMs

The structural maturity of Day18 eCSC-CMs was assessed with confocal microscopy. The z-disc protein α-actinin was distributed longitudinally along the axis of the cell (Figure 6-1A), in contrast to the typical striations (parallel to cell length) seen in adult cardiomyocytes. The longitudinal aggregations at the periphery are presumed to be stress fibres involved in attachment to the substrate. The lack of contractile organisation, highlighted by the absence of sarcomeric z-discs, indicates a primitive morphology, whereby the myofibrils are likely to be somewhat disorganised.

Next, the presence of intracellular membranes was investigated to identify progenitor t-tubules. The caveolar protein Cav3 was used as a marker for membrane structures. Cav3 staining was slightly denser in the perinuclear region but revealed no strongly ordered patterns in the cytoplasm, indicating a lack of progenitor t-tubules (Figure 6-1B).

The extent of CRU development was then assessed. RyR2 labelling was not striated as in the adult cardiomyocyte phenotype, but there was evidence of clustering, with an increased density surrounding the nucleus (Figure 6-1C). The anchoring protein JPH was distributed in small clusters in the cytoplasm, in a similar fashion to the RyR clustering pattern (Figure 6-1D).

The SR distribution was examined by labelling the Ca^{2+} pump protein SERCA, which is reported to be substantially expressed in human embryonic and fetal cardiomyocytes (Kong *et al.*, 2010). SERCA labelling was distributed evenly across the cell. The absence of a pattern suggests that at this timepoint there was minimal regional distribution and limited formation into clusters (Figure 6-1E).

To conclude, eCSC-CMs are structurally immature compared to the adult cardiomyocyte, typified by the absence of sarcomeres and t-tubules, and thus represent an early point in cardiomyocyte development. The organisation of Ca^{2+}-handling structures was similarly immature, which correlates with the lack of order in the contractile machinery.

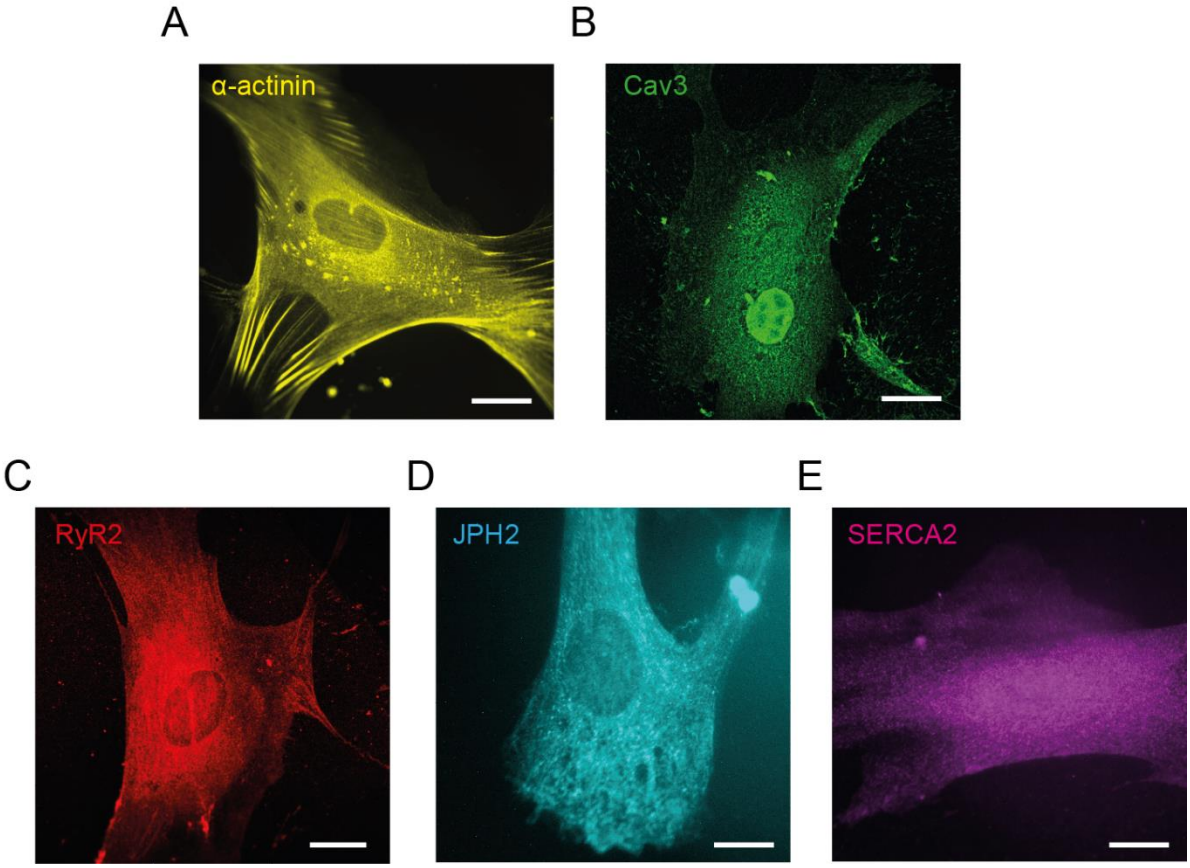

Figure 6-1. eCSC-CM structural maturity

The structural maturity of eCSC-CMs was investigated by confocal imaging. **(A)** The z-disc protein α-actinin had no sarcomeric organisation and was instead arranged into fibres at the periphery. **(B)** The membrane marker Cav3 was denser in the perinuclear region, but suggested an absence of t-tubules. **(C)** RyR labelling was not striated, but formed small clusters that were denser in the perinuclear region. **(D)** JPH formed small clusters on a similar scale to RyR, with no striations visible. **(E)** SERCA had no pattern of staining, consequent with an even cytoplasmic distribution. **Scale bars:** 30 µm.

6.3.2 Structural maturity of iPSC-CMs

The structural maturity of iPSC-CMs at Day4 was evaluated. α-actinin labelling had a regular periodicity resembling that seen in adult z-discs, indicating a moderate degree of maturity of the contractile machinery (Figure 6-2A). The striations were aligned in different directions and were often curved in cells with a rounder morphology. dSTORM imaging revealed aggregations of small α-actinin clusters, which were often ordered into fragmented rows (Figure 6-2B). In addition to the typical transverse z-line striations, some perpendicular bridges of α-actinin also stretched longitudinally, between adjacent z-discs.

Next it was determined whether there were any membrane structures that could be t-tubule precursors. There were no distinct patterns of Cav3 staining within the cytoplasm (Figure 6-3A), suggesting that t-tubules were absent at this timepoint. In addition, dystrophin (a t-tubule component in adult) formed linear streaks at the cell periphery (Figure 6-3B), which resembled the α-actinin pattern seen in eCSC-CM. These observations together confirm the lack of t-tubules, which agrees with literature for iPSC-CMs that have been maintained in culture for relatively short periods of time (Lundy *et al.*, 2013).

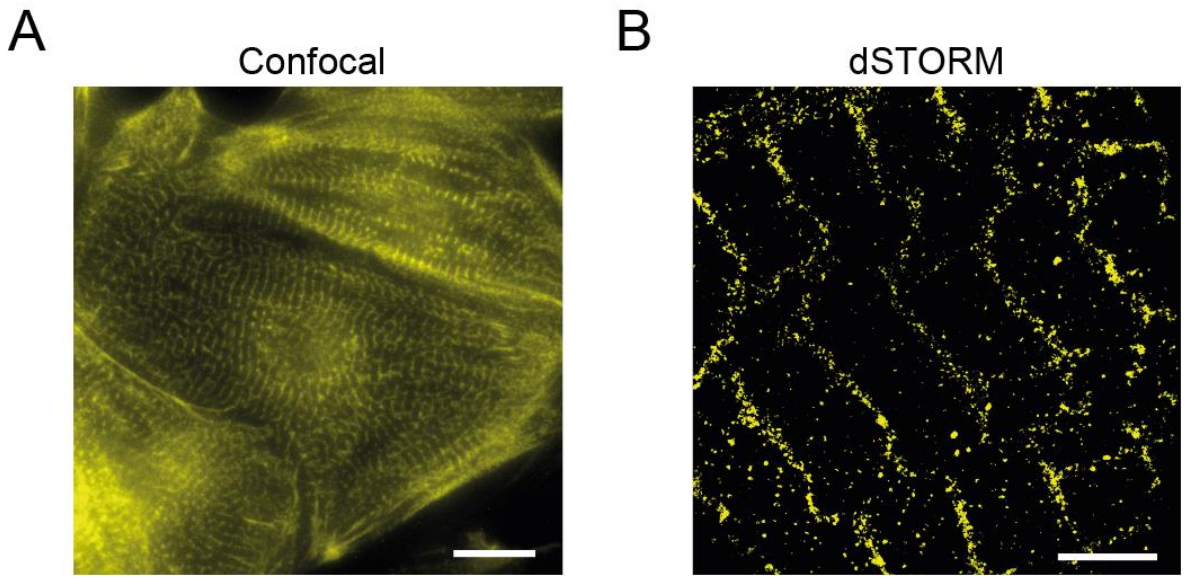

Figure 6-2. iPSC-CM sarcomeric organisation

To investigate the maturity of the contractile machinery, Day4 iPSC-CMs were labelled for the z-disc protein α-actinin. **(A)** Confocal imaging revealed a striated appearance, indicating well-organised sarcomeres. The sarcomeres were not all in the same orientation. **(B)** dSTORM confirmed aggregations of α-actinin proteins into z-discs. Some elements were oriented perpendicular to the typical sarcomeric direction, connecting adjacent z-discs. **Scale bars:** A 20 µm, B 2 µm.

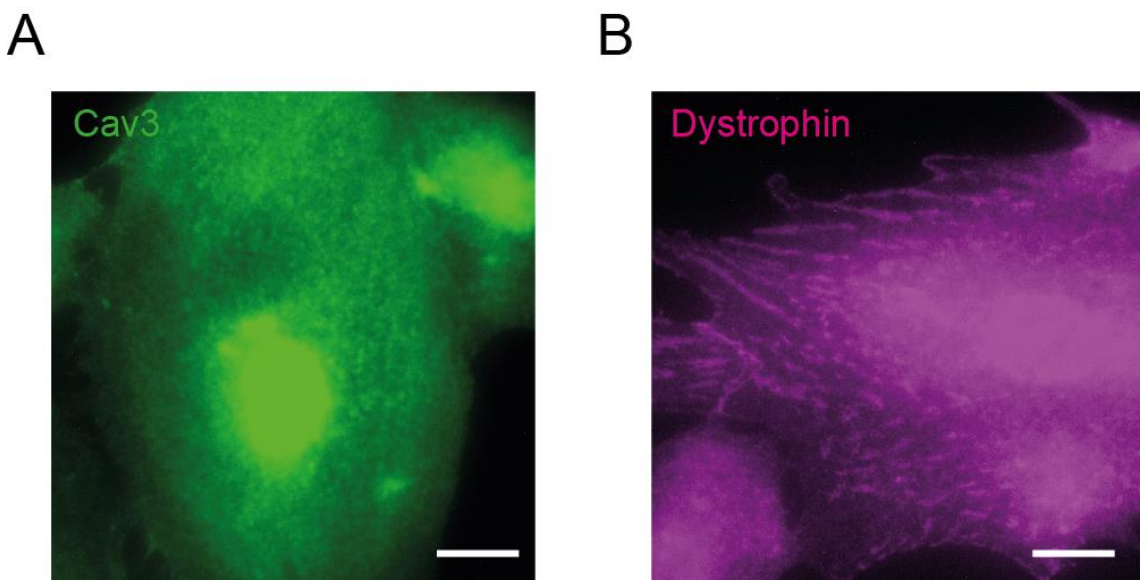

Figure 6-3. iPSC-CM membrane proteins

To investigate the presence of precursor t-tubule structures, Day4 iPSC-CMs were labelled for proteins which are common in the adult t-system, and imaged with widefield. **(A)** Cav3 was distributed evenly in the cytoplasm and **(B)** dystrophin labelled longitudinal elements, which are likely to be stress fibres involved with substrate attachment. These observations suggest no t-tubule structures have developed. **Scale bars:** 20 µm.

6.3.3 iPSC-CM calcium release units

Having observed relative maturity of contractile machinery, but a lack of t-tubules, the extent of CRU organisation was then investigated. Confocal imaging was performed at three timepoints (Day2, Day4 and Day7), to investigate the development of CRUs. At all timepoints, RyR labelling throughout the cytoplasm was punctate, which is indicative of clustering (Figure 6-4A). There was a significant overlap of RyR and JPH labelling, visible as white in the composite images. At the earliest timepoint at Day2, clusters were concentrated in the perinuclear region and did not appear to correlate with the striated organisation of z-discs. By Day4, some striations of RyR were visible without corresponding striations of JPH labelling. In the latest timepoint at Day7, more striated RyR regions were visible, but again without JPH striations.

4x EExM was used to visualise the clustering pattern in CRUs of Day7 iPSC-CMs with improved resolution (Figure 6-4B). The EF in these samples approached 5x, in some places providing sufficient resolution to visualise individual proteins within clusters. The co-clustering of RyR and JPH observed in confocal was confirmed at higher resolution at the cell surface. In the interior, RyR clusters in striations were once again visible without corresponding JPH.

dSTORM was performed to enable a direct comparison with 4x EExM imaging. dSTORM and 4x EExM images from Day4 samples were qualitatively similar (Figure 6-5A), in that both could almost resolve individual proteins. Cluster size was assessed using an area-based analysis, using the assumption that an RyR occupies 900 nm^2, or 0.0009 μm^2. The cluster size distribution in Day4 iPSC-CMs is comparable to that of adult cardiomyocytes, with most clusters possessing less than 10 RyRs (Figure 6-5B). The distributions of cluster size (inset) in Day4 iPSC-CMs, as measured with 4x EExM and dSTORM, were similar. For Day4, the average area of RyR clusters with 4x EExM was 0.006 μm^2, representing a cluster size of 7.14 ± 0.68, which was comparable to the dSTORM average of 6.66 ± 0.25 RyRs per cluster. The average cluster size was larger at Day 7, with 11.85 ± 1.21 RyRs per cluster.

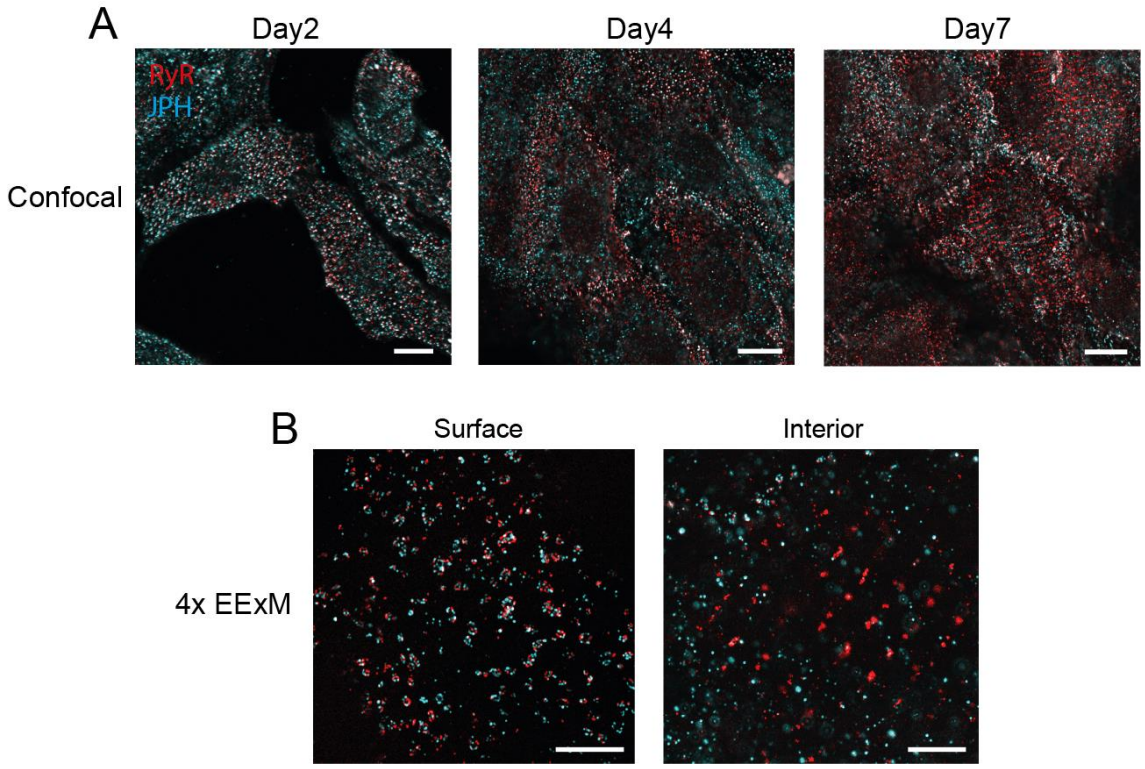

Figure 6-4. iPSC-CM CRU organisation

(A) iPSC-CMs fixed at various timepoints (Day2, Day4 and Day7) were imaged with confocal microscopy to explore development of CRUs. Clustering of RyR was visible even at the earliest Day2 timepoint, which colocalised with JPH. By Day4 there were small regions of striated RyR labelling, while JPH was not striated. At Day7, the striated organisation of RyR was more widespread, once again without corresponding JPH striations. **(B)** 4x EExM of Day7 iPSC-CMs revealed the co-clustering of RyR and JPH. At the surface, RyR and JPH were arranged into small, round clusters, while in the interior RyR clusters began to align in striations, without JPH. EF = 4. **Scale bars:** A 10 µm, B 2.5 µm.

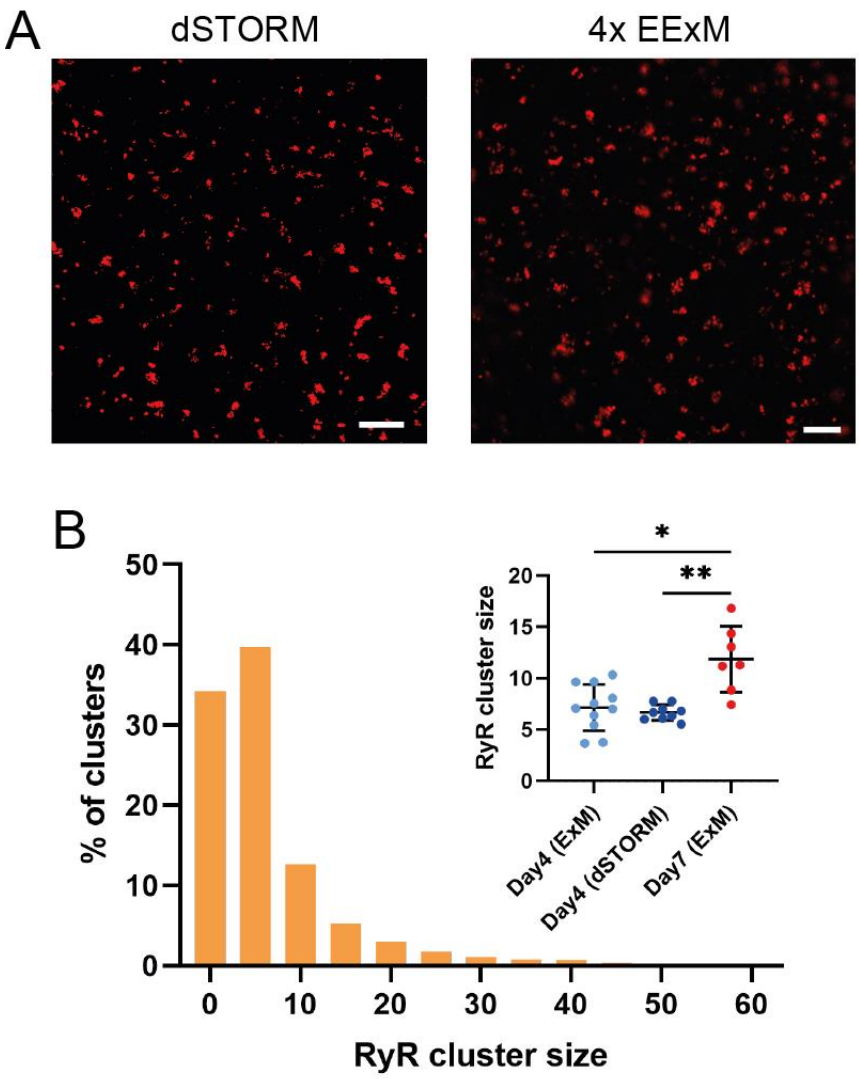

Figure 6-5. iPSC-CM RyR cluster size

(A) RyR surface clusters from Day4 iPSC-CMs were imaged with dSTORM and 4x EExM and were qualitatively similar. **(B)** Histogram of RyR cluster size in Day4 iPSC-CMs, as determined with 4x EExM, shows that the majority (75%) of clusters are smaller than 10 RyRs in size. The inset shows the distributions of cluster size in Day4 as measured by 4x EExM and dSTORM, which were similar. The cluster size in Day7 was larger than Day4 (Kruskall-Wallis test *P<0.05, **P<0.005). (n (cells, clusters) = 11, 4135 Day4 ExM; 9, 2620 Day4 dSTORM; 7,4609 Day7 EExM.) EF = 4. **Scale bars:** 1 µm.

6.3.4 iPSC-CM reticular network

Next, the organisation of the SR network was investigated in relation to RyR clusters. The distribution of various SR and ER proteins was observed in Day4 iPSC-CMs using confocal and 4x EExM. The SR is a specialised (smooth) form of endoplasmic reticulum (ER), but it is not known whether the ER is continuous with the SR or a structurally independent compartment (Michalak and Opas, 2009), although ER-resident proteins have been observed in the SR.

SERCA reportedly has lower gene expression levels in iPSC-CMs compared to adult heart tissue (Rao *et al.*, 2013). The SR Ca^{2+} pump SERCA was distributed throughout the cytoplasm, both in the perinuclear region and out at the periphery, in a continuous web-like network (Figure 6-6A). The best imaging plane for SERCA was slightly above the plane in which surface RyR clusters appeared, which is intuitive given their localisation on the fSR which is positioned further away from the sarcolemma, but could relate to spectral shifts in the z-plane in these datasets. At the higher plane of imaging where SERCA distribution was clearer, RyR clusters were mostly located at the cell periphery. Consequently, the visible colocalisation of SERCA and RyR was relatively low.

Next, the distribution of calnexin was observed, which is an integral, membrane-bound ER chaperone involved in protein folding, which aims to retain unfolded glycoproteins. In contrast to SERCA labelling, calnexin was distributed more sparsely throughout the cytoplasm in smaller curved structures, and visible colocalisation of calnexin and RyR was low (Figure 6-6B).

Next, KDEL was immunolabelled, which is a sequence on soluble ER-resident proteins that is recognised by the KDEL receptor, allowing shuttling of the proteins in vesicles between the ER and cis-golgi. KDEL labelling was slightly denser in the perinuclear region, and was more sparsely distributed compared to SERCA (Figure 6-6C). Once again, colocalisation with RyR was poor.

To observe the full extent of the ER, live cell imaging was performed using ER-Tracker Green, which binds to sulphonylurea receptors. Using ER-Tracker in living cells at timepoint Day7, the labelling was smoother and more continuous than the immunolabelling patterns of individual proteins (Figure 6-6D). The ER-Tracker labelling was denser in the perinuclear region.

The schematic demonstrates the distribution of ER and SR in relation to RyR (Figure 6-E). In each of the dual labels, RyR was poorly colocalized with the ER- and SR-resident proteins. Surface clusters of RyR were typically in a layer at the cell surface which was below that of the ER or SR. Higher in the cell where the SR and ER were more clearly visible, RyR clusters were predominantly at the periphery, with fewer in the cytoplasm and surrounding the nucleus.

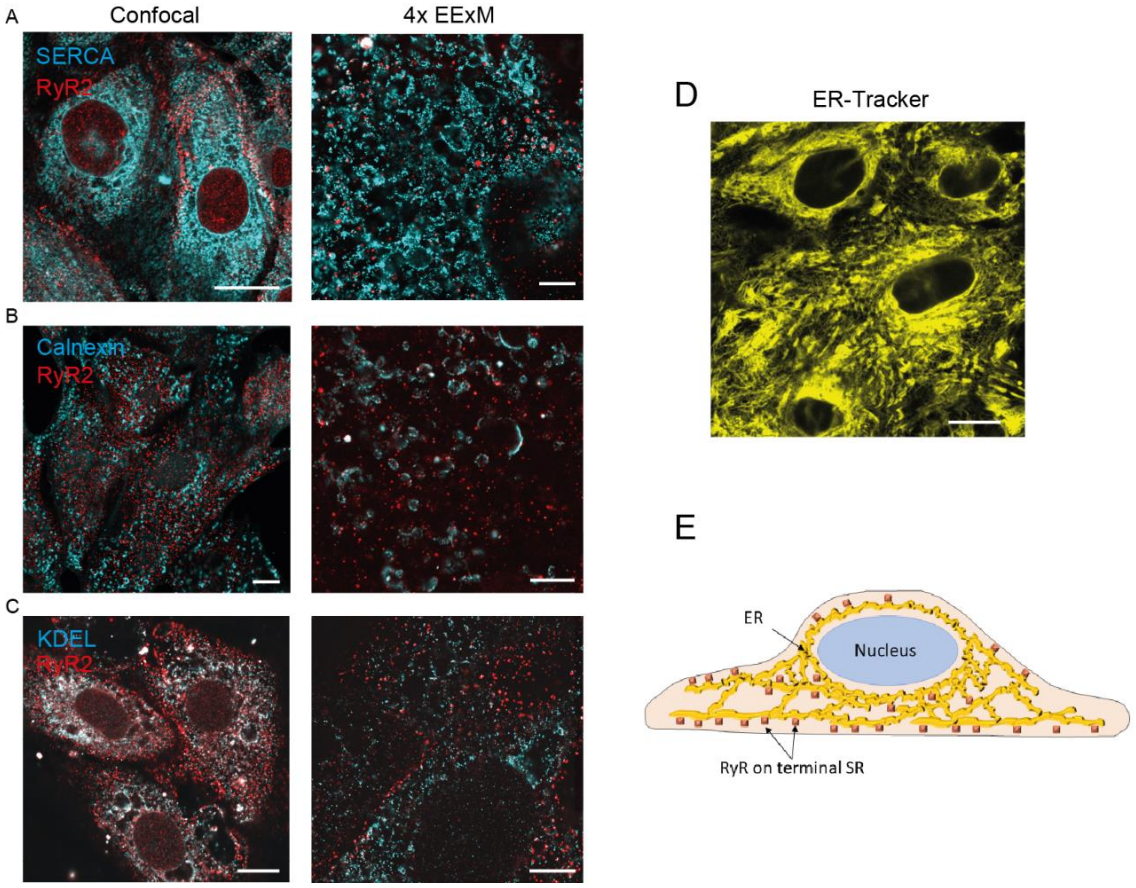

Figure 6-6. iPSC-CM ER distribution

ER and SR proteins in Day4 iPSC-CMs were immunolabelled to understand the organisation of these structures in relation to RyR. **(A)** The SR Ca^{2+} pump SERCA was prominently distributed throughout the cytoplasm. **(B)** The membrane-bound ER protein calnexin labelled small, curved structures, more sparsely distributed. **(C)** KDEL, a sequence on soluble ER-resident proteins, was slightly denser in the perinuclear region. **(D)** ER-Tracker Green in Day7 living cells strongly labelled the perinuclear region in a smooth continuous pattern. **(E)** The schematic demonstrates that most RyR clusters are on the periphery of iPSC-CMs, in a layer below the network of ER and SR. **Scale bars:** A-C confocal 10 µm, ExM 5 µm; D 10 µm.

6.3.5 Alternative Ca^{2+}-handling proteins in iPSC-CMs

The distribution of other Ca^{2+}-handling proteins which are functionally important in SC-CMs was evaluated. In confocal and 4x EExM imaging, IP3R-1 clusters were visible and even aligned into a sarcomeric pattern in some cells, even at the Day4 timepoint (Figure 6-7A). RyR3 labelling was particularly noisy, with some non-specific background labelling (Figure 6-7B), and faint striations visible in small regions.

6.3.6 Isotropy of ExM in iPSC-CMs

The isotropy of expansion was then verified in this new application to iPSC-CMs. In the literature, ExM has been successfully implemented for many types of cultured cells, including HEK293, BS-C-1, HeLa, U20S, Cos7 and cultured neurones. Given that iPSC-CMs pose little mechanical resistance to the expansion process, standard digestion steps using proteinase K were performed.

In adult cardiomyocytes, microscale isotropy was previously verified using the internal calibration structure of the SL (the distance between z-discs). Given that iPSC-CMs possessed robust sarcomeres, SL was suitable for estimating microscale isotropy. The average SL as measured pre-ExM was 1.74 ± 0.08 µm, and as measured and normalised after a 4x expansion was 1.43 ± 0.26 µm. The observation of physical EF being larger than that calculated using SL is consistent with the trend observed in the analysis in Figure 3-7.

The nucleus was used as another internal calibration structure with which to assess microscale isotropy. Pre-expansion and post-expansion (corrected for EF) measurements of the average nuclear width were similar, at 11.7 ± 2.23 µm and 12.4 ± 2.95 µm respectively.

Finally, the consistency of expansion was evaluated using the physical gel size. The average EF calculated using the gel size was 4.44 ± 0.16, and ranged between ~3.5 and 5. The low variation associated with this measurement suggests that the expansion process was consistent and not hindered by insufficient digestion.

While these measures appear to verify macroscale and microscale isotropy of ExM in iPSC-CMs, more rigorous future experiments will be required to confirm this. Nanoscale isotropy will be verified by the use of the intrinsic structure of the nuclear pore complex, which has been used to calibrate EF in other ExM experiments (Pesce *et al.*, 2019).

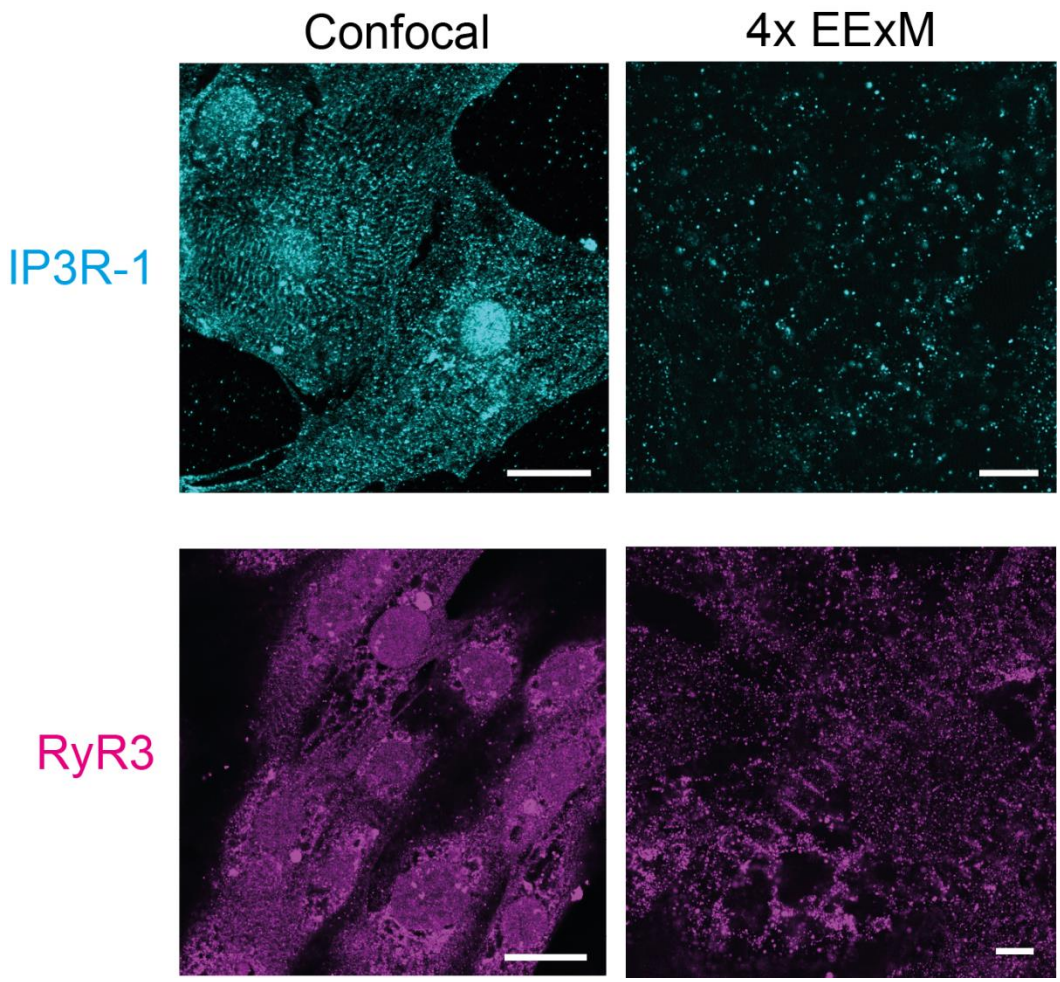

Figure 6-7. iPSC-CM alternative Ca^{2+} handling proteins

The distribution of other Ca^{2+} handling proteins in Day4 iPSC-CMs was observed. IP3R-1 was arranged into clusters and was arranged into clear striations in some cells. RyR3 labelling had high levels of background, evident by the nuclear staining. Despite this, there appeared to be specific binding, indicated by small regions of striations. **Scale bars:** confocal 20 µm, ExM 2.5 µm.

6.4 Discussion

6.4.1 eCSC-CMs structural immaturity

eCSC-CMs represent an early developmental stage, given they are structurally immature compared to the adult phenotype. Sarcomeric units were not yet organised in these cells, with α-actinin distributed axially along the length of the cell instead of in stereotypical z-discs. The patterns prominent at the cell extremities resemble stress fibres, which form in cells grown on rigid substrates (Tojkander et al., 2012), suggesting a role for α-actinin in adhesion and mechano-sensing in eCSC-CMs.

Formation of t-tubules in developing cardiomyocytes is thought to initiate in parallel to proliferation of caveolae (Parton *et al.*, 1997). The minimal Cav3 labelling pattern observed is consistent with low expression levels of Cav3 in SC-CMs (Lieu et al., 2009), and suggests an absence of internal membrane structures which could be precursor t-tubules.

RyR and JPH labelling lacked the stereotypical sarcomeric periodicity, which is perhaps unsurprising given the lack of z-disc organisation. Despite this, there was evidence of primitive Ca^{2+}-release clusters of RyR and JPH. There was no clear pattern to SERCA staining, suggesting low expression at this stage of differentiation.

These results suggest that eCSC-CMs have a primitive Ca^{2+}-release machinery, possibly due to a dependence on other methods of Ca^{2+} signalling not involving the internal SR store, for instance via LTCCs and IP3Rs. Evidently, a lack of t-tubules in eCSC-CMs prevents their use as a tool to study mechanisms of t-tubule remodelling. It is likely that a greater degree of maturity would be achieved given a longer period of differentiation. For instance, cardiomyocytes from embryonic stem cells show greater ultrastructural development when cultured for >35 days compared with earlier time points (Snir et al., 2003).

6.4.2 iPSC-CMs recapitulate elements of adult phenotype

The morphology of iPSC-CMs shared similarities with the adult phenotype, including well-ordered sarcomeres and CRUs comprising colocalised RyR and JPH. The biggest discrepancy between the two developmental stages is the absence of t-tubules in iPSC-CMs. In this way, iPSC-CMs resemble the pathological t-tubule remodelling observed in many branches of HF.

Clustering of RyR in iPSC-CMs was apparent with confocal imaging and confirmed at higher resolution using 4x ExM. This confirms previous observations of punctate surface clustering (X.-H. Zhang *et al.*, 2013) and reinforces the suggestion that there are peripheral couplings of junctional SR adjoined to the sarcolemma in iPSC-CMs (Gherghiceanu *et al.*, 2011). The average cluster size of 7-11 RyRs, in Day4 and Day7 respectively, resembled adult CRUs, which have an average of 8 RyRs per cluster. These values of iPSC-CM cluster size were likely to be over-estimations, given the area-based approach for quantification and the relatively low imaging resolution, which blurs structures to be larger than they are.

By observing iPSC-CMs at three timepoints, aspects of CRU development have been revealed, notably that RyR cluster size increases over the course of days, becomes distributed in the interior to a greater extent and in a more striated arrangement, without corresponding striations of JPH. That peripheral couplings were the main CRU type in early iPSC-CMs was similar to previous findings in developing cardiomyocytes (Franzini-Armstrong *et al.*, 2005). The interior clusters of RyR, which increase in frequency throughout development, are unaccompanied by t-tubules, and are thus independent of the voltage-gated LTCCs. These CRUs are the so-called corbular SR (Ogata and Yamasaki, 1990), which are prominent in myocytes lacking t-tubules such as atrial and avian cardiomyocytes (Shiels and Galli, 2014; Sheard *et al.*, 2019). The sarcomeric distribution of RyR indicates that the junctional SR aligns with the z-discs even without the t-tubules, in order to supply the central myofibrils with Ca^{2+}. Considering that RyR had a striated distribution in the interior before JPH recapitulated previous findings that JPH, while initially localised at the periphery, becomes more colocalised with RyR in the interior as t-tubules develop (Ziman *et al.*, 2010). The concept that JPH arrives later when t-tubules begin to form is intuitive given that JPH helps to fuse the sarcolemmal membrane with the SR, contributing to the formation of stable CRUs (Takeshima *et al.*, 2000).

CRU biogenesis is thought to comprise a hybrid of two mechanisms, that proteins are added to the sarcolemma and flow into the t-tubule invaginations (from the outside in), and that pre-formed vesicles (of already-tethered SR and t-tubule membrane) join prior to meeting the sarcolemma (from the inside out) (Di Maio et al., 2007). The latter mechanism explains the existence of t-tubule profiles which are not continuous with the extracellular space. It is thought that dyads are formed *de novo*, as opposed to inward flow of peripheral couplings upon the T tubule invaginations, given that there is no decrease in the number of peripheral couplings (Di Maio et al., 2007). While there is still more to be understood about CRU development, insight

could be obtained by further examination of the time-course of CRU biogenesis in iPSC-CM development.

T-tubules are not typically found in iPSC-CMs that are maintained in culture. There were no clear patterns of membrane proteins structures Cav3 and dystrophin, which suggested there were no precursor t-tubules at this timepoint. The widefield imaging of membrane proteins here likely lacked the resolution needed to observe small clusters proteins, so future efforts using ExM and dSTORM will be necessary to explore whether nanoscale t-tubule precursors, such as clusters of caveolae, exist at these early timepoints.

Ca^{2+} signalling progresses as cardiomyocytes develop, from a dyssynchronous state largely due to the absence of t-tubules, meaning that clusters of RyR in the interior are activated by Ca^{2+} diffusion from clusters further away (as opposed to direct Ca^{2+} from LTCCs), to a state where interior clusters are introduced to the sarcolemma-associated pool. Once t-tubules begin to form and bring LTCCs into close contact with RyRs, the synchrony of Ca^{2+} signalling improves.

While iPSC-CM exhibit some relatively mature aspects of Ca^{2+} signalling, they more closely resemble neonatal rather than adult cardiomyocytes (Zhang and Morad, 2020). For instance, there are LTCC-modulated, whole-cell Ca^{2+} transients, albeit there is a slower time to peak (Hwang *et al.*, 2015). As is expected for a cell lacking t-tubules, there is a non-uniform spread of Ca^{2+}, with a rise at the periphery before diffusion to the interior (Lee *et al.*, 2011). There has been shown to be caffeine-responsive, ryanodine-sensitive SR Ca^{2+} stores, indicating the importance of RyR. CRUs in iPSC-CMs create stochastic sparks which are predominantly triggered by LTCC-mediated influx (G. Q. Zhang *et al.*, 2013). There is also functional SERCA capable of re-filling the SR, and mature PLB and CSQ activity (Itzhaki *et al.*, 2011). NCX current density is also 2-fold larger in iPSC-CMs compared to the adult (X.-H. Zhang *et al.*, 2015). In culture, these cells spontaneously beat, unlike adult cardiomyocytes, and this is attributed partly to their large surface area:volume ratio.

Regarding alternative pathways for Ca^{2+} release, widespread striations of IP3R-1 were observed in Day4 iPSC-CMs, which was similar to that seen previously (Luo *et al.*, 2020). Previous work has demonstrated that there is an IP3R-releasable Ca^{2+} pool, and that IP3R contributes to whole-cell transients and helps to regulate the frequency of Ca^{2+} release oscillations (Rapila *et al.*, 2008; Itzhaki *et al.*, 2011). While some regions of RyR3 striations were observed here, they were much less prominent than those of RyR2 and IP3R-1. The contribution of RyR3 toward Ca^{2+} signalling in iPSC-CM is not well known.

The layout of several ER and SR components was investigated to understand the spatial distribution of Ca^{2+} stores in relation to the RyR clusters. The colocalisation of SERCA calnexin and KDEL with RyR was low by eye, mainly because the RyR clusters were found at the bottom of the cell, below the plane where ER and SR structures were best visualised. Future experiments would benefit from 2-colour pairings of the ER and SR proteins with RyR and with each other. The distribution of the ER in bulk was also investigated using ER-Tracker in living cells.

Evidently, there are significant structural differences between iPSC-CMs and adult cardiomyocytes, which underlie functional differences in Ca^{2+} signalling. iPSC-CM are unlikely to ever fully recapitulate adult Ca^{2+} functionality (Zhang and Morad, 2020). Research using iPSC-CMs as parallels to adult cardiomyocytes (such as drug efficacy trials) must carefully consider these differences when drawing conclusions about results. The success of these studies hinges on how well these cells mimic adult cardiomyocytes, so efforts to improve structural maturity will be particularly valuable to these studies.

Owing to the enhanced resolution afforded by two super-resolution microscopy techniques ExM and dSTORM, clustering of RyR and JPH in primitive CRUs has been observed in SC-CMs for the first time. While these analyses have so far been exclusively 2D, which has enabled preliminary investigations of general cluster area, 3D imaging will be of use to characterise the full distribution of CRUs in SC-CMs.

6.5 Concluding remarks

This chapter has provided a description of the structural maturity of eCSC-CMs and iPSC-CMs.

eCSC-CMs lacked organisation of sarcomeric z-discs, absence of t-tubules and minimal clustering of RyR and JPH. In this way, eCSC-CMs are unsuitable as a model comparable to adult cardiomyocytes.

iPSC-CMs possessed well-organised contractile machinery, but no t-tubule structures. Primitive CRUs with co-clustered RyR and JPH were present, and there was a progression in terms of the striated RyR alignment between Day4 and Day7. While there are similarities in the structural morphology between iPSC-CMs and adult cardiomyocytes, key differences including a lack of t-tubules must be considered in translational studies using iPSC-CMs.

The macroscale and microscale isotropy of ExM in SC-CMs was verified using intrinsic structures and physical gel size, while verification of nanoscale isotropy is a focus for the future.

Chapter 7. General discussion

7.1 Expansion microscopy

The ExM research area has moved at breakneck speed, pushing the boundaries of light-based microscopy to new frontiers, and shows much promise for the future of scientific research.

10x EExM exists as a genuine competitor to other super-resolution techniques for several reasons. In terms of resolving power, the lateral resolution of 15 nm puts it in the same bracket as DNA-PAINT, and the 35 nm axial resolution is better than almost all SMLM-based techniques. Further, 10x EExM is naturally capable of 3D imaging, with straightforward multi-colour and better imaging depths than competing techniques. Perhaps most importantly is the low cost and ease of use, with all reagents commercially available, straightforward protocols and no specialised equipment required.

The aspects listed above make 10x EExM particularly suited for imaging 3D protein domains deep in the cell. Using 10x EExM it was possible to detail the layout of several proteins in isolated cardiomyocytes, most notably RyR and JPH. In the future, 10x EExM could be used to better describe the layout of other Ca^{2+}-handling proteins, including NCX and SERCA, whose organisation has not been explored in detail at the individual protein level. Recently, click chemistry has now extended the application of ExM to non-protein targets, including lipids, metabolites and DNA/RNA (Sun *et al.*, 2020), which could allow a more complete characterisation of the cardiac system.

10x EExM imaging was performed using isolated adult rat cardiomyocytes, cardiac tissue sections (not shown) and SC-CMs, but the benefits of this technique can be extrapolated to a broad range of sample types. Indeed, variants of ExM have been tailored for samples with unique properties, including bacteria (Lim *et al.*, 2019), *C. elegans* (Yu *et al.*, 2020), plant cells (Kao and Nodine, 2019) lipids (Karagiannis *et al.*, 2019; Götz, Kunz, *et al.*, 2020), fungi (Götz, Panzer, *et al.*, 2020) and paraffin-embedded clinical samples (Zhao *et al.*, 2017). Ultimately, one must consider whether the physical properties of the sample (and the target structures being observed) might hinder even expansion. Further, the amount of fixation has also been shown to directly affect the EF, so must be balanced in order to isotropy and target preservation (Pernal *et al.*, 2020).

The isotropy of ExM for isolated cardiomyocytes was verified using macro-, micro- and nanoscale approaches, capitalising on intrinsic structures such as the SL and z-disc. Synthetic calibration structures with robust dimensions, allowing isotropy to be evaluated in a consistent manner, will be a valuable addition to the ExM research field. Indeed, oligonucleotide origami rulers as calibration structures have proven to be useful in isotropy verification (Scheible and Tinnefeld, 2018).

The X10 gel chemistry used here, wherein free-radical based polymerisation using the self-crosslinking DMAA monomer, could lead to anisotropy due to heterogenous gel structure. Recent innovations in gel chemistry may provide improved isotropy, for instance more homogenous gels formed using non-free radical polymerisation of tetrahedron monomers (Gao *et al.*, 2021), while other techniques which optimise the original gel recipe to preserve ultrastructure (Gambarotto *et al.*, 2019).

Gel chemistries with increased EFs have been devised to enable bigger increases in resolution. While the original recipe expanded by 4-fold (Chen *et al.*, 2015; Tillberg *et al.*, 2016), several recipes have achieved 10-fold in a single step (Truckenbrodt *et al.*, 2018; Damstra *et al.*, 2021) and iterative ExM (requiring multiple separate expansions) has enabled 20-fold expansion (Chang *et al.*, 2017). It is likely that these EFs represent an upper boundary, whereby any further increase may compromise the isotropy or mechanical stability of gels. Furthermore, the actual resolution obtained is governed by the size of the imaging probes. The linkage error, associated with the displacement of the fluorophore from the target (due to the size of the primary and secondary antibody), can be reduced by using smaller probes, such as nanobodies, or by performing post-expansion labelling.

7.2 Calcium release units

The first application of 10x EExM for biological insight was in visualising RyR clusters in isolated adult rat cardiomyocytes. Cross-validations were made comparing imaging of 2D surface clusters by 10x EExM to that obtained with DNA-PAINT. Surface clusters were visually comparable between the two techniques, and the comprehensive quantification of cluster size and NND from DNA-PAINT was recapitulated in 10x EExM imaging. Given that 10x EExM was able to replicate the DNA-PAINT observations (both qualitatively and quantitatively), serves as additional reassurance (on top of the isotropy verification) that 10x EExM is a reliable technique capable of imaging nanoscale structures such as the cardiac dyad.

Owing to the enhanced imaging depth, axial resolution and 3D capabilities of 10x EExM, it was possible to characterise dyads deeper in the cell for the first time. 3D reconstructions of dyads showing the organisation of individual proteins enable a clearer visualisation of cluster morphology in relation to the t-tubule. 2-colour 10x EExM allowed an investigation into the involvement of JPH in dyadic clusters to infer more of the cluster geometry. Future experiments imaging RyR with LTCC would likely yield greater insights into dyad organisation.

With individual protein resolution it was possible to quantify dyads, in terms of cluster size and arrangement, making an improvement over previous attempts using 3D dSTORM (Shen *et al.*, 2018). The amount of JPH per cluster was comparable to RyR and was distributed predominantly along the central backbone of the cluster. Novel 3D analyses and optimised cluster selection approaches will determine whether the values of cluster size calculated here were over-estimations. Furthermore, a more quantified understanding of cluster geometry will require custom-made 3D analysis tools.

While 15 nm axial resolution allowed detection of most RyRs positioned closely in 2D clusters, RyRs were blurred together in some 3D stacks due to limitations in lateral resolution. Further increased resolution for RyR imaging may be achieved by combining X10 with other super-resolution techniques, albeit the difficulties in performing 3D imaging with such techniques may limit their use.

Using 10x EExM imaging it was feasible to provide insight into *in situ* phosphorylation of individual RyRs in clusters for the first time. Highly specific antibodies for pSer2808 allowed the visualisation of RyR phosphorylation, and enabled quantification of the fraction of phosphorylation in the basal state. The sensitivity of this quantification technique was demonstrated in the ability to capably detect a 2-fold increase in experimentally induced hyper-phosphorylation of pSer2808 using isoproterenol and electrical stimulation.

Phosphorylation of pSer2814 and pSer2030 sites has an equally important role in regulating RyR activity, and there is believed to be a compensatory relationship between the various sites. pSer2814 and pSer2030 phosphorylation was not quantified in this study, owing to non-specific labelling with the antibodies for these targets. It is likely that novel probes, or strategies to boost labelling specificity of existing antibodies will be required to better visualise and quantify the incidence of these additional phosphorylation sites *in situ.*

It would be valuable to correlate the degree of RyR phosphorylation with the cluster activity (for instance spark fidelity) through advanced correlated imaging experiments. In this way, the

implications of post-translational modification and cluster organisation on Ca^{2+} release dynamics could be better interpreted.

The post-translational modification is a complex regulatory state, so use of *in situ* observations can be valuable in investigating the effects of kinases, phosphatases, cAMP and PDEs. It would be interesting to study the effects of these candidates on the fractional phosphorylation of the various sites to better characterise the regulatory pathways involved with each phosphorylation site.

7.3 Right ventricular remodelling

MCT-injected animals grew slower and had a weight drop-off coinciding with HF. While *in vivo* measures of hypertrophy were not monitored, the organ weights largely replicated the changes seen in previous studies, indicating pulmonary system remodelling and RV hypertrophy.

The shorter SL in MCT-RV could contribute toward arrhythmic behaviour in MCT-RV cardiomyocytes by increasing the generation of Ca^{2+} waves. In a study which modelled the effects of reducing SL from 2 μm to 1.8 μm, there was a large increase in ability of CRUs on adjacent z-discs to fire (Izu *et al.*, 2006).

At the level of the individual CRU, cluster fragmentation was observed in MCT-RV, entailing smaller interior cluster sizes and reduced density for both RyR and JPH, with slightly increased distances between RyRs. The changes in cluster organisation contribute toward the dysfunctional Ca^{2+} release activity owing to the intimate relationship between structure and function. In particular, lost regulation of RyRs due to a lost stabilising effect of JPH could contribute toward increased spark frequency. The increased SR load, which is a key alteration to the Ca^{2+} homeostasis in MCT-RV cardiomyocytes, will exacerbate channel leakiness that occurs due to nanodomain remodelling.

Increased pSer2808 phosphorylation was observed in MCT-RV dyads, as well as altered patterns of phosphorylation in surface clusters. These changes could be a consequence of increased circulating catecholamines, or changes to phosphatases and PDEs. While one could hypothesise that this hyper-phosphorylation increases channel excitability (and consequently cluster activity), the implications of increased pSer2808 phosphorylation are not straightforward. For instance, the unique RyR behaviours and enhanced excitability occurred

at maximal and minimal phosphorylation states, while intermediate states of phosphorylation were more moderate in activity changes (Carter *et al.*, 2006). The increased fractional phosphorylation in MCT-RV dyads may not be large enough to incur a significant change in channel activity. While hyper-phosphorylation could have a functional impact here, it could simply be a hallmark of PKA activation. Further, the compensatory nature of the phosphorylation sites and the complex network of regulatory factors involved make it difficult to directly conclude causation on function from observations of single components. Unfortunately, there are at present few cell systems which allow a detailed dissection into the role of specific RyR sites in gating activity.

Considering other aspects of MCT pathobiology, microtubule densification occurs as a response to PAH and could contribute to contractile dysfunction (Stones *et al.*, 2013). In addition, microtubule remodelling has been linked to improper JPH trafficking (Prins *et al.*, 2017), which aligns with the observation of reduced JPH. In addition, there is widespread fibrosis, through deposition of collagen, which contribute to diastolic stiffness and further impair contractile function (Wen *et al.*, 2019).

The MCT model of RV HF is useful to understand pathobiology, but care must be made when extrapolating observations made to human HF, given differences. For instance, it is not known whether MCT animals die from progressive PH, failure of the RV or another organ (Gomez-Arroyo *et al.*, 2012).

Regarding the clinical perspectives of these observations of pathological alterations at the cluster level in MCT RV HF, it re-emphasises the need to preserve and restore t-tubule and dyad structure. A more detailed understanding of the mechanisms for t-tubule and dyad remodelling, as well as the phosphorylation pathway, are required to design effective treatment strategies. Presently, treatment options entail optimising preload with diuretics, reducing afterload with pulmonary vasodilators, and improving contractility with inotropic agents (Mehmood and Frank, 2016). β-blockers are a clinically used treatment to improve survival in LV HF, and while they are not currently a therapeutic option for PAH, they could prove to be beneficial in improving RV diastolic function (Fowler, Drinkhill, Norman, *et al.*, 2018). The microtubule depolymerising agent colchicine has been shown to improve RV function, possibly through restoration of dyadic JPH and t-tubule structures (Prins *et al.*, 2017).

7.4 Stem-cell derived cardiomyocyte maturity

SC-CMs could be the vehicle through which the mechanisms of CRU development are discovered. That SC-CMs are adherent and flatter means they are easier to image with ExM techniques than mature cardiomyocytes.

iPSC-CMs are a widely used cell type; for instance, recent publication statistics from Scopus show that in 2020 there were over 200 papers featuring the terms “pluripotent stem cell” and “cardiomyocyte”. The widespread use of iPSC-CMs in cardiac research lends to their commercial availability and value as a model that means fewer animals are required. They have been a powerful *ex vivo* tool for predicting cardiotoxicity of drug treatments (Cohen *et al.*, 2011). Further, their use in transplants to replace lost tissue could potentially provide enormous therapeutic benefits. The primitive morphology of the iPSC-CM could also prove to be a useful test platform in which to upregulate dyadic proteins and observe how they each contribute to dyad function. Crucially, the past and future successes of iPSC-CM research hinges on their maturity, both structurally and functionally, to serve as a model for adult cardiomyocytes.

eCSC-CMs are less widely used compared to iPSC-CMs, likely because they are not commercially available. In addition, it appears eCSC-CMs are less structurally mature than iPSC-CMs, so pose as a less ideal comparison for *in vitro* studies which aim to investigate and parallel the adult phenotype. Still, eCSCs have shown promise in restoring cardiac function after myocardial damage by replacing lost cardiomyocytes (Ellison *et al.*, 2013) and improving contractile function of human engineered cardiac tissues *in vitro* (Murphy *et al.*, 2019). eCSC-CMs could be promising in studying the earliest stages of CRU progenitor development.

In iPSC-CMs there were seen to be progenitor CRUs (comprising co-localised RyR and JPH) even a few days into culture, with no obvious evidence of cytoplasmic membrane structures which could be t-tubule progenitors. Over the course of 7 days there became a more striated distribution of RyR, preceding t-tubule formation, while JPH was not immediately co-localised in a striated fashion. This suggests that JPH arrival at the dyad may occur upon formation of the t-tubules. iPSC-CMs clearly possess an intermediate stage of Ca^{2+}-release machinery maturity, which is perhaps unsurprising given that the myofibrils are less well organized than in the adult form, therefore the organisation of CRUs need not be as well-organized.

Current mechanisms of t-tubule formation include direct invagination from the sarcolemma involving cholesterol-rich lipid rafts called caveolae (Parton *et al.*, 1997), or pre-formed vesicle

fusion (Di Maio *et al.*, 2007). Recently, cholesterol rafts and the Cav3 proteins which form them have been proposed to serve as sites for JPH to anchor (Poulet *et al.*, 2021). Another key component involved in t-tubule biogenesis is the membrane scaffolding protein BIN1 (Lee *et al.*, 2002). BIN1 is a capable of sensing curvature and forming membrane folds (Hong *et al.*, 2014) and also enables delivery of LTCCs via the microtubule cytoskeleton (Hong *et al.*, 2010). Inter-chamber differences in BIN1 protein are linked to the t-tubule density, as there is less BIN1 protein in the atria where there is an absence of t-tubule network (Caldwell *et al.*, 2014). Another more recent discovery is the involvement of the z-disc protein nexilin in t-tubule and CRU formation (Spinozzi *et al.*, 2020). Future efforts seeking to determine the involvement of each of these components, and the timeline of dyad or t-tubule development, will benefit from ExM techniques which provide sufficient resolution to discover these nanoscale, primitive structures.

While some adult-like features were observed in iPSC-CMs, including sarcomeric ordering of z-discs, some parts of their phenotype were immature and unlike adult cardiomyocytes, most critically being the absence of t-tubules. Significant efforts have been made to improve the structural maturity of iPSC-CMs, often aiming to replicate the adult heart microenvironment (Ronaldson-Bouchard *et al.*, 2018). For instance, improved structural maturity has been achieved by the use of electrical stimulation (Nunes *et al.*, 2013), micropatterned substrates (Rao *et al.*, 2013) and longer maintenance in culture (Lundy *et al.*, 2013; Hasan *et al.*, 2020). Additions to the medium have also yielded positive results, for instance supplementation with thyroid and glucocorticoid hormones lead to improved t-tubule development (Parikh *et al.*, 2017).

As discussed in Section 6.4.2, iPSC-CMs demonstrate some aspects of mature EC coupling, in terms of functional LTCC, RyR, NCX, SERCA, culminating in stochastic spark activity and whole-cell transients. It is ultimately difficult to bypass the criticisms that EC coupling in iPSC-CMs will never fully recapitulate native adult cardiomyocytes, and the translation of findings in iPSC-CMs should be made with caution (Koivumaki *et al.*, 2018).

Bibliography

Abbe, E. (1873) ‘Beiträge zur Theorie des Mikroskops und der mikroskopischen Wahrnehmung’, *Archiv für Mikroskopische Anatomie*, 9(1), pp. 413–468. doi:10.1007/BF02956173.

Allen, D.G. and Blinks, J.R. (1978) ‘Calcium transients in aequorin-injected frog cardiac muscle’, *Nature*, 273(5663), pp. 509–513. doi:10.1038/273509a0.

Alvarado, F.J., Chen, X. and Valdivia, H.H. (2017) ‘Ablation of the cardiac ryanodine receptor phospho-site Ser2808 does not alter the adrenergic response or the progression to heart failure in mice. Elimination of the genetic background as critical variable’, *Journal of Molecular and Cellular Cardiology*, 103, pp. 40–47. doi:10.1016/j.yjmcc.2017.01.001.

Archer, C.R., Sargeant, R., Basak, J., Pilling, J., Barnes, J.R. and Pointon, A. (2018) ‘Characterization and Validation of a Human 3D Cardiac Microtissue for the Assessment of Changes in Cardiac Pathology’, *Scientific Reports*, 8(1), p. 10160. doi:10.1038/s41598-018-28393-y.

Asghari, P., Schulson, M., Scriven, D.R.L., Martens, G. and Moore, E.D.W. (2009) ‘Axial Tubules of Rat Ventricular Myocytes Form Multiple Junctions with the Sarcoplasmic Reticulum’, *Biophysical Journal*, 96(11), pp. 4651–4660. doi:10.1016/j.bpj.2009.02.058.

Asghari, P., Scriven, D.R.L., Sanatani, S., Gandhi, S.K., Campbell, A.I.M. and Moore, E.D.W. (2014) ‘Nonuniform and variable arrangements of ryanodine receptors within mammalian ventricular couplons’, *Circulation Research*, 115(2), pp. 252–262. doi:10.1161/CIRCRESAHA.115.303897.

Baddeley, D., Cannell, M.B. and Soeller, C. (2010) ‘Visualization of localization microscopy data’, *Microscopy and Microanalysis: The Official Journal of Microscopy Society of America, Microbeam Analysis Society, Microscopical Society of Canada*, 16(1), pp. 64–72. doi:10.1017/S143192760999122X.

Baddeley, D., Jayasinghe, I., Lam, L., Rossberger, S., Cannell, M.B. and Soeller, C. (2009) ‘Optical single-channel resolution imaging of the ryanodine receptor distribution in rat cardiac myocytes’, *Proc Natl Acad Sci U S A*, 106(52), pp. 22275–80. doi:10.1073/pnas.0908971106.

Baraniak, P.R. and McDevitt, T.C. (2010) ‘Stem cell paracrine actions and tissue regeneration’, *Regenerative medicine*, 5(1), pp. 121–143. doi:10.2217/rme.09.74.

Bassani, J.W., Yuan, W. and Bers, D.M. (1995) ‘Fractional SR Ca release is regulated by trigger Ca and SR Ca content in cardiac myocytes’, *The American Journal of Physiology*, 268(5 Pt 1), pp. C1313-1319. doi:10.1152/ajpcell.1995.268.5.C1313.

Bates, M., Huang, B., Dempsey, G.T. and Zhuang, X. (2007) ‘Multicolor super-resolution imaging with photo-switchable fluorescent probes’, *Science*, 317(5845), pp. 1749–53. doi:10.1126/science.1146598.

Beavers, D.L., Wang, W., Ather, S., Voigt, N., Garbino, A., Dixit, S.S., Landstrom, A.P., Li, N., *et al.* (2013) ‘Mutation E169K in junctophilin-2 causes atrial fibrillation due to impaired RyR2 stabilization’, *J Am Coll Cardiol*, 62(21), pp. 2010–9. doi:10.1016/j.jacc.2013.06.052.

Benkusky, N.A., Weber, C.S., Scherman, J.A., Farrell, E.F., Hacker, T.A., John, M.C., Powers, P.A. and Valdivia, H.H. (2007) 'Intact beta-adrenergic response and unmodified progression toward heart failure in mice with genetic ablation of a major protein kinase A phosphorylation site in the cardiac ryanodine receptor', *Circulation Research*, 101(8), pp. 819–829. doi:10.1161/CIRCRESAHA.107.153007.

Benoist, D., Stones, R., Benson, A.P., Fowler, E.D., Drinkhill, M.J., Hardy, M.E., Saint, D.A., Cazorla, O., *et al.* (2014) 'Systems approach to the study of stretch and arrhythmias in right ventricular failure induced in rats by monocrotaline', *Prog Biophys Mol Biol*, 115(2–3), pp. 162–72. doi:10.1016/j.pbiomolbio.2014.06.008.

Benoist, D., Stones, R., Drinkhill, M., Bernus, O. and White, E. (2011) 'Arrhythmogenic substrate in hearts of rats with monocrotaline-induced pulmonary hypertension and right ventricular hypertrophy', *American journal of physiology. Heart and circulatory physiology*, 300(6), pp. H2230-7. doi:10.1152/ajpheart.01226.2010.

Benoist, D., Stones, R., Drinkhill, M.J., Benson, A.P., Yang, Z., Cassan, C., Gilbert, S.H., Saint, D.A., *et al.* (2012) 'Cardiac arrhythmia mechanisms in rats with heart failure induced by pulmonary hypertension', *American Journal of Physiology - Heart and Circulatory Physiology*, 302(11), pp. H2381–H2395. doi:10.1152/ajpheart.01084.2011.

Bers, D.M. (2002) 'Cardiac excitation-contraction coupling', *Nature*, 415(6868), pp. 198–205. doi:10.1038/415198a.

Bers, D.M. (2012) 'Ryanodine receptor S2808 phosphorylation in heart failure: smoking gun or red herring', *Circ Res*, 110(6), pp. 796–9. doi:10.1161/circresaha.112.265579.

Bovo, E., Huke, S., Blatter, L.A. and Zima, A.V. (2017) 'The effect of PKA-mediated phosphorylation of ryanodine receptor on SR Ca(2+) leak in ventricular myocytes', *J Mol Cell Cardiol*, 104, pp. 9–16. doi:10.1016/j.yjmcc.2017.01.015.

Brandenburg, S., Kohl, T., Williams, G.S., Gusev, K., Wagner, E., Rog-Zielinska, E.A., Hebisch, E., Dura, M., *et al.* (2016) 'Axial tubule junctions control rapid calcium signaling in atria', *J Clin Invest*, 126(10), pp. 3999–4015. doi:10.1172/jci88241.

Brandenburg, S., Pawlowitz, J., Eikenbusch, B., Peper, J., Kohl, T., Mitronova, G.Y., Sossalla, S., Hasenfuss, G., *et al.* (2019) 'Junctophilin-2 expression rescues atrial dysfunction through polyadic junctional membrane complex biogenesis', *JCI insight*, 4(12). doi:10.1172/jci.insight.127116.

Brown, L., Miller, J., Dagger, A. and Sernia, C. (1998) 'Cardiac and Vascular Responses After Monocrotaline-Induced Hypertrophy in Rats', *Journal of Cardiovascular Pharmacology*, 31(1). Available at: https://journals.lww.com/cardiovascularpharm/Fulltext/1998/01000/Cardiac_and_Vascular_Responses_After.16.aspx.

Burgoyne, T., Morris, E.P. and Luther, P.K. (2015) 'Three-Dimensional Structure of Vertebrate Muscle Z-Band: The Small-Square Lattice Z-Band in Rat Cardiac Muscle', *Journal of Molecular Biology*, 427(22), pp. 3527–3537. doi:10.1016/j.jmb.2015.08.018.

Cahoon, C.K., Yu, Z., Wang, Y., Guo, F., Unruh, J.R., Slaughter, B.D. and Hawley, R.S. (2017) 'Superresolution expansion microscopy reveals the three-dimensional organization of the

Drosophila synaptonemal complex', *Proceedings of the National Academy of Sciences*, 114(33), pp. E6857–E6866. doi:10.1073/pnas.1705623114.

Caldwell, J.L., Smith, C.E., Taylor, R.F., Kitmitto, A., Eisner, D.A., Dibb, K.M. and Trafford, A.W. (2014) 'Dependence of cardiac transverse tubules on the BAR domain protein amphiphysin II (BIN-1)', *Circ Res*, 115(12), pp. 986–96. doi:10.1161/circresaha.116.303448.

Cannell, M.B., Cheng, H. and Lederer, W.J. (1994) 'Spatial non-uniformities in [Ca2+]i during excitation-contraction coupling in cardiac myocytes.', *Biophysical Journal*, 67(5), pp. 1942–1956.

Cannell, M.B. and Kong, C.H.T. (2012) 'Local control in cardiac E-C coupling', *Journal of Molecular and Cellular Cardiology*, 52(2), pp. 298–303. doi:10.1016/j.yjmcc.2011.04.014.

Cannell, M.B., Kong, C.H.T., Imtiaz, M.S. and Laver, D.R. (2013) 'Control of Sarcoplasmic Reticulum Ca2+ Release by Stochastic RyR Gating within a 3D Model of the Cardiac Dyad and Importance of Induction Decay for CICR Termination', *Biophysical Journal*, 104(10), pp. 2149–2159. doi:10.1016/j.bpj.2013.03.058.

Carter, S., Colyer, J. and Sitsapesan, R. (2006) 'Maximum phosphorylation of the cardiac ryanodine receptor at serine-2809 by protein kinase a produces unique modifications to channel gating and conductance not observed at lower levels of phosphorylation', *Circ Res*, 98(12), pp. 1506–13. doi:10.1161/01.RES.0000227506.43292.df.

Chang, J.-B., Chen, F., Yoon, Y.-G., Jung, E.E., Babcock, H., Kang, J.S., Asano, S., Suk, H.-J., *et al.* (2017) 'Iterative expansion microscopy', *Nat Meth*, advance online publication. doi:10.1038/nmeth.4261.

Chelu, M.G., Sarma, S., Sood, S., Wang, S., Oort, R.J. van, Skapura, D.G., Li, N., Santonastasi, M., *et al.* (2009) 'Calmodulin kinase II–mediated sarcoplasmic reticulum Ca^{2+} leak promotes atrial fibrillation in mice', *The Journal of Clinical Investigation*, 119(7), pp. 1940–1951. doi:10.1172/JCI37059.

Chen, B., Guo, A., Zhang, C., Chen, R., Zhu, Y., Hong, J., Kutschke, W., Zimmerman, K., *et al.* (2013) 'Critical roles of junctophilin-2 in T-tubule and excitation–contraction coupling maturation during postnatal development', *Cardiovascular Research*, 100(1), pp. 54–62. doi:10.1093/cvr/cvt180.

Chen, F., Tillberg, P.W. and Boyden, E.S. (2015) 'Expansion microscopy', *Science*, 347(6221), pp. 543–548. doi:10.1126/science.1260088.

Cheng, H., Lederer, M.R., Lederer, W.J. and Cannell, M.B. (1996) 'Calcium sparks and [Ca2+]i waves in cardiac myocytes', *American Journal of Physiology-Cell Physiology*, 270(1), pp. C148–C159. doi:10.1152/ajpcell.1996.270.1.C148.

Cheng, H., Lederer, W.J. and Cannell, M.B. (1993) 'Calcium sparks: elementary events underlying excitation-contraction coupling in heart muscle', *Science*, 262(5134), pp. 740–4.

Chen-Izu, Y., Ward, C.W., Stark, W., Banyasz, T., Sumandea, M.P., Balke, C.W., Izu, L.T. and Wehrens, X.H.T. (2007) 'Phosphorylation of RyR2 and shortening of RyR2 cluster spacing in spontaneously hypertensive rat with heart failure', *American Journal of Physiology. Heart and Circulatory Physiology*, 293(4), pp. H2409-2417. doi:10.1152/ajpheart.00562.2007.

Cohen, J.D., Babiarz, J.E., Abrams, R.M., Guo, L., Kameoka, S., Chiao, E., Taunton, J. and Kolaja, K.L. (2011) 'Use of human stem cell derived cardiomyocytes to examine sunitinib mediated cardiotoxicity and electrophysiological alterations', *Toxicol Appl Pharmacol*, 257(1), pp. 74–83. doi:10.1016/j.taap.2011.08.020.

Cohen, Y., Ramon, O., Kopelman, I.J. and Mizrahi, S. (1992) 'Characterization of inhomogeneous polyacrylamide hydrogels', *J Polym Sci Part B Polym Phys*, 30. doi:10.1002/polb.1992.090300913.

Collins, H.E. and Rodrigo, G.C. (2010) 'Inotropic Response of Cardiac Ventricular Myocytes to β-Adrenergic Stimulation With Isoproterenol Exhibits Diurnal Variation', *Circulation Research*, 106(7), pp. 1244–1252. doi:10.1161/CIRCRESAHA.109.213942.

Crossman, D.J., Ruygrok, P.N., Soeller, C. and Cannell, M.B. (2011) 'Changes in the organization of excitation-contraction coupling structures in failing human heart', *PLoS One*, 6(3), p. e17901. doi:10.1371/journal.pone.0017901.

Crossman, D.J., Shen, X., Jüllig, M., Munro, M., Hou, Y., Middleditch, M., Shrestha, D., Li, A., *et al.* (2017) 'Increased collagen within the transverse tubules in human heart failure', *Cardiovascular Research*, 113(8), pp. 879–891. doi:10.1093/cvr/cvx055.

Curran, J., Hinton, M.J., Ríos, E., Bers, D.M. and Shannon, T.R. (2007) 'Beta-adrenergic enhancement of sarcoplasmic reticulum calcium leak in cardiac myocytes is mediated by calcium/calmodulin-dependent protein kinase', *Circulation Research*, 100(3), pp. 391–398. doi:10.1161/01.RES.0000258172.74570.e6.

Damstra, H.G.J., Mohar, B., Eddison, M., Akhmanova, A., Kapitein, L.C. and Tillberg, P.W. (2021) 'Visualizing cellular and tissue ultrastructure using Ten-fold Robust Expansion Microscopy (TREx)', *bioRxiv*, p. 2021.02.03.428837. doi:10.1101/2021.02.03.428837.

Davis, J., Chouman, A., Creech, J., Rocha, A.M. da, Ponce-Balbuena, D., Vazquez, E.N.J., Nichols, R., Lozhkin, A., *et al.* (2021) 'In vitro model of ischemic heart failure using human induced pluripotent stem cell-derived cardiomyocytes', *JCI Insight* [Preprint]. doi:10.1172/jci.insight.134368.

Dhindwal, S., Lobo, J., Cabra, V., Santiago, D.J., Nayak, A.R., Dryden, K. and Samsó, M. (2017) 'A cryo-EM-based model of phosphorylation- and FKBP12.6-mediated allosterism of the cardiac ryanodine receptor', *Science Signaling*, 10(480). doi:10.1126/scisignal.aai8842.

Di Maio, A., Karko, K., Snopko, R.M., Mejia-Alvarez, R. and Franzini-Armstrong, C. (2007) 'T-tubule formation in cardiacmyocytes: two possible mechanisms?', *J Muscle Res Cell Motil*, 28(4–5), pp. 231–41. doi:10.1007/s10974-007-9121-x.

Dignam, J.P., Scott, T.E., Kemp-Harper, B.K. and Hobbs, A.J. (2021) 'Animal models of pulmonary hypertension: Getting to the heart of the problem', *British Journal of Pharmacology* [Preprint]. doi:10.1111/bph.15444.

Du, G.G., Khanna, V.K. and MacLennan, D.H. (2000) 'Mutation of Divergent Region 1 Alters Caffeine and Ca2+ Sensitivity of the Skeletal Muscle Ca2+Release Channel (Ryanodine Receptor)', *Journal of Biological Chemistry*, 275(16), pp. 11778–11783. doi:10.1074/jbc.275.16.11778.

Düring, D.N., Rocha, M.D., Dittrich, F., Gahr, M. and Hahnloser, R.H.R. (2019) 'Expansion Light Sheet Microscopy Resolves Subcellular Structures in Large Portions of the Songbird Brain', *Frontiers in Neuroanatomy*, 13. doi:10.3389/fnana.2019.00002.

Edwards, A.G. and Louch, W.E. (2017) 'Species-Dependent Mechanisms of Cardiac Arrhythmia: A Cellular Focus', *Clinical Medicine Insights. Cardiology*, 11, p. 1179546816686061. doi:10.1177/1179546816686061.

Eisner, D.A., Trafford, A.W., Dñaz, M.E., Overend, C.L. and O'Neill, S.C. (1998) 'The control of Ca release from the cardiac sarcoplasmic reticulum: regulation versus autoregulation', *Cardiovascular Research*, 38(3), pp. 589–604. doi:10.1016/S0008-6363(98)00062-5.

Ellison, G.M., Vicinanza, C., Smith, A.J., Aquila, I., Leone, A., Waring, C.D., Henning, B.J., Stirparo, G.G., *et al.* (2013) 'Adult c-kit(pos) cardiac stem cells are necessary and sufficient for functional cardiac regeneration and repair', *Cell*, 154(4), pp. 827–842. doi:10.1016/j.cell.2013.07.039.

Fabiato, A. and Fabiato, F. (1975) 'Contractions induced by a calcium-triggered release of calcium from the sarcoplasmic reticulum of single skinned cardiac cells', *The Journal of Physiology*, 249(3), pp. 469–495. doi:10.1113/jphysiol.1975.sp011026.

Fill, M. and Gillespie, D. (2021) 'Simulating cardiac Ca2+ release units: effects of RyR cluster size and Ca2+ buffers on diastolic Ca2+ leak', *Pflügers Archiv - European Journal of Physiology*, 473(3), pp. 435–446. doi:10.1007/s00424-021-02539-w.

Fischer, T.H., Eiringhaus, J., Dybkova, N., Förster, A., Herting, J., Kleinwächter, A., Ljubojevic, S., Schmitto, J.D., *et al.* (2014) 'Ca(2+) /calmodulin-dependent protein kinase II equally induces sarcoplasmic reticulum Ca(2+) leak in human ischaemic and dilated cardiomyopathy', *European Journal of Heart Failure*, 16(12), pp. 1292–1300. doi:10.1002/ejhf.163.

Fischer, T.H., Herting Jonas, Tirilomis Theodor, Renner André, Neef Stefan, Toischer Karl, Ellenberger David, Förster Anna, *et al.* (2013) 'Ca2+/Calmodulin-Dependent Protein Kinase II and Protein Kinase A Differentially Regulate Sarcoplasmic Reticulum Ca2+ Leak in Human Cardiac Pathology', *Circulation*, 128(9), pp. 970–981. doi:10.1161/CIRCULATIONAHA.113.001746.

Fish, D.A., Brinicombe, A.M., Pike, E.R. and Walker, J.G. (1995) 'Blind deconvolution by means of the Richardson–Lucy algorithm', *JOSA A*, 12(1), pp. 58–65. doi:10.1364/JOSAA.12.000058.

Fowler, E.D., Benoist, D., Drinkhill, M.J., Stones, R., Helmes, M., Wüst, R.C.I., Stienen, G.J.M., Steele, D.S., *et al.* (2015) 'Decreased creatine kinase is linked to diastolic dysfunction in rats with right heart failure induced by pulmonary artery hypertension', *Journal of Molecular and Cellular Cardiology*, 86, pp. 1–8. doi:10.1016/j.yjmcc.2015.06.016.

Fowler, E.D., Drinkhill, M.J., Norman, R., Pervolaraki, E., Stones, R., Steer, E., Benoist, D., Steele, D.S., *et al.* (2018) 'Beta1-adrenoceptor antagonist, metoprolol attenuates cardiac myocyte Ca2+ handling dysfunction in rats with pulmonary artery hypertension', *Journal of Molecular and Cellular Cardiology*, 120, pp. 74–83. doi:10.1016/j.yjmcc.2018.05.015.

Fowler, E.D., Drinkhill, M.J., Stones, R. and White, E. (2018) 'Diastolic dysfunction in pulmonary artery hypertension: Creatine kinase and the potential therapeutic benefit of beta-blockers', *Clinical and Experimental Pharmacology & Physiology*, 45(4), pp. 384–389. doi:10.1111/1440-1681.12898.

Franzini-Armstrong, C., Protasi, F. and Tijskens, P. (2005) 'The Assembly of Calcium Release Units in Cardiac Muscle', *Annals of the New York Academy of Sciences*, 1047(1), pp. 76–85. doi:https://doi.org/10.1196/annals.1341.007.

Friedberg, M.K. and Redington, A.N. (2014) 'Right Versus Left Ventricular Failure', *Circulation*, 129(9), pp. 1033–1044. doi:10.1161/CIRCULATIONAHA.113.001375.

Frisk, M., Ruud, M., Espe, E.K.S., Aronsen, J.M., Røe, Å.T., Zhang, L., Norseng, P.A., Sejersted, O.M., *et al.* (2016) 'Elevated ventricular wall stress disrupts cardiomyocyte t-tubule structure and calcium homeostasis', *Cardiovascular Research*, 112(1), pp. 443–451. doi:10.1093/cvr/cvw111.

Fu, Y., Shaw, S.A., Naami, R., Vuong, C.L., Basheer, W.A., Guo, X. and Hong, T. (2016) 'Isoproterenol Promotes Rapid Ryanodine Receptor Movement to Bridging Integrator 1 (BIN1)-Organized Dyads', *Circulation*, 133(4), pp. 388–97. doi:10.1161/circulationaha.115.018535.

Fukuda, M., Yamamoto, T., Nishimura, S., Kato, T., Murakami, W., Hino, A., Ono, M., Tateishi, H., *et al.* (2014) 'Enhanced binding of calmodulin to RyR2 corrects arrhythmogenic channel disorder in CPVT-associated myocytes', *Biochemical and Biophysical Research Communications*, 448(1), pp. 1–7. doi:10.1016/j.bbrc.2014.03.152.

Galbraith, C.G. and Galbraith, J.A. (2011) 'Super-resolution microscopy at a glance', *Journal of Cell Science*, 124(Pt 10), pp. 1607–1611. doi:10.1242/jcs.080085.

Gambarotto, D., Zwettler, F.U., Le Guennec, M., Schmidt-Cernohorska, M., Fortun, D., Borgers, S., Heine, J., Schloetel, J.-G., *et al.* (2019) 'Imaging cellular ultrastructures using expansion microscopy (U-ExM)', *Nature Methods*, 16(1), pp. 71–74. doi:10.1038/s41592-018-0238-1.

Gao, M., Maraspini, R., Beutel, O., Zehtabian, A., Eickholt, B., Honigmann, A. and Ewers, H. (2018) 'Expansion Stimulated Emission Depletion Microscopy (ExSTED)', *ACS Nano* [Preprint]. doi:10.1021/acsnano.8b00776.

Gao, R., Asano, S.M., Upadhyayula, S., Pisarev, I., Milkie, D.E., Liu, T.-L., Singh, V., Graves, A., *et al.* (2019) 'Cortical column and whole-brain imaging with molecular contrast and nanoscale resolution', *Science*, 363(6424), p. eaau8302. doi:10.1126/science.aau8302.

Gao, R., Yu, C.-C. (Jay), Gao, L., Piatkevich, K.D., Neve, R.L., Munro, J.B., Upadhyayula, S. and Boyden, E.S. (2021) 'A highly homogeneous polymer composed of tetrahedron-like monomers for high-isotropy expansion microscopy', *Nature Nanotechnology*, pp. 1–10. doi:10.1038/s41565-021-00875-7.

Gherghiceanu, M., Barad, L., Novak, A., Reiter, I., Itskovitz-Eldor, J., Binah, O. and Popescu, L.M. (2011) 'Cardiomyocytes derived from human embryonic and induced pluripotent stem cells: comparative ultrastructure', *Journal of Cellular and Molecular Medicine*, 15(11), pp. 2539–2551. doi:https://doi.org/10.1111/j.1582-4934.2011.01417.x.

Gómez, A.M., Valdivia, H.H., Cheng, H., Lederer, M.R., Santana, L.F., Cannell, M.B., McCune, S.A., Altschuld, R.A., *et al.* (1997) 'Defective Excitation-Contraction Coupling in Experimental Cardiac Hypertrophy and Heart Failure', *Science*, 276(5313), pp. 800–806. doi:10.1126/science.276.5313.800.

Gomez-Arroyo, J.G., Farkas, L., Alhussaini, A.A., Farkas, D., Kraskauskas, D., Voelkel, N.F. and Bogaard, H.J. (2012) 'The monocrotaline model of pulmonary hypertension in perspective', *Am J Physiol Lung Cell Mol Physiol*, 302(4), pp. L363-9. doi:10.1152/ajplung.00212.2011.

Götz, R., Kunz, T.C., Fink, J., Solger, F., Schlegel, J., Seibel, J., Kozjak-Pavlovic, V., Rudel, T., *et al.* (2020) 'Nanoscale imaging of bacterial infections by sphingolipid expansion microscopy', *Nature Communications*, 11(1), p. 6173. doi:10.1038/s41467-020-19897-1.

Götz, R., Panzer, S., Trinks, N., Eilts, J., Wagener, J., Turrà, D., Di Pietro, A., Sauer, M., *et al.* (2020) 'Expansion Microscopy for Cell Biology Analysis in Fungi', *Frontiers in Microbiology*, 11. doi:10.3389/fmicb.2020.00574.

Greyson, C. (2008) 'Pathophysiology of right ventricular failure', *Critical Care Medicine*, 36(1). doi:10.1097/01.CCM.0000296265.52518.70.

Guo, A., Hall, D., Zhang, C., Peng, T., Miller, J.D., Kutschke, W., Grueter, C.E., Johnson, F.L., *et al.* (2015) 'Molecular Determinants of Calpain-dependent Cleavage of Junctophilin-2 Protein in Cardiomyocytes', *Journal of Biological Chemistry*, 290(29), pp. 17946–17955. doi:10.1074/jbc.M115.652396.

Guo Tao, Cornea Razvan L., Huke Sabine, Camors Emmanuel, Yang Yi, Picht Eckard, Fruen Bradley R., and Bers Donald M. (2010) 'Kinetics of FKBP12.6 Binding to Ryanodine Receptors in Permeabilized Cardiac Myocytes and Effects on Ca Sparks', *Circulation Research*, 106(11), pp. 1743–1752. doi:10.1161/CIRCRESAHA.110.219816.

Guo Tao, Zhang Tong, Mestril Ruben, and Bers Donald M. (2006) 'Ca2+/Calmodulin-Dependent Protein Kinase II Phosphorylation of Ryanodine Receptor Does Affect Calcium Sparks in Mouse Ventricular Myocytes', *Circulation Research*, 99(4), pp. 398–406. doi:10.1161/01.RES.0000236756.06252.13.

Gustafsson, M.G.L. (2000) 'Surpassing the lateral resolution limit by a factor of two using structured illumination microscopy', *Journal of Microscopy*, 198(2), pp. 82–87. doi:10.1046/j.1365-2818.2000.00710.x.

Haddad, F., Doyle Ramona, Murphy Daniel J., and Hunt Sharon A. (2008) 'Right Ventricular Function in Cardiovascular Disease, Part II', *Circulation*, 117(13), pp. 1717–1731. doi:10.1161/CIRCULATIONAHA.107.653584.

Haddad, F., Hunt, S.A., Rosenthal, D.N. and Murphy, D.J. (2008) 'Right Ventricular Function in Cardiovascular Disease, Part I', *Circulation*, 117(11), pp. 1436–1448. doi:10.1161/CIRCULATIONAHA.107.653576.

Haddock, P.S., Coetzee, W.A., Cho, E., Porter, L., Katoh, H., Bers, D.M., Jafri, M.S. and Artman, M. (1999) 'Subcellular [Ca2+]i gradients during excitation-contraction coupling in newborn rabbit ventricular myocytes', *Circulation Research*, 85(5), pp. 415–427. doi:10.1161/01.res.85.5.415.

Hadipour-Lakmehsari, S., Driouchi, A., Lee, S.-H., Kuzmanov, U., Callaghan, N.I., Heximer, S.P., Simmons, C.A., Yip, C.M., *et al.* (2019) 'Nanoscale reorganization of sarcoplasmic reticulum in pressure-overload cardiac hypertrophy visualized by dSTORM', *Scientific Reports*, 9(1), p. 7867. doi:10.1038/s41598-019-44331-y.

Halpern, A.R., Alas, G.C.M., Chozinski, T.J., Paredez, A.R. and Vaughan, J.C. (2017) 'Hybrid Structured Illumination Expansion Microscopy Reveals Microbial Cytoskeleton Organization', *ACS Nano* [Preprint]. doi:10.1021/acsnano.7b07200.

Hardy, M.E.L., Pervolaraki, E., Bernus, O. and White, E. (2018) 'Dynamic Action Potential Restitution Contributes to Mechanical Restitution in Right Ventricular Myocytes From Pulmonary Hypertensive Rats', *Frontiers in Physiology*, 9(205). doi:10.3389/fphys.2018.00205.

Hasan, A., Mohammadi, N., Nawaz, A., Kodagoda, T., Diakonov, I., Harding, S.E. and Gorelik, J. (2020) 'Age-Dependent Maturation of iPSC-CMs Leads to the Enhanced Compartmentation of β2AR-cAMP Signalling', *Cells*, 9(10), p. 2275. doi:10.3390/cells9102275.

Hasenfuss, G., Reinecke, H., Studer, R., Meyer, M., Pieske, B., Holtz, J., Holubarsch, C., Posival, H., *et al.* (1994) 'Relation between myocardial function and expression of sarcoplasmic reticulum Ca(2+)-ATPase in failing and nonfailing human myocardium.', *Circulation Research*, 75(3), pp. 434–442. doi:10.1161/01.RES.75.3.434.

Hayashi, T., Martone, M.E., Yu, Z., Thor, A., Doi, M., Holst, M.J., Ellisman, M.H. and Hoshijima, M. (2009) 'Three-dimensional electron microscopy reveals new details of membrane systems for Ca2+ signaling in the heart', *Journal of Cell Science*, 122(7), pp. 1005–1013. doi:10.1242/jcs.028175.

He, J., Conklin, M.W., Foell, J.D., Wolff, M.R., Haworth, R.A., Coronado, R. and Kamp, T.J. (2001) 'Reduction in density of transverse tubules and L-type Ca(2+) channels in canine tachycardia-induced heart failure', *Cardiovasc Res*, 49(2), pp. 298–307.

Heart Statistics, British Heart Foundation (2021) *British Heart Foundation*. Available at: https://www.bhf.org.uk/what-we-do/our-research/heart-statistics (Accessed: 6 January 2021).

Heilemann, M., van de Linde, S., Schüttpelz, M., Kasper, R., Seefeldt, B., Mukherjee, A., Tinnefeld, P. and Sauer, M. (2008) 'Subdiffraction-Resolution Fluorescence Imaging with Conventional Fluorescent Probes', *Angewandte Chemie International Edition*, 47(33), pp. 6172–6176. doi:10.1002/anie.200802376.

Hell, S.W. and Wichmann, J. (1994) 'Breaking the diffraction resolution limit by stimulated emission: stimulated-emission-depletion fluorescence microscopy', *Opt Lett*, 19. doi:10.1364/ol.19.000780.

Hong, T., Yang, H., Zhang, S.-S., Cho, H.C., Kalashnikova, M., Sun, B., Zhang, H., Bhargava, A., *et al.* (2014) 'Cardiac BIN1 folds T-tubule membrane, controlling ion flux and limiting arrhythmia', *Nat Med*, 20(6), pp. 624–632. doi:10.1038/nm.3543.

Hong, T.-T., Smyth, J.W., Gao, D., Chu, K.Y., Vogan, J.M., Fong, T.S., Jensen, B.C., Colecraft, H.M., *et al.* (2010) 'BIN1 Localizes the L-Type Calcium Channel to Cardiac T-Tubules', *PLOS Biology*, 8(2), p. e1000312. doi:10.1371/journal.pbio.1000312.

Hörl, D., Rojas Rusak, F., Preusser, F., Tillberg, P., Randel, N., Chhetri, R.K., Cardona, A., Keller, P.J., *et al.* (2019) 'BigStitcher: reconstructing high-resolution image datasets of cleared and expanded samples', *Nature Methods* [Preprint]. doi:10.1038/s41592-019-0501-0.

Hou, Y., Jayasinghe, I., Crossman, D.J., Baddeley, D. and Soeller, C. (2015) 'Nanoscale analysis of ryanodine receptor clusters in dyadic couplings of rat cardiac myocytes', *J Mol Cell Cardiol*, 80, pp. 45–55. doi:10.1016/j.yjmcc.2014.12.013.

Houser, S.R. (2014) 'Controversies in Cardiovascular Research', *Circulation research*, 114(8), pp. 1320–1327. doi:10.1161/CIRCRESAHA.114.300569.

Huang, B., Wang, W., Bates, M. and Zhuang, X. (2008) 'Three-Dimensional Super-Resolution Imaging by Stochastic Optical Reconstruction Microscopy', *Science*, 319(5864), pp. 810–813. doi:10.1126/science.1153529.

Huff, J., Bergter, A., Birkenbeil, J., Kleppe, I., Engelmann, R. and Krzic, U. (2017) 'The new 2D Superresolution mode for ZEISS Airyscan', *Nature Methods*, 14(12), pp. 1223–1223. doi:10.1038/nmeth.f.404.

Huke, S. and Bers, D.M. (2008) 'Ryanodine receptor phosphorylation at Serine 2030, 2808 and 2814 in rat cardiomyocytes', *Biochemical and Biophysical Research Communications*, 376(1), pp. 80–85. doi:10.1016/j.bbrc.2008.08.084.

Hwang, H.S., Kryshtal, D.O., Feaster, T.K., Sánchez-Freire, V., Zhang, J., Kamp, T.J., Hong, C.C., Wu, J.C., *et al.* (2015) 'Comparable calcium handling of human iPSC-derived cardiomyocytes generated by multiple laboratories', *Journal of Molecular and Cellular Cardiology*, 85, pp. 79–88. doi:10.1016/j.yjmcc.2015.05.003.

Ibrahim, M., Navaratnarajah, M., Siedlecka, U., Rao, C., Dias, P., Moshkov, A.V., Gorelik, J., Yacoub, M.H., *et al.* (2012) 'Mechanical unloading reverses transverse tubule remodelling and normalizes local Ca2+-induced Ca2+release in a rodent model of heart failure', *European Journal of Heart Failure*, 14(6), pp. 571–580. doi:10.1093/eurjhf/hfs038.

Ibrahim, M. and Terracciano, C.M. (2013) 'Reversibility of T-tubule remodelling in heart failure: mechanical load as a dynamic regulator of the T-tubules', *Cardiovasc Res*, 98(2), pp. 225–32. doi:10.1093/cvr/cvt016.

Ishikawa, S., Honda, M., Yamada, S., Morioka, S. and Moriyama, K. (1991) 'Biventricular down-Regulation of Beta-Adrenergic Receptors in Right Ventricular Hypertrophy Induced by Monocrotaline', *Japanese Circulation Journal*, 55(11), pp. 1077–1085. doi:10.1253/jcj.55.1077.

Itzhaki, I., Rapoport, S., Huber, I., Mizrahi, I., Zwi-Dantsis, L., Arbel, G., Schiller, J. and Gepstein, L. (2011) 'Calcium Handling in Human Induced Pluripotent Stem Cell Derived Cardiomyocytes', *PLoS ONE*, 6(4), p. e18037. doi:10.1371/journal.pone.0018037.

Izu, L.T., Means, S.A., Shadid, J.N., Chen-Izu, Y. and Balke, C.W. (2006) 'Interplay of Ryanodine Receptor Distribution and Calcium Dynamics', *Biophysical Journal*, 91(1), pp. 95–112. doi:10.1529/biophysj.105.077214.

Jayasinghe, Baddeley, D., Kong, C.H., Wehrens, X.H., Cannell, M.B. and Soeller, C. (2012) 'Nanoscale Organization of Junctophilin-2 and Ryanodine Receptors within Peripheral

Couplings of Rat Ventricular Cardiomyocytes', *Biophysical Journal*, 102(5), pp. L19–L21. doi:10.1016/j.bpj.2012.01.034.

Jayasinghe, Cannell, M.B. and Soeller, C. (2009) 'Organization of Ryanodine Receptors, Transverse Tubules, and Sodium-Calcium Exchanger in Rat Myocytes', *Biophysical Journal*, 97(10), pp. 2664–2673. doi:10.1016/j.bpj.2009.08.036.

Jayasinghe, Clowsley, A.H., Lin, R., Lutz, T., Harrison, C., Green, E., Baddeley, D., Di Michele, L., *et al.* (2018) 'True Molecular Scale Visualization of Variable Clustering Properties of Ryanodine Receptors', *Cell Reports*, 22(2), pp. 557–567. doi:10.1016/j.celrep.2017.12.045.

Jayasinghe, Crossman, D.J., Soeller, C. and Cannell, M.B. (2010) 'A new twist in cardiac muscle: dislocated and helicoid arrangements of myofibrillar z-disks in mammalian ventricular myocytes', *Journal of Molecular and Cellular Cardiology*, 48(5), pp. 964–971. doi:10.1016/j.yjmcc.2009.12.012.

Jayasinghe, Crossman, D.J., Soeller, C. and Cannell, M.B. (2012) 'Comparison of the organization of t-tubules, sarcoplasmic reticulum and ryanodine receptors in rat and human ventricular myocardium', *Clinical and Experimental Pharmacology and Physiology*, 39(5), pp. 469–476. doi:10.1111/j.1440-1681.2011.05578.x.

Jiang, M.T., Lokuta, A.J., Farrell, E.F., Wolff, M.R., Haworth, R.A. and Valdivia, H.H. (2002) 'Abnormal Ca2+ release, but normal ryanodine receptors, in canine and human heart failure', *Circulation Research*, 91(11), pp. 1015–1022. doi:10.1161/01.res.0000043663.08689.05.

Jungmann, R., Avendano, M.S., Dai, M., Woehrstein, J.B., Agasti, S.S., Feiger, Z., Rodal, A. and Yin, P. (2016) 'Quantitative super-resolution imaging with qPAINT', *Nat Meth*, 13(5), pp. 439–442. doi:10.1038/nmeth.3804.

Jungmann, R., Avendano, M.S., Woehrstein, J.B., Dai, M., Shih, W.M. and Yin, P. (2014) 'Multiplexed 3D cellular super-resolution imaging with DNA-PAINT and Exchange-PAINT', *Nat Meth*, 11(3), pp. 313–318. doi:10.1038/nmeth.2835.

Junker, J., Sommer, J.R., Sar, M. and Meissner, G. (1994) 'Extended junctional sarcoplasmic reticulum of avian cardiac muscle contains functional ryanodine receptors.', *Journal of Biological Chemistry*, 269(3), pp. 1627–1634.

Kao, P. and Nodine, M.D. (2019) 'Transcriptional Activation of Arabidopsis Zygotes Is Required for Initial Cell Divisions', *Scientific Reports*, 9(1), pp. 1–11. doi:10.1038/s41598-019-53704-2.

Kaprielian, R.R., Stevenson, S., Rothery, S.M., Cullen, M.J. and Severs, N.J. (2000) 'Distinct patterns of dystrophin organization in myocyte sarcolemma and transverse tubules of normal and diseased human myocardium', *Circulation*, 101(22), pp. 2586–94.

Karagiannis, E.D., Kang, J.S., Shin, T.W., Emenari, A., Asano, S., Lin, L., Costa, E.K., Consortium, C.I.G.C., *et al.* (2019) 'Expansion Microscopy of Lipid Membranes', *bioRxiv*, p. 829903. doi:10.1101/829903.

Kemi, O.J., Hoydal, M.A., Macquaide, N., Haram, P.M., Koch, L.G., Britton, S.L., Ellingsen, O., Smith, G.L., *et al.* (2011) 'The effect of exercise training on transverse tubules in normal,

remodeled, and reverse remodeled hearts', *Journal of Cellular Physiology*, 226(9), pp. 2235–2243. doi:10.1002/jcp.22559.

Kim, D., Kim, T., Lee, J. and Shim, S.-H. (2019) 'Amplified Expansion Stimulated Emission Depletion Microscopy', *ChemBioChem*, 20(10), pp. 1260–1265. doi:10.1002/cbic.201800775.

Kirshner, H., Pengo, T., Olivier, N., Sage, D., Manley, S. and Unser, M. (2012) 'A PSF-based approach to Biplane calibration in 3D super-resolution microscopy', in *2012 9th IEEE International Symposium on Biomedical Imaging (ISBI). 2012 9th IEEE International Symposium on Biomedical Imaging (ISBI)*, pp. 1232–1235. doi:10.1109/ISBI.2012.6235784.

Kögler, H., Hartmann, O., Leineweber, K., Nguyen van, P., Schott, P., Brodde, O.-E. and Hasenfuss, G. (2003) 'Mechanical Load-Dependent Regulation of Gene Expression in Monocrotaline-Induced Right Ventricular Hypertrophy in the Rat', *Circulation Research*, 93(3), pp. 230–237. doi:10.1161/01.res.0000085042.89656.c7.

Koivumaki, J.T., Naumenko, N., Tuomainen, T., Takalo, J., Oksanen, M., Puttonen, K.A., Lehtonen, S., Kuusisto, J., *et al.* (2018) 'Structural Immaturity of Human iPSC-Derived Cardiomyocytes: In Silico Investigation of Effects on Function and Disease Modeling', *Front Physiol*, 9, p. 80. doi:10.3389/fphys.2018.00080.

Kolstad, T.R., van den Brink, J., MacQuaide, N., Lunde, P.K., Frisk, M., Aronsen, J.M., Norden, E.S., Cataliotti, A., *et al.* (2018) 'Ryanodine receptor dispersion disrupts Ca2+ release in failing cardiac myocytes', *eLife*, 7, p. e39427. doi:10.7554/eLife.39427.

Kong, C.W., Akar, F.G. and Li, R.A. (2010) 'Translational potential of human embryonic and induced pluripotent stem cells for myocardial repair: insights from experimental models', *Thromb Haemost*, 104(1), pp. 30–8. doi:10.1160/th10-03-0189.

Kuramochi, T., Honda, M., Tanaka, K., Enornoto, K., Hashimoto, M. and Morioka, S. (1994) 'Calcium Transients in Single Myocytes and Membranous Ultrastructures During the Development of Cardiac Hypertrophy and Heart Failure in Rats', *Clinical and Experimental Pharmacology and Physiology*, 21(12), pp. 1009–1018. doi:10.1111/j.1440-1681.1994.tb02664.x.

Lahiri, S.K., Quick, A.P., Samson-Couterie, B., Hulsurkar, M., Elzenaar, I., van Oort, R.J. and Wehrens, X.H.T. (2020) 'Nuclear localization of a novel calpain-2 mediated junctophilin-2 C-terminal cleavage peptide promotes cardiomyocyte remodeling', *Basic Research in Cardiology*, 115(4), p. 49. doi:10.1007/s00395-020-0807-1.

Landstrom, A.P., Weisleder, N., Batalden, K.B., Bos, J.M., Tester, D.J., Ommen, S.R., Wehrens, X.H., Claycomb, W.C., *et al.* (2007) 'Mutations in JPH2-encoded junctophilin-2 associated with hypertrophic cardiomyopathy in humans', *J Mol Cell Cardiol*, 42(6), pp. 1026–35. doi:10.1016/j.yjmcc.2007.04.006.

Lawless, M., Caldwell, J.L., Radcliffe, E.J., Smith, C.E.R., Madders, G.W.P., Hutchings, D.C., Woods, L.S., Church, S.J., *et al.* (2019) 'Phosphodiesterase 5 inhibition improves contractile function and restores transverse tubule loss and catecholamine responsiveness in heart failure', *Scientific Reports*, 9(1), p. 6801. doi:10.1038/s41598-019-42592-1.

Lee, E., Marcucci, M., Daniell, L., Pypaert, M., Weisz, O.A., Ochoa, G.C., Farsad, K., Wenk, M.R., *et al.* (2002) 'Amphiphysin 2 (Bin1) and T-tubule biogenesis in muscle', *Science*, 297(5584), pp. 1193–6. doi:10.1126/science.1071362.

Lee, J.K., Kodama, I., Honjo, H., Anno, T., Kamiya, K. and Toyama, J. (1997) 'Stage-dependent changes in membrane currents in rats with monocrotaline-induced right ventricular hypertrophy', *American Journal of Physiology-Heart and Circulatory Physiology*, 272(6), pp. H2833–H2842. doi:10.1152/ajpheart.1997.272.6.H2833.

Lee, Y.-K., Ng, K.-M., Lai, W.-H., Chan, Y.-C., Lau, Y.-M., Lian, Q., Tse, H.-F. and Siu, C.-W. (2011) 'Calcium homeostasis in human induced pluripotent stem cell-derived cardiomyocytes', *Stem Cell Reviews and Reports*, 7(4), pp. 976–986. doi:10.1007/s12015-011-9273-3.

Leineweber, K., Seyfarth, T., Abraham, G., Gerbershagen, H.-P., Heinroth-Hoffmann, I., Pönicke, K. and Brodde, O.-E. (2003) 'Cardiac β-Adrenoceptor Changes in Monocrotaline-Treated Rats: Differences Between Membrane Preparations From Whole Ventricles and Isolated Ventricular Cardiomyocytes', *Journal of Cardiovascular Pharmacology*, 41(3), p. 333.

Li, J., Imtiaz, M.S., Beard, N.A., Dulhunty, A.F., Thorne, R., vanHelden, D.F. and Laver, D.R. (2013) 'ß-Adrenergic Stimulation Increases RyR2 Activity via Intracellular Ca2+ and Mg2+ Regulation', *PLOS ONE*, 8(3), p. e58334. doi:10.1371/journal.pone.0058334.

Li, R., Chen, X., Lin, Z., Wang, Y. and Sun, Y. (2018) 'Expansion enhanced nanoscopy', *Nanoscale* [Preprint]. doi:10.1039/C8NR04267E.

Li, R.C., Tao, J., Guo, Y.B., Wu, H.D., Liu, R.F., Bai, Y., Lv, Z.Z., Luo, G.Z., *et al.* (2013) 'In vivo suppression of microRNA-24 prevents the transition toward decompensated hypertrophy in aortic-constricted mice', *Circ Res*, 112(4), pp. 601–5. doi:10.1161/circresaha.112.300806.

Li, Y., Kranias Evangelia G., Mignery Gregory A., and Bers Donald M. (2002) 'Protein Kinase A Phosphorylation of the Ryanodine Receptor Does Not Affect Calcium Sparks in Mouse Ventricular Myocytes', *Circulation Research*, 90(3), pp. 309–316. doi:10.1161/hh0302.105660.

Lieu, D.K., Liu, J., Siu, C.W., McNerney, G.P., Tse, H.F., Abu-Khalil, A., Huser, T. and Li, R.A. (2009) 'Absence of transverse tubules contributes to non-uniform Ca(2+) wavefronts in mouse and human embryonic stem cell-derived cardiomyocytes', *Stem Cells Dev*, 18(10), pp. 1493–500. doi:10.1089/scd.2009.0052.

Lim, Y., Shiver, A.L., Khariton, M., Lane, K.M., Ng, K.M., Bray, S.R., Qin, J., Huang, K.C., *et al.* (2019) 'Mechanically resolved imaging of bacteria using expansion microscopy', *PLOS Biology*, 17(10), p. e3000268. doi:10.1371/journal.pbio.3000268.

Lin, R., Clowsley, A.H., Lutz, T., Baddeley, D. and Soeller, C. (2019) '3D super-resolution microscopy performance and quantitative analysis assessment using DNA-PAINT and DNA origami test samples', *Methods* [Preprint]. doi:10.1016/j.ymeth.2019.05.018.

Lipsett, D.B., Frisk, M., Aronsen, J.M., Nordén, E.S., Buonarati, O.R., Cataliotti, A., Hell, J.W., Sjaastad, I., *et al.* (2019) 'Cardiomyocyte substructure reverts to an immature phenotype

during heart failure', *The Journal of Physiology*, 597(7), pp. 1833–1853. doi:10.1113/JP277273.

Liu, B., Ho, H.-T., Velez-Cortes, F., Lou, Q., Valdivia, C.R., Knollmann, B.C., Valdivia, H.H. and Gyorke, S. (2014) 'Genetic ablation of ryanodine receptor 2 phosphorylation at Ser-2808 aggravates Ca2+-dependent cardiomyopathy by exacerbating diastolic Ca2+ release', *The Journal of Physiology*, 592(9), pp. 1957–1973. doi:10.1113/jphysiol.2013.264689.

Liu, Y.-W., Chen, B., Yang, X., Fugate, J.A., Kalucki, F.A., Futakuchi-Tsuchida, A., Couture, L., Vogel, K.W., *et al.* (2018) 'Human embryonic stem cell–derived cardiomyocytes restore function in infarcted hearts of non-human primates', *Nature Biotechnology*, 36, p. 597. doi:10.1038/nbt.4162.

Louch, W.E., Bito, V., Heinzel, F.R., Macianskiene, R., Vanhaecke, J., Flameng, W., Mubagwa, K. and Sipido, K.R. (2004) 'Reduced synchrony of Ca2+ release with loss of T-tubules—a comparison to Ca2+ release in human failing cardiomyocytes', *Cardiovascular Research*, 62(1), pp. 63–73. doi:10.1016/j.cardiores.2003.12.031.

Louch, W.E., Hake, J., Mørk, H.K., Hougen, K., Skrbic, B., Ursu, D., Tønnessen, T., Sjaastad, I., *et al.* (2013) 'Slow Ca^{2+} sparks de-synchronize Ca^{2+} release in failing cardiomyocytes: evidence for altered configuration of Ca^{2+} release units?', *Journal of Molecular and Cellular Cardiology*, 58, pp. 41–52. doi:10.1016/j.yjmcc.2013.01.014.

Louch, W.E., Koivumäki, J.T. and Tavi, P. (2015) 'Calcium signalling in developing cardiomyocytes: implications for model systems and disease', *The Journal of Physiology*, 593(5), pp. 1047–1063. doi:10.1113/jphysiol.2014.274712.

Lu, C.-H., Tang, W.-C., Liu, Y.-T., Chang, S.-W., Wu, F.C.M., Chen, C.-Y., Tsai, Y.-C., Yang, S.-M., *et al.* (2019) 'Lightsheet localization microscopy enables fast, large-scale, and three-dimensional super-resolution imaging', *Communications Biology*, 2(1), pp. 1–10. doi:10.1038/s42003-019-0403-9.

Lundy, S.D., Zhu, W.Z., Regnier, M. and Laflamme, M.A. (2013) 'Structural and functional maturation of cardiomyocytes derived from human pluripotent stem cells', *Stem Cells Dev*, 22(14), pp. 1991–2002. doi:10.1089/scd.2012.0490.

Luo, X., Li, W., Künzel, K., Henze, S., Cyganek, L., Strano, A., Poetsch, M.S., Schubert, M., *et al.* (2020) 'IP3R-Mediated Compensatory Mechanism for Calcium Handling in Human Induced Pluripotent Stem Cell-Derived Cardiomyocytes With Cardiac Ryanodine Receptor Deficiency', *Frontiers in Cell and Developmental Biology*, 8. doi:10.3389/fcell.2020.00772.

Lyon, A.R., MacLeod, K.T., Zhang, Y., Garcia, E., Kanda, G.K., Lab, M.J., Korchev, Y.E., Harding, S.E., *et al.* (2009) 'Loss of T-tubules and other changes to surface topography in ventricular myocytes from failing human and rat heart', *Proc Natl Acad Sci U S A*, 106(16), pp. 6854–9. doi:10.1073/pnas.0809777106.

MacDonnell, S.M., García-Rivas, G., Scherman, J.A., Kubo, H., Chen, X., Valdivia, H. and Houser, S.R. (2008) 'Adrenergic regulation of cardiac contractility does not involve phosphorylation of the cardiac ryanodine receptor at serine 2808', *Circulation Research*, 102(8), pp. e65-72. doi:10.1161/CIRCRESAHA.108.174722.

Macquaide, N., Tuan, H.-T.M., Hotta, J., Sempels, W., Lenaerts, I., Holemans, P., Hofkens, J., Jafri, M.S., *et al.* (2015) 'Ryanodine receptor cluster fragmentation and redistribution in persistent atrial fibrillation enhance calcium release', *Cardiovascular Research*, 108(3), pp. 387–398. doi:10.1093/cvr/cvv231.

Marchena, M. and Echebarria, B. (2018) 'Computational Model of Calcium Signaling in Cardiac Atrial Cells at the Submicron Scale', *Frontiers in Physiology*, 9. doi:10.3389/fphys.2018.01760.

Marx, S.O., Gaburjakova, J., Gaburjakova, M., Henrikson, C., Ondrias, K. and Marks, A.R. (2001) 'Coupled gating between cardiac calcium release channels (ryanodine receptors)', *Circulation Research*, 88(11), pp. 1151–1158. doi:10.1161/hh1101.091268.

Marx, S.O., Reiken, S., Hisamatsu, Y., Jayaraman, T., Burkhoff, D., Rosemblit, N. and Marks, A.R. (2000) 'PKA phosphorylation dissociates FKBP12.6 from the calcium release channel (ryanodine receptor): defective regulation in failing hearts', *Cell*, 101(4), pp. 365–376. doi:10.1016/s0092-8674(00)80847-8.

McMartin, L. and Summers, R.J. (1999) 'Functional analysis of desensitization of the β-adrenoceptor signalling pathway in rat cardiac tissues following chronic isoprenaline infusion', *British Journal of Pharmacology*, 127(4), pp. 1012–1020. doi:10.1038/sj.bjp.0702618.

Mehmood and Frank (2016) 'Treatment of right heart failure: is there a solution to the problem?', *e-Journal of cardiology practice*, 14. Available at: https://www.escardio.org/Journals/E-Journal-of-Cardiology-Practice/Volume-14/Treatment-of-right-heart-failure-is-there-a-solution-to-the-problem.

Meissner, G. and Henderson, J.S. (1987) 'Rapid calcium release from cardiac sarcoplasmic reticulum vesicles is dependent on Ca2+ and is modulated by Mg2+, adenine nucleotide, and calmodulin.', *The Journal of biological chemistry*, 262(7), pp. 3065–3073.

Mercadier, J.J., Lompré, A.M., Duc, P., Boheler, K.R., Fraysse, J.B., Wisnewsky, C., Allen, P.D., Komajda, M., *et al.* (1990) 'Altered sarcoplasmic reticulum Ca2(+)-ATPase gene expression in the human ventricle during end-stage heart failure.', *Journal of Clinical Investigation*, 85(1), pp. 305–309.

Michalak, M. and Opas, M. (2009) 'Endoplasmic and sarcoplasmic reticulum in the heart', *Trends in Cell Biology*, 19(6), pp. 253–259. doi:10.1016/j.tcb.2009.03.006.

Minamisawa, S., Oshikawa, J., Takeshima, H., Hoshijima, M., Wang, Y., Chien, K.R., Ishikawa, Y. and Matsuoka, R. (2004) 'Junctophilin type 2 is associated with caveolin-3 and is down-regulated in the hypertrophic and dilated cardiomyopathies', *Biochemical and Biophysical Research Communications*, 325(3), pp. 852–856. doi:10.1016/j.bbrc.2004.10.107.

Minsky, M. (1988) 'Memoir on inventing the confocal scanning microscope', *Scanning*, 10(4), pp. 128–138. doi:10.1002/sca.4950100403.

Moretti, A., Bellin, M., Welling, A., Jung, C.B., Lam, J.T., Bott-Flügel, L., Dorn, T., Goedel, A., *et al.* (2010) 'Patient-Specific Induced Pluripotent Stem-Cell Models for Long-QT Syndrome', *New England Journal of Medicine*, 363(15), pp. 1397–1409. doi:10.1056/NEJMoa0908679.

Munro, M.L., Jayasinghe, I., Wang, Q., Quick, A., Wang, W., Baddeley, D., Wehrens, X.H.T. and Soeller, C. (2016) 'Junctophilin-2 in the nanoscale organisation and functional signalling of ryanodine receptor clusters in cardiomyocytes', *Journal of Cell Science* [Preprint]. doi:10.1242/jcs.196873.

Murphy, J.F., Mayourian, J., Stillitano, F., Munawar, S., Broughton, K.M., Agullo-Pascual, E., Sussman, M.A., Hajjar, R.J., *et al.* (2019) 'Adult human cardiac stem cell supplementation effectively increases contractile function and maturation in human engineered cardiac tissues', *Stem Cell Research & Therapy*, 10(1), p. 373. doi:10.1186/s13287-019-1486-4.

Neef Stefan, Dybkova Nataliya, Sossalla Samuel, Ort Katharina R., Fluschnik Nina, Neumann Kay, Seipelt Ralf, Schöndube Friedrich A., *et al.* (2010) 'CaMKII-Dependent Diastolic SR Ca2+ Leak and Elevated Diastolic Ca2+ Levels in Right Atrial Myocardium of Patients With Atrial Fibrillation', *Circulation Research*, 106(6), pp. 1134–1144. doi:10.1161/CIRCRESAHA.109.203836.

Nunes, S.S., Miklas, J.W., Liu, J., Aschar-Sobbi, R., Xiao, Y., Zhang, B., Jiang, J., Massé, S., *et al.* (2013) 'Biowire: a platform for maturation of human pluripotent stem cell–derived cardiomyocytes', *Nature Methods*, 10(8), pp. 781–787. doi:10.1038/nmeth.2524.

Obayashi, M., Xiao, B., Stuyvers, B.D., Davidoff, A.W., Mei, J., Chen, S.R.W. and ter Keurs, H.E.D.J. (2006) 'Spontaneous diastolic contractions and phosphorylation of the cardiac ryanodine receptor at serine-2808 in congestive heart failure in rat', *Cardiovascular Research*, 69(1), pp. 140–151. doi:10.1016/j.cardiores.2005.07.010.

Ogata, T. and Yamasaki, Y. (1990) 'High-resolution scanning electron microscopic studies on the three-dimensional structure of the transverse-axial tubular system, sarcoplasmic reticulum and intercalated disc of the rat myocardium', *The Anatomical Record*, 228(3), pp. 277–287. doi:10.1002/ar.1092280307.

Ollion, J., Cochennec, J., Loll, F., Escudé, C. and Boudier, T. (2013) 'TANGO: a generic tool for high-throughput 3D image analysis for studying nuclear organization', *Bioinformatics*, 29(14), pp. 1840–1841. doi:10.1093/bioinformatics/btt276.

van Oort, R.J., Garbino, A., Wang, W., Dixit, S.S., Landstrom, A.P., Gaur, N., De Almeida, A.C., Skapura, D.G., *et al.* (2011) 'Disrupted junctional membrane complexes and hyperactive ryanodine receptors after acute junctophilin knockdown in mice', *Circulation*, 123(9), pp. 979–88. doi:10.1161/circulationaha.110.006437.

Parikh, S.S., Blackwell, D.J., Gomez-Hurtado, N., Frisk, M., Wang, L., Kim, K., Dahl, C.P., Fiane, A., *et al.* (2017) 'Thyroid and Glucocorticoid Hormones Promote Functional T-Tubule Development in Human-Induced Pluripotent Stem Cell–Derived CardiomyocytesNovelty and Significance', *Circulation Research*, 121(12), pp. 1323–1330. doi:10.1161/circresaha.117.311920.

Parton, R.G., Way, M., Zorzi, N. and Stang, E. (1997) 'Caveolin-3 associates with developing T-tubules during muscle differentiation', *The Journal of Cell Biology*, 136(1), pp. 137–154. doi:10.1083/jcb.136.1.137.

Peng, W., Shen, H., Wu, J., Guo, W., Pan, X., Wang, R., Chen, S.R.W. and Yan, N. (2016) 'Structural basis for the gating mechanism of the type 2 ryanodine receptor RyR2', *Science (New York, N.Y.)*, 354(6310). doi:10.1126/science.aah5324.

Pernal, S.P., Liyanaarachchi, A., Gatti, D.L., Formosa, B., Pulvender, R., Kuhn, E.R., Ramos, R., Naik, A.R., *et al.* (2020) 'Nanoscale imaging using differential expansion microscopy', *Histochemistry and Cell Biology* [Preprint]. doi:10.1007/s00418-020-01869-7.

Pesce, L., Cozzolino, M., Lanzanò, L., Diaspro, A. and Bianchini, P. (2019) 'Measuring expansion from macro- to nanoscale using NPC as intrinsic reporter', *Journal of Biophotonics*, 12(8), p. e201900018. doi:10.1002/jbio.201900018.

Pinali, C., Malik, N., Davenport, J.B., Allan, L.J., Murfitt, L., Iqbal, M.M., Boyett, M.R., Wright, E.J., *et al.* (2017) 'Post-Myocardial Infarction T-tubules Form Enlarged Branched Structures With Dysregulation of Junctophilin-2 and Bridging Integrator 1 (BIN-1)', *Journal of the American Heart Association*, 6(5). doi:10.1161/jaha.116.004834.

Potenza, D.M., Janicek, R., Fernandez-Tenorio, M., Camors, E., Ramos-Mondragón, R., Valdivia, H.H. and Niggli, E. (2018) 'Phosphorylation of the ryanodine receptor 2 at serine 2030 is required for a complete β-adrenergic response', *The Journal of General Physiology*, p. jgp.201812155. doi:10.1085/jgp.201812155.

Poulet, C., Sanchez-Alonso, J., Swiatlowska, P., Mouy, F., Lucarelli, C., Alvarez-Laviada, A., Gross, P., Terracciano, C., *et al.* (2021) 'Junctophilin-2 tethers T-tubules and recruits functional L-type calcium channels to lipid rafts in adult cardiomyocytes', *Cardiovascular Research* [Preprint]. doi:10.1093/cvr/cvaa033.

Power, A.S., Hickey, A.J., Crossman, D.J., Loiselle, D.S. and Ward, M.L. (2018) 'Calcium mishandling impairs contraction in right ventricular hypertrophy prior to overt heart failure', *Pflugers Arch* [Preprint]. doi:10.1007/s00424-018-2125-0.

Prins, K.W., Tian, L., Wu, D., Thenappan, T., Metzger, J.M. and Archer, S.L. (2017) 'Colchicine Depolymerizes Microtubules, Increases Junctophilin-2, and Improves Right Ventricular Function in Experimental Pulmonary Arterial Hypertension', *J Am Heart Assoc*, 6(6). doi:10.1161/jaha.117.006195.

Prisco, S.Z., Thenappan, T. and Prins, K.W. (2020) 'Treatment Targets for Right Ventricular Dysfunction in Pulmonary Arterial Hypertension', *JACC: Basic to Translational Science*, 5(12), pp. 1244–1260. doi:10.1016/j.jacbts.2020.07.011.

Proenza, C., O'Brien, J., Nakai, J., Mukherjee, S., Allen, P.D. and Beam, K.G. (2002) 'Identification of a region of RyR1 that participates in allosteric coupling with the alpha(1S) (Ca(V)1.1) II-III loop', *The Journal of Biological Chemistry*, 277(8), pp. 6530–6535. doi:10.1074/jbc.M106471200.

Rao, C., Prodromakis, T., Kolker, L., Chaudhry, U.A.R., Trantidou, T., Sridhar, A., Weekes, C., Camelliti, P., *et al.* (2013) 'The effect of microgrooved culture substrates on calcium cycling of cardiac myocytes derived from human induced pluripotent stem cells', *Biomaterials*, 34(10), pp. 2399–2411. doi:10.1016/j.biomaterials.2012.11.055.

Rapila, R., Korhonen, T. and Tavi, P. (2008) 'Excitation–Contraction Coupling of the Mouse Embryonic Cardiomyocyte', *The Journal of General Physiology*, 132(4), pp. 397–405. doi:10.1085/jgp.200809960.

Rayleigh, Lord (1903) 'On the Theory of Optical Images, with special reference to the Microscope', *Journal of the Royal Microscopical Society*, 23(4), pp. 474–482. doi:10.1111/j.1365-2818.1903.tb04831.x.

Reiken, S., Gaburjakova, M., Guatimosim, S., Gomez, A.M., D'Armiento, J., Burkhoff, D., Wang, J., Vassort, G., *et al.* (2003) 'Protein kinase A phosphorylation of the cardiac calcium release channel (ryanodine receptor) in normal and failing hearts. Role of phosphatases and response to isoproterenol', *The Journal of Biological Chemistry*, 278(1), pp. 444–453. doi:10.1074/jbc.M207028200.

Respress, J.L., van Oort, R.J., Li, N., Rolim, N., Dixit, S.S., deAlmeida, A., Voigt, N., Lawrence, W.S., *et al.* (2012) 'Role of RyR2 phosphorylation at S2814 during heart failure progression', *Circulation Research*, 110(11), pp. 1474–1483. doi:10.1161/CIRCRESAHA.112.268094.

Reynolds, J.O., Chiang, D.Y., Wang, W., Beavers, D.L., Dixit, S.S., Skapura, D.G., Landstrom, A.P., Song, L.-S., *et al.* (2013) 'Junctophilin-2 is necessary for T-tubule maturation during mouse heart development', *Cardiovascular Research*, 100(1), pp. 44–53. doi:10.1093/cvr/cvt133.

Reynolds, J.O., Quick, A.P., Wang, Q., Beavers, D.L., Philippen, L.E., Showell, J., Barreto-Torres, G., Thuerauf, D.J., *et al.* (2016) 'Junctophilin-2 gene therapy rescues heart failure by normalizing RyR2-mediated Ca2+ release', *International Journal of Cardiology*, 225, pp. 371–380. doi:10.1016/j.ijcard.2016.10.021.

Rodriguez, P., Bhogal, M.S. and Colyer, J. (2003) 'Stoichiometric Phosphorylation of Cardiac Ryanodine Receptor on Serine 2809 by Calmodulin-dependent Kinase II and Protein Kinase A', *Journal of Biological Chemistry*, 278(40), pp. 38593–38600. doi:10.1074/jbc.M301180200.

Røe, Å.T., Frisk, M. and Louch, W.E. (2015) 'Targeting Cardiomyocyte Ca(2+) Homeostasis in Heart Failure', *Current Pharmaceutical Design*, 21(4), pp. 431–448. doi:10.2174/1381612821041412041241 29.

Ronaldson-Bouchard, K., Ma, S.P., Yeager, K., Chen, T., Song, L., Sirabella, D., Morikawa, K., Teles, D., *et al.* (2018) 'Advanced maturation of human cardiac tissue grown from pluripotent stem cells', *Nature* [Preprint]. doi:10.1038/s41586-018-0016-3.

Sabourin, J., Angèle, B., Catherine, R.-M., Mélanie, L., Ana-Maria, G., Jean-Pierre, B., Frédéric, P., Marc, H., *et al.* (2018) 'Ca2+ handling remodeling and STIM1L/Orai1/TRPC1/TRPC4 upregulation in monocrotaline-induced right ventricular hypertrophy', *Journal of Molecular and Cellular Cardiology*, 118, pp. 208–224. doi:10.1016/j.yjmcc.2018.04.003.

Sacconi, L., Ferrantini, C., Lotti, J., Coppini, R., Yan, P., Loew, L.M., Tesi, C., Cerbai, E., *et al.* (2012) 'Action potential propagation in transverse-axial tubular system is impaired in heart

failure', *Proceedings of the National Academy of Sciences*, 109(15), pp. 5815–5819. doi:10.1073/pnas.1120188109.

Saito, A., Seiler, S., Chu, A. and Fleischer, S. (1984) 'Preparation and morphology of sarcoplasmic reticulum terminal cisternae from rabbit skeletal muscle', *The Journal of Cell Biology*, 99(3), pp. 875–885. doi:10.1083/jcb.99.3.875.

Satin, J., Itzhaki, I., Rapoport, S., Schroder, E.A., Izu, L., Arbel, G., Beyar, R., Balke, C.W., *et al.* (2008) 'Calcium Handling in Human Embryonic Stem Cell-Derived Cardiomyocytes', *STEM CELLS*, 26(8), pp. 1961–1972. doi:10.1634/stemcells.2007-0591.

Satoh, H., Delbridge, L.M., Blatter, L.A. and Bers, D.M. (1996) 'Surface:volume relationship in cardiac myocytes studied with confocal microscopy and membrane capacitance measurements: species-dependence and developmental effects.', *Biophysical Journal*, 70(3), pp. 1494–1504.

Scheible, M.B. and Tinnefeld, P. (2018) 'Quantifying Expansion Microscopy with DNA Origami Expansion Nanorulers', *bioRxiv* [Preprint]. doi:10.1101/265405.

Seidel, T., Fiegle, D.J., Baur, T.J., Ritzer, A., Nay, S., Heim, C., Weyand, M., Milting, H., *et al.* (2019) 'Glucocorticoids preserve the t-tubular system in ventricular cardiomyocytes by upregulation of autophagic flux', *Basic Research in Cardiology*, 114(6), p. 47. doi:10.1007/s00395-019-0758-6.

Seidel, T., Navankasattusas, S., Ahmad, A., Diakos, N.A., Xu, W.D., Tristani-Firouzi, M., Bonios, M.J., Taleb, I., *et al.* (2017) 'Sheet-Like Remodeling of the Transverse Tubular System in Human Heart Failure Impairs Excitation-Contraction Coupling and Functional Recovery by Mechanical UnloadingClinical Perspective', *Circulation*, 135(17), pp. 1632–1645. doi:10.1161/circulationaha.116.024470.

Shang, W., Lu, F., Sun, T., Xu, J., Li, L.-L., Wang, Y., Wang, G., Chen, L., *et al.* (2014) 'Imaging Ca $^{2+}$ Nanosparks in Heart With a New Targeted Biosensor', *Circulation Research*, 114(3), pp. 412–420. doi:10.1161/CIRCRESAHA.114.302938.

Sheard, T.M.D., Kharche, S.R., Pinali, C. and Shiels, H.A. (2019) '3D ultrastructural organisation of calcium release units in the avian sarcoplasmic reticulum', *Journal of Experimental Biology*, 222(7), p. jeb197640. doi:10.1242/jeb.197640.

Shen, X., Brink, J.V.D., Hou, Y., Colli, D., Le, C., Kolstad, T.R., MacQuaide, N., Carlson, C.R., *et al.* (2018) '3D dSTORM imaging reveals novel detail of ryanodine receptor localization in rat cardiac myocytes', *J Physiol* [Preprint]. doi:10.1113/jp277360.

Shi, X., Li, Q., Dai, Z., Tran, A., Feng, S., Ramirez, A.D., Lin, Z., Wang, X., *et al.* (2019) 'Label-retention expansion microscopy', *bioRxiv*, p. 687954. doi:10.1101/687954.

Shiels, H.A. and Galli, G.L. (2014) 'The sarcoplasmic reticulum and the evolution of the vertebrate heart', *Physiology (Bethesda)*, 29(6), pp. 456–69. doi:10.1152/physiol.00015.2014.

Smith, A.J., Lewis, F.C., Aquila, I., Waring, C.D., Nocera, A., Agosti, V., Nadal-Ginard, B., Torella, D., *et al.* (2014) 'Isolation and characterization of resident endogenous c-Kit+ cardiac stem cells from the adult mouse and rat heart', *Nat Protoc*, 9(7), pp. 1662–81. doi:10.1038/nprot.2014.113.

Sobie, E.A., Guatimosim, S., Gómez-Viquez, L., Song, L.-S., Hartmann, H., Saleet Jafri, M. and Lederer, W.J. (2006) 'The Ca2+ leak paradox and "rogue ryanodine receptors": SR Ca2+ efflux theory and practice', *Progress in Biophysics and Molecular Biology*, 90(1), pp. 172–185. doi:10.1016/j.pbiomolbio.2005.06.010.

Soeller, C. and Cannell, M.B. (1997) 'Numerical simulation of local calcium movements during L-type calcium channel gating in the cardiac diad.', *Biophysical Journal*, 73(1), pp. 97–111.

Soeller, C. and Cannell, M.B. (1999) 'Examination of the transverse tubular system in living cardiac rat myocytes by 2-photon microscopy and digital image-processing techniques', *Circ Res*, 84(3), pp. 266–75.

Soeller, C., Crossman, D., Gilbert, R. and Cannell, M.B. (2007) 'Analysis of ryanodine receptor clusters in rat and human cardiac myocytes', *Proc Natl Acad Sci U S A*, 104(38), pp. 14958–63. doi:10.1073/pnas.0703016104.

Sommer, J.R. and Johnson, E.A. (1969) 'Cardiac muscle', *Zeitschrift für Zellforschung und Mikroskopische Anatomie*, 98(3), pp. 437–468. doi:10.1007/BF00346685.

Song, K.-H., Zhang, Y., Wang, G., Sun, C. and Zhang, H.F. (2019) 'Three-dimensional biplane spectroscopic single-molecule localization microscopy', *Optica*, 6(6), pp. 709–715. doi:10.1364/OPTICA.6.000709.

Song, L.-S., Sobie, E.A., McCulle, S., Lederer, W.J., Balke, C.W. and Cheng, H. (2006) 'Orphaned ryanodine receptors in the failing heart', *Proceedings of the National Academy of Sciences of the United States of America*, 103(11), pp. 4305–4310. doi:10.1073/pnas.0509324103.

Sossalla, S., Fluschnik, N., Schotola, H., Ort, K.R., Neef, S., Schulte, T., Wittköpper, K., Renner, A., *et al.* (2010) 'Inhibition of elevated Ca2+/calmodulin-dependent protein kinase II improves contractility in human failing myocardium', *Circulation Research*, 107(9), pp. 1150–1161. doi:10.1161/CIRCRESAHA.110.220418.

Spinozzi, S., Liu, C., Chen, Z., Feng, W., Zhang, L., Ouyang, K., Evans, S.M. and Chen, J. (2020) 'Nexilin Is Necessary for Maintaining the Transverse-Axial Tubular System in Adult Cardiomyocytes', *Circulation. Heart Failure*, 13(7), p. e006935. doi:10.1161/CIRCHEARTFAILURE.120.006935.

Stange, M., Xu, L., Balshaw, D., Yamaguchi, N. and Meissner, G. (2003) 'Characterization of recombinant skeletal muscle (Ser-2843) and cardiac muscle (Ser-2809) ryanodine receptor phosphorylation mutants', *The Journal of Biological Chemistry*, 278(51), pp. 51693–51702. doi:10.1074/jbc.M310406200.

Stensløkken, K.-O., Rutkovskiy, A., Kaljusto, M.-L., Hafstad, A.D., Larsen, T.S. and Vaage, J. (2009) 'Inadvertent phosphorylation of survival kinases in isolated perfused hearts: a word of caution', *Basic Research in Cardiology*, 104(4), pp. 412–423. doi:10.1007/s00395-009-0780-1.

Stern, M.D. (1992) 'Theory of excitation-contraction coupling in cardiac muscle', *Biophysical Journal*, 63(2), pp. 497–517. doi:10.1016/S0006-3495(92)81615-6.

Stones, R., Benoist, D., Peckham, M. and White, E. (2013) 'Microtubule proliferation in right ventricular myocytes of rats with monocrotaline-induced pulmonary hypertension', *Journal of Molecular and Cellular Cardiology*, 56, pp. 91–96. doi:10.1016/j.yjmcc.2012.12.010.

Sun, D., Fan, X., Zhang, H., Huang, Z., Tang, Q., Li, W., Bai, J., Lei, X., *et al.* (2020) 'Click-ExM enables expansion microscopy for all biomolecules', *bioRxiv*, p. 2020.03.19.998039. doi:10.1101/2020.03.19.998039.

Sun, X.H., Protasi, F., Takahashi, M., Takeshima, H., Ferguson, D.G. and Franzini-Armstrong, C. (1995) 'Molecular architecture of membranes involved in excitation-contraction coupling of cardiac muscle', *J Cell Biol*, 129(3), pp. 659–71.

Takahashi, K. and Yamanaka, S. (2006) 'Induction of pluripotent stem cells from mouse embryonic and adult fibroblast cultures by defined factors', *Cell*, 126(4), pp. 663–676. doi:10.1016/j.cell.2006.07.024.

Takeshima, H., Komazaki, S., Nishi, M., Iino, M. and Kangawa, K. (2000) 'Junctophilins: A Novel Family of Junctional Membrane Complex Proteins', *Molecular Cell*, 6(1), pp. 11–22. doi:10.1016/S1097-2765(05)00005-5.

Takeshima, H., Nishimura, S., Matsumoto, T., Ishida, H., Kangawa, K., Minamino, N., Matsuo, H., Ueda, M., *et al.* (1989) 'Primary structure and expression from complementary DNA of skeletal muscle ryanodine receptor', *Nature*, 339(6224), pp. 439–445. doi:10.1038/339439a0.

Tillberg, P.W., Chen, F., Piatkevich, K.D., Zhao, Y., Yu, C.C., English, B.P., Gao, L., Martorell, A., *et al.* (2016) 'Protein-retention expansion microscopy of cells and tissues labeled using standard fluorescent proteins and antibodies', *Nat Biotechnol*, 34(9), pp. 987–92. doi:10.1038/nbt.3625.

Tokunaga, M., Imamoto, N. and Sakata-Sogawa, K. (2008) 'Highly inclined thin illumination enables clear single-molecule imaging in cells', *Nature Methods*, 5(2), pp. 159–161. doi:10.1038/nmeth1171.

de Tombe, P.P. and ter Keurs, H.E.D.J. (2016) 'Cardiac muscle mechanics: Sarcomere length matters', *Journal of molecular and cellular cardiology*, 91, pp. 148–150. doi:10.1016/j.yjmcc.2015.12.006.

Truckenbrodt, S., Maidorn, M., Crzan, D., Wildhagen, H., Kabatas, S. and Rizzoli, S.O. (2018) 'X10 expansion microscopy enables 25-nm resolution on conventional microscopes', *EMBO reports*, p. e45836. doi:10.15252/embr.201845836.

Truckenbrodt, S., Sommer, C., Rizzoli, S.O. and Danzl, J.G. (2019) 'A practical guide to optimization in X10 expansion microscopy', *Nature Protocols* [Preprint]. doi:10.1038/s41596-018-0117-3.

Uchinoumi, H., Yang, Y., Oda, T., Li, N., Alsina, K.M., Puglisi, J.L., Chen-Izu, Y., Cornea, R.L., *et al.* (2016) 'CaMKII-dependent phosphorylation of RyR2 promotes targetable pathological RyR2 conformational shift', *Journal of Molecular and Cellular Cardiology*, 98, pp. 62–72. doi:10.1016/j.yjmcc.2016.06.007.

Uehara, A., Yasukochi, M., Mejía-Alvarez, R., Fill, M. and Imanaga, I. (2002) 'Gating kinetics and ligand sensitivity modified by phosphorylation of cardiac ryanodine receptors', *Pflügers Archiv*, 444(1), pp. 202–212. doi:10.1007/s00424-002-0791-3.

Ujihara, Y., Mohri, S. and Katanosaka, Y. (2016) 'Effects of induced Na+/Ca2+ exchanger overexpression on the spatial distribution of L-type Ca2+ channels and junctophilin-2 in pressure-overloaded hearts', *Biochemical and Biophysical Research Communications*, 480(4), pp. 564–569. doi:10.1016/j.bbrc.2016.10.090.

Ullrich, N.D., Valdivia, H.H. and Niggli, E. (2012) 'PKA phosphorylation of cardiac ryanodine receptor modulates SR luminal Ca2+ sensitivity', *Journal of Molecular and Cellular Cardiology*, 53(1), pp. 33–42. doi:10.1016/j.yjmcc.2012.03.015.

Vatta, M., Stetson, S.J., Perez-Verdia, A., Entman, M.L., Noon, G.P., Torre-Amione, G., Bowles, N.E. and Towbin, J.A. (2002) 'Molecular remodelling of dystrophin in patients with end-stage cardiomyopathies and reversal in patients on assistance-device therapy', *Lancet*, 359(9310), pp. 936–41. doi:10.1016/s0140-6736(02)08026-1.

Vaziri, A., Tang, J., Shroff, H. and Shank, C.V. (2008) 'Multilayer three-dimensional super resolution imaging of thick biological samples', *Proceedings of the National Academy of Sciences*, 105(51), pp. 20221–20226. doi:10.1073/pnas.0810636105.

Vicinanza, C., Aquila, I., Scalise, M., Cristiano, F., Marino, F., Cianflone, E., Mancuso, T., Marotta, P., *et al.* (2017) 'Adult cardiac stem cells are multipotent and robustly myogenic: c-kit expression is necessary but not sufficient for their identification', *Cell Death and Differentiation*, 24(12), pp. 2101–2116. doi:10.1038/cdd.2017.130.

Wagner, E., Lauterbach, M.A., Kohl, T., Westphal, V., Williams, G.S., Steinbrecher, J.H., Streich, J.H., Korff, B., *et al.* (2012) 'Stimulated emission depletion live-cell super-resolution imaging shows proliferative remodeling of T-tubule membrane structures after myocardial infarction', *Circ Res*, 111(4), pp. 402–14. doi:10.1161/circresaha.112.274530.

Walker, M.A., Williams, G.S.B., Kohl, T., Lehnart, S.E., Jafri, M.S., Greenstein, J.L., Lederer, W.J. and Winslow, R.L. (2014) 'Superresolution modeling of calcium release in the heart', *Biophysical Journal*, 107(12), pp. 3018–3029. doi:10.1016/j.bpj.2014.11.003.

Walweel, K., Gomez-Hurtado, N., Rebbeck, R.T., Oo, Y.W., Beard, N.A., Molenaar, P., Remedios, C. dos, Helden, D.F. van, *et al.* (2019) 'Calmodulin inhibition of human RyR2 channels requires phosphorylation of RyR2-S2808 or RyR2-S2814', *Journal of Molecular and Cellular Cardiology*, 130, pp. 96–106. doi:10.1016/j.yjmcc.2019.03.018.

Wang, H., Naghavi, M., Allen, C., Barber, R.M., Bhutta, Z.A., Carter, A., Casey, D.C., Charlson, F.J., *et al.* (2016) 'Global, regional, and national life expectancy, all-cause mortality, and cause-specific mortality for 249 causes of death, 1980–2015: a systematic analysis for the Global Burden of Disease Study 2015', *The Lancet*, 388(10053), pp. 1459–1544. doi:10.1016/S0140-6736(16)31012-1.

Wang, W., Landstrom, A.P., Wang, Q., Munro, M.L., Beavers, D., Ackerman, M.J., Soeller, C. and Wehrens, X.H.T. (2014) 'Reduced junctional Na+/Ca2+-exchanger activity contributes to sarcoplasmic reticulum Ca2+ leak in junctophilin-2-deficient mice', *American Journal of*

Physiology-Heart and Circulatory Physiology, 307(9), pp. H1317–H1326. doi:10.1152/ajpheart.00413.2014.

Wang, Y., Yu, Z., Cahoon, C.K., Parmely, T., Thomas, N., Unruh, J.R., Slaughter, B.D. and Hawley, R.S. (2018) 'Combined expansion microscopy with structured illumination microscopy for analyzing protein complexes', *Nature Protocols* [Preprint]. doi:10.1038/s41596-018-0023-8.

Wehrens, X.H.T., Lehnart, S.E., Reiken, S., Vest, J.A., Wronska, A. and Marks, A.R. (2006) 'Ryanodine receptor/calcium release channel PKA phosphorylation: a critical mediator of heart failure progression', *Proceedings of the National Academy of Sciences of the United States of America*, 103(3), pp. 511–518. doi:10.1073/pnas.0510113103.

Wehrens, X.H.T., Lehnart Stephan E., Reiken Steven R., and Marks Andrew R. (2004) 'Ca2+/Calmodulin-Dependent Protein Kinase II Phosphorylation Regulates the Cardiac Ryanodine Receptor', *Circulation Research*, 94(6), pp. e61–e70. doi:10.1161/01.RES.0000125626.33738.E2.

Wei, S., Guo, A., Chen, B., Kutschke, W., Xie, Y.P., Zimmerman, K., Weiss, R.M., Anderson, M.E., *et al.* (2010) 'T-tubule remodeling during transition from hypertrophy to heart failure', *Circ Res*, 107(4), pp. 520–31. doi:10.1161/circresaha.109.212324.

Wen, J., Wang, J., Tang, X., Deng, S., Dai, J., Li, X. and Cai, W. (2019) 'DHT deteriorates the progression of monocrotaline-induced pulmonary arterial hypertension: effects of endogenous and exogenous androgen', *American Journal of Translational Research*, 11(9), pp. 5752–5763.

Winterflood, C.M., Platonova, E., Albrecht, D. and Ewers, H. (2015) 'Dual-color 3D superresolution microscopy by combined spectral-demixing and biplane imaging', *Biophysical Journal*, 109(1), pp. 3–6. doi:10.1016/j.bpj.2015.05.026.

Witcher, D.R., Kovacs, R.J., Schulman, H., Cefali, D.C. and Jones, L.R. (1991) 'Unique phosphorylation site on the cardiac ryanodine receptor regulates calcium channel activity', *The Journal of Biological Chemistry*, 266(17), pp. 11144–11152.

Wu, Y., Temple Joel, Zhang Rong, Dzhura Igor, Zhang Wei, Trimble Robert, Roden Dan M., Passier Robert, *et al.* (2002) 'Calmodulin Kinase II and Arrhythmias in a Mouse Model of Cardiac Hypertrophy', *Circulation*, 106(10), pp. 1288–1293. doi:10.1161/01.CIR.0000027583.73268.E7.

Wypijewski, K.J., Tinti, M., Chen, W., Lamont, D., Ashford, M.L.J., Calaghan, S.C. and Fuller, W. (2015) 'Identification of Caveolar Resident Proteins in Ventricular Myocytes Using a Quantitative Proteomic Approach: Dynamic Changes in Caveolar Composition Following Adrenoceptor Activation', *Molecular & Cellular Proteomics*, 14(3), pp. 596–608. doi:10.1074/mcp.M114.038570.

Xiao, B., Jiang, M.T., Zhao, M., Yang, D., Sutherland, C., Lai, F.A., Walsh, M.P., Warltier, D.C., *et al.* (2005) 'Characterization of a novel PKA phosphorylation site, serine-2030, reveals no PKA hyperphosphorylation of the cardiac ryanodine receptor in canine heart failure', *Circulation Research*, 96(8), pp. 847–855. doi:10.1161/01.RES.0000163276.26083.e8.

Xiao, B., Zhong, G., Obayashi, M., Yang, D., Chen, K., Walsh, M.P., Shimoni, Y., Cheng, H., *et al.* (2006) 'Ser-2030, but not Ser-2808, is the major phosphorylation site in cardiac ryanodine

receptors responding to protein kinase A activation upon β-adrenergic stimulation in normal and failing hearts', *Biochemical Journal*, 396(1), pp. 7–16. doi:10.1042/BJ20060116.

Xie, Y.P., Chen, B., Sanders, P., Guo, A., Li, Y., Zimmerman, K., Wang, L.C., Weiss, R.M., *et al.* (2012) 'Sildenafil prevents and reverses transverse-tubule remodeling and Ca(2+) handling dysfunction in right ventricle failure induced by pulmonary artery hypertension', *Hypertension*, 59(2), pp. 355–62. doi:10.1161/hypertensionaha.111.180968.

Xu, H., Tong, Z., Ye, Q., Sun, T., Hong, Z., Zhang, L., Bortnick, A., Cho, S., *et al.* (2019) 'Molecular organization of mammalian meiotic chromosome axis revealed by expansion STORM microscopy', *Proceedings of the National Academy of Sciences*, p. 201902440. doi:10.1073/pnas.1902440116.

Xu, M., Wu, H.D., Li, R.C., Zhang, H.B., Wang, M., Tao, J., Feng, X.H., Guo, Y.B., *et al.* (2012) 'Mir-24 regulates junctophilin-2 expression in cardiomyocytes', *Circ Res*, 111(7), pp. 837–41. doi:10.1161/circresaha.112.277418.

Xu, M., Zhou, P., Xu, S.-M., Liu, Y., Feng, X., Bai, S.-H., Bai, Y., Hao, X.-M., *et al.* (2007) 'Intermolecular failure of L-type Ca2+ channel and ryanodine receptor signaling in hypertrophy', *PLoS biology*, 5(2), p. e21. doi:10.1371/journal.pbio.0050021.

Xun, A., Curran Jerry W., Shannon Thomas R., Bers Donald M., and Pogwizd Steven M. (2005) 'Ca2+/Calmodulin–Dependent Protein Kinase Modulates Cardiac Ryanodine Receptor Phosphorylation and Sarcoplasmic Reticulum Ca2+ Leak in Heart Failure', *Circulation Research*, 97(12), pp. 1314–1322. doi:10.1161/01.RES.0000194329.41863.89.

Yan, Z., Bai, X., Yan, C., Wu, J., Li, Z., Xie, T., Peng, W., Yin, C., *et al.* (2015) 'Structure of the rabbit ryanodine receptor RyR1 at near-atomic resolution', *Nature*, 517(7532), pp. 50–55. doi:10.1038/nature14063.

Yoshie, H., Tobise, K. and Onodera, S. (1994) 'INTRAVENTRICULAR CHANGES IN THE β-ADRENOCEPTOR-ADENYLATE CYCLASE SYSTEM OF THE RAT HEART WITH THE PROGRESS OF MONOCROTALINE-INDUCED RIGHT VENTRICULAR HYPERTROPHY', *Japanese Circulation Journal*, 58(11), pp. 855–865. doi:10.1253/jcj.58.855.

Yu, C.-C. (Jay), Barry, N.C., Wassie, A.T., Sinha, A., Bhattacharya, A., Asano, S., Zhang, C., Chen, F., *et al.* (2020) 'Expansion microscopy of C. elegans', *eLife*. Edited by A.F. Dernburg and D. Ron, 9, p. e46249. doi:10.7554/eLife.46249.

Yuchi, Z., Lau, K. and Van Petegem, F. (2012) 'Disease mutations in the ryanodine receptor central region: crystal structures of a phosphorylation hot spot domain', *Structure (London, England: 1993)*, 20(7), pp. 1201–1211. doi:10.1016/j.str.2012.04.015.

Zhang, C., Chen, B., Guo, A., Zhu, Y., Miller, J.D., Gao, S., Yuan, C., Kutschke, W., *et al.* (2014) 'Microtubule-Mediated Defects in Junctophilin-2 Trafficking Contribute to Myocyte Transverse-Tubule Remodeling and Ca2+ Handling Dysfunction in Heart Failure', *Circulation*, 129(17), pp. 1742–1750. doi:10.1161/circulationaha.113.008452.

Zhang, G.Q., Wei, H., Lu, J., Wong, P. and Shim, W. (2013) 'Identification and Characterization of Calcium Sparks in Cardiomyocytes Derived from Human Induced Pluripotent Stem Cells', *PLOS ONE*, 8(2), p. e55266. doi:10.1371/journal.pone.0055266.

Zhang, H., Cannell, M.B., Kim, S.J., Watson, J.J., Norman, R., Calaghan, S.C., Orchard, C.H. and James, A.F. (2015) 'Cellular Hypertrophy and Increased Susceptibility to Spontaneous Calcium-Release of Rat Left Atrial Myocytes Due to Elevated Afterload', *PLOS ONE*, 10(12), p. e0144309. doi:10.1371/journal.pone.0144309.

Zhang, H., Makarewich, C.A., Kubo, H., Wang, W., Duran, J.M., Li, Y., Berretta, R.M., Koch, W.J., *et al.* (2012) 'Hyperphosphorylation of the cardiac ryanodine receptor at serine 2808 is not involved in cardiac dysfunction after myocardial infarction', *Circulation Research*, 110(6), pp. 831–840. doi:10.1161/CIRCRESAHA.111.255158.

Zhang, H.B., Li, R.C., Xu, M., Xu, S.M., Lai, Y.S., Wu, H.D., Xie, X.J., Gao, W., *et al.* (2013) 'Ultrastructural uncoupling between T-tubules and sarcoplasmic reticulum in human heart failure', *Cardiovasc Res*, 98(2), pp. 269–76. doi:10.1093/cvr/cvt030.

Zhang, J., Liu, Z., Masumiya, H., Wang, R., Jiang, D., Li, F., Wagenknecht, T. and Chen, S.R.W. (2003) 'Three-dimensional localization of divergent region 3 of the ryanodine receptor to the clamp-shaped structures adjacent to the FKBP binding sites', *The Journal of Biological Chemistry*, 278(16), pp. 14211–14218. doi:10.1074/jbc.M213164200.

Zhang, S., Liu, Z., Zou, C. and Wang, L. (2012) 'Effect of metoprolol on sarcoplasmic reticulum Ca2+ leak in a rabbit model of heart failure', *Chinese Medical Journal*, 125(5), p. 815. doi:10.3760/cma.j.issn.0366-6999.2012.05.016.

Zhang, X. and Morad, M. (2020) 'Ca2+ signaling of human pluripotent stem cells-derived cardiomyocytes as compared to adult mammalian cardiomyocytes', *Cell Calcium*, 90, p. 102244. doi:10.1016/j.ceca.2020.102244.

Zhang, X.-H., Haviland, S., Wei, H., Sarić, T., Fatima, A., Hescheler, J., Cleemann, L. and Morad, M. (2013) 'Ca2+ signaling in human induced pluripotent stem cell-derived cardiomyocytes (iPS-CM) from normal and catecholaminergic polymorphic ventricular tachycardia (CPVT)-afflicted subjects', *Cell Calcium*, 54(2), pp. 57–70. doi:10.1016/j.ceca.2013.04.004.

Zhang, X.-H., Wei, H., Šarić, T., Hescheler, J., Cleemann, L. and Morad, M. (2015) 'Regionally diverse mitochondrial calcium signaling regulates spontaneous pacing in developing cardiomyocytes', *Cell Calcium*, 57(5–6), pp. 321–336. doi:10.1016/j.ceca.2015.02.003.

Zhao, Y., Bucur, O., Irshad, H., Chen, F., Weins, A., Stancu, A.L., Oh, E.Y., DiStasio, M., *et al.* (2017) 'Nanoscale imaging of clinical specimens using pathology-optimized expansion microscopy', *Nat Biotechnol* [Preprint]. doi:10.1038/nbt.3892.

Ziman, A.P., Gomez-Viquez, N.L., Bloch, R.J. and Lederer, W.J. (2010) 'Excitation-contraction coupling changes during postnatal cardiac development', *J Mol Cell Cardiol*, 48(2), pp. 379–86. doi:10.1016/j.yjmcc.2009.09.016.

Zuo, X.-R., Wang, Q., Cao, Q., Yu, Y.-Z., Wang, Hui, Bi, L.-Q., Xie, W.-P. and Wang, Hong (2012) 'Nicorandil Prevents Right Ventricular Remodeling by Inhibiting Apoptosis and Lowering Pressure Overload in Rats with Pulmonary Arterial Hypertension', *PLOS ONE*, 7(9), p. e44485. doi:10.1371/journal.pone.0044485.

Appendix - main abbreviations

CICR - Ca^{2+}-induced Ca^{2+} release

CRU - Ca^{2+} release unit

CVD - cardiovascular disease

DNA-PAINT - DNA point accumulation for imaging in nanoscale topography

dSTORM - direct STORM

EC - excitation-contraction

EF - expansion factor

ExM - expansion microscopy

FWHM - full width half maximum

HF - heart failure

JPH - junctophilin 2

LTCC - L-type Ca^{2+} channel

LV - left ventricle

MCT – monocrotaline

NND – nearest neighbour distance

PAH - pulmonary arterial hypertension

P_o – open probability

proExM - protein retention ExM

PSF - point spread function

RV - right ventricle

RyR - ryanodine receptor

SC-CM – stem cell-derived cardiomyocyte

iPSC-CM – induced pluripotent stem cell-derived cardiomyocyte

eCSC-CM – endogenous cardiac stem cell-derived cardiomyocyte

SL - sarcomere length

SMLM - single molecule localization microscopy

SR - sarcoplasmic reticulum

X10 - X10 expansion microscopy

10x EExM – 10x enhanced expansion microscopy